ADVANCED SIGNAL PROCESSING STRATEGIES FOR SEARCH AND RESCUE SATELLITE AIDED TRACKING

By

© KWAI-SUM, THOMAS CHUNG, B.Eng., M. Eng.

A Thesis

Submitted to the School of Graduate Studies

in Partial Fulfilment of the Requirements

for the Degree

Doctor of Philosophy

McMaster University

October 1988

ADVANCED SIGNAL PROCESSING STRATEGIES FOR SARSAT

TO MARIA

Doctor of Philosophy (1988)
(Electrical Engineering)

McMASTER UNIVERSITY
Hamilton, Ontario

TITLE: ADVANCED SIGNAL PROCESSING STRATEGIES FOR SEARCH AND RESCUE SATELLITE AIDED TRACKING

AUTHOR: Kwai-Sum Thomas Chung,
B.Eng. (McMaster University, 1980)
M. Eng. (McMaster University, 1982)

SUPERVISOR: Dr. C.R. Carter.

NUMBER OF PAGES: xix, 172

ABSTRACT

Search and rescue satellite aided tracking (SARSAT) involves the use of satellites in low-polar orbits which relay the emergency signals of distressed vehicles to an earth station for signal analysis. A significant number of lives have been saved by using SARSAT. The program originated from the efforts of the three member countries of Canada, the United States and France who formed a joint venture with the Soviet Union in a program referred to as COSPAS/SARSAT. Since then, the United Kingdom, Norway and Sweden have joined the program and it is expected that the system will be used worldwide.

In this thesis, three different models for emergency locator transmitter (ELT) signals are proposed. Some basic concepts and a theoretical analysis of the spectra produced by these signal models are studied. The first model, the Ideal Coherent Model ELT, produces a highly idealized spectrum which does not exist in practice. The second model, the Non-Ideal Coherent Model ELT, is capable of producing a wide range of spectra which can be closely related to actual ELT signals. Mathematical analysis identifies a design problem not previously recognized and provides the basis for a new design specification which should become mandatory. The third model, the Non-Coherent Model ELT, represents a class of ELT signals having very poor spectral properties. This type of ELT design should be avoided.

The performance of several different signal processors is evaluated using real ELT signals. The periodogram gives good performance for coherent ELT signals. However, the linear spectral estimation technique is not suitable for determining carrier frequency for non-coherent ELT signals. Use of a modified maximum entropy method in detecting these type of signals is demonstrated. In addition, spectrum ranking, sub-group averaging and spectrum levelling are found to benefit the spectral performance of the signal processors.

In SARSAT signal environment, it is possible to receive many simultaneous emergency beacon signals combined with interference of various types. The thesis also examines the sources of interference which enter the 121.5/243 MHz frequency bands of the SARSAT system.

ACKNOWLEDGEMENTS

I would like to express my sincere thanks to Dr. C.R. Carter, for his support and guidance throughout the course of this research. I also gratefully acknowledge the contributions of Dr. K.M. Wong and Dr. T.J. Kennett for serving on my supervisory committee.

Special thanks go to H.L. Werstiuk, Dr. E.J. Hayes, Dr. R. Bibby, J.V. King and R.J. Keightley of the SARSAT group at the Communications Research Centre, Ottawa, for their many stimulating discussions and enthusiastically supporting this program. I also acknowledge the Canadian Department of National Defense for allowing use of the dot charts of satellite pass data. I also thank the support of the Natural Sciences and Engineering Research Council of Canada for funding this project through a strategic grant.

I am most thankful to Dr. Q.T. Zhang and Dr. M. Shafi for the numerous discussions which allowed me to gain a further insight into the problems that I encountered. I also wish to thank my friends and colleagues at the Communications Research Laboratory at McMaster University for participating in many lively discussions.

I wish to thank Engineering Word Processing for being so cooperative and helpful in the typing of this manuscript.

Finally, my deepest gratitude is reserved for my wife, Maria, whose patience and encouragement helped me to complete this work.

TABLE OF CONTENTS

TABLE OF CONTENTS (continued)

TABLE OF CONTENTS (continued)

TABLE OF CONTENTS (continued)

LIST OF ILLUSTRATIONS

LIST OF ILLUSTRATIONS (continued)

LIST OF ILLUSTRATIONS (continued)

LIST OF ILLUSTRATIONS (continued)

LIST OF ILLUSTRATIONS (continued)

LIST OF ILLUSTRATIONS (continued)

LIST OF ILLUSTRATIONS (continued)

LIST OF ILLUSTRATIONS (continued)

LIST OF ILLUSTRATIONS (continued)

LIST OF TABLES

CHAPTER 1
INTRODUCTION

1.1 SARSAT PROGRAM

The primary objective of Search And Rescue Satellite-Aided Tracking (SARSAT) is to locate distressed aircraft. The system became a reality with the launch of a Soviet satellite in the summer of 1982. Since that time, two more Soviet satellites and two American satellites have been launched and a significant number of rescues have taken place thus demonstrating the success of the program [1-4]. Originally the program involved Canada, the United States and France forming the SARSAT group while the Soviet Union established a separate but compatible program called COSPAS with the overall program being referred to as COSPAS/SARSAT. More recently, the United Kingdom, Norway and Sweden have joined the program and other countries will soon be involved.

The system, illustrated in Fig. 1.1, relies on the use of the emergency locator transmitter (ELT) unit which is carried by aircraft or the emergency position indicating radio beacon (EPIRB) used by marine vessels and activated in times of emergency. Since the equipment is similar in operation, only the ELT signals will be described and will be referred to simply as 'emergency signals'. The ELT signal radiates from a whip antenna in all directions and is received by an orbiting satellite as it sweeps out a path over the search and rescue region of interest. The satellite is at 850 km polar orbit. A repeater on board the satellite relays the emergency signal to an earth station where the signal is analysed to extract the position of the accident. Note that it is necessary for both the accident site and earth station to be within sight of the satellite simultaneously.

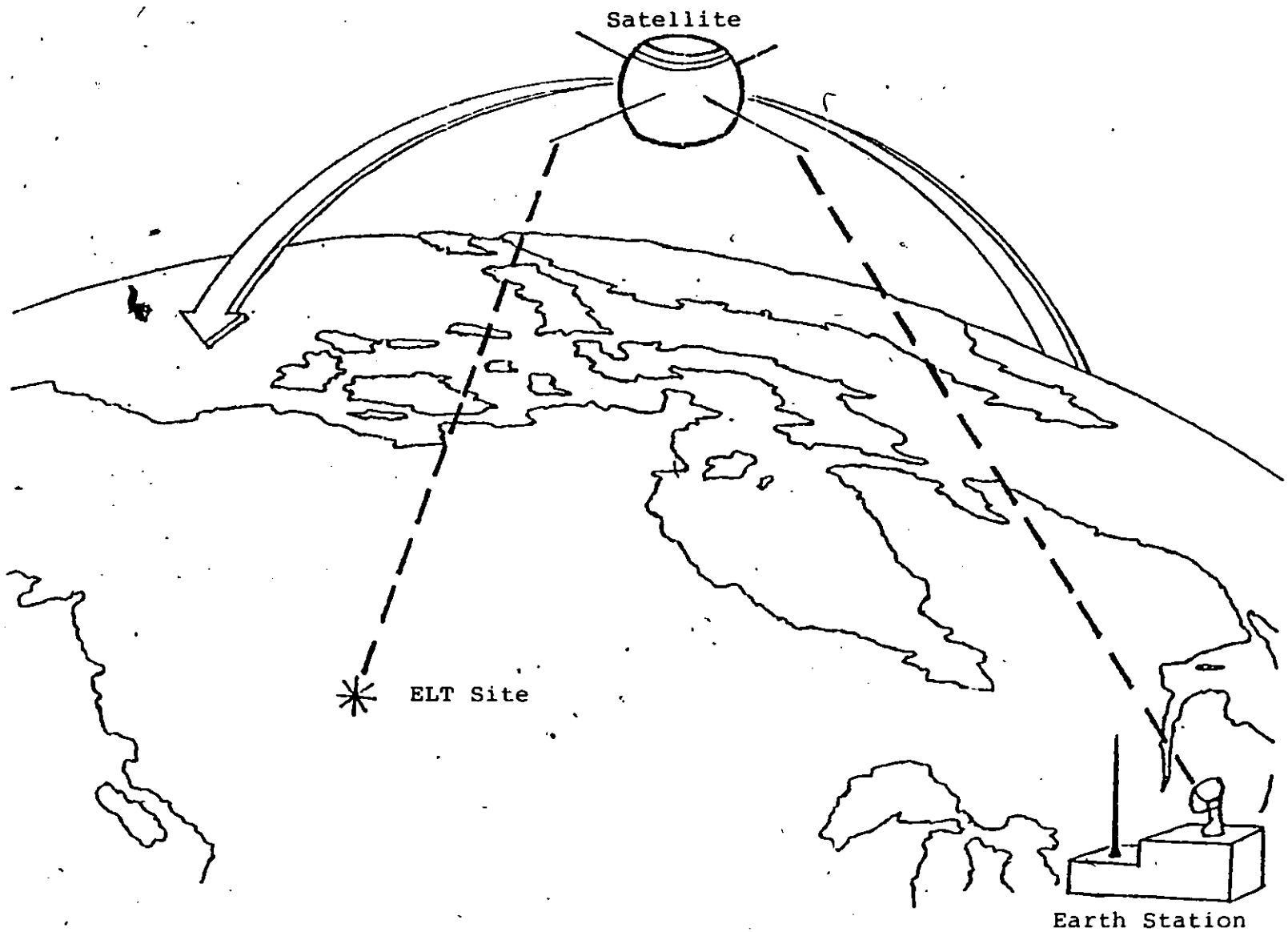

Fig. 1.1 A schematic diagram of COSPAS/SARSAT system.

Due to the relative motion between the satellite and ELT source, the signal received at the spacecraft is Doppler shifted, as illustrated in Fig. 1.2. The zero Doppler shift frequency occurs at the inflection point of the Doppler curve and is the point of closest approach of the satellite to the accident site. Consequently, this frequency must be determined with as much accuracy as possible since the slope of the Doppler curve at this point is used to calculate the range from satellite to transmitting source. With the range and the known position of the satellite, the location of emergency signal source can be estimated. This estimate is passed to a Rescue Coordination Centre (RCC) which speedily dispatches search aircraft to the emergency site.

The main advantages of SARSAT are: 1) the satellite has a wide field of view and one pass covers many thousands of square kilometers; 2) an early indication of a possible air crash or marine accident is given by simply receiving the emergency signal; 3) the ELT or EPIRB location is calculated thus eliminating grid searches by aircraft which are usually time-consuming and expensive; 4) the estimate of ELT or EPIRB location is improved with further passes of the satellites; 5) an approximate time of the incident is provided simply by noting when the signal is first received: and 6) by detailed signal analysis, the ELT or EPIRB can be identified as to type and possibly manufacture.

One of the key factors in estimating the location of a distressed vehicle, is the measurement of carrier frequency of the ELT signal. Many problems exist in measuring this frequency using automatic processing by computer, since: 1) the signal is far from ideal due to the modulation and variations in carrier frequency; 2) a significant change in Doppler shift may exist from second to second due to motion of the spacecraft; 3) the signal of interest may well be immersed in a background of a large number of false alarms (false alarms are emergency signals accidently activated by platforms not in distress), satellite receiver noise, and interference from myriad sources (terrestrial and airborne). Replacing the existing ELT

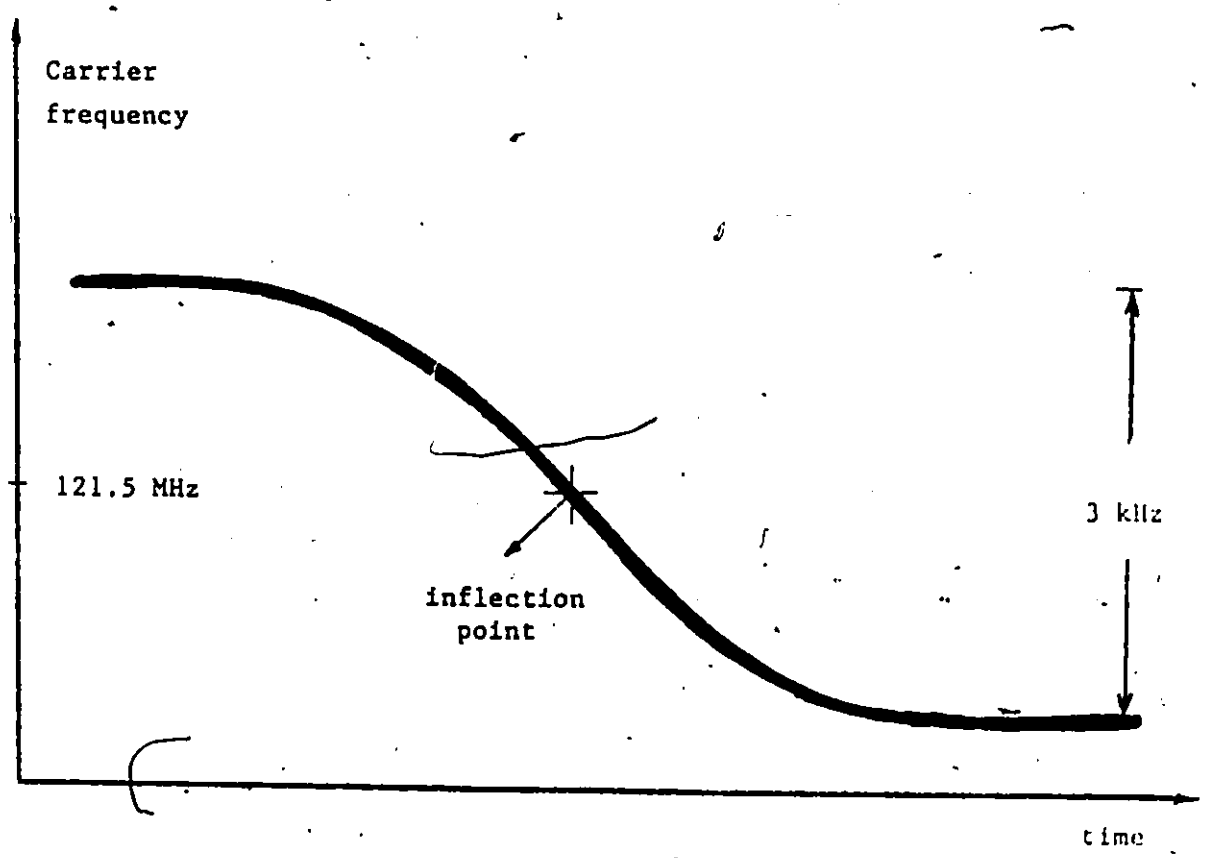

Fig. 1.2 ELT carrier frequency versus time showing the Doppler shift as a function of time.

and EPIRB units with new improved models is impractical since over 500,000 units are now in the field worldwide. Thus, it is important to develop methods for processing the existing emergency signals.

1.2 SCOPE OF THESIS

The primary problem encountered for the SARSAT system is that the ELT signals are far from ideal. Thus, an array of different methods is required in order to best accommodate the different signals. This dissertation investigates modern signal processing strategies as applied to SARSAT system.

In Chapter 2, three different models for ELT signals are proposed. The first model, the Ideal Coherent model ELT, produces a highly idealized spectrum which does not exist in practice. The second model, the Non-Ideal Coherent model ELT, is capable of producing a wide range of spectra which can be closely related to actual ELT signals. Mathematical analysis identifies a design problem not previously recognized and provides the basis for a new design specification which should become mandatory. The third model, the Non-Coherent model ELT, represents a class of ELT signals having very poor spectral properties. This type of ELT model design should be avoided.

The basic concepts in the processing of real and computer generated ELT signals are presented in Chapter 3. The issues covered in this thesis include spectral estimators, receiver noise, Doppler frequency shift and carrier frequency stability. The discussion provides an insight into the benefits of signal processing methods.

The performance of several different signal processors using real ELT signals are evaluated in Chapter 4. The matched filter technique offers results with the maximum signal-to-noise ratio, but the implementation is very costly. The periodogram gives good performance for coherent ELT signals. However, the method is incapable of determining

carrier frequency for Non-Coherent ELT signals. Use of the modified maximum entropy method in detecting these Non-Coherent ELT signals is demonstrated.

Two post-processing techniques are introduced in Chapter 5. The order statistic technique reduces the interference produced by the ELT sidebands while maintaining good detection performances on weak signals. The spectrum leveller technique provides a better detection thresholding.

Chapter 6 provides a survey of interfering sources in the frequency band of SARSAT system. The interference can be classified as continuous wave, narrowband and wideband. The effects of interference on the SARSAT system and how this interference may affect the processing of ELT signals are also discussed in this chapter. In addition, examples of interference received by the SARSAT system are examined and three different methods of measuring the satellite pass activity are described.

The final chapter gives conclusions of the investigation and suggestions for further research for SARSAT program.

CHAPTER 2

ELT SIGNAL ANALYSIS

2.1 ELT SIGNALS

The emergency locator transmitter is a low-power radio transmitter (100 mW) which emits an amplitude modulated carrier signal. Typical ELT units use very simple circuits, having in some cases poor, short-term carrier oscillator stability due to variations in the power supply voltage or loading of the carrier oscillator caused by the modulation being applied to the amplifier stages.

The emergency signal, illustrated in Fig. 2.1, comprises N pulse-null pairs each of duration T_i where $1 \leq i \leq N$ [5]. The 'ON' pulse duration is dT_i where d is the duty cycle. In practice, a small amount of signal may be present in the null portion but its contribution to the power spectrum is negligible. Usually T_1 is of the order of 0.7 ms and T_N is approximately 1.7 ms and the duration varies in an exponential manner, as shown.

The carrier frequency of the ELT signal is 121.5 MHz, with an optional value of 243 MHz. The total sweep duration T_S ranges from 0.25 s to 0.5 s and the sweep is repetitive. A summary of the pertinent specifications is given in Table. 2.1. Our discussion centres on the use of the 121.5 MHz carrier although the results also apply to the 243 MHz signal. A new band of frequency at 406 MHz is in the experimental stage and this will not be addressed. The distress signal received at the earth station is converted to a frequency band between 0 and 25 KHz. The nominal value of any ELT signal is 121.5 MHz and this is mixed to fall at the bandcenter frequency of 12.5 KHz. Due to satellite motion, there is a Doppler frequency shift in the signal of up to about ±3 KHz for the ELT signals and a further ±3 KHz spread due to

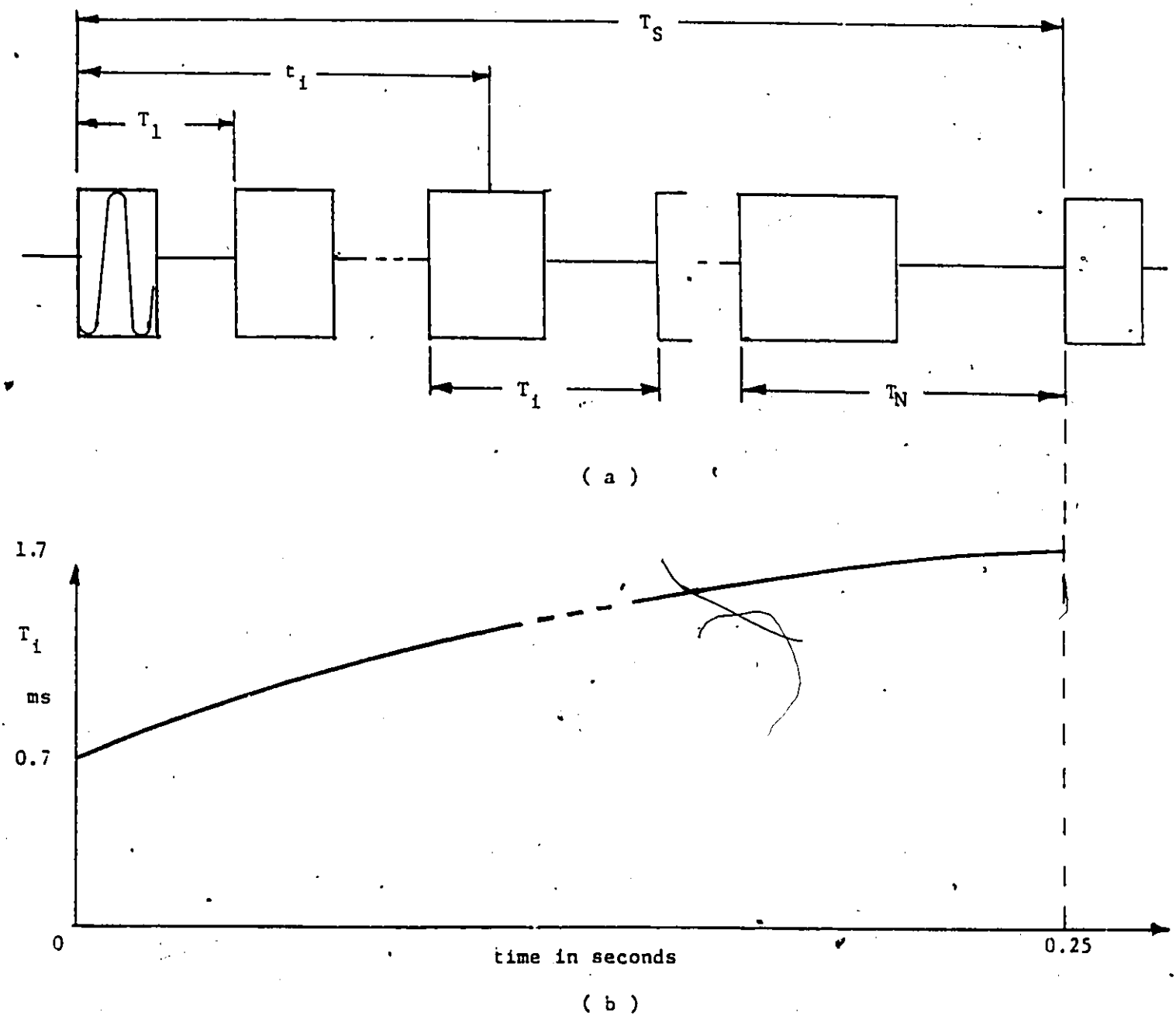

Fig. 2.1 (a) ELT signal comprising N pulse-null pairs of carrier.
(b) Variation in duration of the pulse-null pairs versus time.

carrier frequency	121.5 MHz (optional 243 MHz)
frequency tolerance	±50 ppm
power output	approximately 100 mW
modulation type	pulse
pulse duration	33% to 55%
percentage modulation	>85%
modulation frequency	downward swept
sweep rate	2 to 4 sweeps/second
modulation frequency change	700 Hz minimum
modulation frequency limits	300-1600 Hz

Table 2.1 ELT signal specifications.

differences in crystal operation between ELT units. Thus, the 25 KHz bandwidth appears to be adequate although some signals may fall outside this range.

2.2 ELT MODELS

There is a multitude of equipment manufacturers producing ELT units having different characteristics within the range of the specifications. In general, the ELT units can be divided into three models. The Ideal Coherent Model produces a highly idealized spectrum which is not found to exist in practice. The second model called the Non-Ideal Coherent Model is capable of producing a wide range of spectra and represents a large number of real ELT signals. Use of this model leads to a new design specification which should become mandatory. The third model called the Non-Coherent Model demonstrates the degradation caused by not providing continuous operation of the ELT carrier oscillator.

2.2.1 Ideal Coherent Model

The Ideal Coherent Model, includes those units which can be represented by a constant frequency oscillator that is switched to the power amplifier as illustrated in Fig. 2.2(a). We see that in Fig. 2.2(b), the phase from pulse to pulse is continuous.

2.2.2 Non-Ideal Coherent Model

The Non-Ideal Coherent Model can also be represented by Fig. 2.2. However, it is possible that the frequency of the carrier oscillator during the ON time is slightly different from the value during the OFF time. This change can be caused by: 1) a variation in power supply voltage feeding the oscillator due to the change in load current supplied to the power amplifier, or 2) a variation in the input impedance to the switch as seen by the crystal oscillator as the switch is opened and closed.

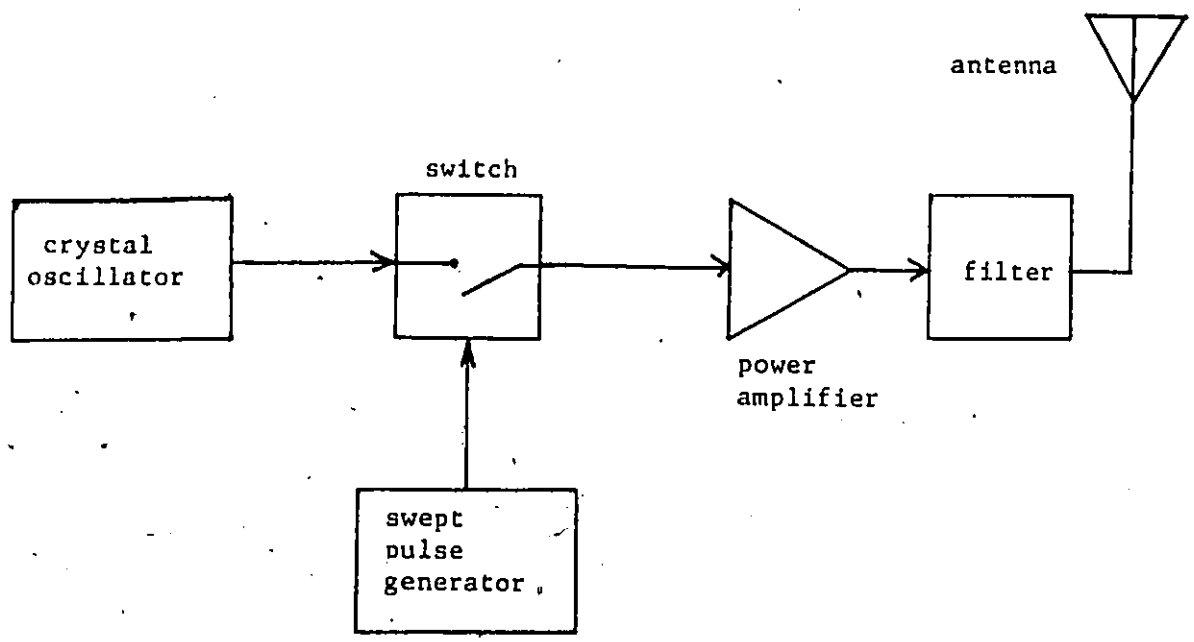

(a)

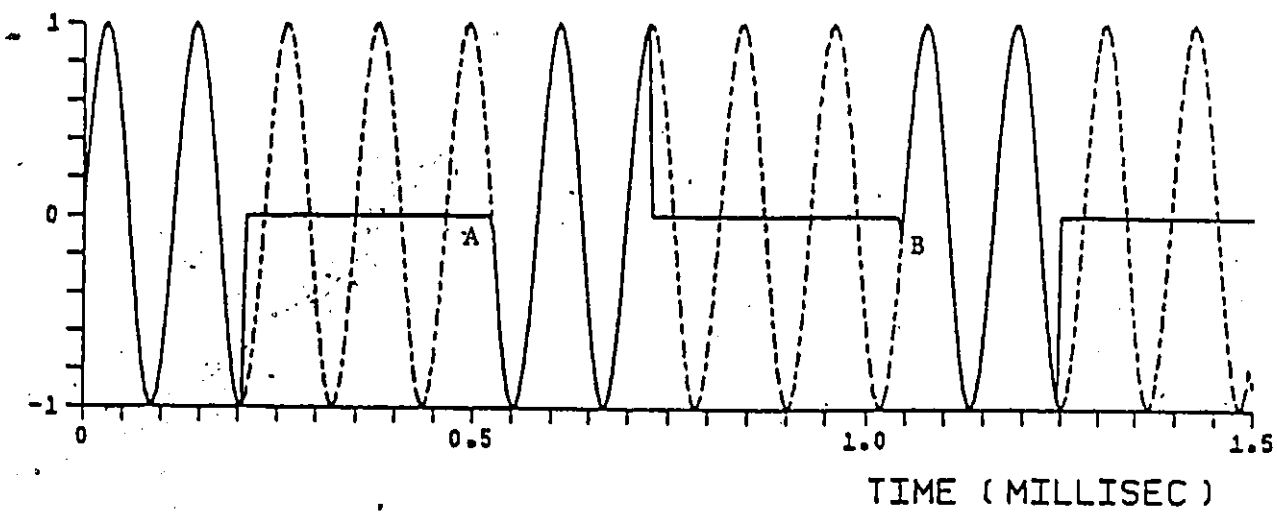

(b)

Fig. 2.2 (a) Block diagram for a coherent ELT unit.

(b) Portion of a coherent ELT signal with the ON time as a solid line and the OFF time dotted. Note the phase continuity at points A and B.

2.2.3 Non-Coherent Model

The Non-Coherent Model includes those ELT units which can be represented by an oscillator which is switched ON and OFF by the modulator, as shown in Fig. 2.3(a). In this case, the phase from pulse to pulse is no longer related, as shown in Fig. 2.3(b). This results in a very broad spectrum which is difficult to process using spectral estimation techniques.

For these three models, we now compute the resulting spectra for the transmitted ELT signals.

2.3 SIGNAL SPECTRA FOR ELT SIGNALS

2.3.1 General Expression

The ELT signal illustrated in Fig. 2.1 can be represented by a set of N pulse-null pairs in the time domain. Mathematically, we have

$$s(t) = \sum_{i=1}^{N} s_i(t) \tag{2.1}$$

where $s_i(t)$ is the signal for the ith pulse. Thus,

$$\begin{aligned} s_i(t) &= A\cos(2\pi f_c t + \theta_i) \qquad t_i - \frac{dT_i}{2} \le t \le t_i + \frac{dT_i}{2} \\ &= 0 \qquad\qquad \text{otherwise} \end{aligned} \tag{2.2}$$

where

$A =$ amplitude of the signal

$f_c =$ carrier frequency of the pulse

$t_i =$ time shift from the centre of the first pulse to the centre of the ith pulse

$T_i =$ the duration of the ith pulse-null pair

$d =$ duty cycle

$\theta_i =$ phase shift of the ith pulse described later in detail.

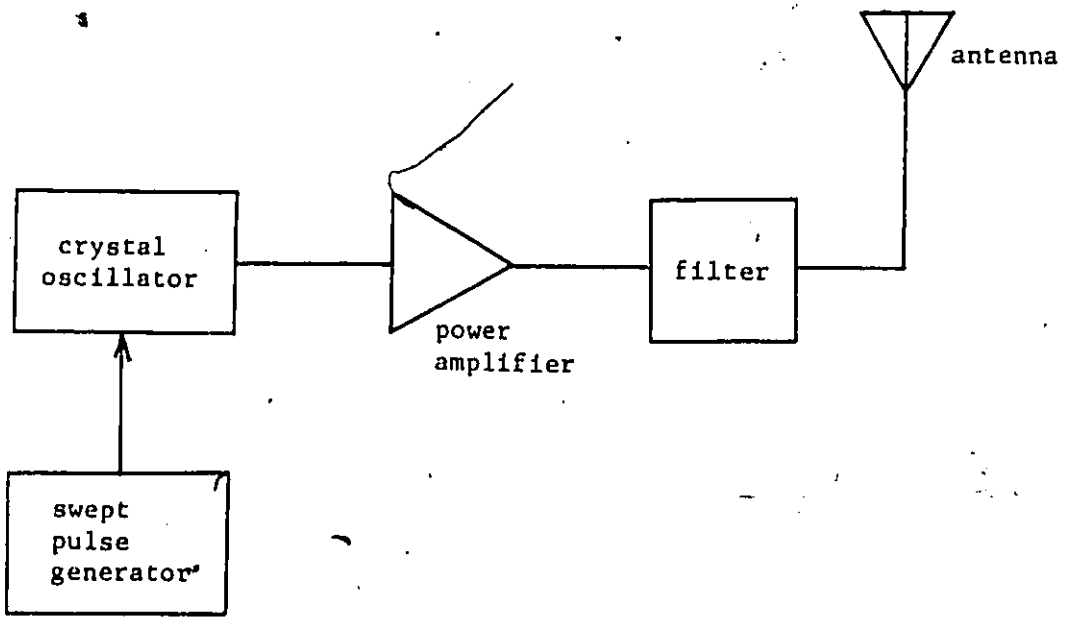

(a)

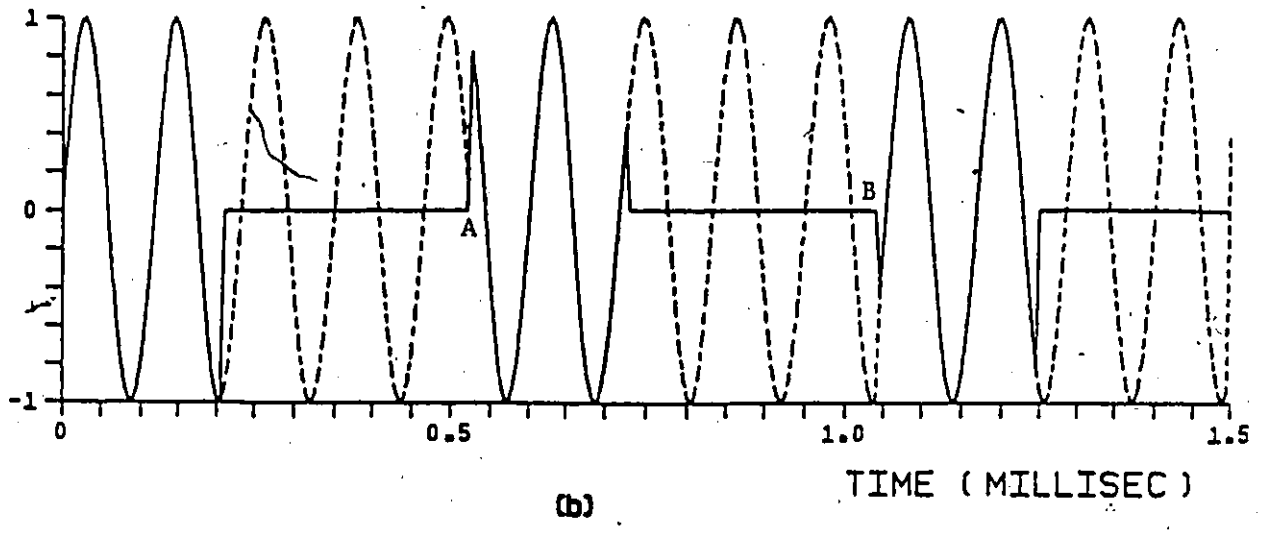

(b)

Fig. 2.3 (a) Block diagram for a non-coherent ELT unit

(b) Portion of a non-coherent ELT signal with the ON time as a solid line and the OFF time dotted. Note the phase discontinuity at points A and B.

The spectrum for this signal can be determined by summing the spectra from the individual components.

Thus, the spectrum of the first pulse can be easily calculated by noting that the Fourier transform is given by

$$F_1(f) = \frac{A d T_1}{2} \operatorname{sinc}[(f - f_c) d T_1] \tag{2.3}$$

where T_1 equals the duration of the first pulse-null pair, and θ_1 is arbitrarily taken to be zero.

Using linearity and the shifting property, the Fourier transform for N pulses is simply

$$F_N(f) = \sum_{i=1}^{N} F_i'(f) \quad f \geq 0 \tag{2.4}$$

where

$$F_i'(f) = F_i(f) \exp[-j(2\pi f t_i - \theta_i)]$$

$$F_i(f) = \frac{A d T_i}{2} \operatorname{sinc}[(f - f_c) d T_i]$$

Hence, the Fourier transform of N pulses of signal is

$$F_N(f) = \sum_{i=1}^{N} \frac{A d T_i}{2} \operatorname{sinc}[(f - f_c) d T_i] \cdot \exp[-j(2\pi f t_i - \theta_i)] \tag{2.5}$$

This relation can be used to determine the spectra produced by three different models, described next, which may arise in practice.

2.3.2 Spectra for Ideal Coherent Model ELT

For this case, it is assumed that the crystal controlled oscillator has constant frequency over the entire signal. This would imply no short-term variation in carrier frequency. Consequently, it is noted that the exponential term in eq. (2.5) must be exactly unity when $f = f_c$. Hence,

$$\theta_i = 2\pi f_c t_i \tag{2.6}$$

Substituting this relation in eq. (2.5) produces

$$F_{IC}(f) = \frac{Ad}{2} \sum_{i=1}^{N} T_i \,\mathrm{sinc}[(f-f_c)\,dT_i] \cdot \exp[-j2\pi(f-f_c)\,t_i] \tag{2.7}$$

If the duration of signals processed is small compared to the total in a sweep, then T_i is nearly constant (i.e. $T_i = T$) and t_i for the first N pulses is very nearly given by

$$t_i = \frac{(i-1)}{N} T_D \tag{2.8}$$

where T_D = duration of N pulses or the window length of data.

With these simplifications, we have

$$F_{IC}(f) = \frac{AdT}{2} \,\mathrm{sinc}[(f-f_c)\,dT] \sum_{i=0}^{N-1} \exp[-j2\pi(f-f_c)\frac{i}{N} T_D] \tag{2.9}$$

The summation can be further simplified since

$$\sum_{i=0}^{N-1} \exp[-j2\pi(f-f_c)\frac{i}{N} T_D] = \frac{1-\exp[-j2\pi(f-f_c)T_D]}{1-\exp[-j2\pi(f-f_c)T_D/N]} \tag{2.10}$$

Computing the spectrum, we get

$$S_{IC}(f) = \left[\frac{AdT}{2}\right]^2 \mathrm{sinc}^2[(f-f_c)\,dT] \cdot \left\{\frac{\sin\left(\pi(f-f_c)T_D\right)}{\sin\left(\frac{\pi(f-f_c)T_D}{N}\right)}\right\}^2 \tag{2.11}$$

From this expression, we see that the spectrum is the product of two relations, the first being the sinc function which has a peak at $f = f_c$ and first nulls at $f_c \pm 1/dT$. The second relation is the ratio of two sines which produces a multi-peak pattern with the peaks being located at $f = f_c \pm (Nm/T_D)$, $m = 1, 2, 3, \ldots$. Figure 2.4 illustrates a plot of the two components and the overall relation for $(AdT/2) = 1$. Note that the bandwidth of the centre peak between nulls is $2/T_D$; thus, a more accurate measure of carrier frequency can be obtained simply by increasing the window length of data.

In Fig. 2.4(c), we see that the peak at $f = f_c$ is due to the carrier frequency while the peaks at other frequencies are due to the sidebands. This is demonstrated in Fig. 2.5 for three different values of T, which represent the beginning, middle and end of the frequency sweep of

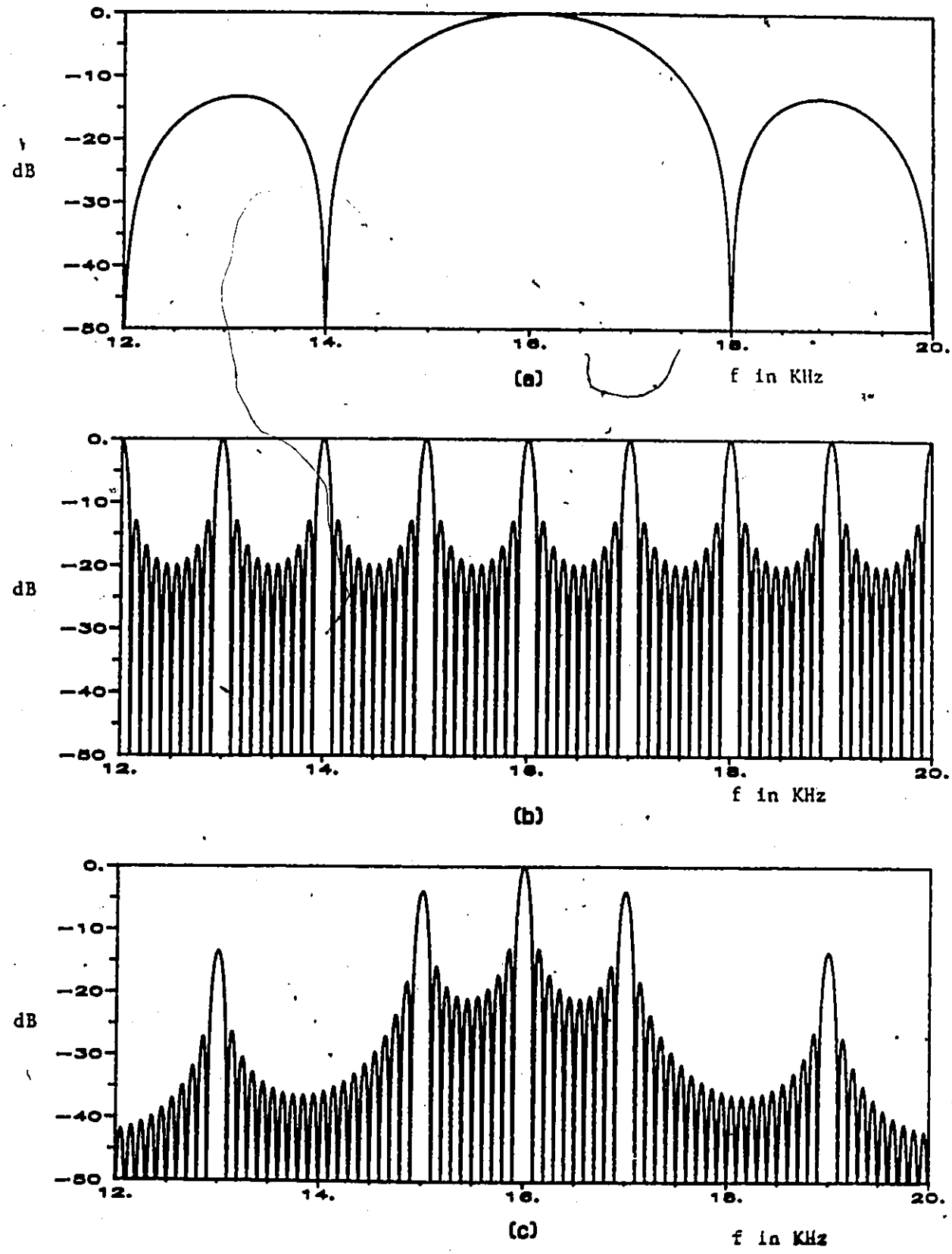

Fig. 2.4 (a) Plot of $\text{sinc}^2[(f-f_c)dT]$ for $f_c = 16\text{KHz}$, $d = 0.5$ and $T = 1\text{ms}$.

(b) Plot of square of ratio of two sines for $f_c = 16\text{KHz}$, $T_D = 10\text{ms}$ and $N = 10$.

(c) Plot of $S_{IC}(f)$ for $(AdT/2) = 1$.

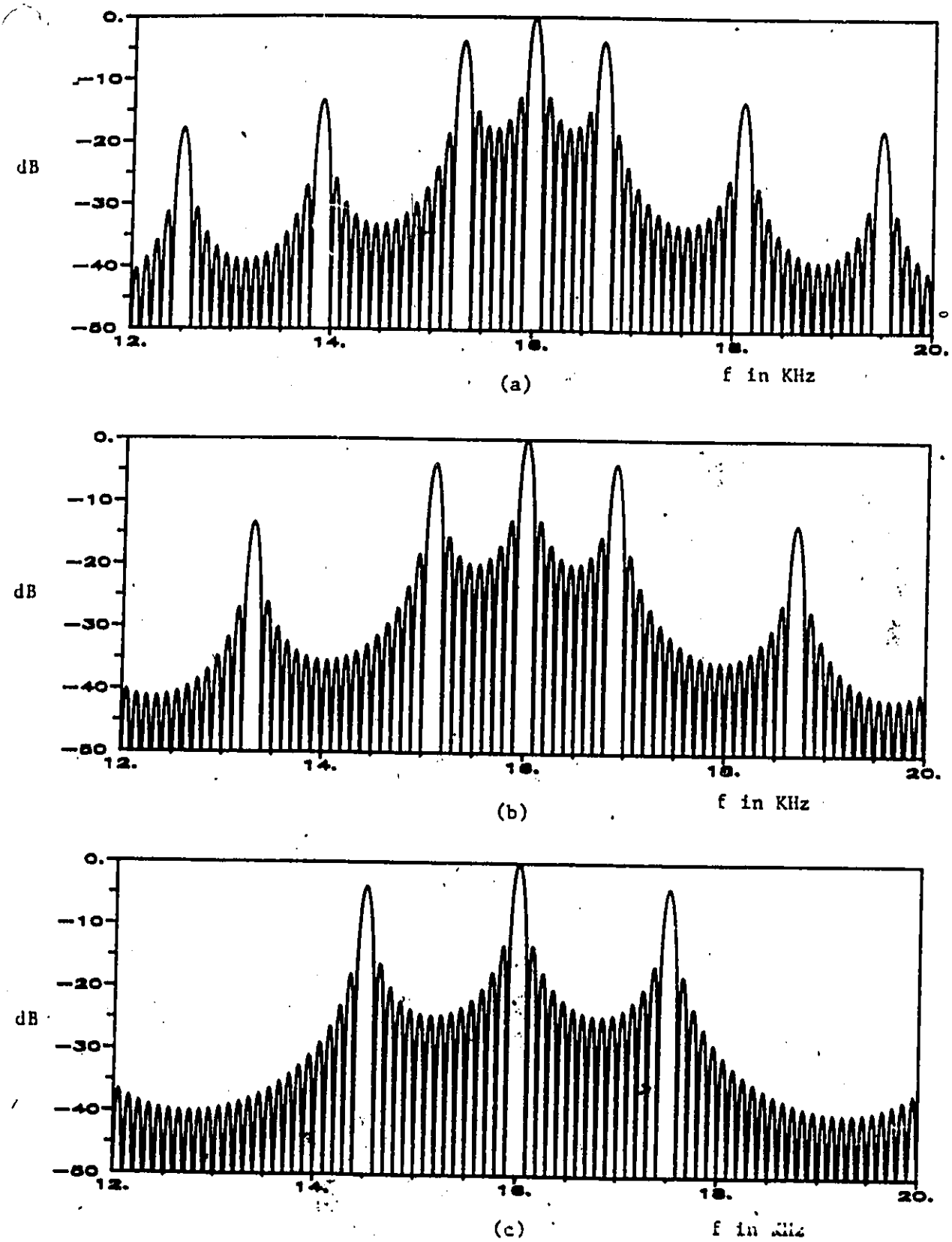

Fig. 2.5 Plot of $S_{IC}(f)$ for $T = 1.42$ ms (top), $T = 1.11$ms (centre) and $T = 0.67$ms (bottom) with $d = 0.5$, $f_c = 16$KHz, $T_D = 10$ms and $(AdT/2) = 1$.

a typical ELT signal. In each case, the peak at $f = f_c$ remains stationary while the sideband peaks move toward f_c as T increases.

Unfortunately, this ideal spectrum does not accurately reflect the operation of actual ELT units since here the sidebands are symmetric in amplitude, while in practice, the sidebands are usually asymmetric. Thus, a modification to the model is required, which is discussed next.

2.3.3 Spectra for Non-Ideal Coherent Model ELT

For this case, it is assumed that the crystal controlled oscillator operates at frequency f_c when the switch is closed and $f_c + f_p$ when the switch is open, as illustrated in Fig. 2.6; due to the problems previously discussed. From eq. (2.2), the phase shift at the beginning of the second pulse when no frequency pulling is present is just

$$\theta_{2c} = 2\pi f_c \left[\frac{dT_1}{2} + (1-d)T_1 \right] \tag{2.12}$$

When frequency pulling occurs, the phase shift at the beginning of the second pulse is

$$\theta_{2p} = 2\pi f_c \frac{dT_1}{2} + 2\pi (f_c + f_p)(1-d)T_1 \tag{2.13}$$

Thus, the additional phase shift due to frequency-pulling is

$$\begin{aligned} \Delta\theta &= \theta_{2p} - \theta_{2c} \\ &= +2\pi f_p (1-d) T_1 \end{aligned} \tag{2.14}$$

Consequently, for the ith pulse, the total additional phase shift is

$$\Delta\theta_i = \sum_{j=1}^{i-1} 2\pi f_p (1-d) T_j ; \qquad i = 2,3,4 \ldots N \tag{2.15}$$

Then,

$$F_{NC}(f) = \frac{Ad}{2} \sum_{i=1}^{N} T_i \operatorname{sinc}[(f-f_c) d T_i] \exp\{-j[2\pi (f-f_c) t_i - \Delta\theta_i^*]\} \tag{2.16}$$

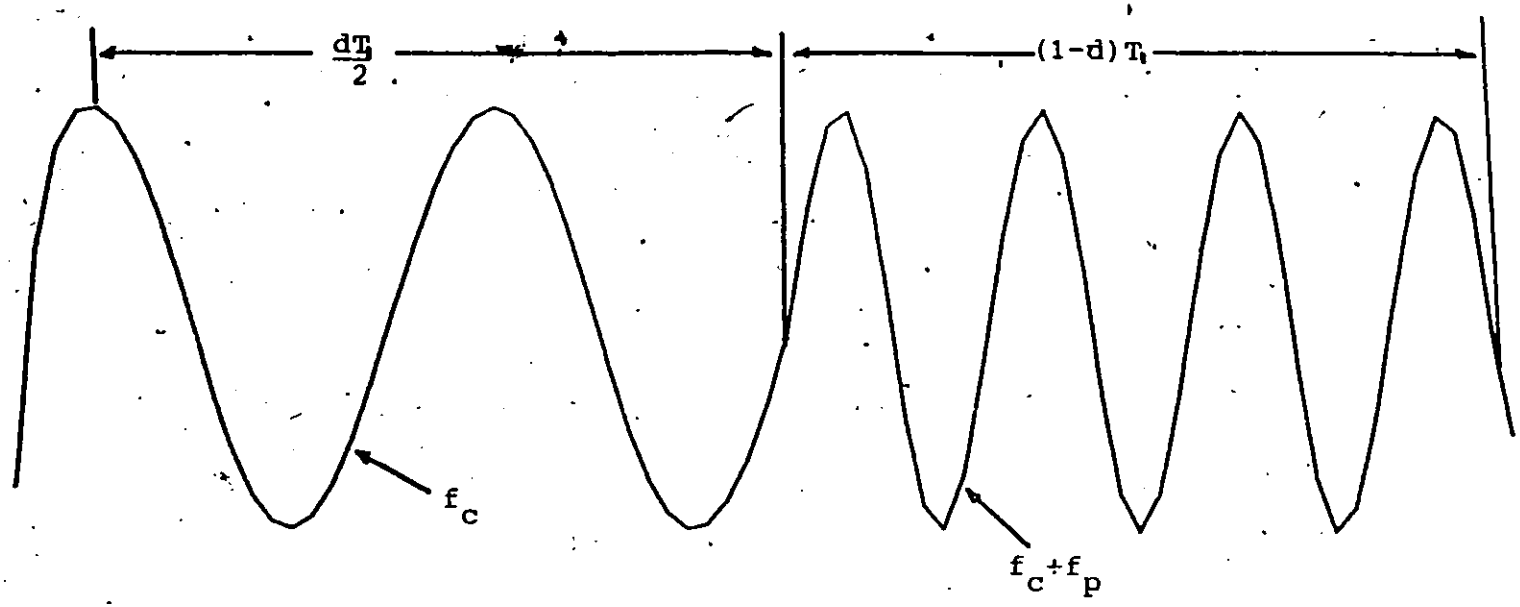

Fig. 2.6 Phase shift produced by the two-frequency model.

If the duration of the signal processed is small compared to the total sweep, then T_i is nearly constant and eq. (2.8) applies. Thus, the simplified expression becomes

$$F_{NC}(f) = \frac{AdT}{2} \operatorname{sinc}[(f - f_c)dT] \cdot \sum_{i=0}^{N-1} \exp\left\{-j2\pi\left[(f-f_c)\frac{iT_D}{N} - f_p(1-d)iT\right]\right\} \tag{2.17}$$

Note $T = T_D/N$, define $f_s = f_p(1-d)$ to be the frequency shift and substitute into the summation in eq. (2.17). Thus,

$$F_{NC}(f) = \frac{AdT}{2} \cdot \operatorname{sinc}[(f - f_c)dT] \cdot \sum_{i=0}^{N-1} \exp\left\{-j2\pi\left[(f-f_c-f_s)\frac{iT_D}{N}\right]\right\} \tag{2.18}$$

Computing the spectrum, we get

$$S_{NC} = \left[\frac{AdT}{2}\right]^2 \operatorname{sinc}^2[(f-f_c)dT] \cdot \left\{\frac{\sin[\pi(f-f_c-f_s)T_D]}{\sin\left[\frac{\pi(f-f_c-f_s)T_D}{N}\right]}\right\}^2 \tag{2.19}$$

Once again, we note that the spectrum is the product of two relations, the first being the sinc function and the second being the ratio of two sine functions. However, the sine functions now have a frequency shift f_s which shifts the multi-peak pattern, as illustrated in Fig. 2.7 for three different values of f_s.

Of considerable concern is the fact that the first nulls of the sinc function and the peaks of the sine relation can overlap as illustrated. The most serious occurrence of this takes place when

$$f - f_c - f_s \Big|_{f = f_c \pm \frac{1}{(dT)}} = 0 \tag{2.20}$$

since the carrier peak now coincides with the null of the sinc function. In this situation, carrier peaks are lost for a considerable portion of the sweep and one set of sidebands is enhanced while the other set is diminished.

Since $f_s = f_p(1-d)$, we find that the amount of frequency shift required to null the carrier peak is given by

$$f_p = \pm \frac{1}{d(1-d)T} \tag{2.21}$$

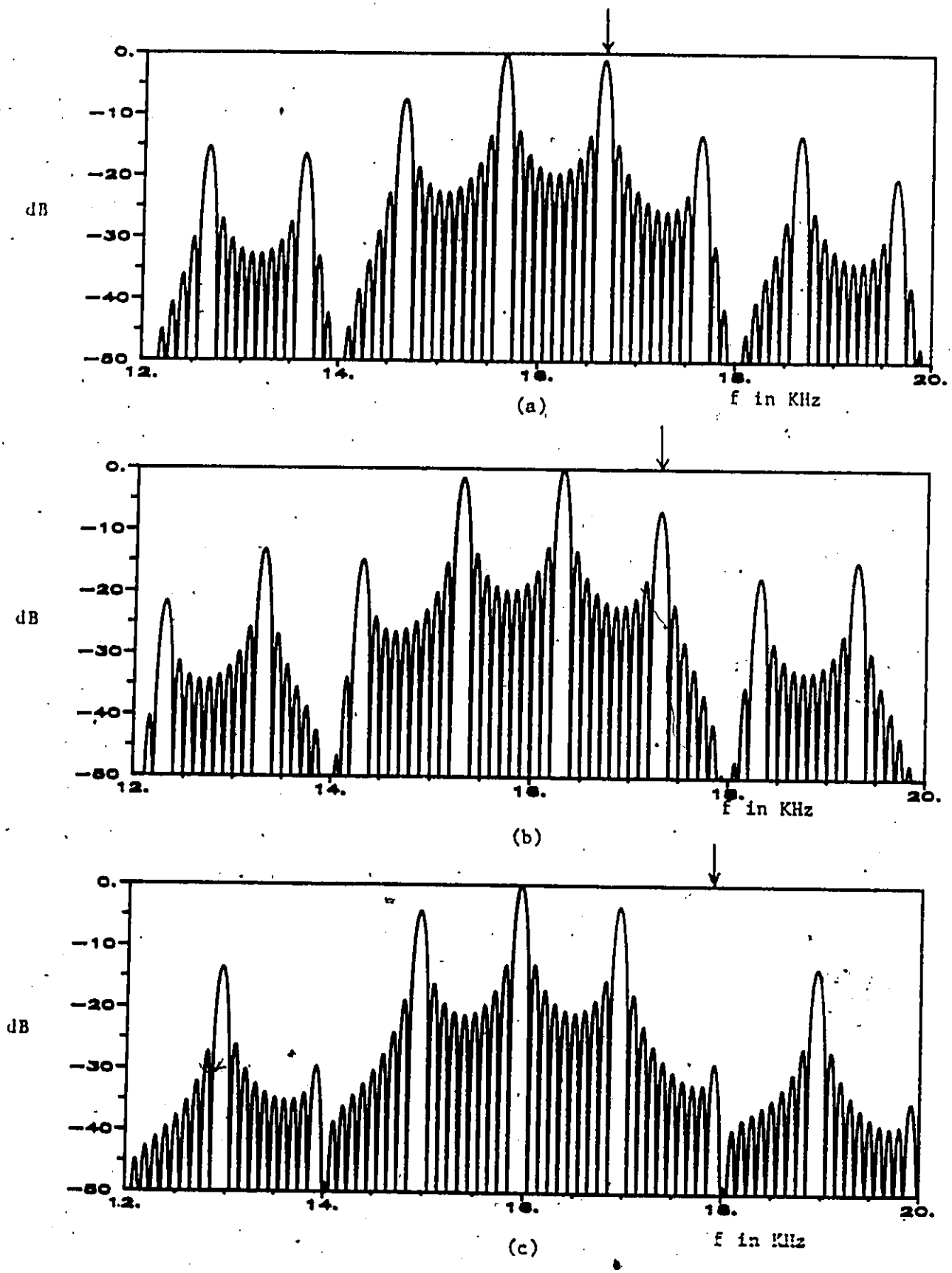

Fig. 2.7 Plot of $S_{NC}(f)$ for $T=1ms$, $f_c=16KHz$, $d=0.5$, $T_D=10ms$ and $f_s=650Hz$ (top), $f_s=1300Hz$ (centre) and $f_s=1950Hz$ (bottom). Note that the centre peak moves to the right as indicated by the arrow.

In order to evaluate the maximum permissible frequency shift for nulling to occur, we evaluate eq. (2.21) using maximum values for both $d(1-d)$ and T. The first expression is maximum at $d = 0.5$ and, from Table 2.1, the maximum of T is $(1/300)\mathrm{Hz}^{-1}$. This results in a value of $f_{pmax} = 1200$ Hz. Since, in practice, this value provides the upper bound, it is suggested that the total frequency change over the duration of the sweep be no more than 600 Hz (half the maximum or alternatively ± 300 Hz). Note that this is independent of carrier frequency.

2.3.4 Spectra for Non-Coherent Model ELT

This model assumes the use of a crystal oscillator which is switched ON and OFF by the pulse modulation signal, as shown in Fig. 2.3. Note that this is completely different from the previous models in that here the oscillator is completely OFF between pulses; thus, there is absolutely no phase coherence between pulses.

In this case, the Fourier transform is given by

$$F_{NN}(f) = \sum_{i=1}^{N} \frac{Ad\,T_i}{2} \operatorname{sinc}[(f-f_c)dT_i] \exp[-j(2\pi f t_i - \theta_i)]$$

where θ_i is assumed to be a uniformly distributed random variable between 0 and 2π. If the number of pulses is small, as before, the spectrum is

$$S_{NN}(f) = \left[\frac{AdT}{2}\right]^2 \operatorname{sinc}^2[(f-f_c)dT] \sum_{i=1}^{N} \exp[-j(2\pi f t_i - \theta_i)] \tag{2.22}$$

which is not particularly useful. However, since θ_i is a random variable, we can evaluate the averaged spectrum through

$$S_{NA}(f) = E\{F_{NN}(f) \cdot F^*_{NN}(f)\}$$

$$= \left[\frac{AdT}{2}\right]^2 \operatorname{sinc}^2[(f-f_c)dT] \cdot E\left\{\sum_{i=1}^{N} \exp[-j(2\pi f t_i - \theta_i)] \sum_{k=1}^{N} \exp[+j(2\pi f t_k - \theta_k)]\right\}$$

$$\left[\frac{AdT}{2}\right]^2 N \operatorname{sinc}^2[(f-f_c)dT] \tag{2.23}$$

since the expectation of the sum of all the products for $i \neq k$ is zero. We note here that the averaged spectrum has a shape which is $\operatorname{sinc}^2[(f-f_c)dT]$, illustrated in Fig. 2.4. This averaged spectrum is far broader than the previous spectra since the nulls are now at a frequency 1/(dT) above and below f_c. Thus, carrier frequency estimation for non-coherent ELT signals cannot easily be performed by use of a simple linear estimator such as Fourier transform.

2.4 COMPARISON OF REAL AND MODELLED ELT SPECTRA

Since the expected bandwidth of the ELT signals at 121.5 MHz is only 25 KHz, this frequency band is linearly mixed to the range from 0 to 25 KHz in order to facilitate easier processing. We refer to signals in the 0 to 25 KHz range as 'mixed carrier frequencies' in order to distinguish from the true carrier frequencies at 121.5 MHz.

A testbed of 20 ELT units has been constructed at the Communications Research Centre, Ottawa, which permits signals from one to ten ELT units to be independently mixed to the frequency range from 0 to 25 KHz and combined producing a composite signal with the 'mixed carrier frequencies'. These ELT units are from different manufacturers and are numbered consecutively from 1 to 20, that is ELT01, ELT02, and so on. Using an instrumentation tape recorder, a selection of different ELT signals exhibiting Non-Ideal Coherent and Non-Coherent operation was recorded. The signals experience no Doppler shift and the carrier-to-noise density ratio, discussed in detail in Chapter 3, is high (approximately 50 dBHz). Table 2.2 lists the specifications for the five ELT signals provided by the SARSAT group at the Communications Research Centre.

ELT NO.	MANUFACTURER	MODEL NUMBER	POWER OUTPUT AT 121.5 MHZ	ACTUAL CARRIER FREQUENCY MHZ
01	Pointer	Sentry C-4000	417 mW	121.497595
07	Pointer	Sentry C-4000	303 mW	121.497710
12	Garrett	Rescu 88C	132 mW	121.498645
17	Narco	ELT 10	340 mW	* UNABLE TO MEASURE
19	Narco	ELT 10	277 mW	* UNABLE TO MEASURE

* No identifiable peak for carrier frequency was present.

Table 2.2 Specifications for five ELT units.

Now that the ELT spectra are mathematically defined in the previous section, it is useful to compute the spectra of computer generated ELT signals which represent the models developed and compare these spectra with those produced by real signals.

Using the Ideal Coherent Model ELT, an ELT signal with $d=0.5$ has been generated with carrier frequency equal to $f_c = 16.2$ KHz and the spectrum has been calculated by employing a set of 25 Blackman windowed 2048-point periodograms, as illustrated in Fig. 2.8. The dynamic range of each plot is 20 dB and approximately two sweeps of the ELT signal are provided. At the bottom of the plot is the averaged spectrum which is simply the normalized sum of the 25 periodograms.

This theoretical model can be compared with the actual spectra observed from three different manufactured ELT units. The first is ELT01, a Pointer Model Sentry C-4000 ELT. A portion of the signal is illustrated in Fig. 2.9(a), which shows the pulse modulated characteristics. Fig. 2.9(b) provides an expanded view showing the sinusoidal carrier which indicates a mixed carrier frequency of approximately 16 KHz. Periodograms of the signal are plotted in Fig. 2.10. Again, the dynamic range for each plot is 20 dB and approximately two sweeps of the signal are present. We note that the amplitude of the sidebands of the Pointer ELT do not agree with the Ideal Coherent Model.

Using the Non-Ideal Coherent Model, we plot the spectra for $f_c = 15.7$ KHz and $f_p = 1$ KHz with $d = 0.5$, as shown in Fig. 2.11. Comparing with Fig. 2.10, we note that the agreement is remarkable in that the carrier is at constant frequency and the first upper and lower sidebands slide reasonably smoothly toward the carrier with time. In addition, the first lower sideband in both the modelled signal and the real signal is considerably stronger than the first upper sideband. The second upper sideband is nearly absent in both and the third upper sideband is quite prominent in both. The lower second and third sidebands are also in agreement. Finally, we note close agreement in the averaged spectra.

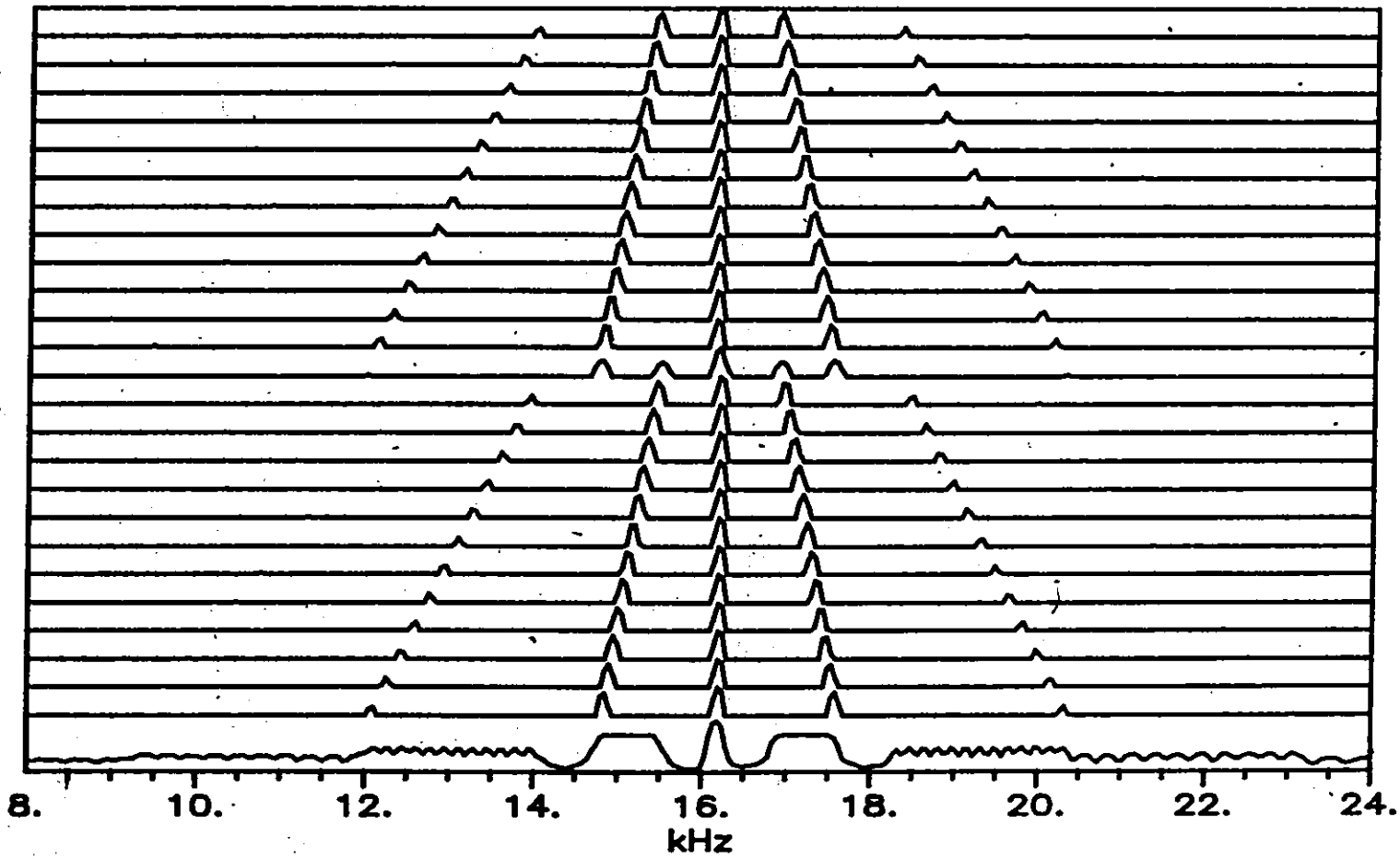

Fig. 2.8 Sequence of 25 consecutive Ideal Coherent ELT model periodograms (bottom to top) with the averaged spectrum given at the bottom. For each of the 25 traces, $T_D = 20ms$, $d = 0.5$ and $f_c = 16.2KHz$. Note the symmetry of the spectra around the 16.2KHz centre frequency and the sweep of the modulation. The second upper and lower sidebands are reduced below the $-20dB$ threshold by the sinc component of $S_{IC}(f)$.

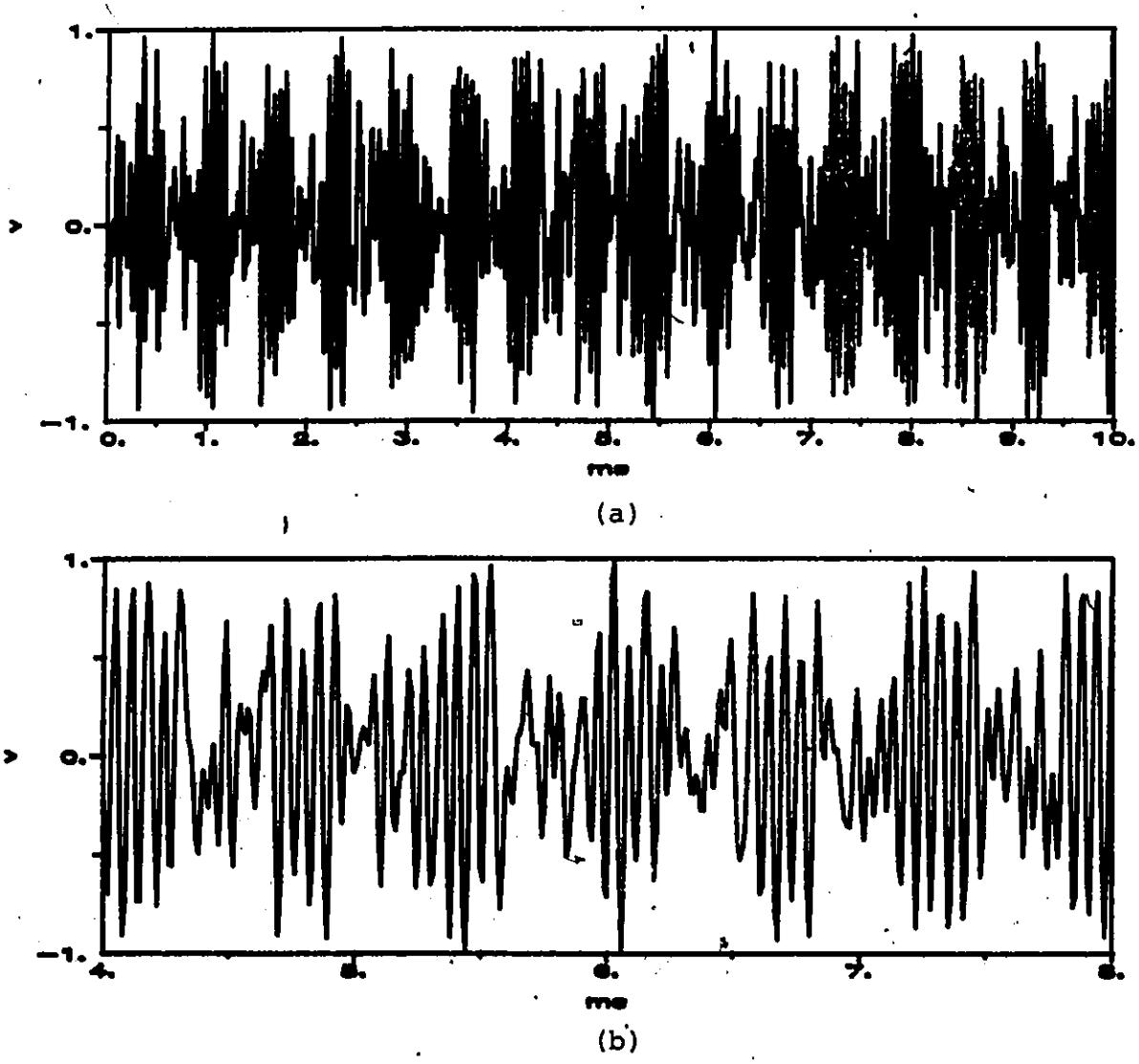

Fig. 2.9 (a) A 10ms portion of a Pointer ELT01 ELT signal.
(b) Expanded view showing the signal details.

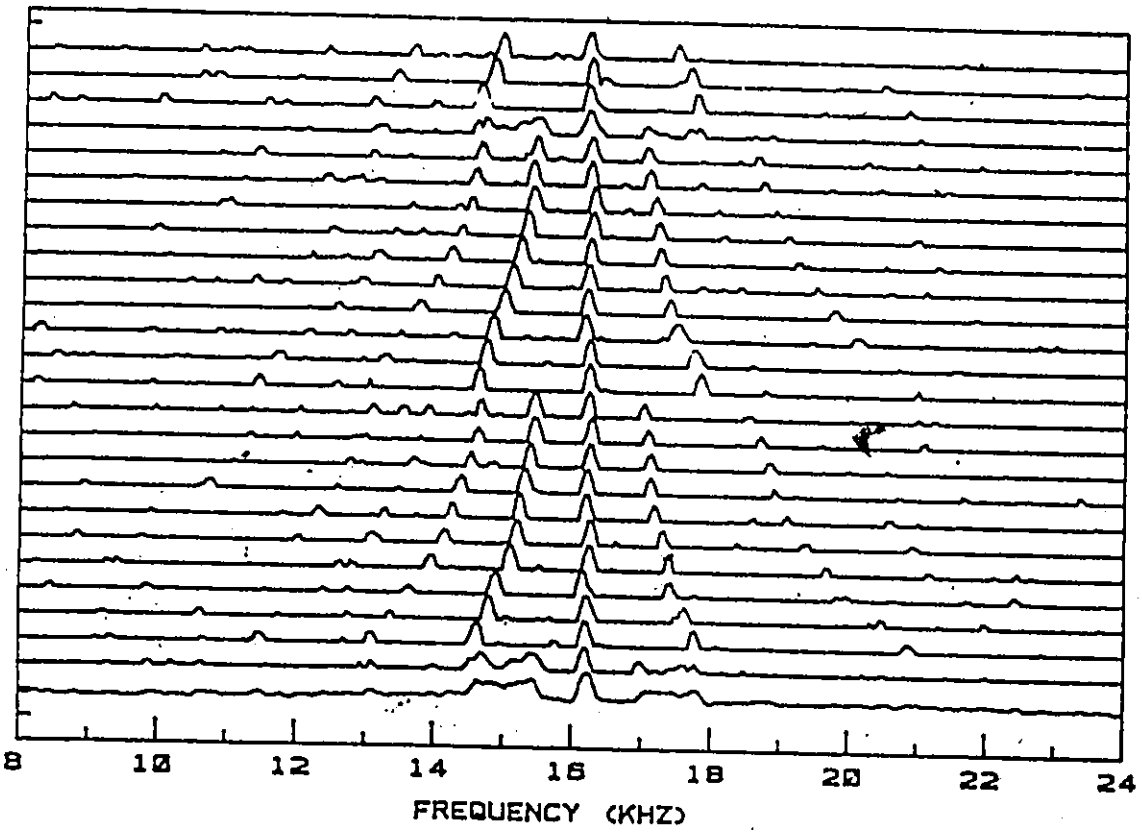

Fig. 2.10 Sequence of 25 consecutive Pointer ELT periodograms with the averaged spectrum given at the bottom. Note the asymmetry of the sidebands around the 16.2KHz centre frequency. For each trace, T_D= 20ms.

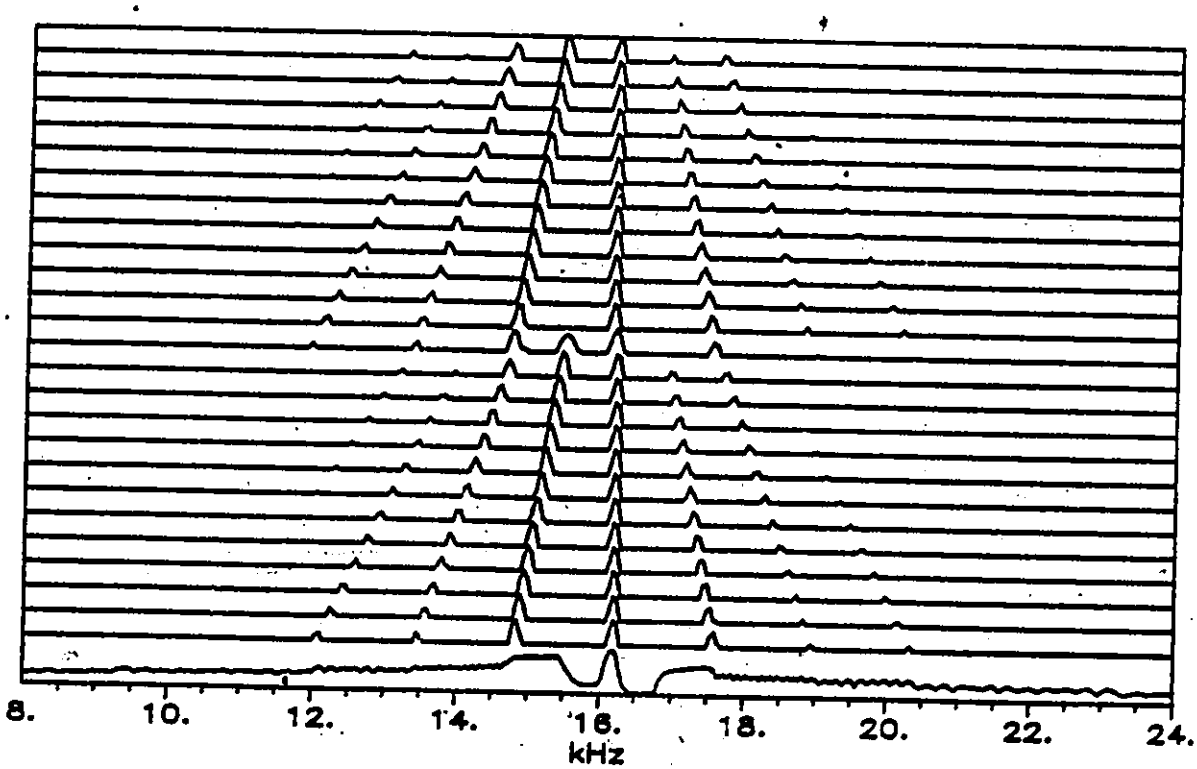

Fig. 2.11 Sequence of 25 consecutive Non-Ideal-Coherent ELT model periodograms with the averaged spectrum at the bottom. By choosing f_c = 15.7KHz and f_D= 1KHz, an asymmetry is produced which corresponds more closely to the observed Pointer ELT spectra. For each trace, T_D = 20ms and d = 0.5.

We examined a second coherent ELT signal, ELT12, a Garrett Model Rescu-88 C ELT. Periodograms for this ELT are given in Fig. 2.12. Since the amplitudes of the first sidebands are unequal, the Ideal Coherent Model is inadequate. However, by using the Non-Ideal Coherent Model with f_c = 16.75 KHz, f_p =-0.5 KHz and d = 0.36, we obtain the plots of Fig. 2.13. Again, we see that the agreement is good in that the carrier remains constant and the first upper and lower sidebands are well defined. The upper second sidebands are both well defined and the lower second sidebands are both diminished. The averaged spectra are in good agreement.

The third is ELT17, a Narco Model ELT 10. The waveform, shown in Fig. 2.14(a) illustrates the pulse modulated characteristic of the ELT signal and Fig. 2.14(b) provides an expanded view of the waveform showing that the mixed carrier frequency is approximately 18 KHz. From spectral plots described later, it is shown that a small phase shift exists between consecutive pulses. Further examination shows that this ELT signal is also non-ideal coherent. However, in this case, the modulation interacts with the phase shift to produce a null at the carrier frequency. The spectra for the Narco ELT17 is given in Fig. 2.15. In this case, it appears that carrier component of the spectrum is nulled at a frequency approximately two-thirds along the sweep. Using the Non-Ideal Coherent Model with f_c = 17.5 KHz, f_p = 4 KHz and d = 0.5, we plot Fig. 2.16 and once again the model obtains a good agreement with the actual signal. Note that the averaged spectra in both cases indicates a large amount of the power in the lower sideband while the carrier component is weakened. Clearly, this condition should be avoided if automated spectral estimation techniques are to be employed.

ELT19 is also a Narco Model ELT 10. Again, the signal has a pulse modulated characteristics, as demonstrated in Fig. 2.17(a). Using the expanded view of Fig. 2.17(b), we see that the mixed carrier frequency of the signal is approximately 15 KHz. Although the

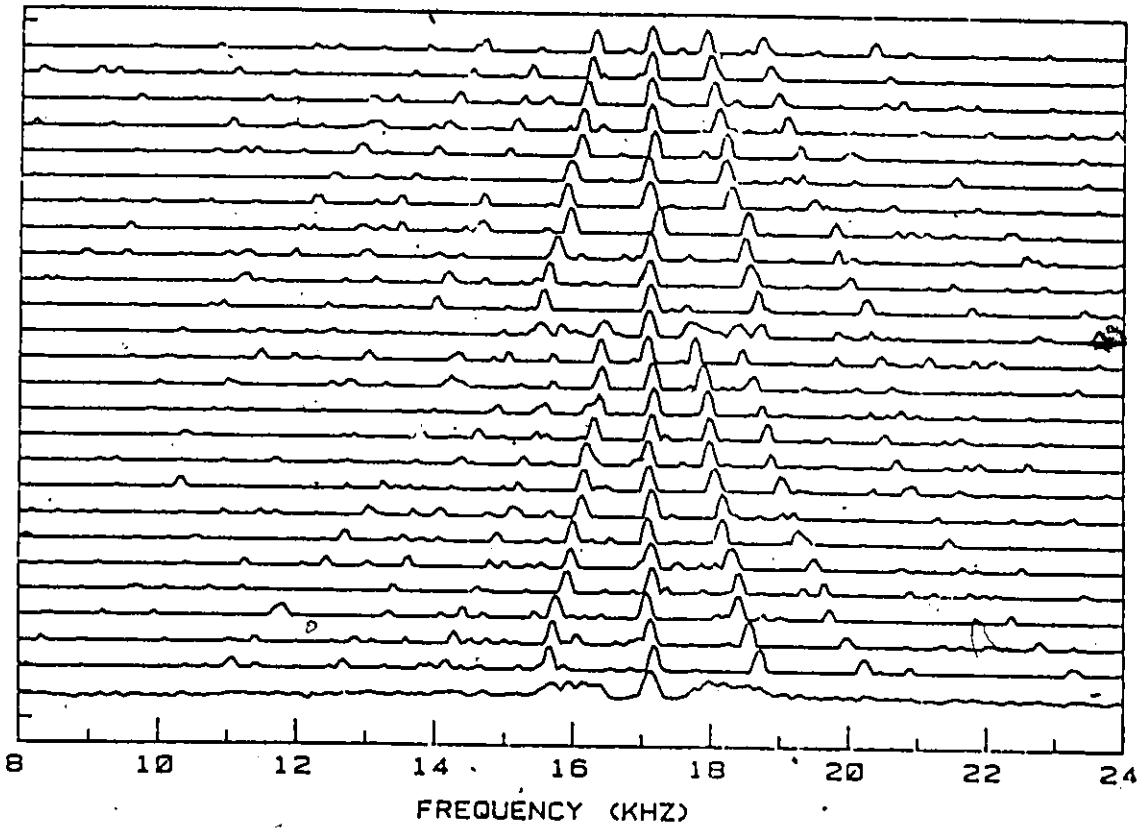

Fig. 2.12 Sequence of 25 consecutive Garrett ELT periodograms with the averaged spectrum at the bottom. Note that the lower second sideband nearly disappears. For each trace, $T_D = 20$ms.

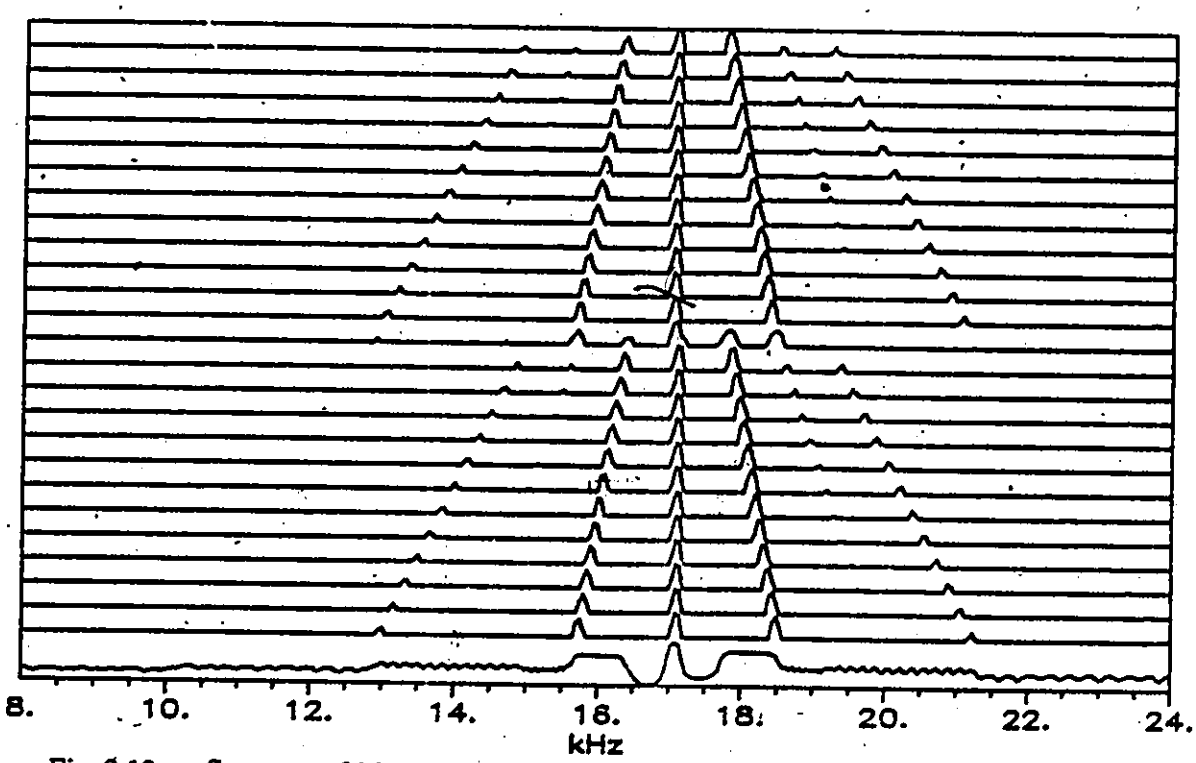

Fig. 2.13 Sequence of 25 consecutive Non-Ideal Coherent ELT model periodograms with the averaged spectrum at the bottom. By choosing $f_c = 16.75$KHz, $f_p = -0.5$KHz and $d = 0.36$, the spectral waveforms are found to agree well with the observed Garrett spectra. For each trace $T_D = 20$ms.

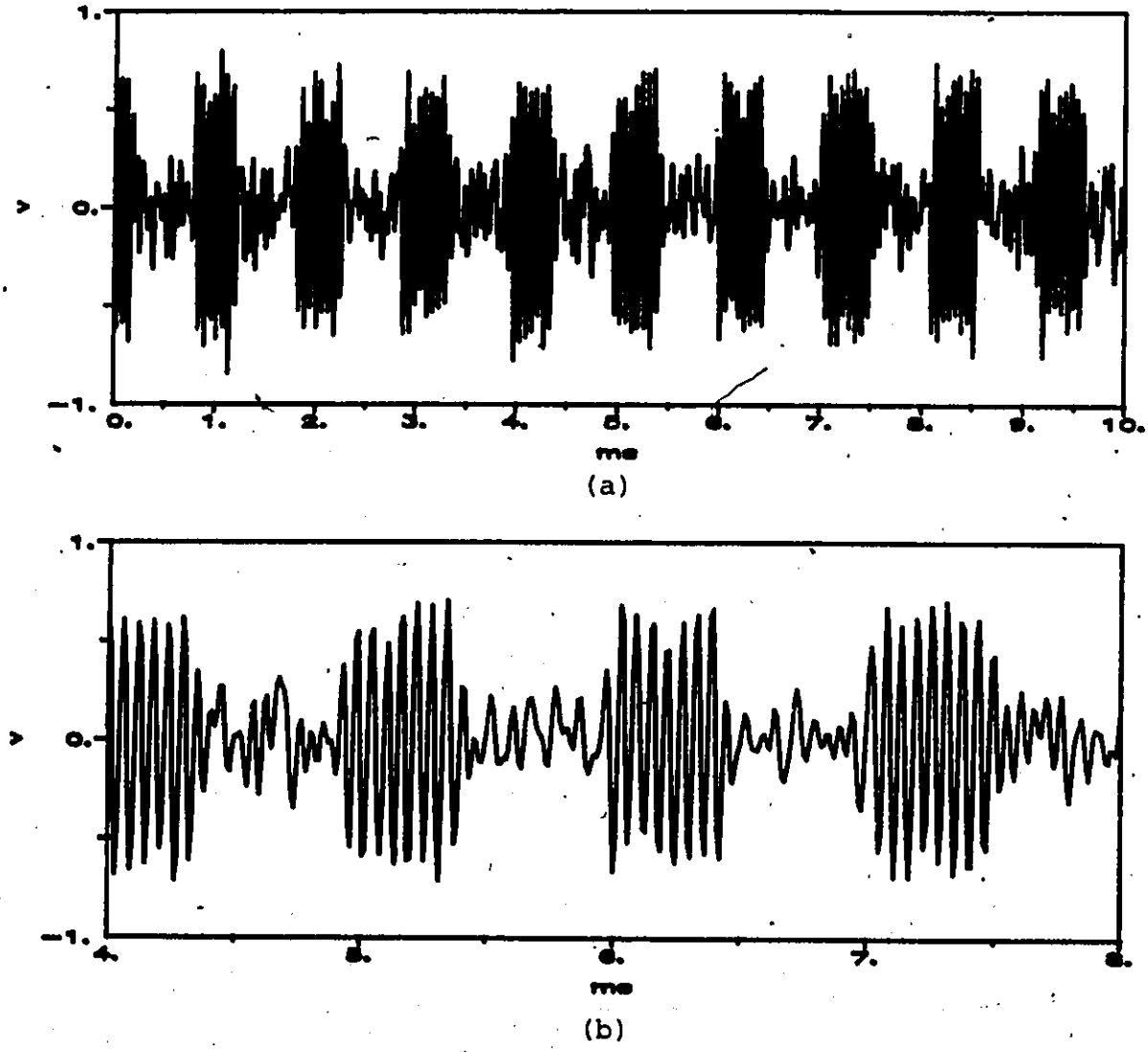

Fig. 2.14 (a) A 10ms portion of a Narco ELT17 ELT signal.
(b) Expanded view showing the signal details.

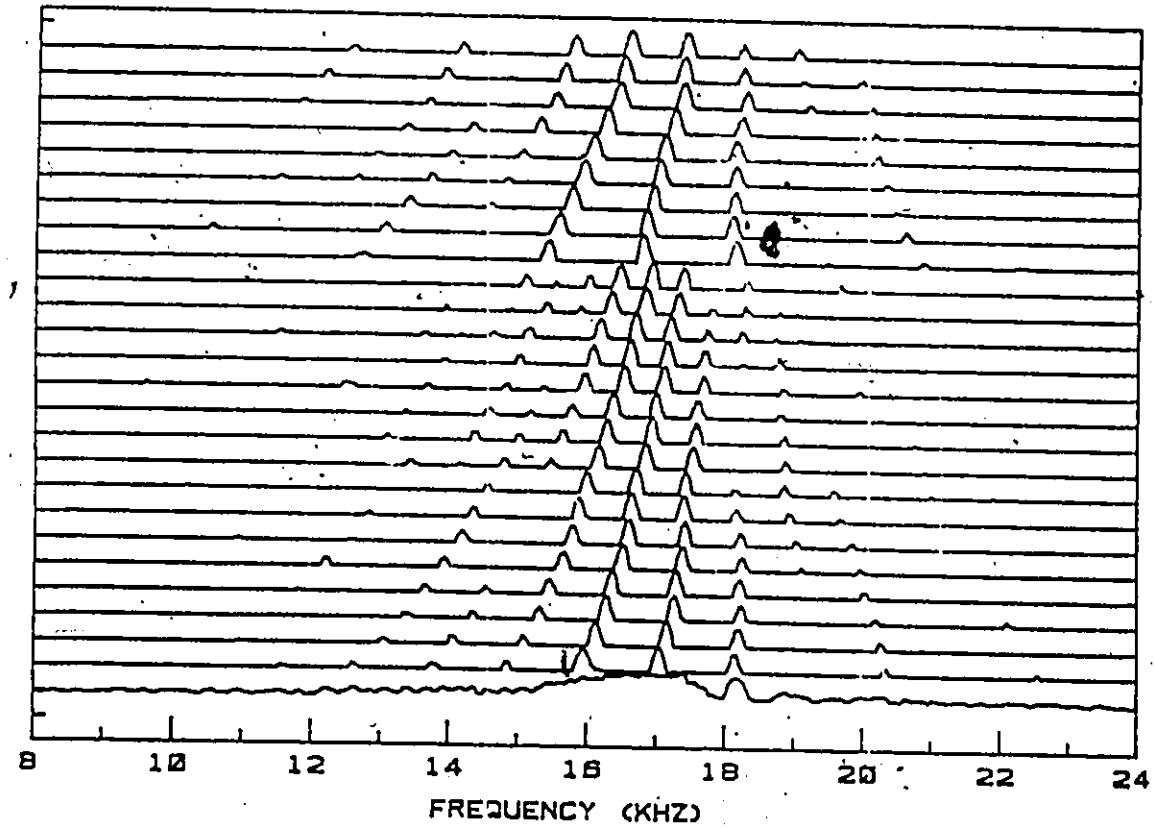

Fig. 2.15 Sequence of 25 consecutive Narco ELT periodograms with the averaged spectrum at the bottom. Note that the carrier peak at 18.1KHz disappears for a considerable portion of the time. For each trace $T_D = 20$ms.

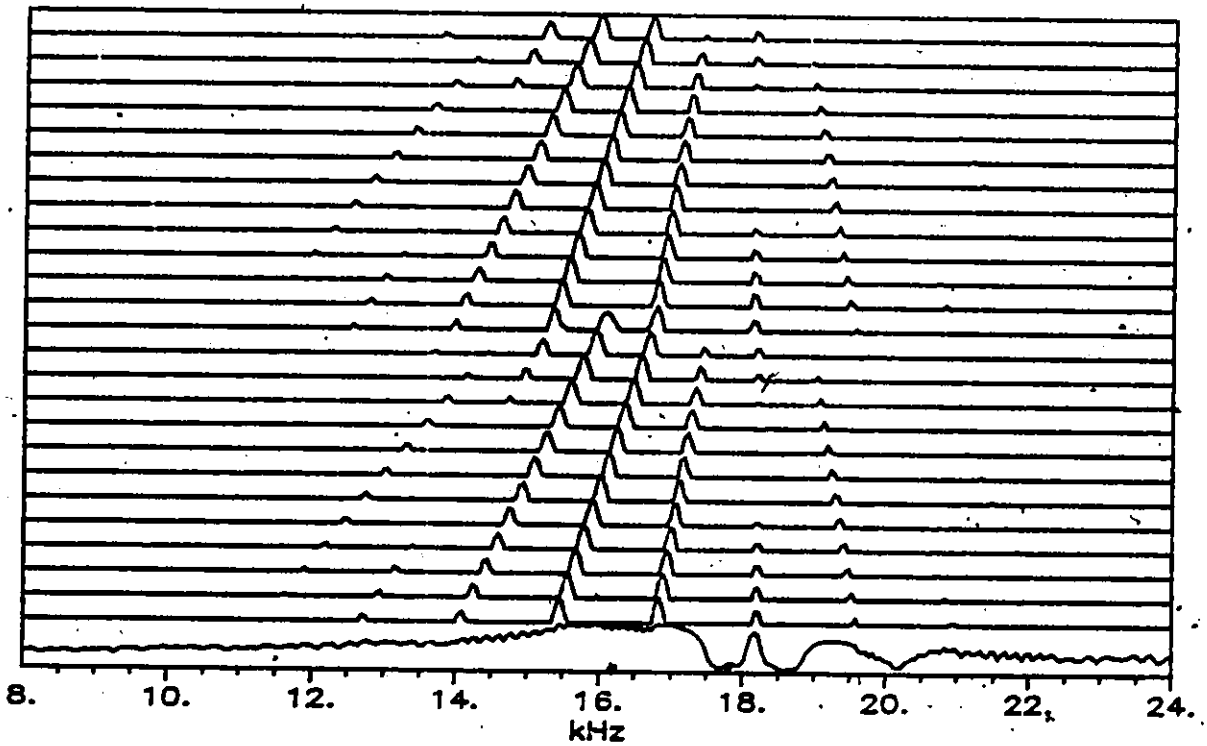

Fig. 2.16 Sequence of 25 consecutive Non-Ideal Coherent ELT model periodograms with the averaged spectrum at the bottom. By choosing $f_c = 17.5$KHz, $f_p = 4$KHz and $d = 0.5$, the spectral waveform produce a spectrum which closely represents the Narco spectrum. For each trace, $T_D = 20$ms.

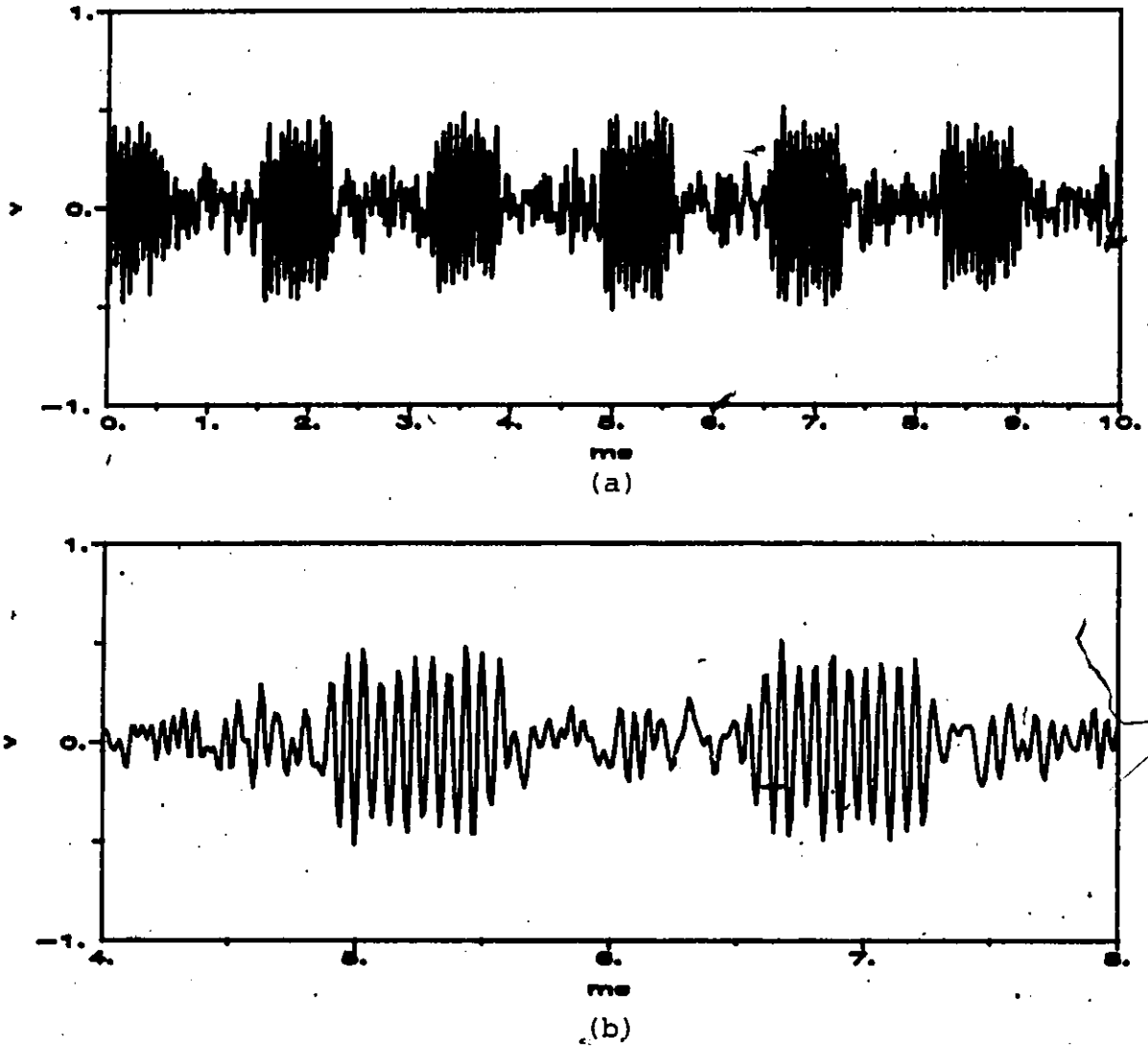

Fig. 2.17 (a) A 10ms portions of a Narco ELT19 ELT signal.
(b) Expanded view showing the signal details.

time plot of the signal indicates relatively clean pulses which would normally lead to good spectral estimates of the carrier frequency, this is misleading since the phase characteristic is random.

We generate a Non-Coherent Model ELT signal by using phase randomization for each of the signal pulses. The spectral plot is given in Fig. 2.18 where we see that the individual periodograms have a very wide bandwidth. Comparing the averaged spectrum with the prediction of Fig. 2.4(a), we again find close agreement. Thus, if automatic spectral estimation techniques are to be employed, this design for ELT signals should be avoided at all costs.

2.5 SUMMARY

Three different models for ELT signals have been developed and the Non-Ideal Coherent Model is found to accurately predict the spectra of available real signals. Use of this model leads to the prediction of a highly undesirable design hazard which has been verified by computer simulation and demonstrated by an actual ELT signal. This hazard arises due to an interaction between the modulation and the short term frequency instability of the carrier oscillator. Thus, it is concluded that an additional design specification should be applied to the manufacture of ELT units. Use of Non-Coherent ELT signals should be prohibited.

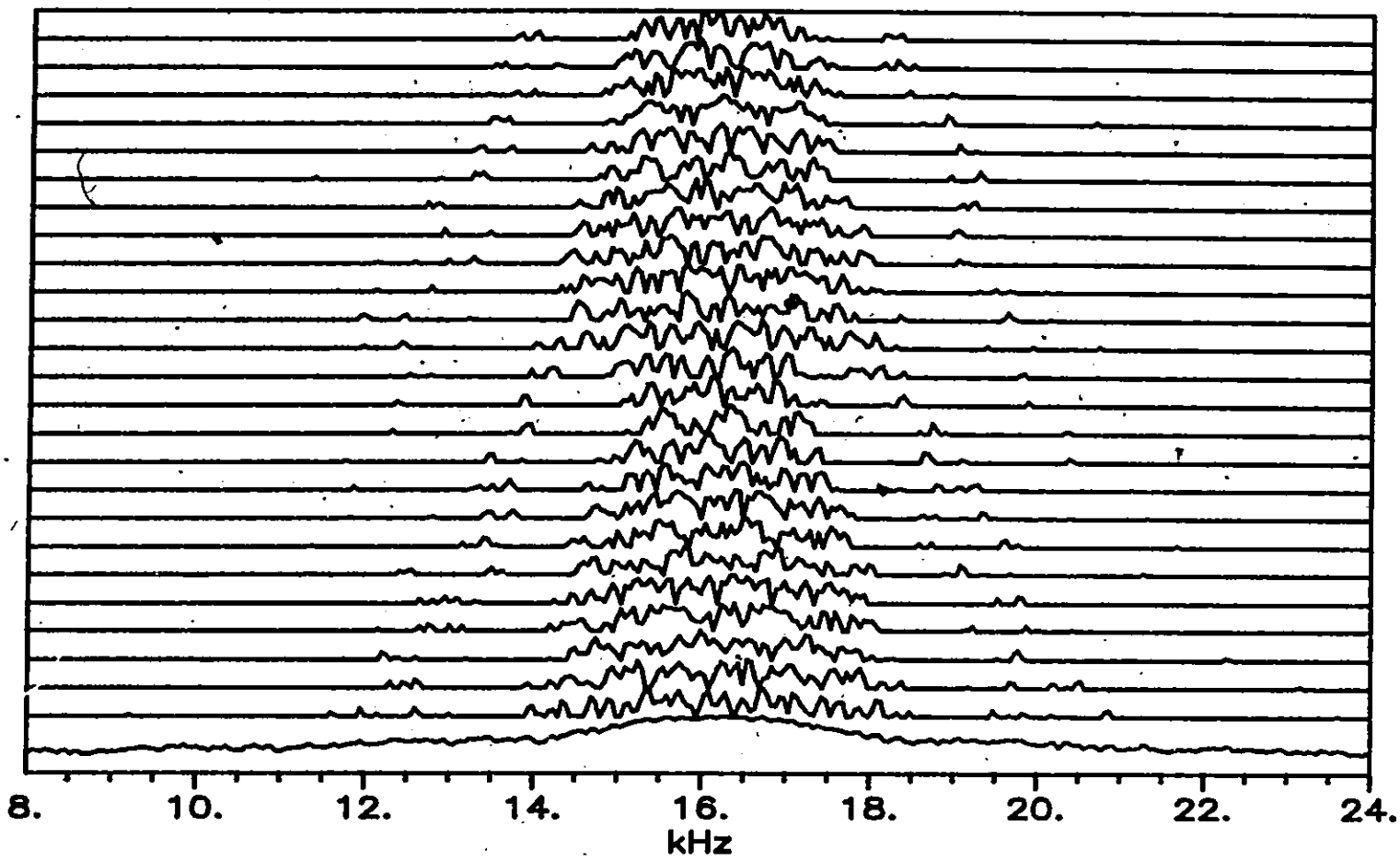

Fig. 2.18 Sequence of 25 consecutive Non-Coherent ELT model periodograms with the averaged spectrum at the bottom. Here we see a very broad averaged spectrum which is difficult to process for carrier frequency measurement. For each trace, $T_D = 20$ms.

CHAPTER 3

BASIC CONCEPTS IN THE PROCESSING OF SARSAT SIGNALS

3.1 BASIC ISSUES

There are many practical limitations governing the accuracy in measuring the carrier frequency of any emergency signal [6]. These include: 1) the performance of the spectral estimator; 2) the receiver noise at the input to the satellite amplifier; 3) the change in Doppler shift due to satellite motion; and 4) the ELT or EPIRB carrier frequency stability. These issues will now be considered in order.

3.2 SPECTRAL ESTIMATOR

Modern spectral analysis recognizes both the linear and non-linear estimators. The linear spectral estimator considered here is the periodogram and the non-linear technique is the maximum entropy method (MEM).

For the periodogram, the frequency resolution is limited to approximately $f_R = 1/T_D$, where T_D is the window length of data for the rectangular window. Applying another window function increases the value of f_R; for example, the Kaiser window with -60 dB sidelobe level has a 3 dB bandwidth approximately 1.8 times higher than that of the rectangular window [7]. In addition, averaging contiguous periodograms further increases the value of f_R.

For the maximum entropy method, the window length of the data is no longer a restriction. Instead, the sharpness of the spectral estimate is controlled by the relative locations of the poles with respect to the unit circle in the z^{-1} plane. This in turn is related to the order of the MEM, which will be discussed in Chapter 4.

3.3 MINIMUM DETECTABLE CARRIER-TO-NOISE DENSITY RATIO

Measurement of signal detectability in the SARSAT system is based on the strength of the carrier peak as presented by the spectral estimate. Since the estimate of spectrum is normally presented as a power density versus frequency plot, the SARSAT signal is specified in terms of carrier-to-noise density ratio (CNDR).

For the periodogram, the minimum detectable value of CNDR for an Ideal Coherent ELT signal can be easily estimated. We note that the spectrum of an unmodulated carrier with amplitude A_C having duration T_D is simply $S_C(f) = [A_C T_D/2]^2 \, \mathrm{sinc}^2[(f-f_c)T_D]$, where f_c is the carrier frequency. In addition, the periodogram can be viewed as simply a parallel bank of filters, each with frequency response given by $\mathrm{sinc}[(f-f_c)T_D]$. Thus, the periodogram is a matched filter to the window of carrier with constant frequency.

The window of carrier of duration T_D has total energy of

$$E_C = 1/2 A_C^2 T_D \tag{3.1}$$

For the Ideal Coherent emergency signal, the energy in the same duration is

$$E_{IC} = 1/2 \, A^2 d \, T_D \tag{3.2}$$

If the energy of both signals is the same, then

$$A_C = d^{1/2} A \tag{3.3}$$

Using this relation and comparing the spectral peaks of the window of carrier and the coherent ELT signal given by eq. (2.11), we find when $f=f_c$,

$$\frac{S_{IC}(f)}{S_C(f)} = \frac{[A T_D d/2]^2}{[A_C T_D/2]^2} = d \tag{3.4}$$

Therefore, the loss in detection due to the modulation is d. Since d ranges from 0.55 down to 0.33, this loss is of the order of 2.6 to 4.8 dB.

Now, the maximum detectable signal-to-noise ratio at the output of a matched filter is given by [8]

$$SNR_{MAX} = \frac{2E}{N_0} \tag{3.5}$$

where E is the energy of the signal and N_0 is the noise spectral density. For the window of carrier, the total energy is given by eq. (3.1), and, consequently,

$$SNR_{MAX} = \frac{A_C^2 T_D}{N_0} = 2\,CNDR\,T_D \tag{3.6}$$

where $CNDR \doteq A_c^2/2N_0$. CNDR has the dimensions of dBHz and is defined as the ratio of signal power to noise density over the 3 dB bandwidth produced by the FFT. Taking account of the loss d, the minimum detectable CNDR for the emergency signal is simply

$$CNDR_{MIN} = \frac{SNR_{MAX}}{2d\,T_D} \tag{3.7}$$

Since the periodogram is equivalent to the magnitude square of the output of a filter, the amplitude distribution for input additive white Gaussian noise (AWGN) is Chi-square. When pulsed signals are present with AWGN, the output is Rician and the detection problem is identical to the envelope detection of radar pulses. Normally, the spectra of contiguous windows of data are averaged to reduce the variance of the spectral estimate. Assuming a total length of 1 s of data and 1 K periodograms, each of duration 20 ms (50,000 sample per second sampling rate), which are the values presently being used, there are 50 independent windows of data.

Referring to a standard text [9], we find that for probability of detection of 0.95 and 50 integrated pulses, the SNR varies from 0 dB to 2.5 dB for false alarm probabilities in the range from 10^{-4} to 10^{-12}. Using the above values, we find that the minimum detectable CNDR of 1 s of data with d = 0.4 is in the range of 19 to 21.5 dBHz, assuming a 1-dB threshold. If d = 0.55 (the maximum value), then these values are reduced by about 1.5 dBHz. Each doubling of the length of the periodogram, for the same 1 s duration of data,

reduces the value of CNDR by 1.5 dBHz. Thus, the 4 K FFT has a 3 dBHz advantage over the 1 K FFT and resolution four times better for the same record length of data.

The minimum detectable value of CNDR has been tested by computer simulation by averaging the 1 K periodograms of 50 contiguous blocks of Ideal Coherent signal with total duration 1 s. The simulation was tested with different combinations of carrier frequency and CNDR values. Using the 20 dBHz and 25 dBHz values with d = 0.4, we see from Fig. 3.1 that at 25 dBHz, the signal is easily detected while at 20 dBHz, detection (with threshold at, say, –1 dB) would be achieved only with a large number of false alarms. Thus, the calculated value is in agreement with the simulation.

3.4 EFFECTS OF CHANGE IN DOPPLER FREQUENCY SHIFT

The third practical limitation is due to the satellite motion. The change in Doppler shift can be determined by analysing a satellite in orbit around a spherical earth [10] or more simply by using a 'flat earth' approximation which is reasonably accurate at minimum 'satellite-to-ELT' distance. Using the flat-earth model of Fig. 3.2, we find that the carrier frequency of the ELT signal received at the satellite is given by

$$f_r = f_c - f_d \frac{x}{\sqrt{x^2 + h^2 + z_o^2}} \tag{3.8}$$

where f_r = received frequency at the satellite

f_c = carrier frequency of ELT unit

f_d = Doppler shift of the signal

= v_s/λ

v_s = velocity of the satellite

λ = wavelength of the carrier

x = distance along the flight path

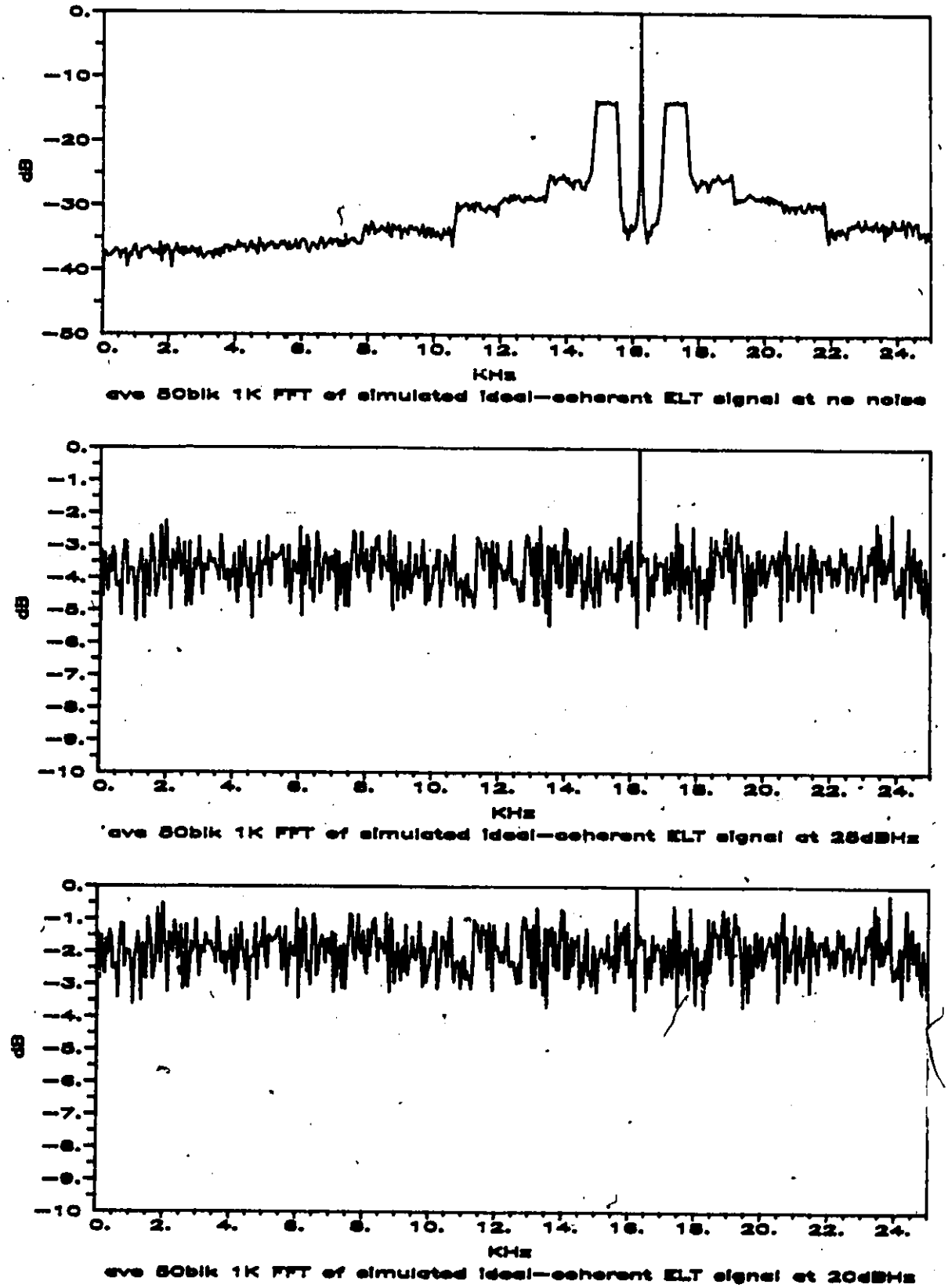

Fig. 3.1 Averaged spectra for 50 blocks of 1K periodograms at different values of carrier-to-noise density ratio. (a) CNDR = infinity, (b) CNDR = 25dBHz and (c) CNDR = 20dBHz.

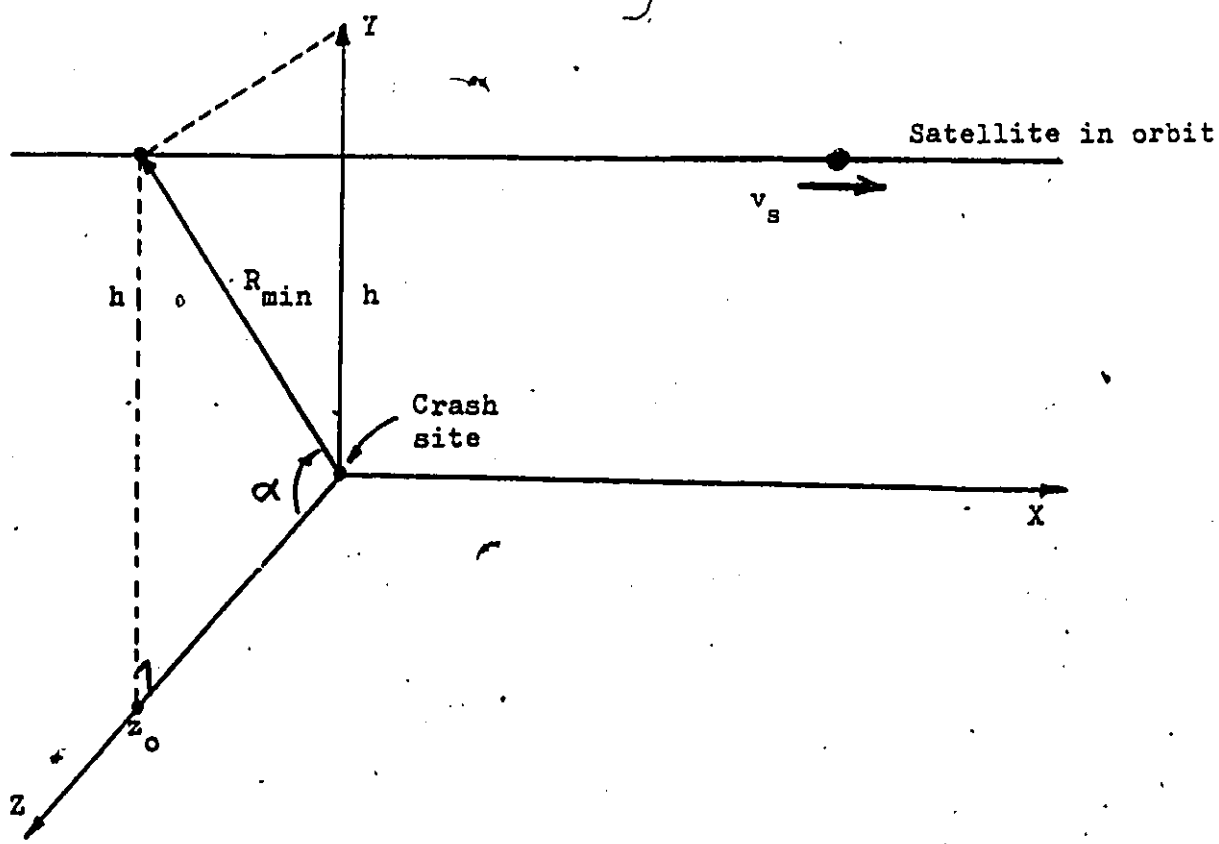

Fig. 3.2 Flat-earth model of the SARSAT geometry.

h = altitude of the satellite

z_0 = displacement of unknown magnitude.

Calculating the first derivative with respect to time, we have

$$f_r' = \frac{df_r}{dt} = -v_s f_d \left| \frac{h^2 + h^2 \cot^2 \alpha}{(x^2 + h^2 + z_0^2)^{3/2}} \right| \tag{3.9}$$

since the satellite travels at a velocity of $v_s = dx/dt$. The satellite is closest to the crash site when $x = 0$ yielding

$$f_r' = \frac{-v_s f_d}{(h^2 + z_0^2)^{1/2}} \Bigg|_{x=0} = \frac{-v_s f_d}{R_{min}} \tag{3.10}$$

where R_{min} is the distance from ELT site to satellite at the inflection point. Thus

$$R_{min} = \frac{-v_s f_d}{f_r' \Big|_{x=0}} \tag{3.11}$$

The value of f_r' at R_{min} is determined by deducing the location of the inflection point in the S-shaped curve and measuring f_r' at that point.

The maximum value of f_r' is approximately 27.5 Hz/s, occurring at the inflection point of the S-shaped curve (Fig. 1.2) for an overhead satellite pass. Since the measurement of carrier frequency in the vicinity of this inflection point is most important in determining ELT or EPIRB location, it is vital that the signal processing performs well under this changing Doppler shift condition.

For the case of an ELT signal with perfect carrier stability, the minimum window length of the periodogram can be deduced for the case of a signal with the maximum change in Doppler shift. (Signals with smaller Doppler shifts could obviously benefit from longer window lengths.) For a period of T_W, the maximum change in Doppler shift is just $f'_r T_W$ Hz. If the window length of the periodogram is T_D, then the 3dB bandwidth of one frequency bin is approximately W/T_D, where W is the increase in bandwidth due to the window. For example,

the Kaiser window with sidelobes reduced to -60 dB has a 3 dB bandwidth approximately 1.8 times higher than that of the rectangular window [7].

Let the total number of windows in time T_W be M or $T_W = MT_D$. Then, from Fig. 3.3,

$$W/T_D = f_r' T_W = f_r' MT_D$$

or

$$M = W/(f_r' T_D^2) \tag{3.12}$$

For $f_r' = 27.5$ Hz/s, $T_D = 0.020$ s (for the 1 K FFT) and $W = 1.8$ we find that $M = 163$ blocks of data. Thus, the processing time should be approximately $T_W = 3.3$ s.

A second restriction on the time between frequency estimates relates to the velocity of the satellite with respect to earth. Since the satellite velocity is approximately 7.6 km/s with respect to the earth, an error of $\pm 3.8\, T_W$ km exists due to interpoint resolution. Thus, if the total processing time is restricted, to say 1 s (which is assumed here), in order to give more precise timing estimates, then $MT_D = 1$s. From eq. (3.12), we find that $T_D = 65$ ms. This value is almost exactly half-way between the window length of the 2 K FFT (40 ms) and the window length of the 4 K FFT (80 ms). Since the calculation gives the minimum window length, we choose the 4 K FFT with $M = 12$ (and observe that the higher order FFT improves detection and resolution for all passes that are not directly overhead).

3.5 CARRIER FREQUENCY STABILITY

Usually, the carrier frequency of an emergency signal has a certain long term drift caused by temperature variations and changes in the power supply voltage feeding the oscillator. In addition, there is a frequency jitter associated with the signal. The sum total of these two effects can be used to label particular signals provided the effect of Doppler shift is removed. The carrier frequency can be expressed by the relation

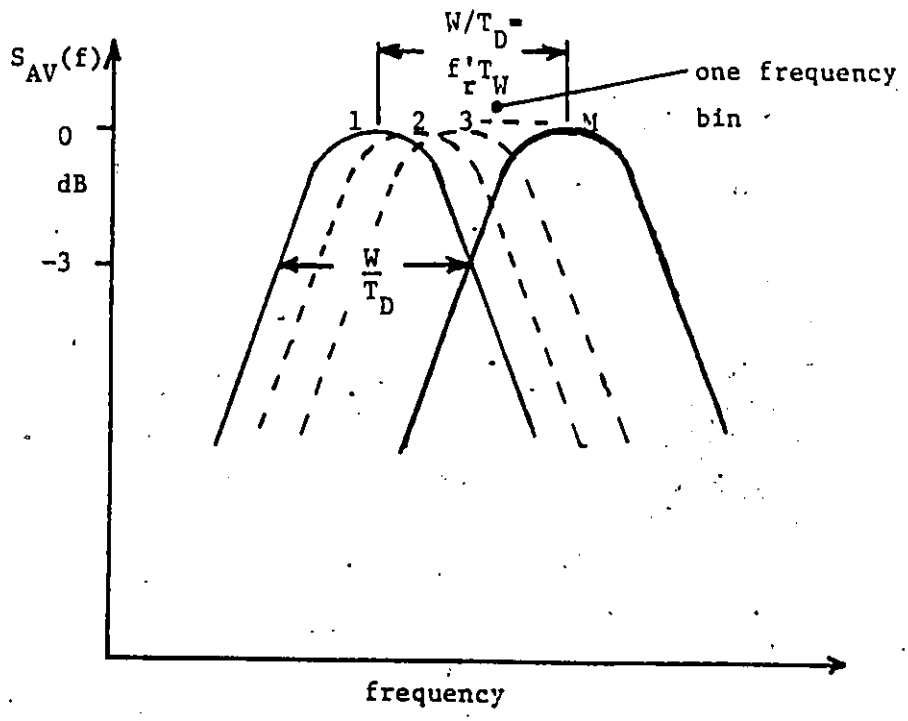

Fig. 3.3 Maximum number of signal spectra falling in one frequency bin of width W/T_D when change in Doppler shift occurs.

$$f_c = f_o + F_d't + f_j \tag{3.13}$$

where

f_o = nominal carrier frequency

F_d' = constant value frequency drift in Hz/s

f_j = frequency jitter

If we assume that the frequency drift term is a linear function of time, i.e., F_d' is constant, then substituting eq. (3.13) into eq. (2.2) results in a summation of Fresnel's sine and cosine integrals. While mathematically correct, the method gives little insight as to the resulting spectrum. Thus, we attempt another approach.

From eq. (2.11), we note that the spectrum for an Ideal Coherent signal has a well defined carrier peak at frequency $f = f_c$. To a first approximation, the sinc function is approximately unity and the sine function in the denominator varies N times more slowly than the sine function in the numerator and can be replaced with $\pi(f-f_c)T_D/N$.

Thus, near the carrier peak, we have approximately,

$$S_{IC} = \left(\frac{AdNT}{2}\right)^2 \operatorname{sinc}^2[\pi(f-f_c)T_D] \tag{3.14}$$

The effect of the frequency drift on this signal is similar to FM increasing the bandwidth by $F_d'T_D$, as illustrated in Fig. 3.4 and the measured 3 dB bandwidth with any window is now

$$B_M = F_d'T_D + \frac{W}{T_D} \tag{3.15}$$

where W is the increase in bandwidth due to the window.

For the case of frequency jitter and noise, it is assumed that the long term effect is stationary. Consequently, for coherent emergency signals, the overall bandwidth of the signal is given by

$$B_E = F_d'T_D + \frac{W}{T_D} + B_J \tag{3.16}$$

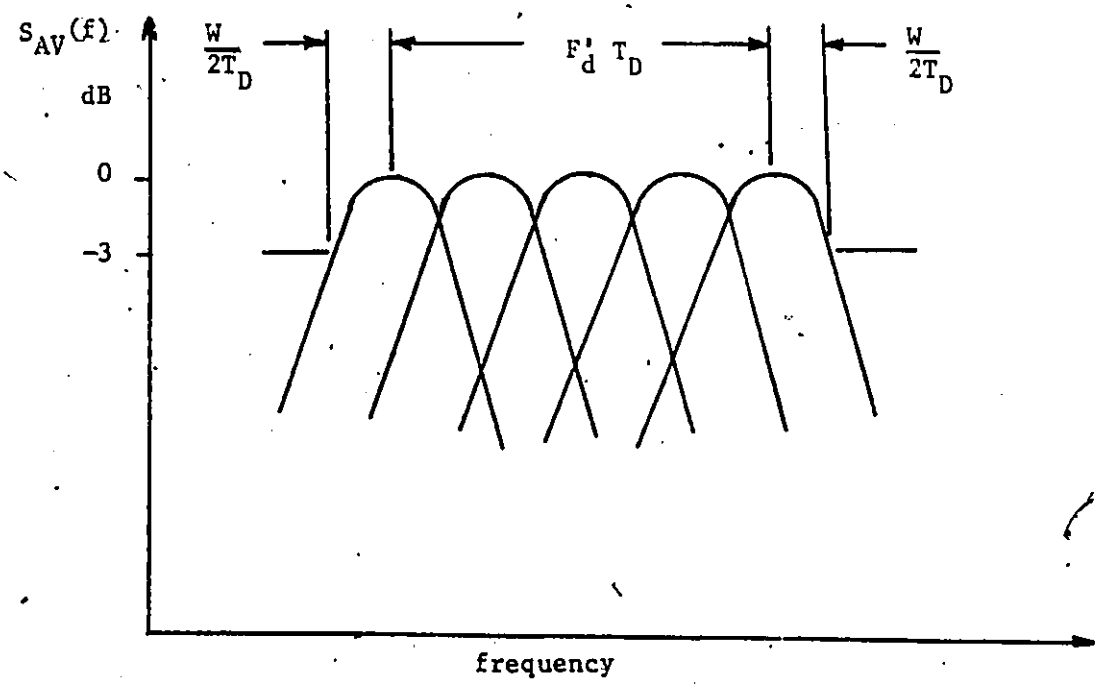

Fig. 3.4 Increase in spectral bandwidth due to constant frequency change drift in the ELT carrier frequency.

where B_J is the bandwidth contribution produced by jitter and noise.

Taking account of the change in Doppler shift due to satellite motion, f_r', we find the measured 3 dB bandwidth for an averaged spectrum of duration MT_D is

$$B_T = B_E + f_r' M T_D \tag{3.17}$$

The value of B_E is a characteristic of the signal itself and can be separated from the Doppler shift in a practical way by simply computing the averaged periodograms in two or more consecutive time intervals. We note that the change in centre frequency is a measure of the change in Doppler shift which in turn provides f_r'. By computing B_T at several different times along the pass, f_r' is obtained and B_E can be calculated using eq. (3.17), provided that the resolution of the FFT is less than the bandwidth of the signal.

Three examples of this are given for real satellite pass data in Fig. 3.5 for signals A, B and C. The average of twelve 4K-periodograms is taken for three 1 s durations with the interval between each estimate being 5 s. For signal A, we find the frequency change from plot to plot is approximately 26.2 Hz, resulting in $f_r' = 5.2$ Hz/s. The averaged value of B_T is approximately 23 Hz. With $M = 12$ ($T_D = 0.08$ s), we substitute into eq. (3.17) and get:

$$B_T = 23 \text{ Hz} = (B_E + 5.2 \times 12 \times 0.08) \text{ Hz}$$

or

$$B_E = 18.0 \text{ Hz}.$$

Although the calculated bandwidth of signal A is 18.0 Hz, we note that this value is essentially equal to the resolution of the FFT. Consequently, we can say only that the signal has a bandwidth less than or equal to 18 Hz and a Doppler shift of 5.2 Hz/s.

For signals B and C, the same analysis can be applied resulting in bandwidths of 15 Hz and 75 Hz, respectively. We note that for signal B, the change in Doppler shift is negligible and again the bandwidth measurements is restricted by the resolution of the FFT. For signal C, the change in Dop[illegible]ency (6 Hz/s) is slightly higher than for signal A, and

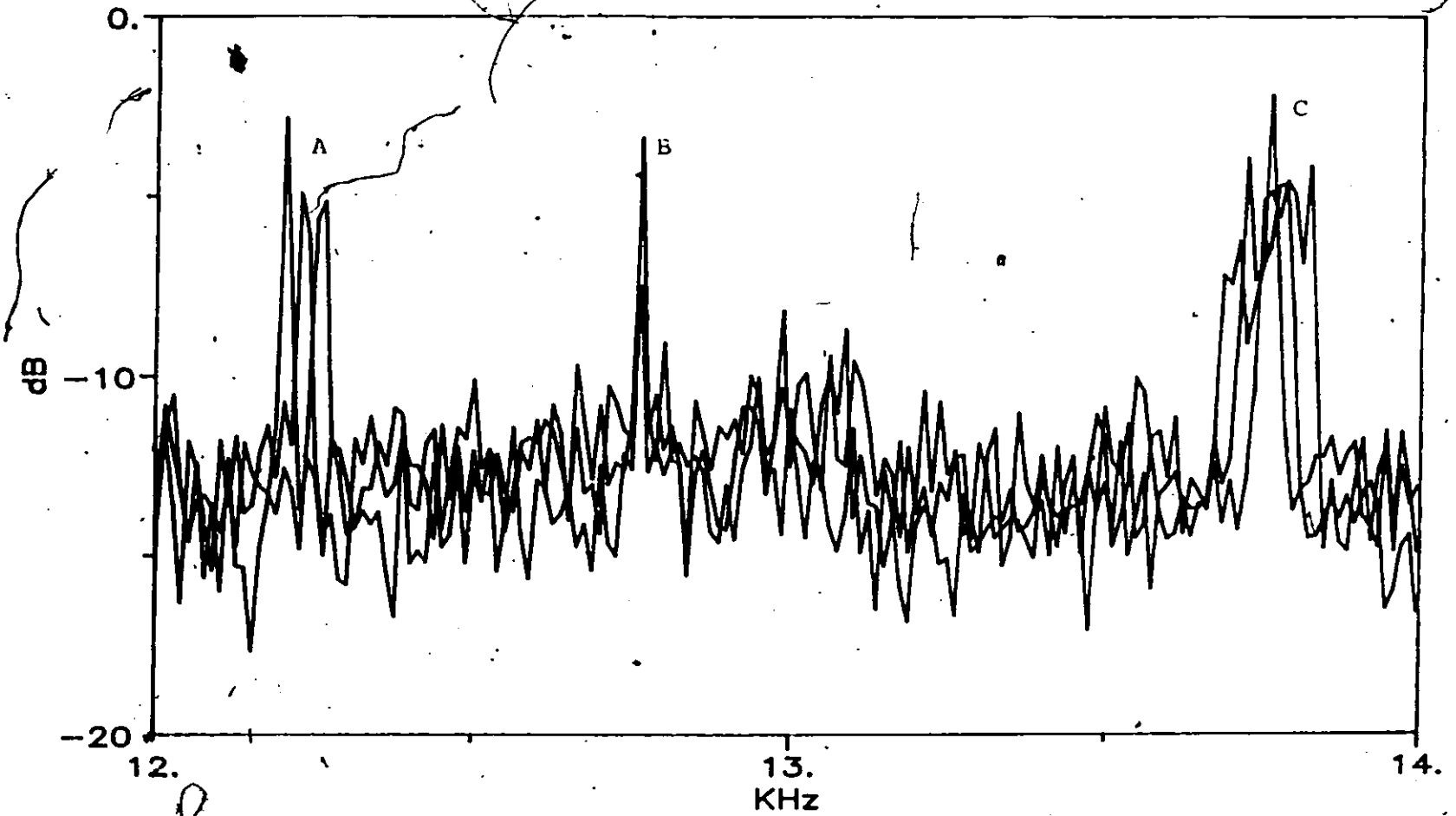

Fig. 3.5 Superposition of three one-second spectral estimates (each the average of 12 4K-point periodograms) taken at consecutive 5sec intervals from orbit 661.

the bandwidth is very much higher than the resolution of the FFT. Thus, using signal bandwidth and Doppler shifts, three different signals have been labelled and the differences between their bandwidths and Doppler shifts [A = (18, 5.2) B = (15, 0), C = (75, 6)] are measurable.

3.6 SUMMARY

In this Chapter, we examine the basic issues in the processing of SARSAT signals. Use of the periodogram rather than the matched filter degrades the signal-to-noise ratio by 2.6 to 4.8 dB for an ideal ELT signal. For non-ideal signals, the degradation is greater.

Assuming an ideal ELT signal, the minimum carrier-to-noise density ratio (CNDR) that can be detected for 1s of data averaging 50 blocks of 1K periodogram is approximately 20 dBHz. A near optimal choice for processing this 1s of data using the FFT is the averaging of 12 blocks of 4K periodograms.

CHAPTER 4

SIGNAL PROCESSING STRATEGIES

There are many problems to be solved for the signal processing of SARSAT signals since the spectral properties of ELT and EPIRB signals vary considerably [5]. It has already been shown that these signals generate not only carrier peaks but also sideband peaks which produce in-band interference [12]. As a result, a matched filter receiver is difficult to design. In the real environment, there are numerous other interferers which add to the already crowded spectrum. This topic will be discussed in Chapter 6.

In this chapter, we examine the performance of different processing strategies on real signals recorded from an ELT testbed at the Communications Research Centre in Ottawa, Canada. It is found that the periodogram-based processor presently in use is suitable for estimating good quality ELT signals. In addition, the maximum entropy method is found to be effective in processing ELT signals having non-coherent characteristics.

4.1 THE MATCHED FILTER METHOD

In this section we investigate the implementation of matched filter structure as applied to the detection of ELT signals. It is shown that, in general, a direct implementation of matched filtering cannot be applied to the ELT signals. This is due mainly to the requirement of the large number of matched filters which would be needed. However, by employing the modulating wave of the ELT signal, a matched filter response can be approximated. This method provides signal enchancement of the computation of spectrum for coherent ELT signals.

Before we discuss the design of matched filter for ELT signals, it is first necessary to understand the ELT signal model. This issue has been studied in Chapter 2. However, for convenience, the spectral expression of an Ideal Coherent model ELT signal (see eq. (2.11)) is repeated here,

$$S_{IC}(f) = \left(\frac{AdT}{2}\right)^2 \text{sinc}^2[(f - f_c)\,dT] \left\{ \frac{\sin^2[\pi(f - f_c)T_D]}{\sin^2[\pi(f - f_c)\frac{T_D}{N}]} \right\} \tag{4.1}$$

Our intention is to develop a matched filter structure which has a spectral expression similar to that of eq. (4.1). We want to show that an exact matched filter response can be achieved simply by employing the modulating wave of the signal. This method is tested using three different schemes: 1) the time domain approach; 2) the frequency domain approach and 3) the autocorrelation function approach.

4.1.1 The Matched Filter Structure

Consider the network depicted in Fig. 4.1. The circuit consists of a set of delay elements, feeding multipliers connected to a summer. This is equivalent to the structure of a transversal filter.

The input to the network is a pulse carrier signal of duration dT given by

$$x(t) = A\cos[2\pi f_c t] \qquad -\frac{dT}{2} \le t \le \frac{dT}{2} \tag{4.2}$$

where A is the amplitude of the pulse; f_c is the carrier frequency; T is the pulse-null duration and d is the duty cycle. The basic increment of delay is equal to the duration of the pulse (i.e T) and the weights are defined by

$$w_m = \exp[j2m\pi f_s T] \qquad m = 0,1,2,\ldots,M\text{-}1 \tag{4.3}$$

where f_s is an adjustable constant to be described later.

The output at the summer can be expressed by

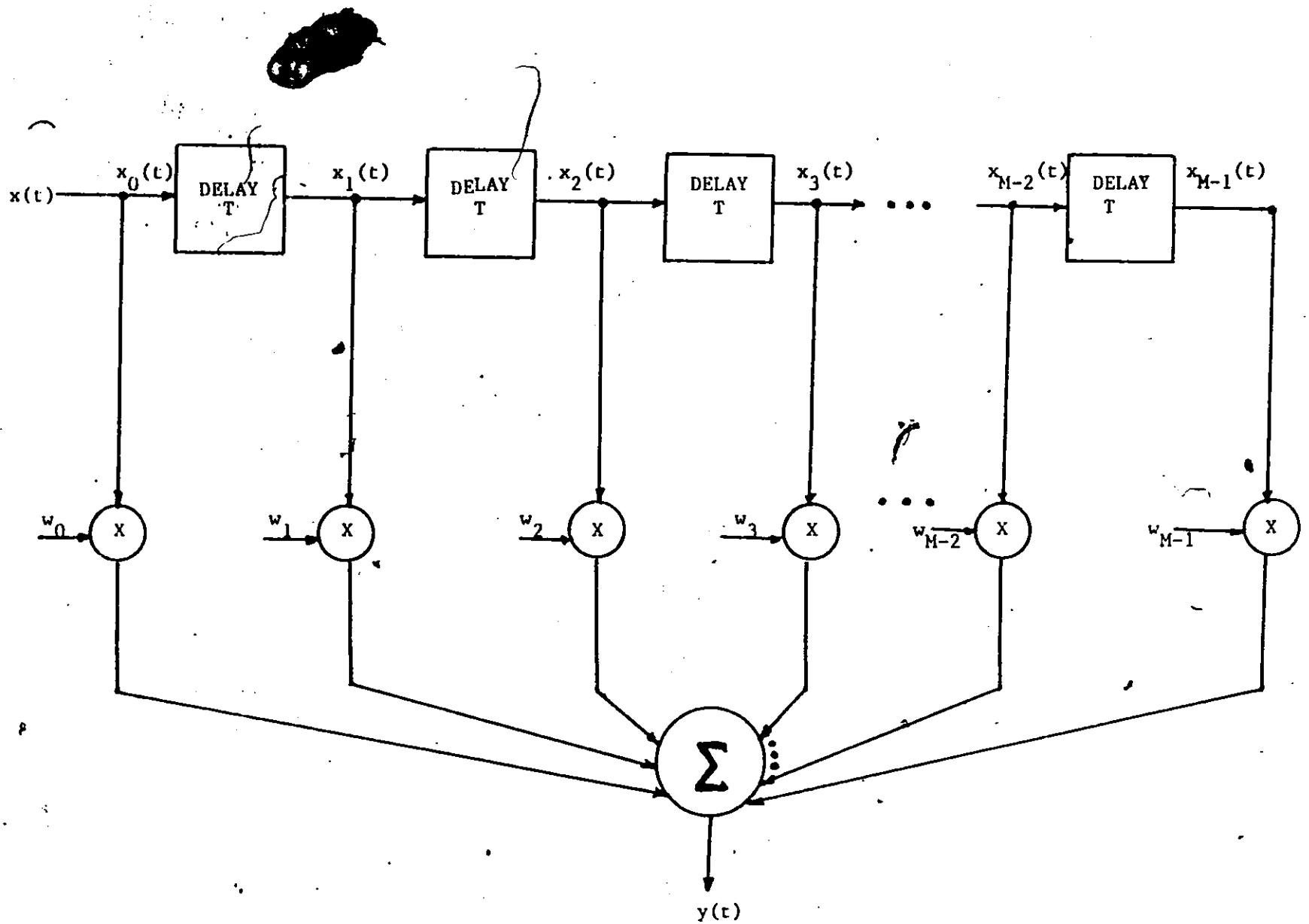

Fig. 4.1 A transversal filter implemented as a matched filter for the detection of ELT signal.

$$y(t) = A \sum_{m=0}^{M-1} \cos[2\pi f_c (t - mT)] \exp[j2m\pi f_s T] \tag{4.4}$$

Evaluating the Fourier transform of y(t), we get

$$Y(f) = X(f) \sum_{m=0}^{M-1} \exp[-j2m\pi(f - f_s)T] \tag{4.5}$$

where $X(f) = (AdT/2)\mathrm{sinc}[(f - f_c)dT]$. The expression can be further simplified since

$$\begin{aligned} \sum_{m=0}^{M-1} \exp[-j2m\pi(f - f_s)T] &= \frac{1 - \exp[-j2M\pi(f - f_s)T]}{1 - \exp[-j2\pi(f - f_s)T]} \\ &= \frac{\sin[M\pi(f - f_s)T]}{\sin[\pi(f - f_s)T]} \exp[-j(M-1)\pi(f - f_s)T] \end{aligned} \tag{4.6}$$

Computing the spectrum of Y(f), we have

$$S_Y(f) = \left(\frac{AdT}{2}\right)^2 \mathrm{sinc}^2[(f - f_c)dT] \left\{\frac{\sin^2[M\pi(f - f_s)T)]}{\sin^2[\pi(f - f_s)T]}\right\} \tag{4.7}$$

We see that the spectrum is also a product of two relations, the first being the sinc function which has a peak at $f = f_c$ and the first nulls at $f_c \pm (1/dT)$. The second relation is the ratio of two sines, which produces a multi-peak pattern with the peaks located at $f = f_s \pm (m/T)$, $m = 0,1,2,\ldots$ and the bandwidth of each peaks is $2/(MT)$. Comparing eq. (4.1) with eq. (4.7), the only difference in both expressions is the ratio of the two sines. The former equation has the ratio governed by the carrier frequency (f_c), the window length of the data (T_D) and the number of pulse-null pairs (N). The ratio from eq. (4.7) is affected by the amount of frequency shift (f_s), the duration of the pulse-null (T) and the number of delay elements (M). By manipulating these parameters, the spectrum calculated from eq. (4.7) becomes identical to eq. (4.1). This occurs when $f_s = f_c$. In addition, $MT = T_D$ for the filter and $T = T_D/N$ for the signal (which implies that $M = N$). This is an exact matched case.

The result of eq. (4.7) leads to a possible implementation of a matched filter receiver, which can be applied to the detection of ELT signals. However, in practice, receiver requires a set of matched filter responses which represent a replica of the modulated signal

over the entire bandwidth of the ELT signal spectrum. Although these responses can be modelled by employing eq. (4.7), the design of such a receiver is costly. It is due to the fact that there is a large number of ELT units in operation. Depending on the design specification, these electronic devices generate ELT signals which produce a wide range of spectra. Thus, a direct implementation of matched filter for ELT signals is not feasible. In the following section, we propose a strategy that provides signal enhancement for measuring ELT signal spectra.

4.1.2 An Exact Matched Filter Implementation

The typical ELT signal is a train of pulse-modulated carrier signal. The modulating wave is characterized by the pulse-null pairs. The pulse-null pairs have duty cycles ranging from 33% to 55% and the duration varies from approximately 0.7 ms (beginning of a sweep) to about 1.7 ms (end of a sweep). Depending on the particular ELT unit, one sweep of the signal may vary from 0.25 s to 0.5 s. We understand that the overall spectral characteristic of the ELT signal depends on the modulating wave. Once the modulation waveform is known, the carrier signal in a noisy background can be detected by the matched filter technique. In general, a matched filter for ELT signals is very difficult to develop. It is because of the range of specifications for the ELT units. However, by making use of the modulating wave, it is possible to provide a detection technique which is similar to that of matched filtering. Three approachs are applied to the method. First, we evaluate the Fourier transform of the product of the ELT signal and its baseband signal (time domain approach). Second, the convolution of the Fourier transform of the ELT signal and its baseband signal is calculated (frequency domain approach). Third, the autocorrelation function of the modulated signal and the modulating waveform are multiplied and the spectrum is measured (autocorrelation function approach). In each case, we study the

situation at exact matched response. Then, we discuss how the method can be implemented. The performance of the strategies is tested at different signal-to noise ratios and the results are discussed in a later section.

A. Time Domain Approach

The equation represents the output of a matched filter is [11].

$$y_j(T) = \int_0^T x(\tau)\,\phi_j(\tau)\,d\tau \tag{4.8}$$

We note that $y_j(T) = x_j$, where x_j is the j-th output produced by the received signal x(t) with respect to the j-th reference signal $\phi_j(t)$. The $\phi_j(t)$ is actually the filter response of a matched filter. At exact match (EXM), the output of the filter becomes

$$y_{EXM}(t)dt = x(t)\,\phi_{EXM}(t)dt \qquad 0 \le t \le T \tag{4.9}$$

where $\phi_{EXM}(t)$ defines the exact matched response of the filter to the input signal. Suppose the received signal x(t) is defined by

$$x(t) = A\,\mathrm{rect}\left(\frac{t}{T}\right)\cos(2\pi f_c t) \tag{4.10}$$

where the function rect(t/T) is defined by

$$\mathrm{rect}(t) = \begin{cases} 1 & 1/2 \le t \le 1/2 \\ 0 & |t| > 1/2 \end{cases} \tag{4.11}$$

In order to have an exact match response, $\phi_{EXM}(t)$ must be identical to the modulating waveform

$$\phi_{EXM}(t) = \mathrm{rect}\left(\frac{t}{T}\right) \tag{4.12}$$

Therefore, the matched filter output for a pulse-modulated carrier signal at exact match is expressed by

$$\begin{aligned} y_{EXM}(t) &= x(t)\,\phi_{EXM}(t) \\ &= [A\,\mathrm{rect}\left(\frac{t}{T}\right)\cos(2\pi f_c t)]\,\mathrm{rect}\left(\frac{t}{T}\right) \end{aligned} \tag{4.13}$$

Since the rectangular function is defined by eq. (4.11), the spectrum of $y_{EXM}(t)$ is shown by

$$S_{Y_{EXM}}(f) = \left(\frac{AdT}{2}\right)^2 \operatorname{sinc}^2[(f-f_c)dT] \tag{4.14}$$

which is similar to the expression obtained from eq. (4.1) with the exception of the ratio of two sines. This method is applied to the detection of ELT signal. In this test, the simulated Ideal Coherent ELT signal s(t) is multiplied by the modulating signal m(t). The product is then input to a FFT processor. The spectrum is found to have the same set of spectral characteristics as the ELT signal itself, which is illustrated in Fig. 4.2.

B. Frequency Domain Approach

The Fourier transform of the pulse-modulated carrier signal x(t) described by eq. (4.10) is

$$F_x(f) = \frac{AdT}{2} \operatorname{sinc}[(f-f_c)dT] \tag{4.15}$$

and the Fourier transform of the exact matched filter response shown in eq. (4.12) is

$$F_{\Phi_{EXM}}(f) = dT \operatorname{sinc}[fdT] \tag{4.16}$$

The convolution of these two functions gives the Fourier transform of the matched filter output

$$F_{Y_{EXM}}(f) = F_x(f) * F_{\Phi_{EXM}}(f) \tag{4.17}$$

It is well known that the multiplication of two functions in time domain is transformed into the convolution of their individual Fourier transforms in the frequency domain. The spectrum calculated from eq. (4.17) is equal to the expression given in eq. (4.14). The purpose of introducing eq. (4.17) is that in dealing with filtering design we often refer to the frequency domain. Thus, eq. (4.17) has its importance for implementation purposes. The usual steps to evaluate a convolution is to multiply the inverse Fourier transform of the two functions and find the Fourier transform of the product. Another way of solving the equation is to multiply the Fourier transform of the two functions and take the inverse Fourier transform of the

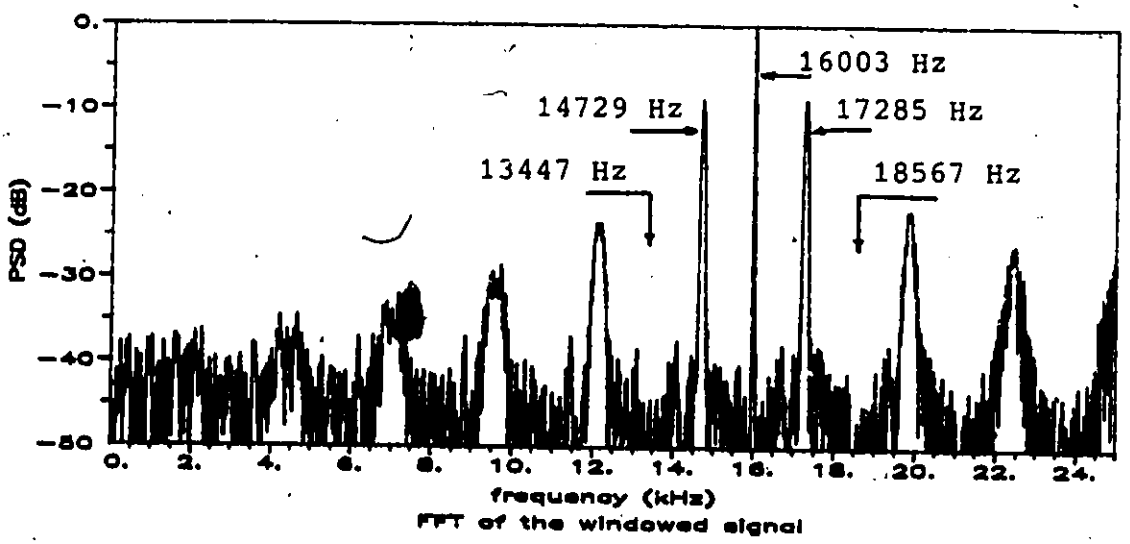

Fig. 4.2 Spectrum of a 4K-points simulated Ideal Coherent ELT signal.

product. Both procedures can be easily implemented using an array processor typed computer.

C. Autocorrelation Function Approach

The Fourier transform is equivalent to a set of filters each having the $\mathrm{sinc}^2[(f-f_{c_i})T]$ frequency response, where f_{c_i} is the centre frequency of the i-th filter and T is the time duration of the Fourier transform. For a window length T of carrier at frequency f_c, the frequency response is $\mathrm{sinc}^2[(f-f_c)T]$. Thus, the Fourier transform automatically provides a matched filter implementation when the input signal is a length of unmodulated carrier at constant frequency f_c. Also we know that the autocorrelation function (ACF) and power spectral density form a Fourier transform pair according to Wiener-Khintchine relations

$$S(f) = \int_{-\infty}^{\infty} R(\tau)\exp(-j2\pi f\tau)\,d\tau \tag{4.18}$$

$$R(\tau) = \int_{-\infty}^{\infty} S(f)\exp(j2\pi f\tau)\,df \tag{4.19}$$

where S(f) is the spectrum of the signal and $R(\tau)$ is the autocorrelation function. It is possible to relate the ACF of a signal as a matched filter response.

When the signal is a length of unmodulated carrier with frequency f_c and amplitude A, then $R(\tau)$ is the product of a cosine term and the triangular envelope function

$$R(\tau) = \frac{A^2}{2}\left(1 - \frac{|\tau|}{T}\right)\cos(2\pi f_c\tau), \qquad |\tau| < T \tag{4.20}$$

For a pulse-modulated carrier signal x(t) defined by eq. (4.10), depending on the duty cycle, the ACF of the signal $R_x(\tau)$ has the similar form as in eq. (4.20). $R_x(\tau)$ is equal to $R(\tau)$ if the duty cycle is 100 %.

Since the spectrum is simply the Fourier transform of the ACF, we expected that the triangular autocorrelation function is the matched filter representation for an unmodulated length of carrier signal. Hence, if we have any waveform which has an ACF

approximately equal to eq. (4.20), then the inverse Fourier transform provides a matched filter response for this signal.

Suppose a modulating waveform m(t) consists of N pulse-null pairs with duty cycle d and duration T. The N-lag ACF, $R_m(\tau)$, of this waveform is sketched in Fig. 4.3. The equations for this function are,

$$R_{m_+}(\tau) = \frac{A^2}{N}\sum_{n=1}^{N-1}\left\{(N-n)\left(\frac{dT-|\tau-nT|}{T}\right)\right\} \qquad nT-dT\le\tau\le nT+dT \tag{4.21}$$

$$R_{m_0}(\tau) = A^2\left(\frac{dT-|\tau|}{T}\right) \qquad -dT\le\tau\le dT \tag{4.22}$$

$$R_{m_-}(\tau) = \frac{A^2}{N}\sum_{n=1}^{N-1}\left\{(N-n)\left(\frac{dT-||\tau|-nT|}{T}\right)\right\} \qquad -(nT+dT)\le\tau\le-(nT-dT) \tag{4.23}$$

where the subscript '+' indicates the positive lag part, '0' is the zero lag part and '−' denotes the negative lag. For a pulse-modulated signal described by eq. (4.10), the ACF $R_x(\tau)$ is just the product of $\cos(2\pi f_c\tau)$ with each of the equations defined by eq. (4.21), (4.22) and (4.23).

Following the previous discussion, we want to investigate an exact matched filter representation by means of the ACFs. The ACF of the pulse-modulated signal is multiplied by the ACF of the baseband signal,

$$R_{m_+}(\tau)R_{x_+}(\tau) = \left(\frac{A^2}{NT}\right)^2\sum_{n=1}^{N-1}\left\{(N-n)^2(dT-|\tau-nT|)^2\right\} \cdot\cos(2\pi f_c\tau) \qquad nT-dT\le\tau\le nT+dT \tag{4.24}$$

$$R_{m_0}(\tau)R_{x_0}(\tau) = \left(\frac{A^2}{T}\right)^2(dT-|\tau|)^2\cos(2\pi f_c\tau) \qquad -dT\le\tau\le dT \tag{4.25}$$

$$R_{m_-}(\tau)R_{x_-}(\tau) = \left(\frac{A^2}{NT}\right)^2\sum_{n=1}^{N-1}\left\{(N-n)^2(dT-||\tau|-nT|)^2\right\} \cdot\cos(2\pi f_c\tau) \qquad -(nT+dT)\le\tau\le-(nT-dT) \tag{4.26}$$

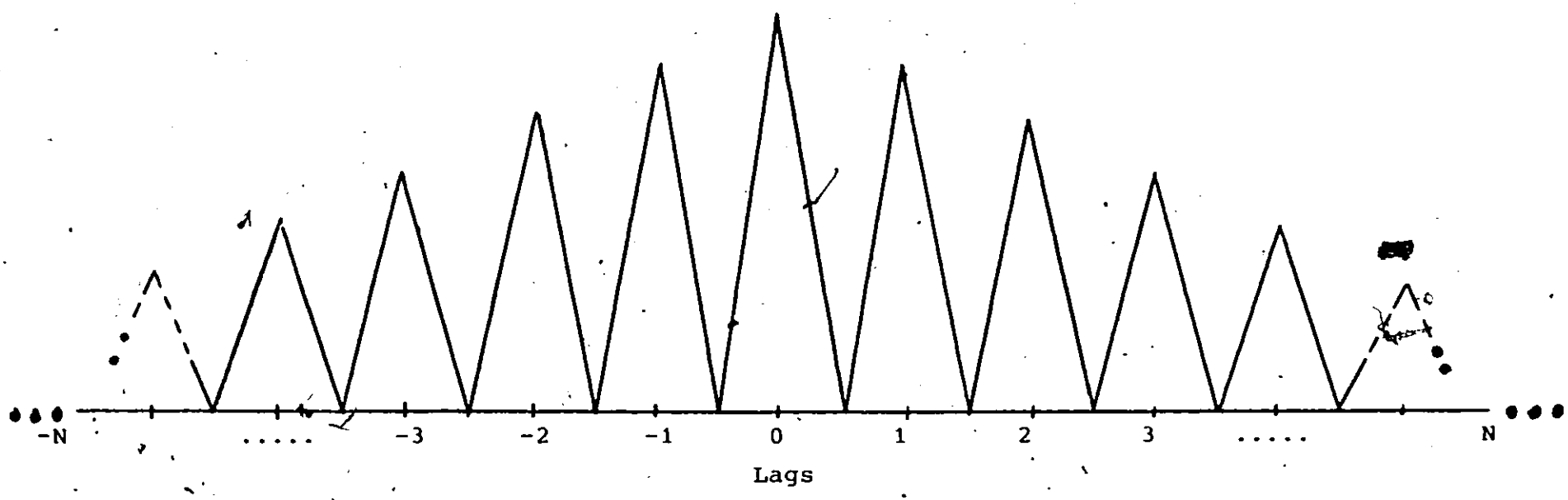

Fig 4.3 The N-lag autocorrelation function of N pulse-null pairs modulation waveform.

The power spectral density is evaluated by using the Fourier transform,

$$S_{R_m R_n}(f) = S_1 S_2 \tag{4.27}$$

where

$$S_1 = \left(\frac{A^2}{2\pi(f-f_c)}\right)^2 \frac{d}{T}\,(1 - \mathrm{sinc}[2(f-f_c)dT]) \tag{4.28}$$

$$S_2 = 1 + \frac{2}{N^2}\sum_{n=1}^{N-1}\left\{(N-n)^2 \cos[2\pi(f-f_c)nT]\right\} \tag{4.29}$$

The functions of S_1, S_2 and $S_{R_m R_n}(f)$ are plotted in Fig. 4.4. From these expressions, we see that the wide bandwidth of S_1 passes all the peaks that are generated by the component S_2. Thus the autocorrelation function approach is not an adequate method.

4.1.3 The Structure of Matched Filter

In the previous sections, using three different approaches we have examined the spectrum of a simulated Ideal Coherent ELT signal at the output of an exact matched filter. It has been shown that both the time and frequency methods provided better spectral estimates than the autocorrelation function.

According to eq. (4.9), implementation of a matched filter using the time domain technique requires two steps. The input signal is multiplied by a reference (or replica) waveform and the product is integrated over the interval T. For ELT signal processing, a large number of reference waveforms is needed to ensure matched filter operation. Thus, this method involves a large amount of computing time.

The fast Fourier transform (FFT) algorithm is the most efficient way of evaluating a discrete Fourier transform. From the expression given by eq. (4.17), the spectrum at the output of the matched filter can be estimated by the convolution of the individual Fourier transforms of the input signal and the reference waveform. By means of the FFT, convolution can be easily implemented.

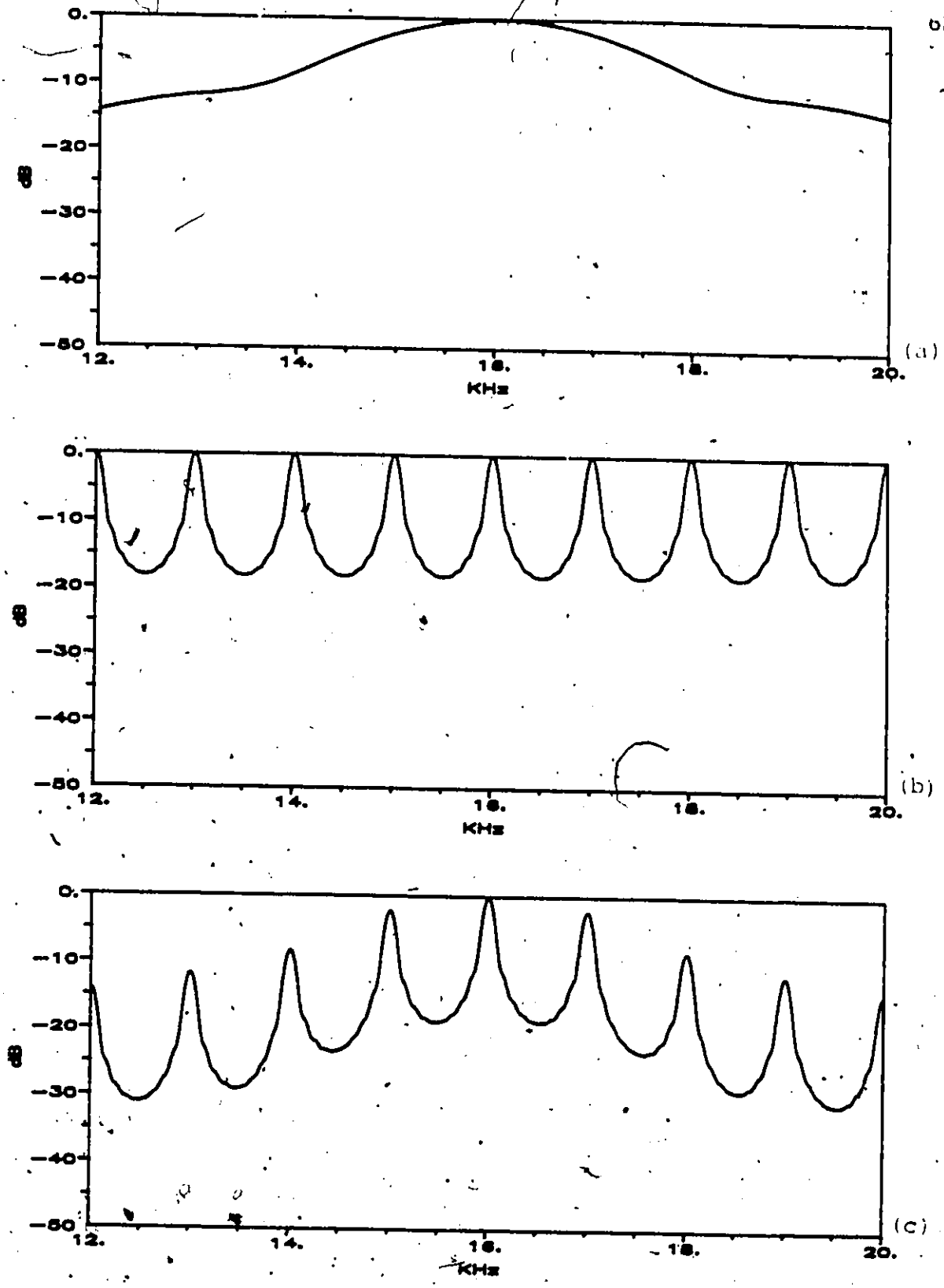

Fig. 4.4. (a) Plot of eq. (4.28) for $f_c = 16$KHz, $d = 0.5$ and $T = 1$ms.

(b) Plot of eq. (4.29) for $N = 10$.

(c) Plot of $S_{R_{mPx}}(f)$, eq. (4.27).

The spectrum of the modulating wave m(t) for simulated Ideal Coherent ELT signal is shown in Fig. 4.5. We note that the locations of the sideband peaks with the respect to the baseband frequency are determined by the duration of the pulse-null pairs and the duty cycle. Following the same analogy as in eq. (4.7), the spectrum can be expressed as

$$S_m(f) = \left(\frac{AdT}{2}\right)^2 \mathrm{sinc}^2(fdT)\,\frac{\sin^2(M\pi fT)}{\sin^2(\pi fT)} \tag{4.30}$$

We note that eq. (4.30) defines the spectrum of a baseband signal. A set of frequency response of baseband signals with different pulse-null pairs duration and duty cycle can be generated and stored in a computer. The spectrum of the matched filter output can then be estimated using eq. (4.17) and the fast Fourier transform. This technique is more efficient than applying the time domain approach, where replica of received signal is required.

4.1.4 The Matched Filter Performance with Variations in Noise Background

The problem of processor performance for a weak ELT signal immersed in additive white Gaussian noise (AWGN) must be considered since it is important that these signals not be missed.

A simplify mathed filter structure is sketched in Fig. 4.6. The signal x(t) and noise n(t) are summed at the input and fed to a multiplier which multiplies its input by a reference waveform $\phi(t)$. The output of the multiplier is then integrated over a period of T seconds. Using a maximum likelihood type of estimator, it is also possible to employ matched filters for spectral estimator [13].

The matched filter is known to have the maximum value of output signal-to-noise ratio which depends only upon the ratio of the signal energy to the spectral density of the white noise at the filter output [11]. This relation is already formulated in eq. (3.5). In order to demonstrate its performance, simulated Ideal Coherent ELT signal is used. The signal has

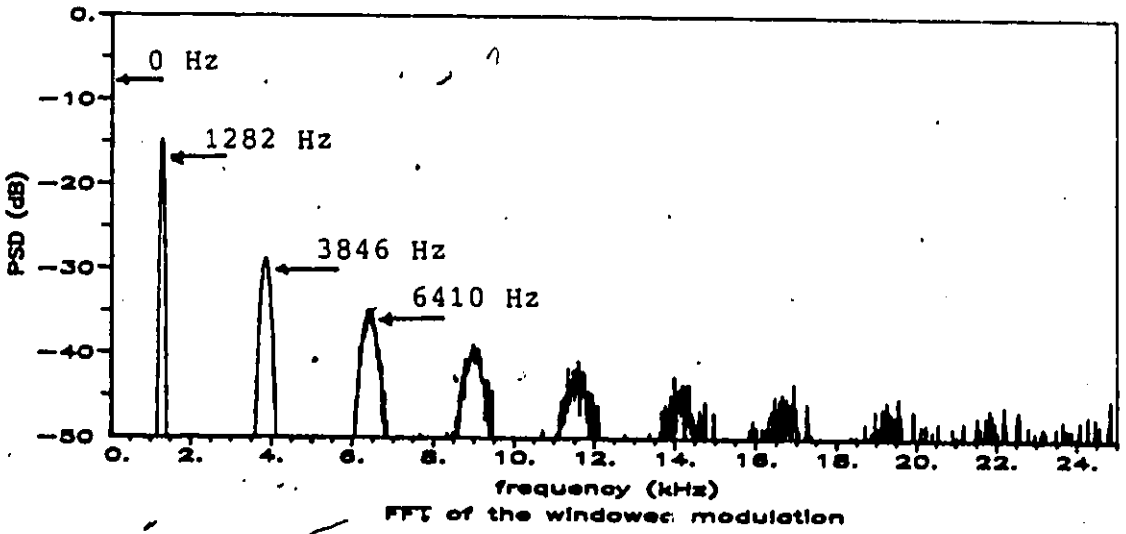

Fig. 4.5 The spectrum of the modulating wave for simulated Ideal Coherent ELT signal.

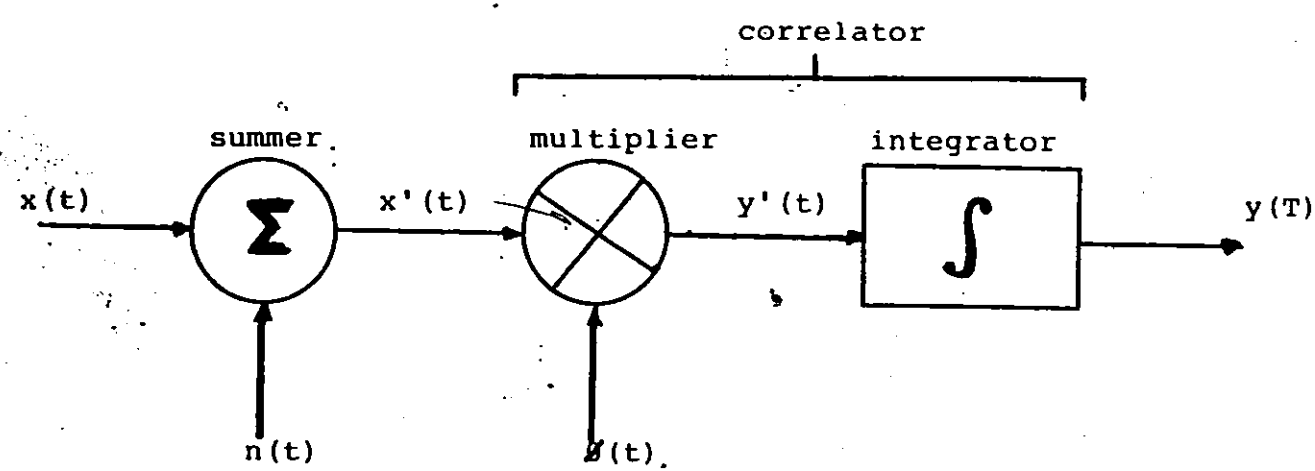

Fig. 4.6 Matched filter structure.

a duration of 82 ms (4096 points) with carrier frequency 16 KHz and carrier-to-noise density ratio 30 dBHz. The spectral plot in Fig. 4.7(a) is the periodogram, of the signal, which clearly illustrates that the large background of noise variance obscures the carrier peak detection.

Assume the simulated signal enters a matched filter receiver. The reference waveform $\phi(t)$ is designed to be a replica, of the input signal, which is perfectly aligned in time. The spectrum at the output of the filter is provided in Fig. 4.7(b). (The spectrum is evaluated according to the frequency domain approach described by eq. (4.17)). We observed that the background noise level is reduced and signal detection is easier. The magnitude of improvement is about 3dB which is in good agreement with the definition of eq. (3.5). Figure 4.8 are the comparison at 25 dBHz. Again the matched filter produces a better spectrum estimation than the non-filter result. (In section 3.3, it has been shown that using the averaged periodogram the minimum detectable CNDR for simulated Ideal Coherent ELT signal is 20 dBHz which is based on the averaging of 50 records of 1K periodogram with total signal length 1 second).

In practice, each matched filter is tuned to a different frequency producing a contiguous set across the band of interest. Normally, this would require very complex implementation scheme and a large amount of computer time. In this case, we have to search for an alternative processor whose performance is acceptable when AWGN is present.

4.2 THE FAST FOURIER TRANSFORM METHOD

In order to provide an efficient means in locating ELT sources, it is necessary to collect enough information from the received SARSAT signals. Therefore, the accuracy of estimating ELT position is strongly dependent on the method employed for signal processing. Digital signal processing techniques based on the estimation of power spectral densities are required for this application. The presently used SARSAT signal processor uses the averaged

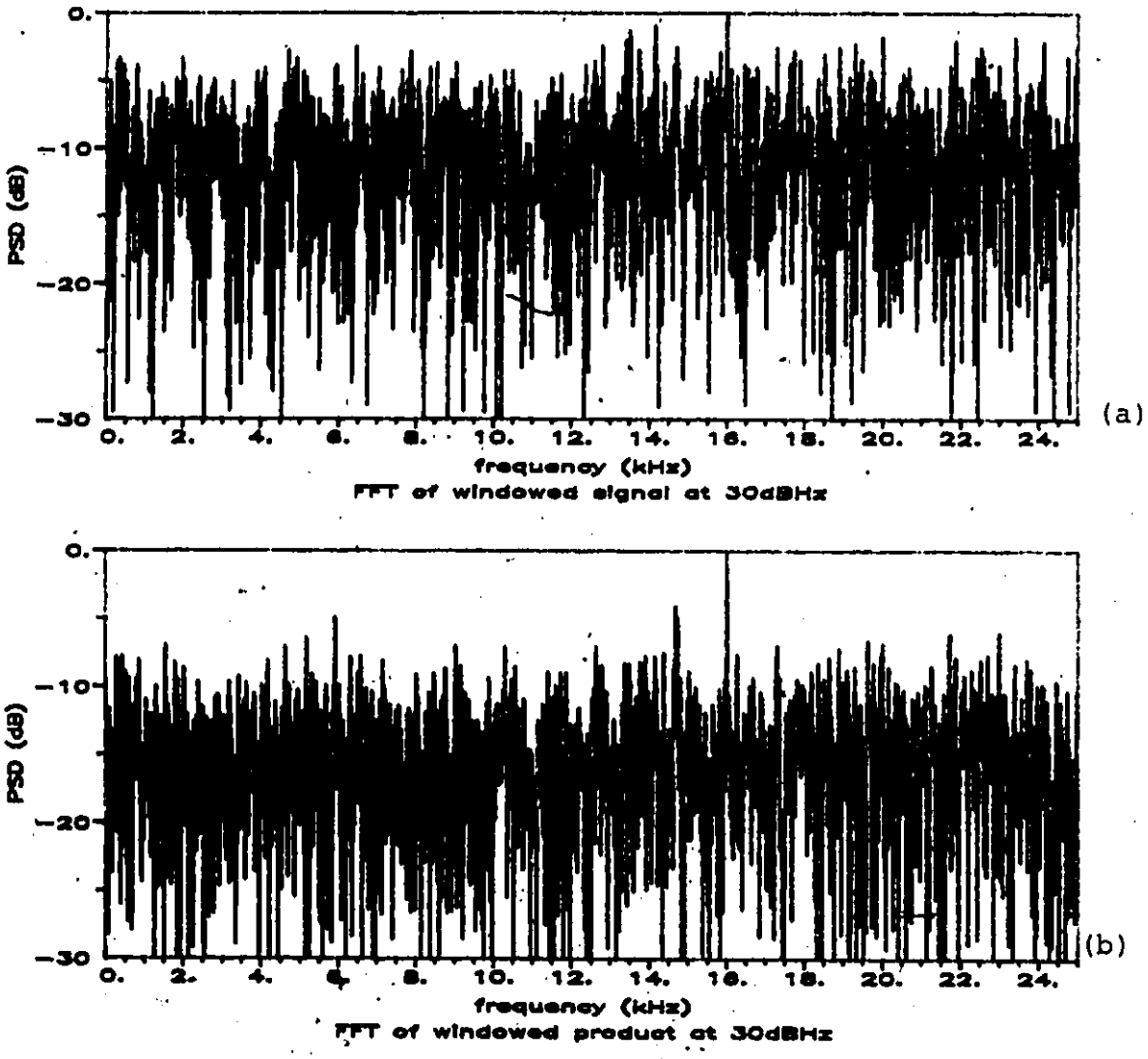

Fig. 4.7 (a) The spectrum of an Ideal Coherent ELT signal simulated at carrier frequency 16KHz and added noise 30dBHz.

(b) The spectrum of the simulated Ideal Coherent ELT signal at f_c=16KHz and CNDR=30dBHz using frequency approach.

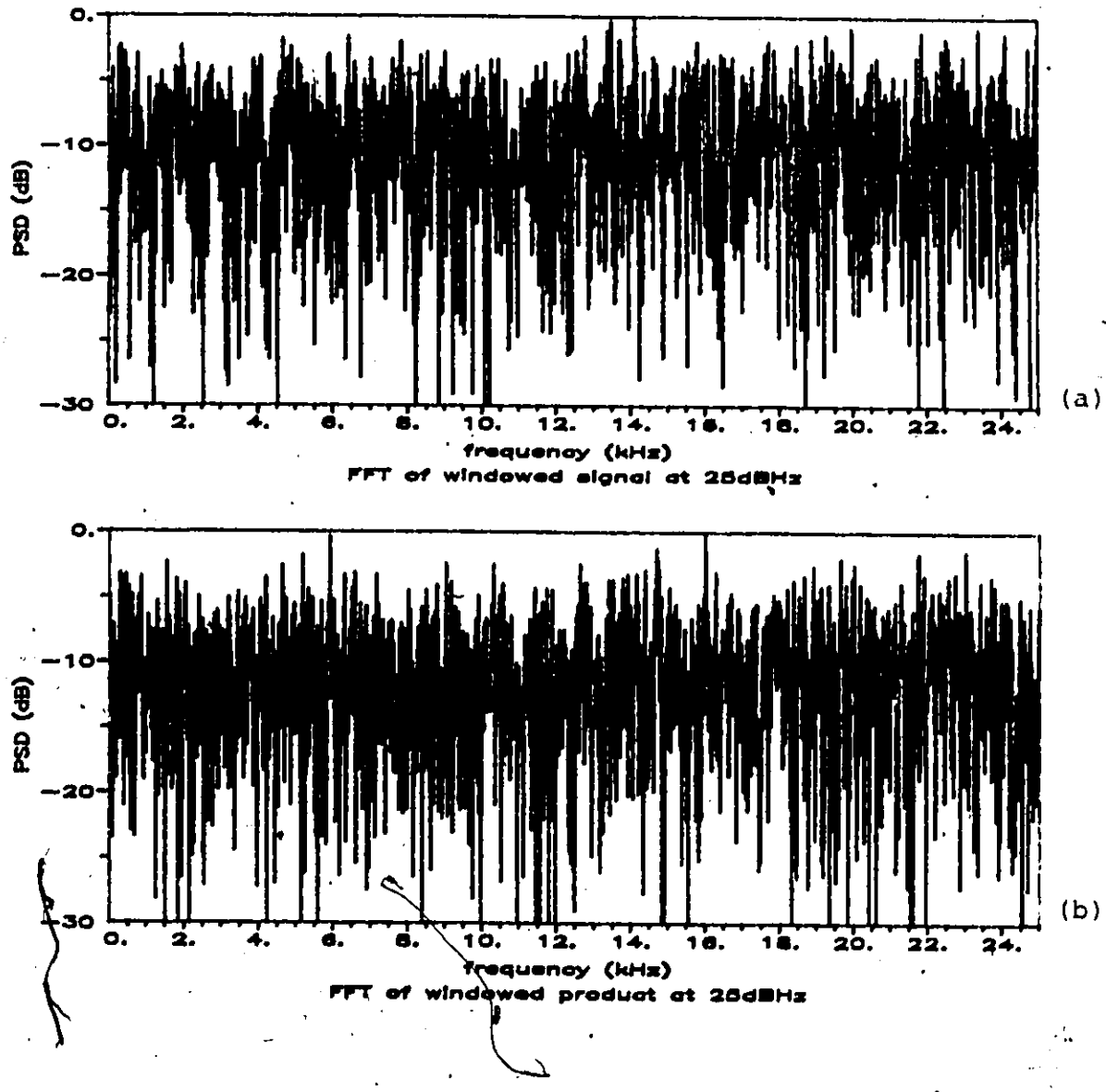

Fig. 4.8 (a) The spectrum of a simulated Ideal Coherent ELT signal at $f_c = 16$KHz and CNDR = 25dBHz.

(b) The spectrum at the output of the matched filter for the simulated Ideal Coherent ELT signal at $f_c = 16$KHz and CNDR = 25dBHz. The exact matched filter response is the signal modulating wave. Frequency approach is used.

periodogram method. This technique is widely applied in the field of power spectrum estimation. Our discussion follows the material given in [14] and [15].

4.2.1 The Periodogram As An Estimate Of The Power Spectrum

As an estimate of the power density spectrum we consider the discrete Fourier transform (DFT) of the real finite length sequence $\{x(n)\}$ for $0 \le n \le N-1$,

$$X(k) = \sum_{n=0}^{N-1} x(n)\, e^{-j\frac{2\pi}{N}nk} \qquad k = 0, 1, 2, \ldots, N-1 \tag{4.31}$$

A highly efficient procedure for computing eq. (4.31) is the fast Fourier transform (FFT) algorithm. The spectrum estimate of $\{x(n)\}$ is the magnitude squared of the DFT normalized by the length of the data record,

$$I_N(f_k) = \frac{1}{N} \left| X(k) \right|^2 \tag{4.32}$$

This function is often called the periodogram. The power spectral estimation measured by the periodogram method is very straightforward and easy to be implemented. However, it gives non-consistent estimates of the power spectral density no matter how long the data record becomes and, in fact, actually, the variance does not approach zero as the record length increases. Averaging of the periodogram is often used as a technique for overcoming this problem. This method also enhances the detection of signals that are embedded in noise.

4.2.2 The Averaging Periodogram

When the signal is noisy, a processing advantage can be realized by using spectrum averaging in which the signal is divided into contiguous segments and then taking the arithmetic average of the periodogram of the individual segments at each frequency. Since both signal and noise are continuously present, spectral peaks at the signal carrier frequency

should be highly correlated from segment to segment whereas noise peaks would be totally uncorrelated and full benefit is derived by averaging the spectra.

For the sequence $\{x(n)\}$ consisting of N samples, we form K subsequences each of length M such that

$$x_r(n) = x[n+(r-1)M] \qquad r = 1,2,3,\ldots,K \tag{4.33}$$

Next, we apply a window to each subsequence and compute the windowed FFT to give

$$X_r(k) = \sum_{n=0}^{M-1} x_r(n)\, w(n)\, e^{-j\frac{2\pi}{M}nk} \qquad k = 0, 1, 2, \ldots, M-1 \tag{4.34}$$

where w(n) is the window function.

Now, the periodogram can be computed from

$$I_r(f_k) = \frac{1}{U} \left| X_r(k) \right|^2 \tag{4.35}$$

where $f_k = k/M$ is the DFT frequency, and

$$U = \sum_{n=0}^{M-1} w^2(n)$$

which is the energy of the window function.

Finally, we simply average the periodogram of the K subsequences to give the power density spectrum. Thus,

$$S_{FFT_{AVE}}(f_k) = \frac{1}{K} \sum_{r=1}^{K} I_r(f_k) \tag{4.36}$$

The operation of averaging periodogram based on eq. (4.36) is often referred to as Welch method [14].

If the signal has constant carrier frequency, the averaged FFT should give the best output signal-to-noise performance when the background is additive white Gaussian noise (AWGN) since all carrier peaks will add linearly while the noise adds in a root mean-square

sense. We now apply these two signal processing methods to the real ELT signals described in Section 2.5.

4.2.3 The Processing of Real ELT Signals with the FFT

Data collection for a number of real ELT signals are provided by the Communications Research Centre (CRC), Ottawa. These data were recorded from an ELT testbed. A 25 KHz bandwidth channel centered on the nominal ELT carrier frequency of 121.5 MHz is mixed down to a frequency range of 0 to 25 KHz for signal processing. The analog signals were digitized using an 8-bit analogue to digital converter at a sampling frequency of 100 KHz [16].

A set of 25 Hanning windowed 4K-periodogram of the Pointer ELT01 ELT signal are computed and plotted for 1 s of data in Fig. 4.9(a). It was found that the Hanning, Hamming, Blackman and Kaiser windows all give approximately the same performance [17]. Each periodogram represents 40 ms of data and is plotted with 20 dB dynamic range proceeding from bottom to top. We note that the sweep is approximately 250 ms and the frequency of the carrier peak is almost constant.

Figure 4.9(b) illustrates a single periodogram over a 40 dB dynamic range. We see that the first lower and upper sidebands at A and B, respectively, are unequal indicating a Non-Ideal Coherent signal. The averaged spectrum, illustrated in Fig. 4.9(c) clearly shows the spectrum peak at approximately 16.2 KHz which is in agreement with the frequency observed from the time-plotted waveform of Fig. 2.9. In addition, we see that the peaks from the averaged upper and lower sidebands produce two bands of interference which can obstruct the detection of other ELT signals.

Figure 4.10(a) illustrates the spectra produced by the 25 Hanning windowed 4K-periodograms of Narco ELT17 ELT signal which is also Non-Ideal Coherent. We observe that

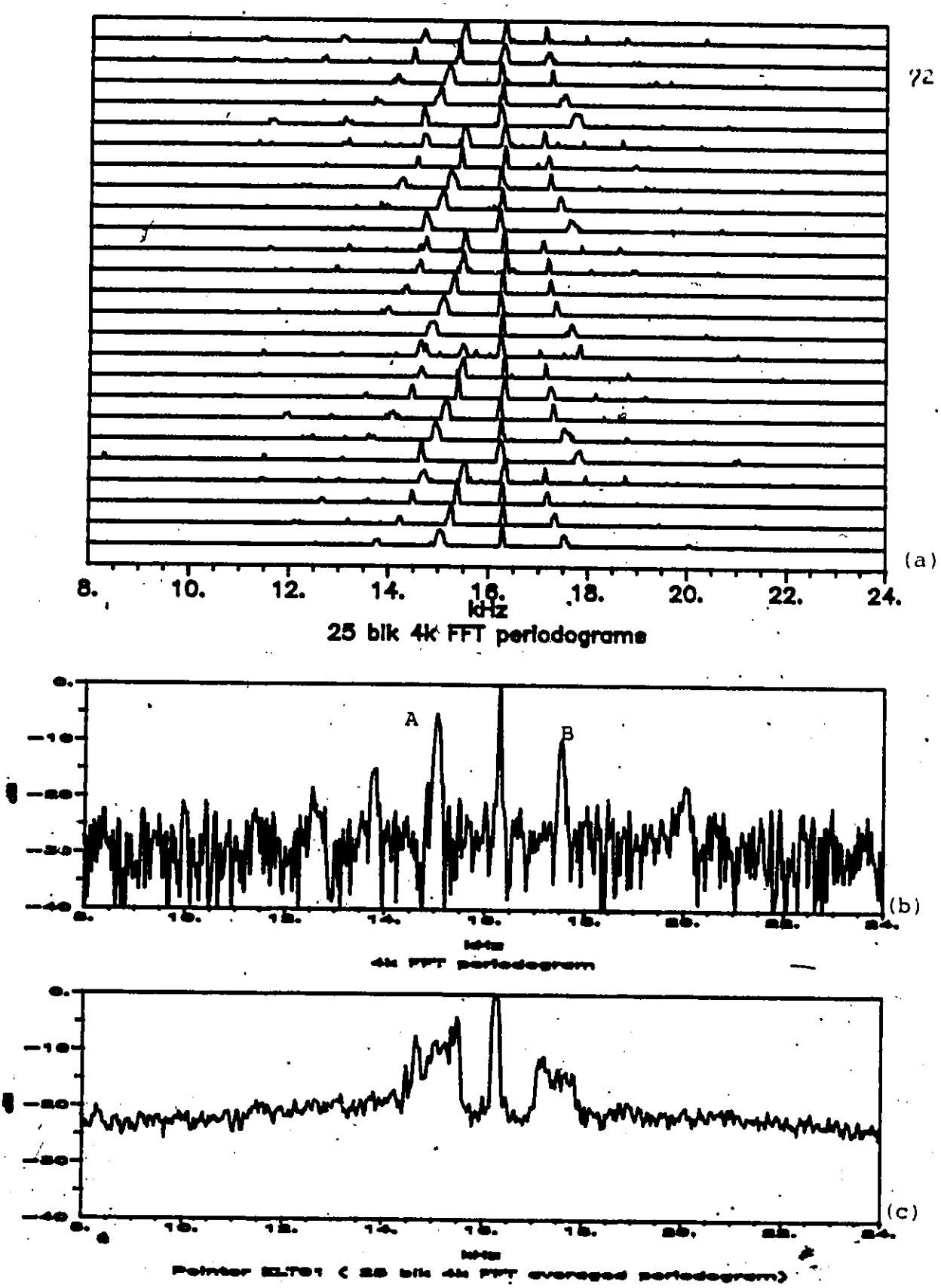

Fig. 4.9 (a) A set of 25 periodograms (from bottom to top) of the Pointer ELT signal. Note the near-constant carrier frequency peak at 16.2KHz and the sidebands which slide in towards the carrier indicating a sweep of approximately 250ms.

(b) Detailed view of the bottom periodogram.

(c) Averaged periodogram showing the carrier peak and the averaged sidebands.

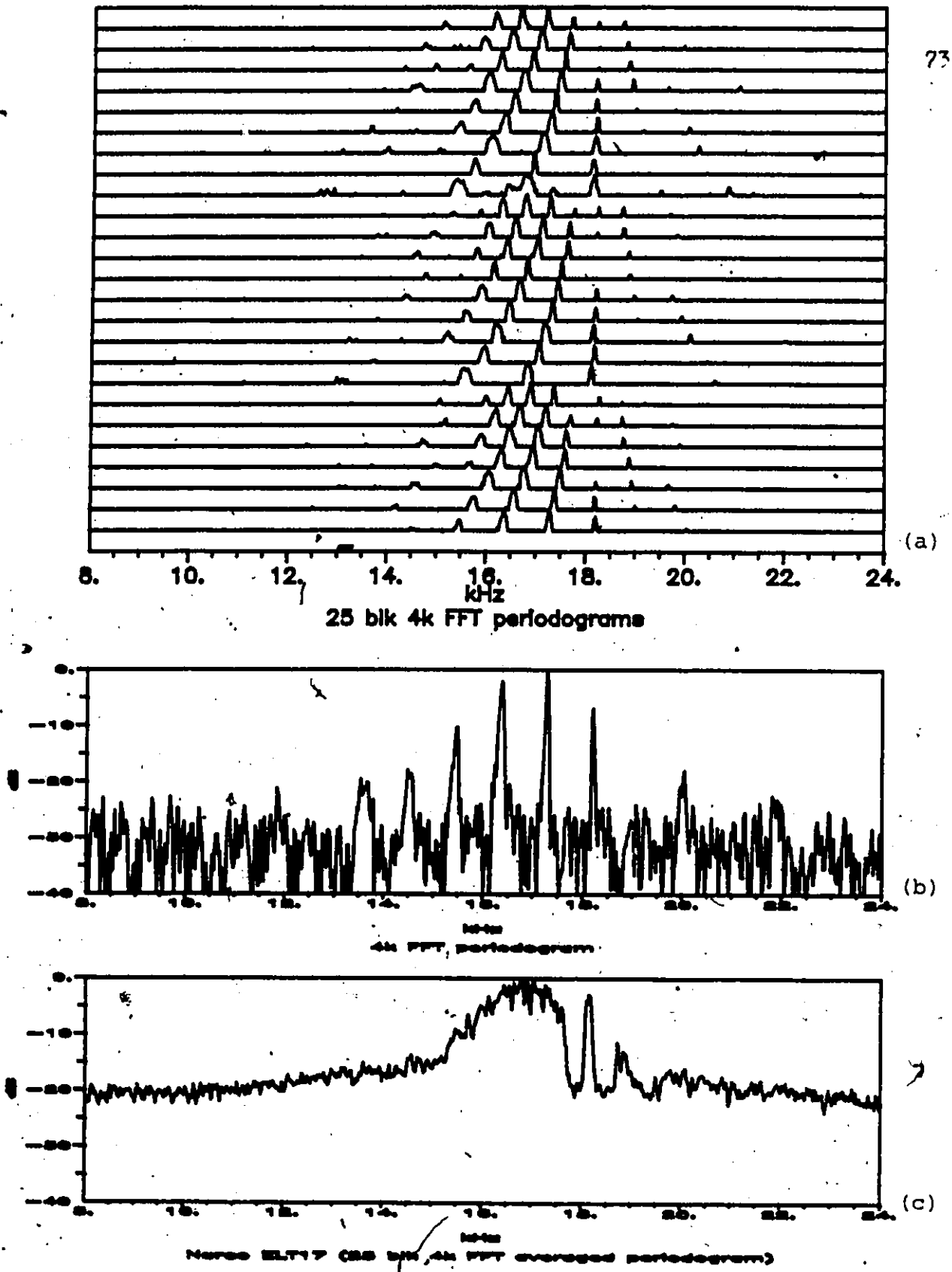

Fig. 4.10 (a) A set of 25 periodograms (from bottom to top) of the Narco ELT17 ELT signal. Note the near-constant carrier frequency peak at 18.2KHz. Due to the interaction between the modulation and the pulling of the carrier frequency, the lower sidebands are more prominent than the upper sidebands.

(b) Detailed view of the bottom periodogram.

(c) Averaged periodogram showing the carrier peak and the averaged sidebands.

the mixed carrier component occurs at approximately 18.2 KHz as was observed from the time plot (see Fig. 2.14). Figure 4.10(b) illustrates the asymmetry in the amplitude of the sidebands around the carrier and the averaged spectrum, shown in Fig. 4.10(c), is dominated by the lower sideband. This effect is due to the pulse-to-pulse phase shift of the modulated signal [5]. We see that a large portion of the spectrum is contained in the sideband energy.

Figure 4.11(a) demonstrates the spectra produced by 25 Hanning windowed 4K-periodogram of Narco ELT19 ELT signal illustrating the dire consequences of random phase shift between consecutive pulses of the signal. Even though the pulse of Fig. 2.17 are strong and well defined (the mixed carrier frequency of the signal is approximately 15 KHz), the periodograms exhibit a high degree of randomness with no clear indication of carrier frequency or modulation sweep. Figure 4.11(b) illustrates the details for one plot and Fig. 4.11(c) shows the averaged plot where we see that the 3 dB bandwidth is broadened to 1/T, where T is the average width of a pulse (approximately 0.5 ms).

Figure 4.12(a) depicts the periodograms when five ELT signals are added. (In addition to the three signals aforementioned, there is ELT07, a Pointer model Sentry C-4000 ELT and ELT12, a Garrett model Rescue 88C ELT both of which are Non-Ideal Coherent with good spectral properties). The mixed carrier frequencies of the composite signal selected were Pointer ELT01 at 22.7 KHz, Pointer ELT07 at 19.5 KHz, Garrett ELT12 at 13.3 KHz, Narco ELT17 at 9.3 KHz and Narco ELT19 at 16.5 KHz. The spectrum becomes quite 'busy' with the combination of ELT spectrum peaks and sidelobes, as this can be seen clearly in Fig. 4.12(b). Of considerable concern is the problem of thresholding this combined signal. Using the averaged periodogram result in Fig. 4.12(c), a simple threshold will detect not only the spectrum peaks, but also the large sideband portions of the spectrum thus creating large amounts of irrelevant information.

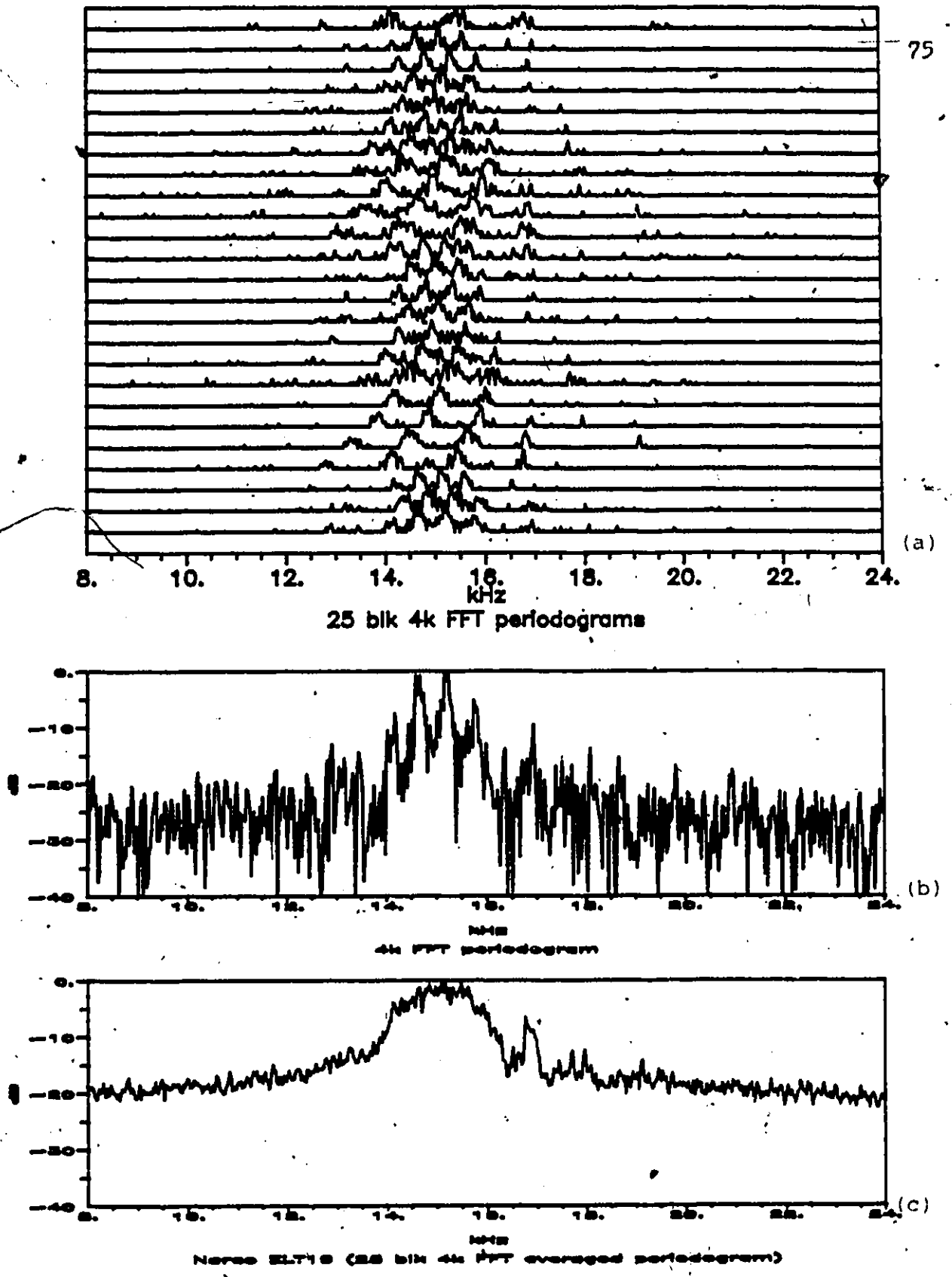

Fig. 4.11 (a) A set of 25 periodograms (from bottom to top) of the Narco ELT19 ELT signal. Note that the carrier frequency is not well defined.

(b) Detailed view of the bottom periodogram.

(c) Averaged periodogram showing the carrier peak and averaged sidebands.

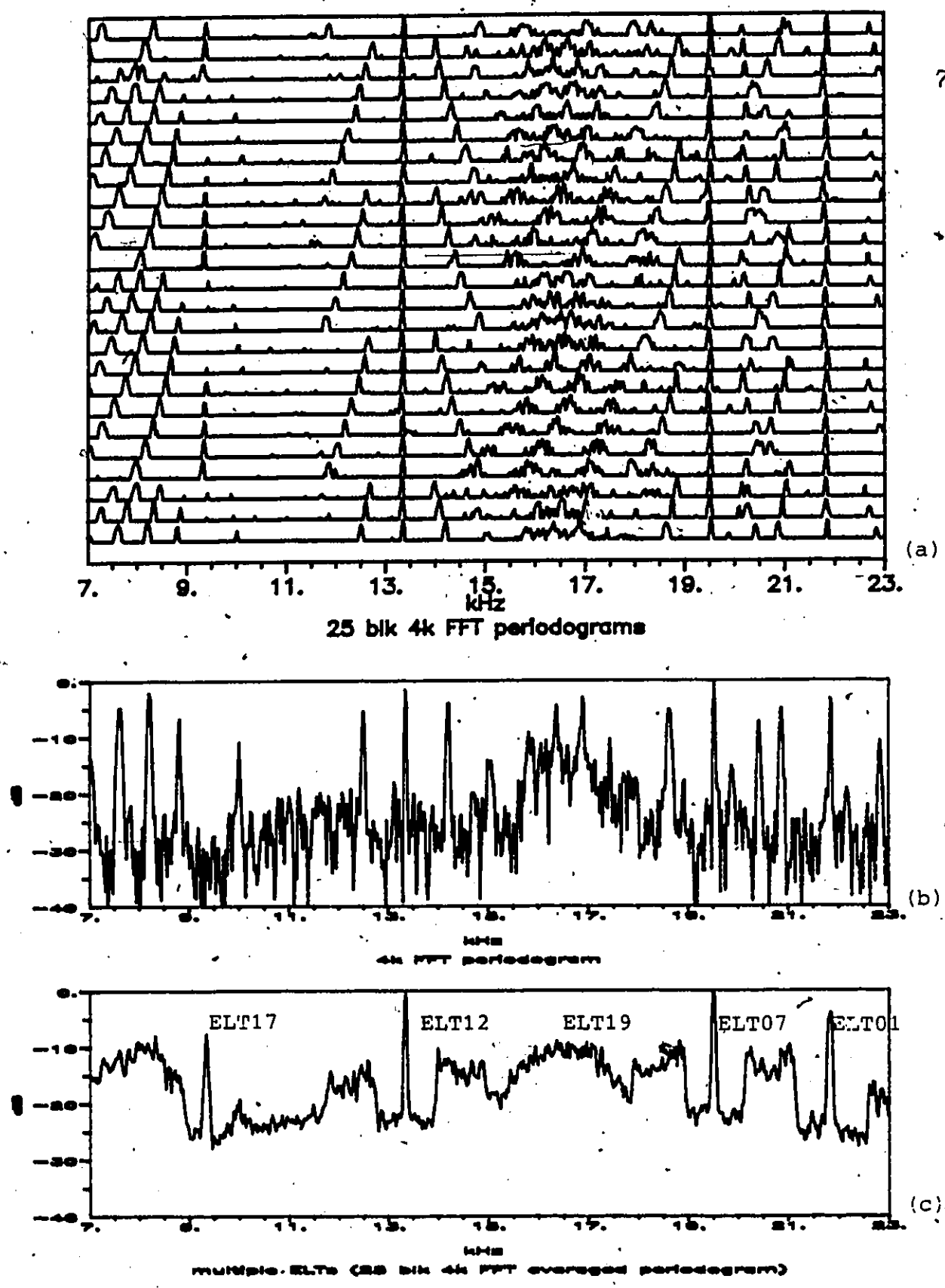

Fig. 4.12 (a) A set of 25 periodograms (from bottom to top) of the combined ELT signals. Note the near-constant carrier frequency peaks at 9.3KHz, 13.3KHz, 19.5KHz and 22.7KHz indicating the presence of Non-Ideal Coherent ELT signals.

(b) Detailed view of the bottom periodogram.

(c) Average of the 25 periodograms.

The above results demonstrated that use of the periodogram gave good performance to the estimate of carrier frequency of a limited class of ELT signals such as the Pointer and Garrett type model ELT. For measuring the carrier frequency of the Narco type ELT signals, the method described encounters difficulties. In view of this circumstances, we explore various signal processing methods.

4.3 THE MAXIMUM ENTROPY METHOD

Averaging periodogram is a standard practice to reducing the variance of spectral estimate. This is performed by taking the mean of a number of successive periodograms. However, there are several shortcomings in this method. Averaging of periodograms generates broad sideband spectra that obscure and distort other spectral components that are present. In fact, the sidebands of strong signals tend to mask out any weaker signals that may overlap within the frequency band. In general, the use of FFT is accompanied by a pre-processing stage called windowing which is used to alleviate the problem of sidelobes in the Fourier spectrum. However, the window function increases the bias in the spectral estimate. It is because the spectral estimate is affected by the spectrum of the window which is independent of the data set.

We have also seen that both phase incoherence and frequency instability of the ELT signals further hamper the spectral estimation by the FFT. Several studies have indicated that the carrier frequency of this 'ill-conditioned' ELT signal can be estimated by means of a parametric spectrum estimation method, which is the maximum entropy method (MEM) [17]-[19].

4.3.1 The Maximum Entropy Method As An Estimate Of The Power Spectrum

The maximum entropy method of spectrum estimation is generally regarded as having several advantages over the fast Fourier transform method in its frequency resolving capability [20]. In order to clarify the MEM processor, we note that the method is data-dependent and window-free. The principle of the MEM is to select the spectrum which corresponds to the most random or the most unpredictable time series whose autocorrelation function agrees with a set of known values. This condition is equivalent to the extrapolation of the autocorrelation function of the available data by maximizing the entropy of the process [21].

For a weakly stationary zero mean time series $\{x(n)\}$ $(0 \le n \le N-1)$, the spectral estimate defined by the MEM at frequency f_k is

$$S_{MEM}(f_k) = \frac{P(M)}{\left| 1 + \sum_{m=1}^{M} a(m) \exp(-j2\pi m f_k \Delta t) \right|^2} \tag{4.37}$$

where $P(M) =$ prediction error power obtained with a prediction error filter of order M.

$a(m) =$ prediction error filter coefficients $(m = 1,2,\ldots,M)$

$\Delta t =$ sampling time

The values of P(M) and a(m) are determined by the equation

$$\sum_{k=0}^{M} a(k) R_x(m-k) = \begin{cases} P(M) & m=0 \\ 0 & m=1,2,3,\ldots,M \end{cases} \tag{4.38}$$

where $R_x(.)$ is the autocorrelation of the time series $\{x(n)\}$ with lag m-k. This equation represents a prediction error filter equation of order M. An efficient algorithm for solving eq. (4.38) recursively is outlined by Burg [22]. Other papers have been written describing algorithms for calculating the filter coefficients [23].

The spectral estimate calculated by the FFT can be performed in near real time operation, whereas it is difficult for the MEM to achieve the same speed. This is mainly due to

the recursive structure of the algorithm. While it is true that a large part of the time required to calculate the MEM spectral estimate is spent on determining the filter coefficients, a relatively small reduction in the overall time can be realized by using the FFT to evaluate the spectrum [24]. It is noted that the denominator of eq. (4.37) can be written as a discrete Fourier transform by substituting $f_k = n\Delta f$ where n is any integer and Δf is the frequency step. Then

$$S_{MEM}(n\Delta f) = \frac{P(M)}{\left| 1 + \sum_{m=1}^{M} a(m) \exp(-j2\pi mn\Delta f\Delta t) \right|^2} \tag{4.39}$$

From the sampling theorem, we have $N\Delta f\Delta t = 1$ (where N is the data length). The denominator in eq. (4.39) is simply the magnitude squared of the DFT given by eq. (4.31). The spectral estimate of MEM can then be obtained by calculating the FFT of the M value of the prediction error filter coefficients, padded with zeros to produce a set of length N.

As compared to the Fourier transform procedures which have already been implemented in real time environment, the computation complexity of the maximum entropy method may be a limitation in this application. However, a concurrent very large scale integration (VLSI) architecture to compute the maximum entropy method based on the covariance-lattice method is provided by [25]. The availability of low cost, high performance VLSI circuits may allow the computation of complex algorithms to be done in real time signal processing applications.

4.3.2 The Averaging Maximum Entropy Method

In analogy with the averaging periodogram procedure for reducing the variance of the estimators, we expect that the frequency resolution for the MEM could be benefited by the same scheme. First, the N data record of the sequence {x(n)} is segmented into K non-overlapping subsequence. The power spectral density estimate associated with each of these

K segment is evaluated according to eq. (4.37). These estimates are then averaged directly,

$$S_{MEM_{AVE}}(f_k) = \frac{1}{K} \sum_{r=1}^{K} S_{r_{MEM}}(f_k) \tag{4.40}$$

Unlike the periodogram, the MEM can have several averaging procedures. It is primarily due to its parametric nature. We note that the spectrum evaluated by eq. (4.37) uses the coefficients of the prediction error filter. At each of the M stage of the prediction error filter, there is a reflection coefficient associated with it [23]. Thus, these two sets of parameters can also be included for spectral averaging purpose [26]. In our case, we only consider the power spectral density averaging defined by eq. (4.40).

4.3.3 The Processing Of Real ELT Signals Using The MEM

For the same 4K data sets of real ELT signals previously used for periodograms, we compute the MEM spectral estimates. One problem to be solved in evaluating a reasonable MEM spectrum is to determine an optimum number of prediction error filter coefficients. This number corresponds to the filter order of the MEM. For a pure sinusoidal waveform, three different objective criteria are suggested for selecting the filter order. These are the final prediction error criterion (FPE), the information theoretic criterion (AIC) and the auto-regressive transfer function criterion (CAT) [21]. Since the ELT signal is not a pure sinusoidal, the described criteria cannot be applied.

In practice, a higher order of MEM estimate improves the sharpness of carrier peaks of ideal constant frequency sinusoidal waveforms. Unfortunately, there is a price to be paid for using the MEM processor when high order estimates are required. This price takes the form of a greatly increased number of computations. (For the HP 1000 computer system with an array processor, this increase is of the order of 30 to 50 times for the 4K point computation with MEM order 500 as compared to the 4K FFT. However, we note that this

computing system is well designed for the FFT and ill configured for the MEM. Thus, it is possible that advanced equipment suited for the MEM may resolve this dilemma.)

A set of 25 4K MEM estimates of the Pointer ELT01 ELT signal are computed and plotted for 1 s of data in Fig. 4.13(a). The filter order used is 100. The plots follow the same format as presented for the periodograms. We note that, in general, the MEM processor produces a smoother spectral estimate than the periodogram. A single MEM estimate of the Pointer ELT signal is given in Fig. 4.13(b). We find that the MEM has less sideband interference than the periodogram and yet the performance is also comparable. The averaged MEM spectrum of the 1 s data is shown in Fig. 4.13(c). The result shows that a better dynamic range for signal detection can be achieved over the averaged periodogram.

The MEM estimate of Narco ELT17 ELT signal is provided in Fig. 4.14(a). The single and averaged MEM estimates are presented in Fig. 4.14(b) and Fig. 4.14(c) respectively. The output of the MEM processor exhibits a high degree of fluctuation from one duration of the signal to another. This situation is particularly conspicuous near the end of a sweep (point A) where the sideband peaks are crowded together toward the carrier frequency peak. In this case the MEM filter at 100 fails to isolate these components. The remedy is to employ a higher prediction error filter order.

The results for processing Narco ELT19 ELT signal using the MEM processor is illustrated in Fig. 4.15. Although this ELT unit generates a non-coherent characteristic signal, the MEM can still provide a relatively smooth spectral estimation. Similar to the plots obtained from Fig. 4.14, we observe that for a better frequency resolution, a higher filter order is required.

For the composite signal of five ELT signals, the MEM estimate results are given in Fig. 4.16. The plots show that we experience the same situation as described above.

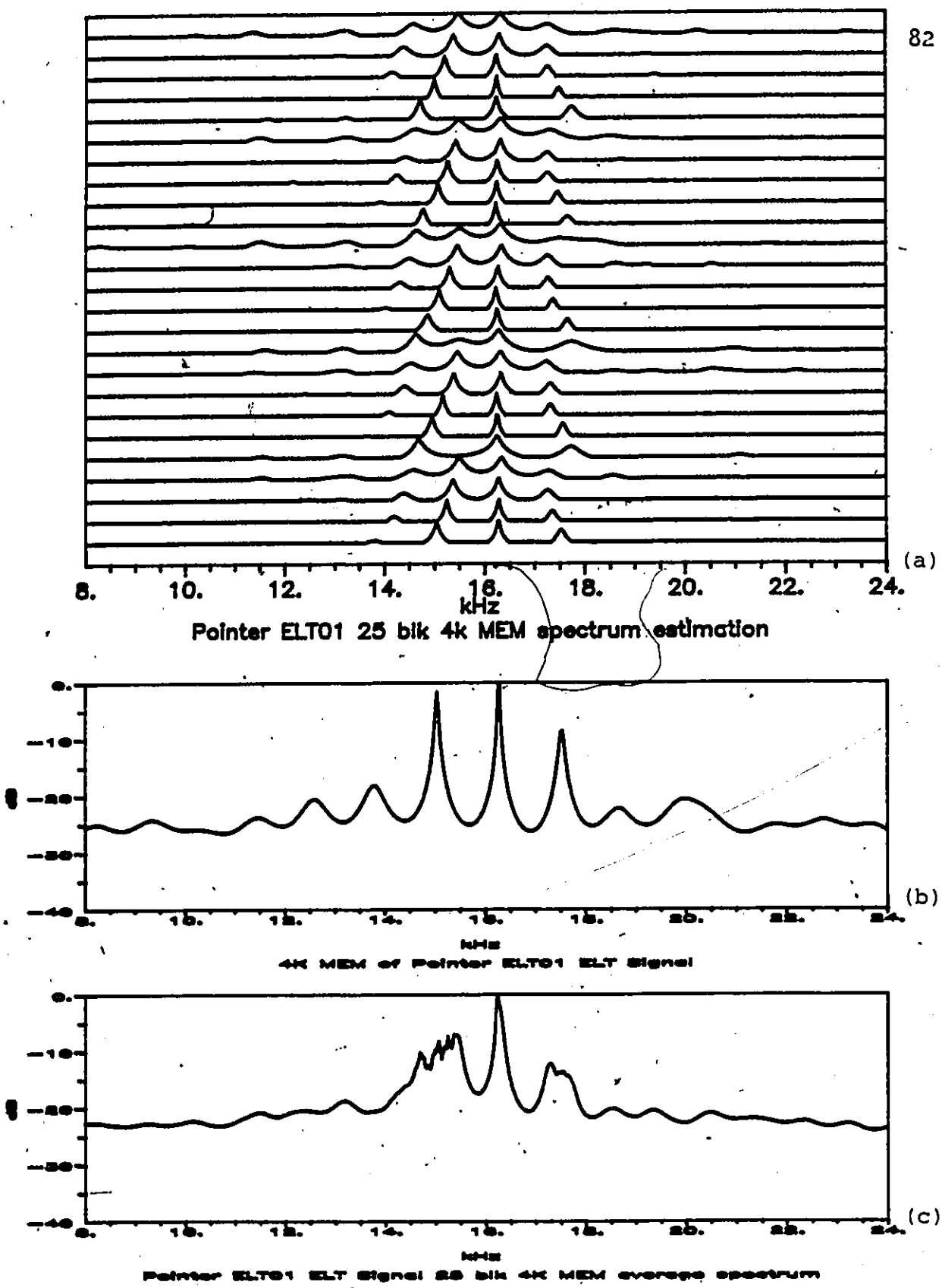

Fig. 4.13 (a) A set of 25 MEM estimates at order 100 of the Pointer ELT01 ELT signal.

(b) Detailed view of the bottom spectrum.

(c) Averaged spectrum of the MEM estimate. Note the spectrum is smoother than the averaged periodogram.

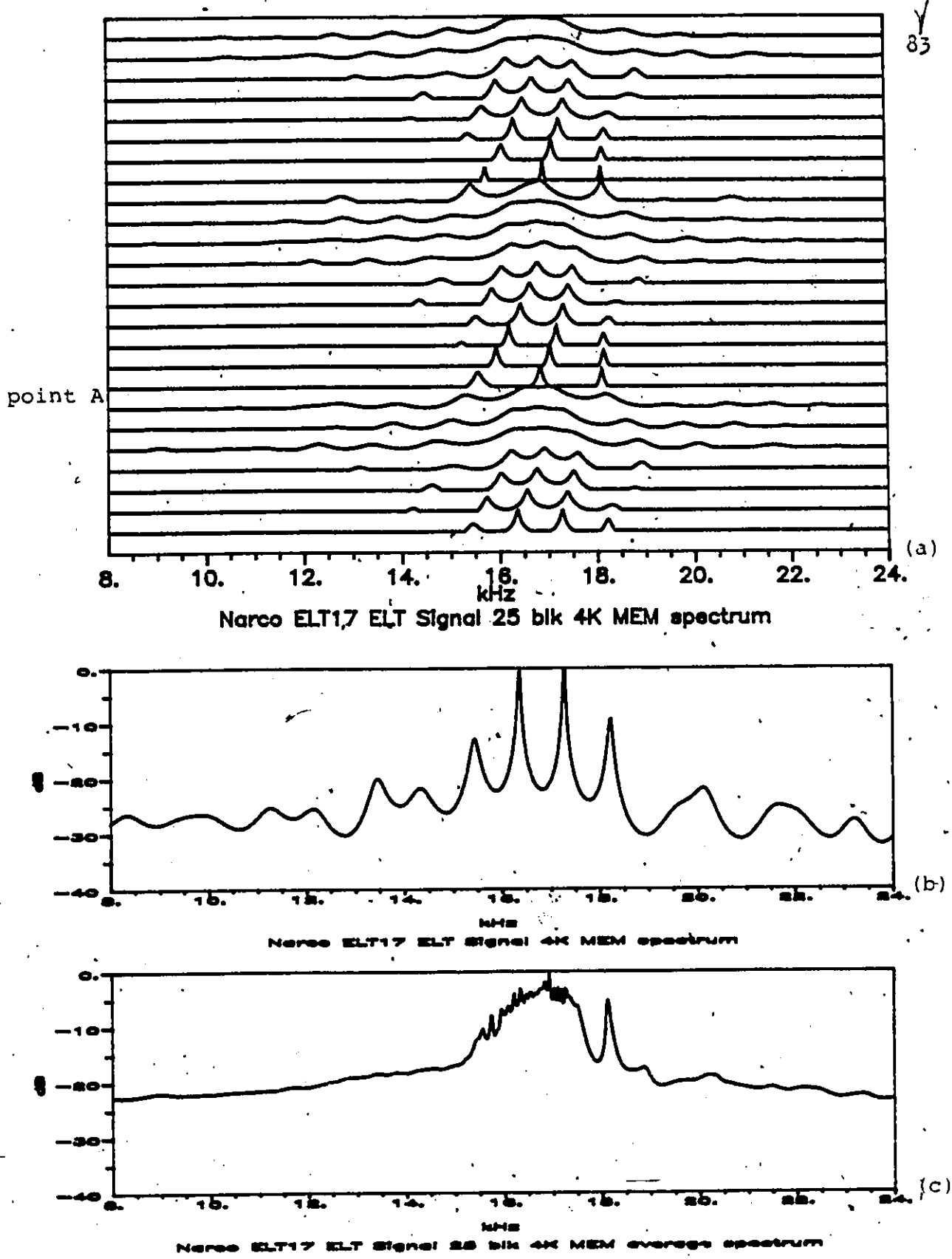

Fig. 4.14 (a) A set of 25 MEM estimates at order 100 of the Narco ELT17 ELT signal.

(b) Detailed view of the bottom estimate.

(c) Averaged spectrum of the MEM estimate.

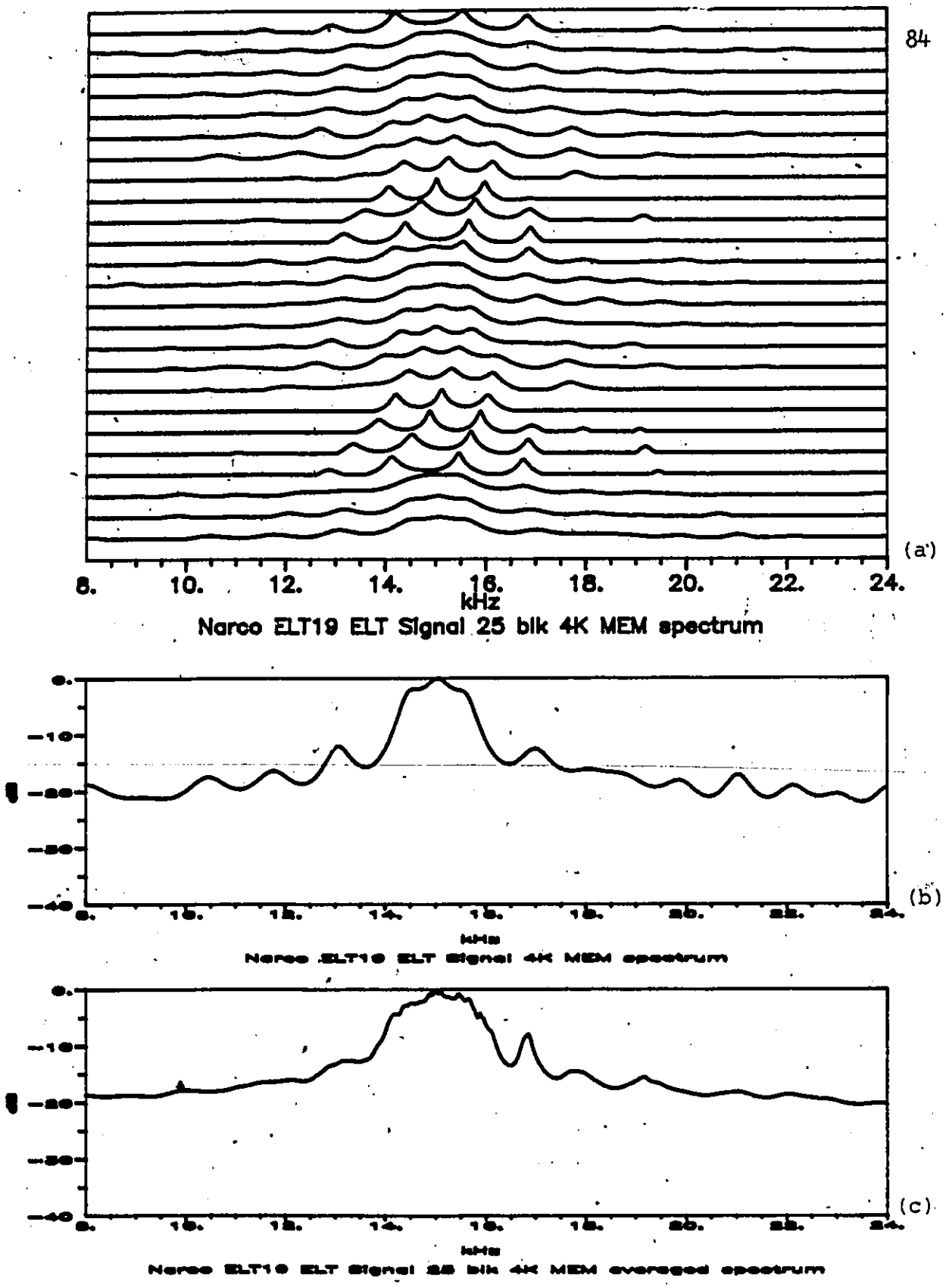

Fig. 4.15 (a) A set of 25 MEM estimates at order 100 of the Narco ELT19 ELT signal.

(b) Detailed view of the bottom estimate.

(c) Averaged spectrum of the MEM estimate.

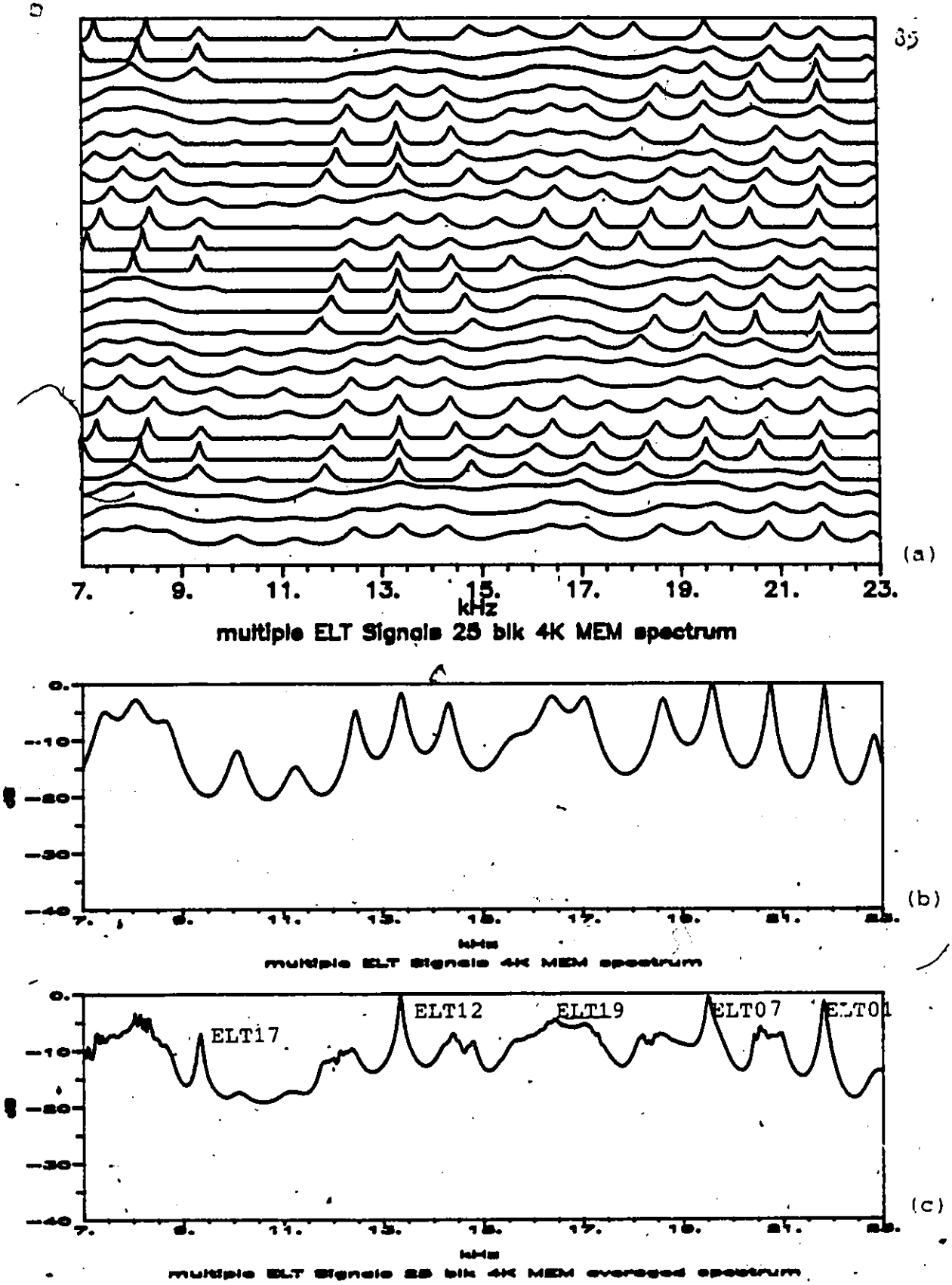

Fig. 4.16 (a) A set of 25 MEM estimates at order 100 of the combined ELT signals.

(b) Detailed view of the bottom estimate.

(c) Averaged spectrum of the MEM estimate.

The prediction error filter influences the detection performance. A low order of prediction error filter produces a smoothed spectrum and obviates the resolution advantage of the MEM. Increasing the filter order of MEM has the effect of reducing interference from neighbouring frequency components. On the other hand, it also introduces spurious peaks. It is suggested in [19] that in estimating the power spectrum of a given time series, by means of the MEM, the frequency resolution is improved significantly if the autocorrelation function (ACF) is used as a preprocessor. This procedure follows the Wiener-Khintchine relations with Fourier transform replaced by MEM estimate. The results are found to be somewhat more reliable in practice than simply calculating the MEM estimate from the data sequence.

For a finite duration sequence $\{x(n)\}$, $0 \le n \le N-1$, the autocorrelation function is estimated by,

$$R(m) = \frac{1}{N} \sum_{n=0}^{N-1-m} x(n)\, x(m+n) \qquad \text{for} \quad 0 \le m \le N-1 \tag{4.41}$$

and this is called a biased estimate. By taking the autocorrelation function of the data sequence, a good deal of information about periodicities of the signal can be obtained and yet for spectrum estimation the spectral peaks reinforced and the noise effects reduced [27]. This approach provides a priori knowledge about the signal whose power spectrum has to be estimated. This operation is referred as ACFMEM technique.

Also, it has been shown in [17] that bandpass filtering (BPF) of the data provides certain advantages in the processing of emergency signals with poor spectral properties when the ACFMEM processor is applied. Another advantage of using bandpass filter is that a low order of MEM can be used in opposing of high value of filter order when multiple signals are processed. This directly reduces the computation time. This procedure is referred as BPFACFMEM or modified MEM processor. Since both autocorrelation function and bandpass filtering are linear processes, mathematically, they do not affect the result of

periodogram. The modified MEM technique performs best in processing signals with multiple carrier components.

We note that for the Narco ELT19 ELT signal, the carrier frequency cannot be extracted by using the periodogram since the signal is non-coherent. The MEM estimator is somewhat more flexible. The processor can be tested with different value of prediction error filter orders until a reasonable power spectrum can be obtained. However, the value of the filter order can be very large magnitude. Thus, a direct MEM approach is not wise.

In order to combat the above situation, we explore the modified MEM processor by testing the procedure with composite signal. First the Narco ELT19 ELT signal is isolated by bandpass filtering. The filter is finite impulse response with bandwidth 3 KHz centered at approximately the centre frequency of the peak of the periodogram of the Non-Coherent signal. Then compute the autocorrelation function of the resulting sequence followed by calculation of the MEM estimate at order 3. The operation is applied to the 25 records of 4K data. The result is illustrated in Fig. 4.17(a). A sample of the estimate is given in Fig. 4.17(b) and the average of the 25 spectra is presented in Fig. 4.17(c). We see that the peak of the averaged spectrum indicates a mixed carrier frequency of approximately 16.55 KHz. Unfortunately, the peak of the averaged spectrum is somewhat ragged due to the variance in the peak locations of the individual estimates. This leads to the investigation of a new post-processing technique.

4.4 SUMMARY

Several spectrum estimates are introduced as the possible candidates to tackle the problems of processing of ELT signals.

From the expression given by the spectrum of an Ideal Coherent ELT signal model the filter response of a matched filter to the signal is designed. A direct implementation of

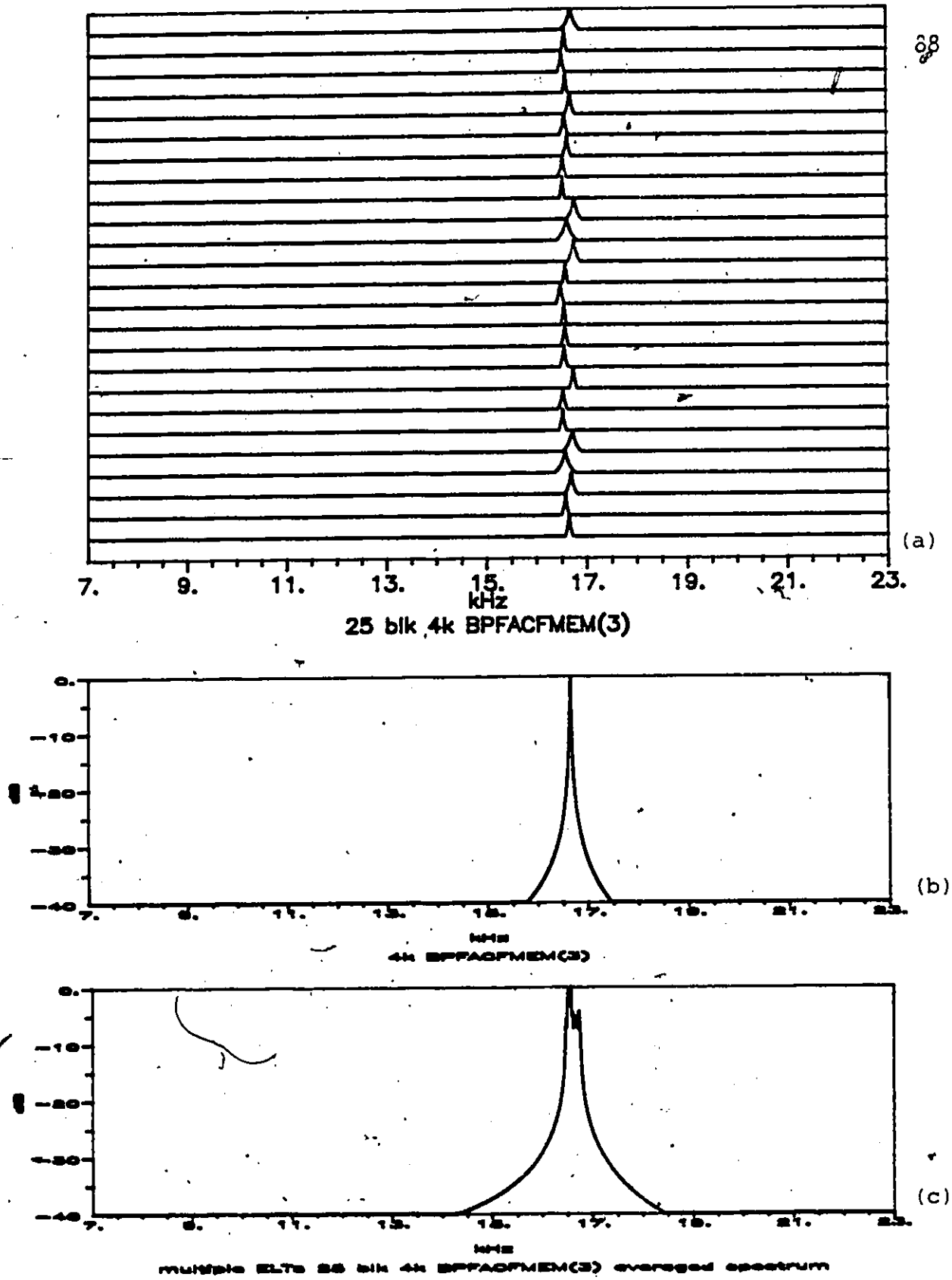

Fig. 4.17 (a) A set of 25 modified MEM estimates at order 3 for the combined ELT signal.

(b) Detailed view of the bottom estimate.

(c) Averaged spectrum of the modified MEM estimate.

matched filter for ELT signal is shown to be very difficult. However, the degree of complexity can be reduced by implementing the spectrum according to the equation given by the convolution of the Fourier transform of the input signal and the baseband signal. This method can be carried out by the operation of the fast Fourier transform algorithm. We have also shown that matched filter technique improves the spectral performance of by 3 dB in the presence of added white Gaussian noise.

The averaged periodogram is found to give good signal detection properties with Non-Ideal Coherent ELT signals but tends to generate strong interference due to sidebands.

In processing Non-Ideal Coherent ELT signals, the modified maximum entropy method is proved to be a promising estimation techniques.

CHAPTER 5

THE ORDER STATISTIC AND SPECTRUM LEVELLER TECHNIQUES

Examining the ELT signals spectra of the 25 records 4K point data from Fig. 4.9 to Fig. 4.17, we note that the carrier peaks for each of the coherent ELT signals are approximately stationary since they have the same amplitude and the same carrier frequency for all spectra estimates. However, the background interference due to sidebands is distributed in frequency. Improvements in signal detection and interference suppression can be achieved by introducing a more sophisticated post-processor. Thus, for discriminating signals from interference, it might be useful to apply order statistic [28] to the power estimates. We observe that, in the present situation, ranking the spectra at each frequency will cause most of the interference to 'float' to the upper spectral estimates while leaving the lower estimates with less interference and an improved signal-to-interference ratio [29]. Based on the order statistic, we develop a post-processor, called ranked spectrum. The processor relies on ranking the spectral components of the K spectra for a one second period of data to produce a set of ranked spectra. Three different procedures for exploiting the ranked spectrum are examined. First, is the minimum selection spectrum in which the lowest ranked spectrum is chosen. Second, is the median selection spectrum in which the middle spectrum is selected. Third, the averaged ranked spectrum which relies on averaging contiguous sets of the ranked spectra. It is shown that this last processor incorporates many desirable features not found in the averaging processor.

A spectrum leveller is a simple method to provide an estimate of the thresholding level. This technique is employed by computing a running average across a certain number of

points of the averaged spectral plot in order to locate an estimate of the level. Then the averaged spectral plot is adjusted using this leveller.

5.1 A POST-PROCESSOR BASED ON AN ORDER STATISTIC

The averaged periodogram reduces the variance of the power spectrum estimates; however, it has several shortcomings. There is a tradeoff between frequency bias and the variance of the estimate [14]. For a fixed record length, increasing the number of periodograms decreases the variance at the expense of reducing the estimate resolution. This argument is true, only, when the estimates do not include any strong interfering source in the data sequence otherwise the Fourier transform based power spectrum estimator breaks down and the estimate suffers severe bias and large variance [30].

In view of this, we introduce an ordered statistic based post-processor which provides an estimate with an adequate amount of signal strength while reducing local interference or noise in the signal.

Using the periodogram calculated from eq. (4.35), and according to increasing amplitude, we order the K amplitude of $I_r(f_k)$ at each frequency f_k to form K ordered periodograms. This procedure is formulated as follow,

$$I'_1(f_k) < I'_2(f_k) < \ldots < I'_n(f_k) < \ldots < I'_K(f_k) \tag{5.1}$$

where

$$I'_1(f_k) = \min\{I_r(f_k)\} \qquad \text{for } r = 1,2,3,\ldots,K$$

$$I'_n(f_k) = \text{n-th largest value of } I_r(f_k)$$

$$I'_K(f_k) = \max\{I_r(f_k)\} \qquad \text{for } r = 1,2,3,\ldots,K$$

This procedure is also applied to the spectra obtained from the maximum entropy method. Eq. (5.1) can be implemented on a computer by using sorting algorithms. Because of the ordering process, this post-processor has a nonlinear behaviour. The central idea of the

ordered statistic based post-processor is to select one certain estimate $I'_n(f_k)$ from eq. (5.1) and to employ it as an estimate for the average spectrum as observed in the reference time span. Since the high end of the ranked spectrum absorbes most of the interference and the low end contains mostly noise, the selected estimate $I'_n(f_k)$ maintains the desired carrier frequency estimate with reduced interference and noise. This is particularly useful for processing an ELT signal which has the spectral property similar to that of Narco ELT17 ELT model. The large portion of spectrum contains in the sideband energy can be eliminated as a result of this process.

5.2 THE MINIMUM SELECTION AND MEDIAN SELECTION OF THE ORDER STATISTIC

At the output of the ordered statistic post-processor, there is a new set of estimates whose magnitude are obtained by sorting the magnitude of the periodograms (or MEM estimates) in order from largest to smallest value. The advantage of this method is that for a signal power density exceeding the noise power density, most of the random contributions, such as sidebands interference and background noise, to the spectral estimate are suppressed by selecting a proper ranked estimate. From the set of ordered spectra, each estimate represents a different degree of local roughness in the signal. Of considerable concern are the levels that contain the minimum values, the median values and the maximum values. These selected values are of particular significance in actual practice.

We SEE that most of the randomness with large magnitude values is allocated on the top of the ranked estimates. This spectrum provides a large biased estimate of the signal. Thus, we do not consider the maximum selection.

If the minima of all values are selected, we then have the minimum spectrum given by

$$S_{MIN}(f_k) = I'_1(f_k) \tag{5.2}$$

This is called the minimum selection. Theoretically, the minimum selection gives the greatest reduction in sideband interference and interference due to broadband sources of all ranked spectra. However, there is a problem of signal detectability which must not be overlooked. For signals with poor carrier frequency stability, the magnitudes of the carrier peaks are reduced by the minimum selection. The variance of the spectral estimate of the background noise in the minimum selection is the greatest among the others. Signal detection is, therefore, further hampered.

In order to ameliorate the difficulty with minimum selection, we propose that the ranked spectrum closer to the centre gives good detection properties for carrier frequency. We refer this as the median selection. The median spectrum is defined by

$$S_{MED}(f_k) = I'_M(f_k) \quad M = \frac{K+1}{2} \tag{5.3}$$

The rationale behind the use of the median selection is that it represents the mean value of the spectrum estimate of our observation.

The results of the ordered statistic post-processor as applied to the processing of the real ELT signal spectra are now discussed.

5.3 THE APPLICATION OF ORDER STATISTIC TECHNIQUE TO THE ELT SIGNAL SPECTRA

The spectra obtained from the periodograms and the MEM are ranked accordingly and their performance are compared. The procedure applied to the periodogram is referred as Fourier transform based order statistic (FFTOS) and to the MEM is called maximum entropy method based order statistic (MEMOS).

5.3.1 Fourier Transform Based Order Statistic

Ranking, applied to the Pointer ELT01 spectral plots of Fig. 4.9, produces the set of ranked periodograms illustrated in Fig. 5.1(a). We note that the sideband interference is greatly reduced toward the lower ranked values of the plot. The bottom trace is the minimum selection and is shown in detail in Fig. 5.1(b). The minimum spectrum has almost no sideband interference. However, the carrier peak is substantially reduced from the averaged value and the variance of the noise is greatly increased. The reduction in carrier peak value is caused by jitter in the carrier oscillator of the ELT unit. Further problems can arise for satellite pass data to the Doppler shift caused by satellite motion. The median selection (or the 13th spectral plot of Fig. 5.1(a)) is given in Fig. 5.1(c). The spectrum has a sharp carrier peak and almost no sideband interference. Comparing this result with the averaging periodogram depicted in Fig. 4.9(c), we see that the median selection has better spectral performance.

A similar result is obtained when the method is applied to the Narco ELT17 spectra (Fig. 4.10). The set of ranked spectra in Fig. 5.2(a) shows that the sideband interference is contained largely in the uppermost periodograms while the lower periodograms have poor carrier detection properties. The minimum spectrum is shown in Fig. 5.2(b). The median spectrum in Fig. 5.2(c) however provides greatly reduced sideband interference with good carrier detection properties. The lower sideband interference is shown to be very prominent in the averaging periodogram whereas in the median selection this adversity is eliminated.

Figure 5.3 demonstrates the performance of ranking for the Narco ELT19 spectra. It is clear that neither the minimum selection nor the median selection offer much hope of carrier detection. It will be seen later, this signal benefits greatly from use of the modified maximum entropy method.

For the multiple ELT signal, the plots of Fig. 5.4 illustrates the advantages of order statistic. The median selection clearly indicates the carrier frequencies of four of the five ELT

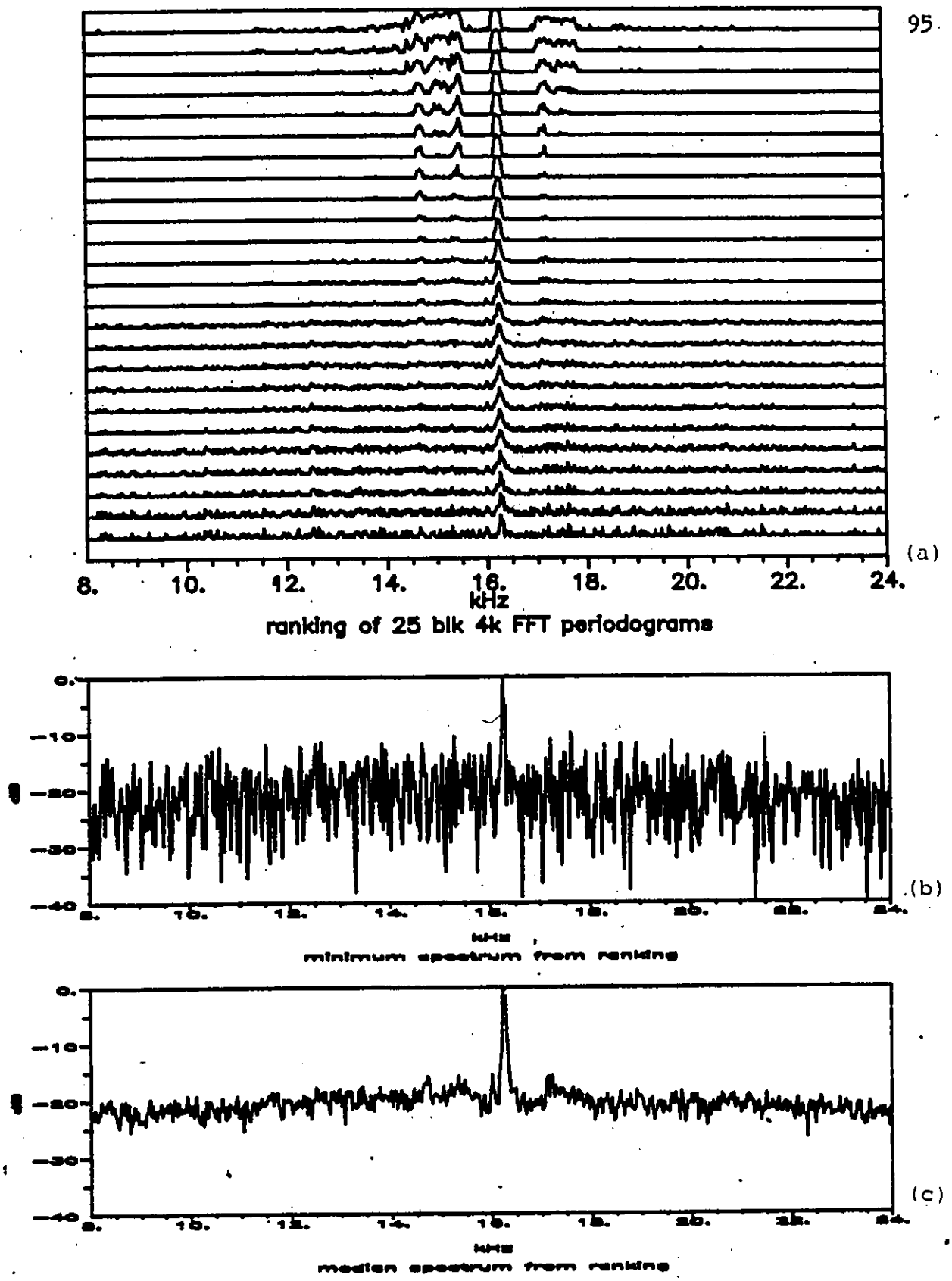

Fig. 5.1 (a) Ranked periodograms for the Pointer ELT01 spectra of Fig. 4.9.

(b) Minimum-selection from the ranked periodograms.

(c) Median-selection from the ranked periodograms.

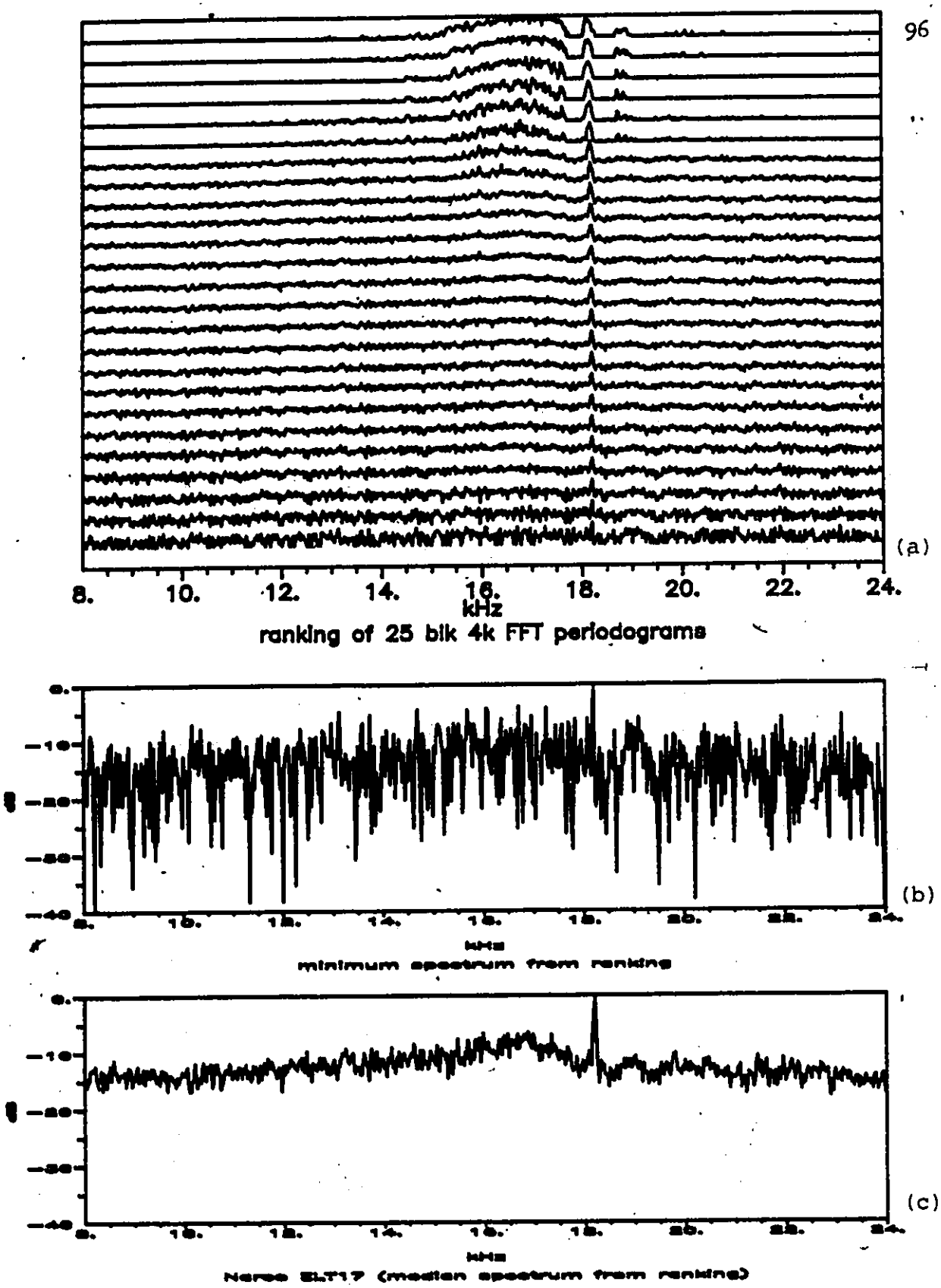

Fig. 5.2 (a) Ranked periodograms for the Narco ELT17 spectra of Fig. 4.10.

(b) Minimum-selection from the ranked periodograms.

(c) Median-selection from the ranked periodograms.

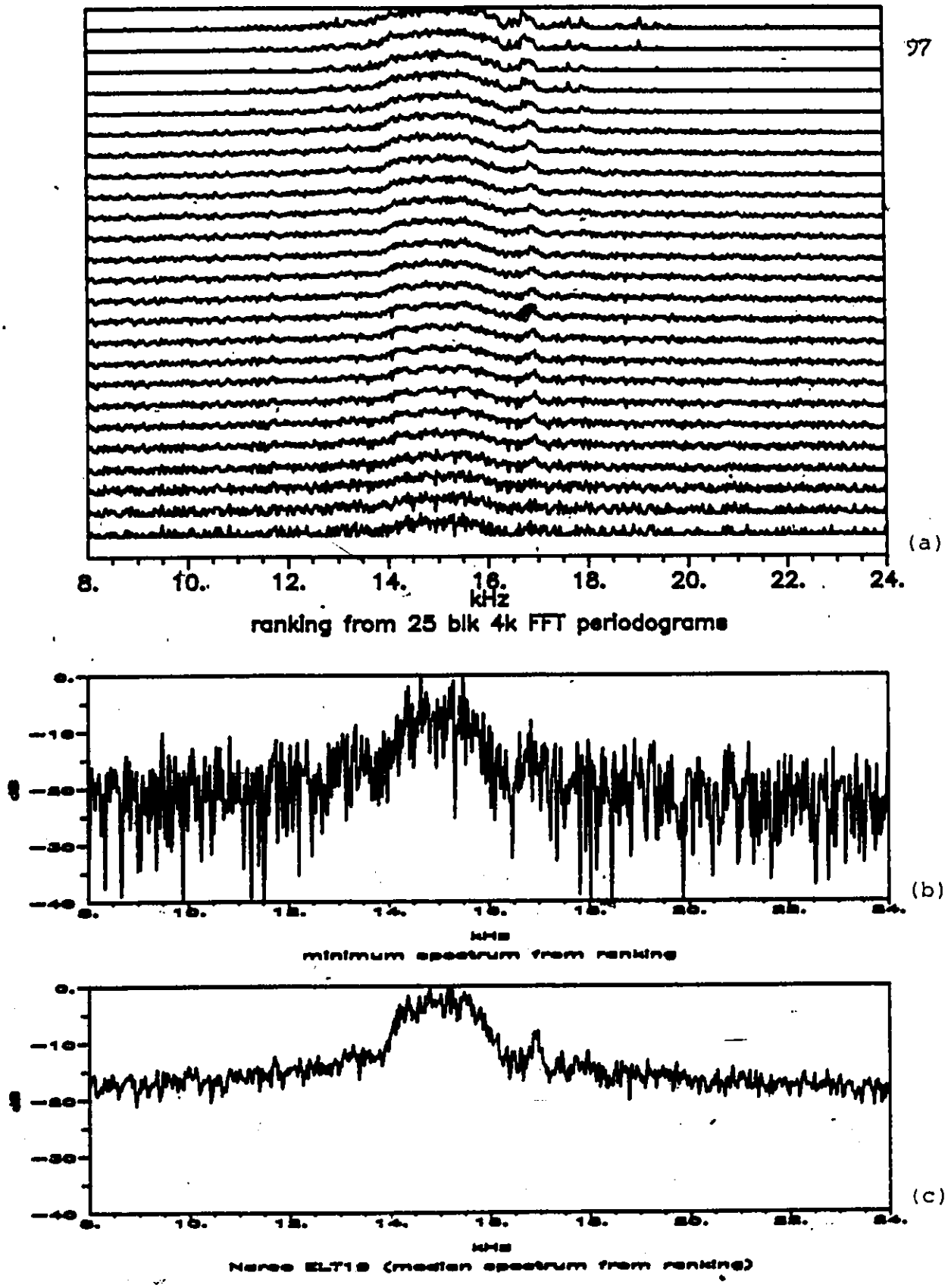

Fig. 5.3 (a) Ranked periodograms for the Narco ELT19 spectra of Fig. 4.11.

(b) Minimum-selection from the ranked periodograms.

(c) Median-selection from the ranked periodograms.

signals. Further, the sideband interference is largely reduced leaving a spectral plot which is easily thresholded.

From the results of the ranked periodograms, it appears that the desired reduction in sideband interference can be achieved along with good ELT signal peak detection by choosing the median selection rather than the minimum selection.

5.3.2 Maximum Entropy Method Based Order Statistic

Following the ranking procedure, we obtain the plots of Fig. 5.5 which demonstrate the spectra of the MEM (order 100) estimates of Pointer ELT01 signal. We note that the performance of MEMOS is not as satisfactory as the FFTOS. It is mainly due to the MEM dependence on the order of the prediction error filter. A low order of MEM yields a smoothed spectrum at the expense of reducing frequency resolution. A high order of MEM, although improving frequency resolution, also generates spurious peaks which increase false alarm rate. Therefore, in order to make MEMOS performs well, an appropriate choice of filter order is important. The upper and lower sidebands in the median selection of Fig. 5.5(c) of the MEMOS of Pointer ELT01 signal is the consequence of the described dilemma. Again, the situation plagues the MEMOS performance, as shown in Fig. 5.6 and Fig. 5.7, of the ranked results of the MEM estimates of the Narco ELT17 and ELT19 signals.

For signals with good spectral characteristics, such as Pointer and Garrett ELT model, we know that the median selection from FFTOS gives best spectrum estimation. However, for signal with poor spectral properties, we have to engage modified maximum entropy method as discussed in Section 4.3.3.

Figure 5.8(a) is the MEMOS of the composite ELT signals. The minimum selection shown in Fig. 5.8(b) and the median selection shown in Fig. 5.8(c) indicate the presence of Pointer ELT01, ELT07 and Garrett ELT12 signals. The detection of Narco type ELT signal is

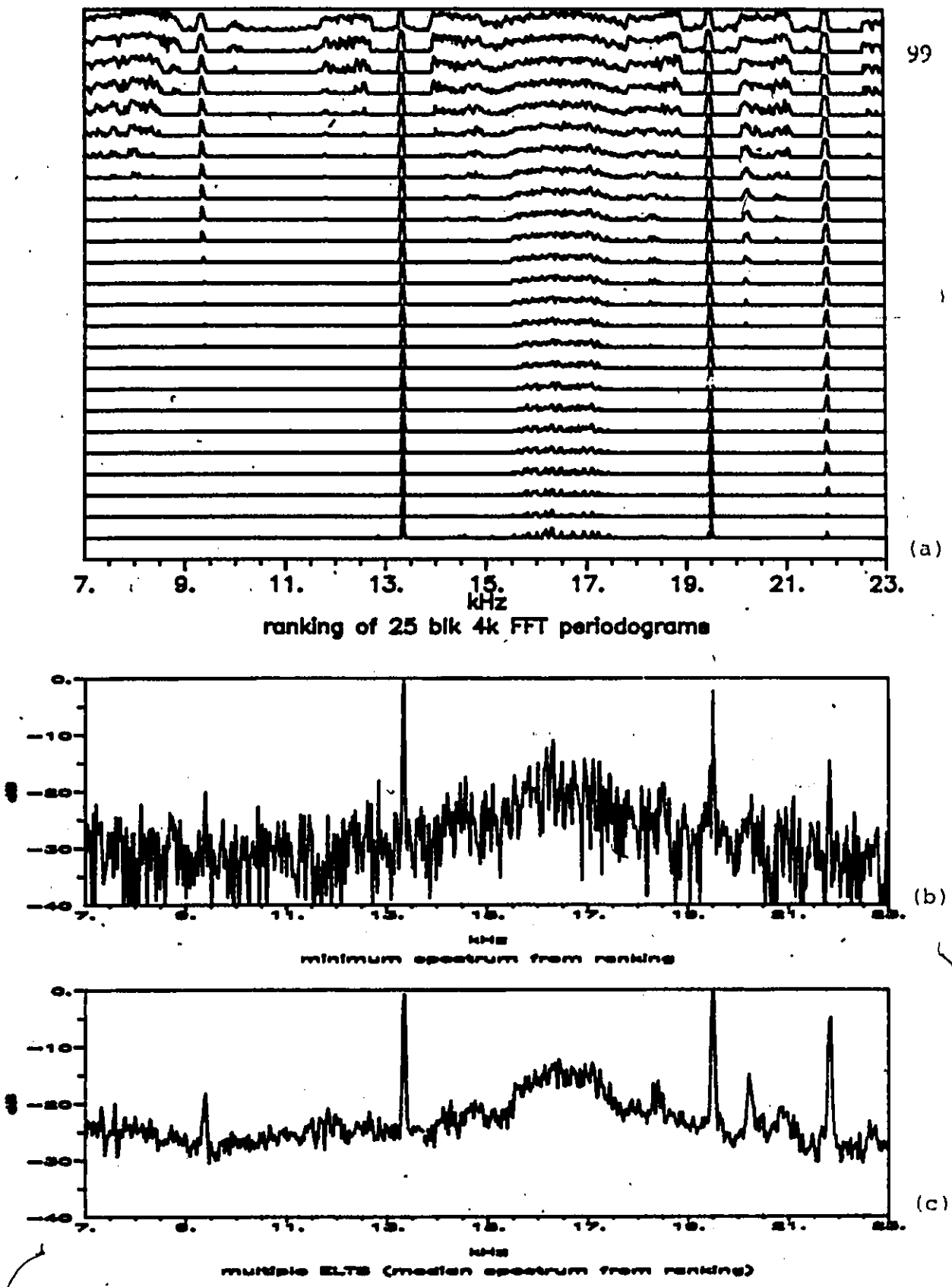

Fig. 5.4 (a) Ranked periodegrams for the combined ELT signals spectra of Fig. 4.12.

(b) Minimum-selection from the ranked periodograms.

(c) Median-selection from the ranked periodograms.

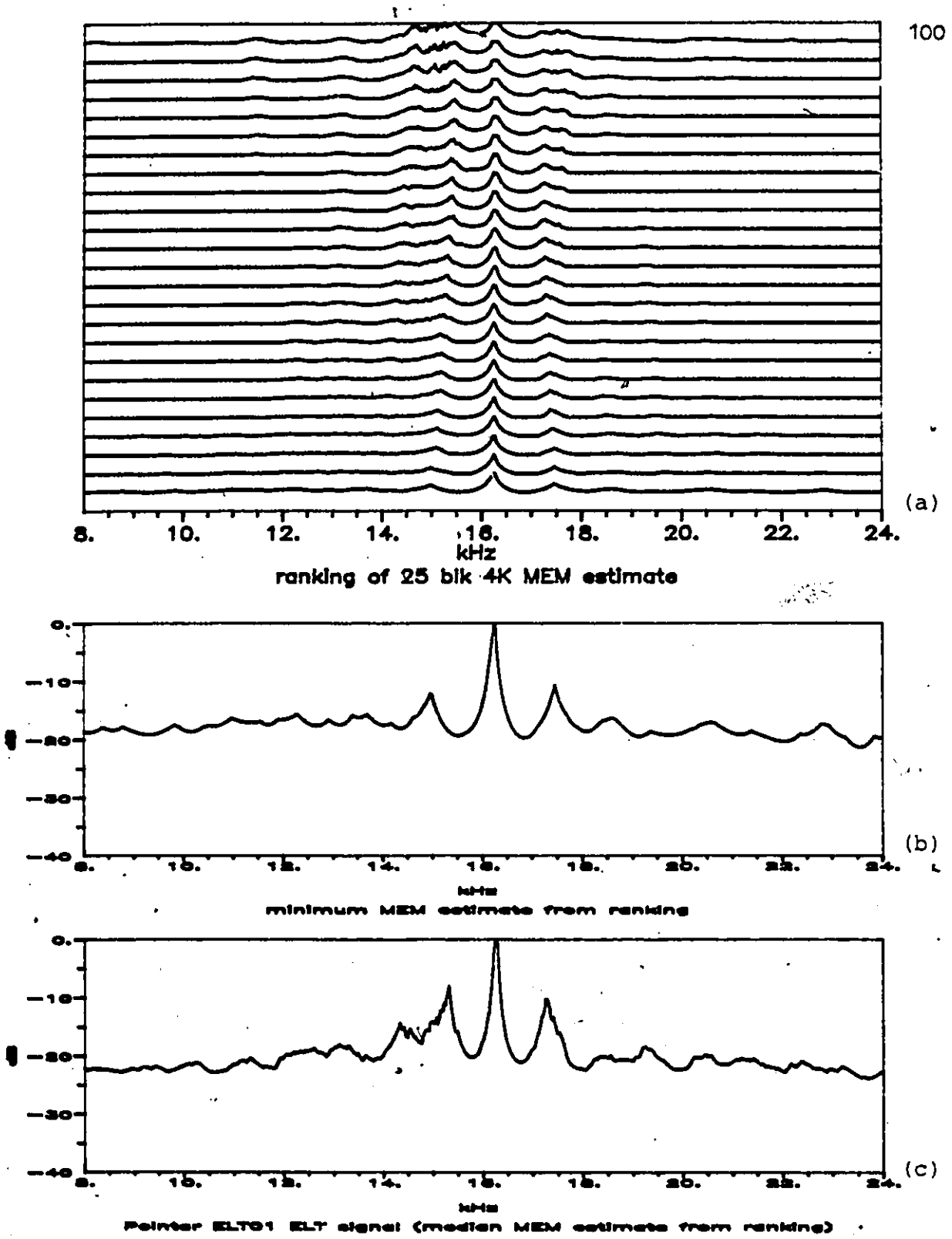

Fig. 5.5 (a) Ranked MEM estimates for the Pointer ELT01 signal spectra of Fig. 4.13.

(b) Minimum-selection from the ranked MEM estimates.

(c) Median-selection from the ranked MEM estimates.

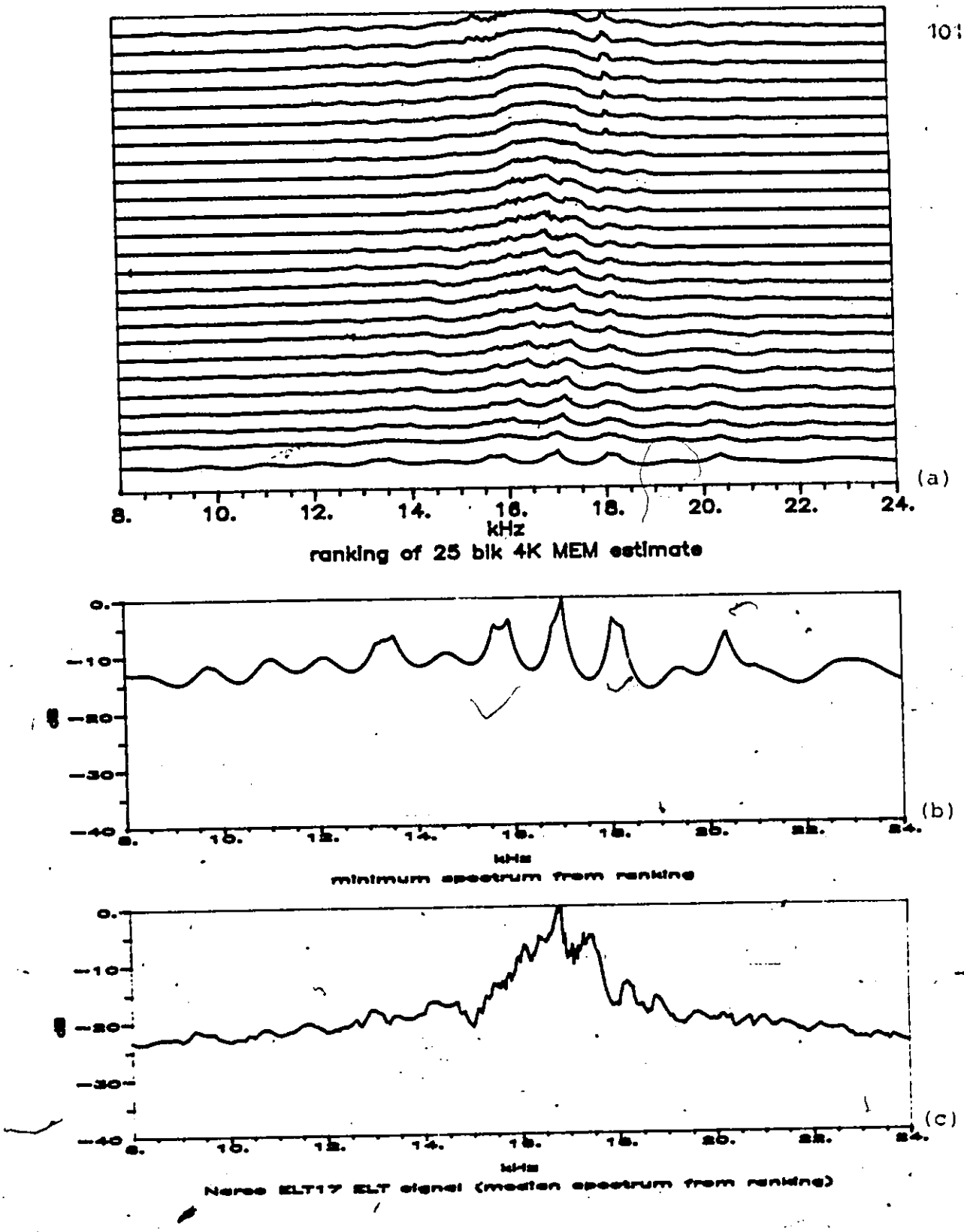

Fig. 5.6 (a) Ranked MEM estimates for the Narco ELT17 signal spectra of Fig. 4.14.

(b) Minimum-selection from the ranked MEM estimates.

(c) Median-selection from the ranked MEM estimates.

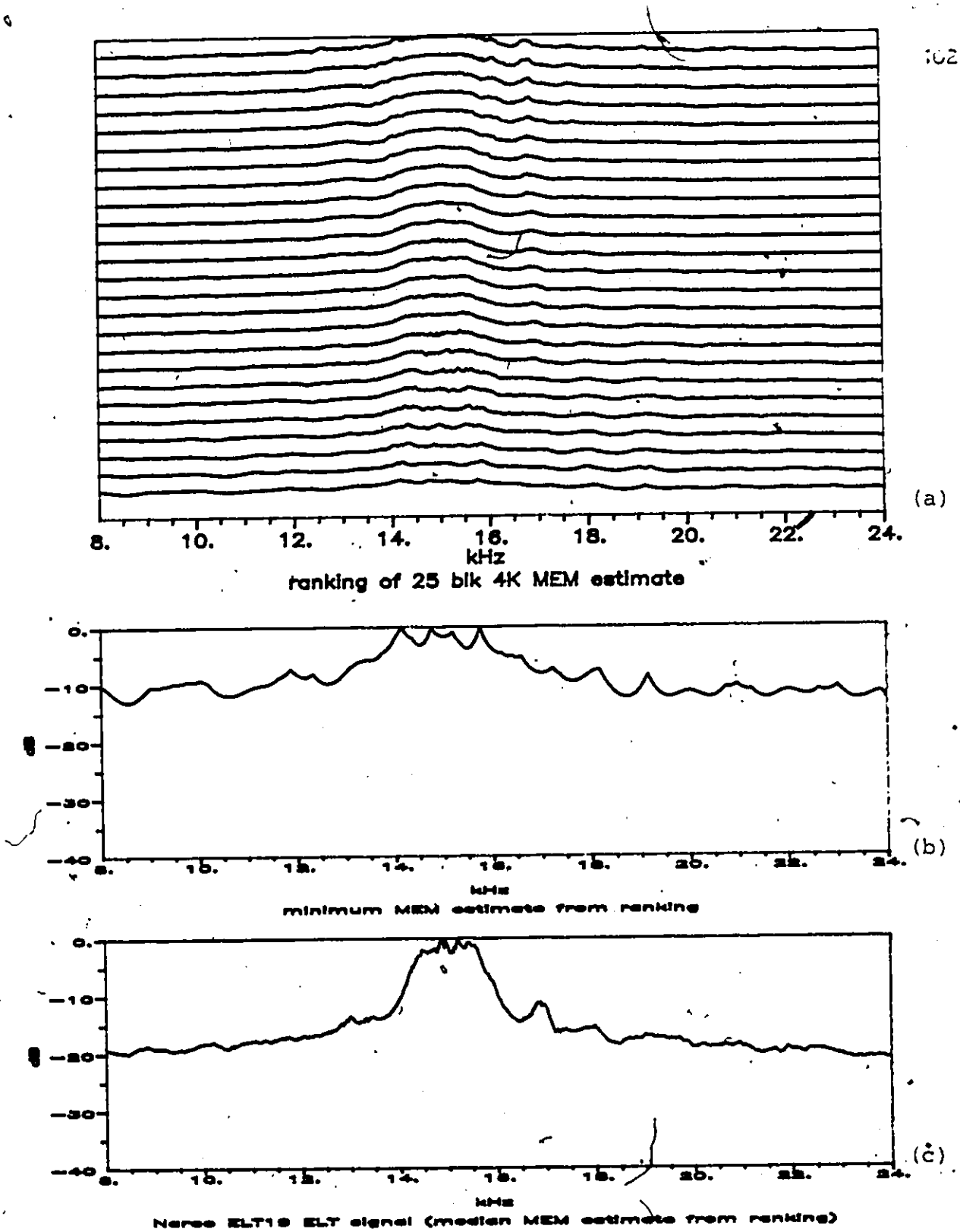

Fig. 5.7 (a) Ranked MEM estimates for the Narco ELT19 signal spectra of Fig. 4.15.

(b) Minimum-selection from the ranked MEM estimates.

(c) Median-selection from the ranked MEM estimates.

shown to be successful by employing averaged modified MEM. Nevertheless, the spectral peak of the averaged spectrum line-splitting (Fig. 4.17). The ordered statistic of the modified MEM is given in Fig. 5.9. The minimum selection and the median selection provide distinct and well defined estimate of the mixed carrier frequency, of the Non-Coherent ELT signal, which is never measured by any of the suggested processors.

We see that ranking is useful in reducing the interference due to sidebands and other broadband interference. As a result we choose the median selection as the desire spectrum estimation of the signal. It is also hope that some benefit could be derived by averaging K of these ranked spectra just as in the case of averaged FFT (or MEM). This process is now examined in detail.

5.4 THE AVERAGING SPECTRUM FROM THE ORDER STATISTIC

The estimation of power spectrum utilizing the principle of averaging produces smoothed spectrum. This is valid as long as the data sequence contains consistent values. When the data set experiences either high-noise or high-interference situations, the averaged processor provides estimate with undesirable features, such as large bias and variance. We note that, by ranking the periodograms, all the high values float to the top few traces. Further, the bottom traces contain noise and carrier peak estimates which are highly sensitive to Doppler shift and ELT carrier instability. The median selection, from the set of ranked spectra, is shown to be a reasonable solution for power spectrum estimation. However, in the case when the signal is corrupted by burst noise or interference, the median selection also gives biased estimation. The operation of order statistic on the power spectra exhibits a mean of isolating the contributions of interference and noise to the power spectrum of the signal.

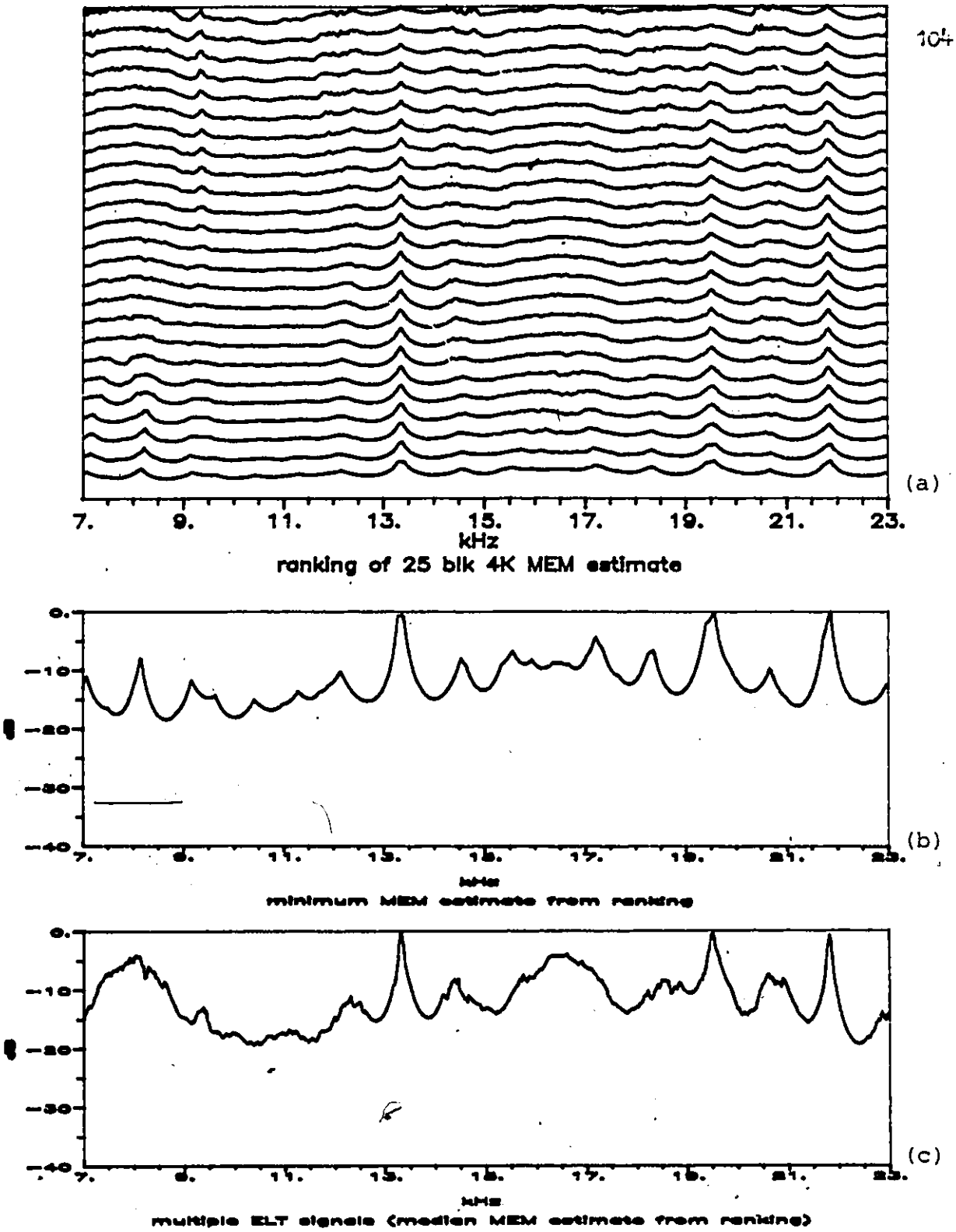

Fig. 5.8 (a) Ranked MEM estimates for the combined ELT signals spectra of Fig. 4.16.

(b) Minimum-selection from the ranked MEM estimates.

(c) Median-selection from the ranked MEM estimates.

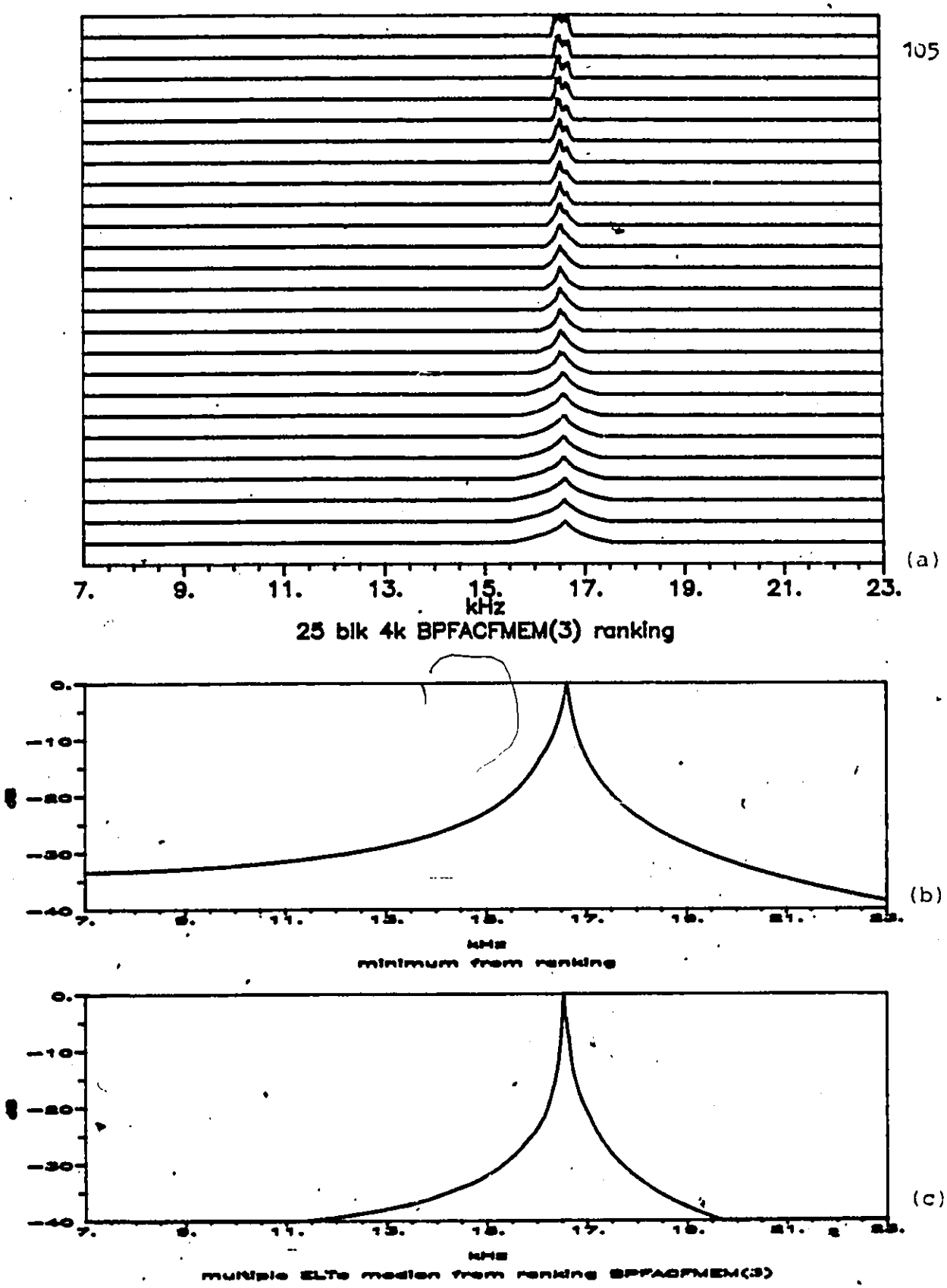

Fig. 5.9 (a) Ranked modified MEM estimates for the combined ELT signal spectra of Fig. 4.17.

(b) Minimum-selection from the ranked modified MEM estimates.

(c) Median-selection from the ranked modified MEM estimates.

Instead of averaging the entire spectra, we trim a fixed number of traces from the top and bottom of the ranked set of spectra. The level of sideband interference and the sensitivity to variation in the carrier peaks will be reduced. Signal detection is then improved by averaging the remaining traces, using the relation

$$S_{RAV}(f_k) = \frac{1}{J_o} \sum_{n=J}^{J+J_o-1} I'_n(f_k) \tag{5.4}$$

where $1 \leq J \leq K$ and J_o is the number of periodograms to be averaged. The endeavour has received much attention in the field of image processing [31] and sonar signal processing [30] [32]. For $J_o = 1$ and $J = (K+1)/2$, eq. (5.4) reduces to the median selection and for $J_o = 1$ and $J = 1$ it becomes the minimum selection. The only problem to be resolved is to determine the number of top and bottom traces to be discarded.

For the multiple ELT ranked spectral plots of Fig. 5.4, the spectra have been averaged in groups of five and are plotted in Fig. 5.10. We see that the top plot, which contains the average of the top five traces, has not only strong signal peak components but considerable interference from the sidebands as well. The second group of five has far less sideband interference while maintaining the same signal peak components as the top group. The remaining three groups show somewhat less sideband interference than the top two groups, but also substantially less detection capability for detecting the Narco ELT17 signal. Hence, we shall select the second group, namely blocks 16–20. Comparing Fig. 5.10(b) and Fig. 4.12(c) (which is the averaging periodogram), we note that the level sideband interference of the former is far less than that of the latter for most of the frequency band.

The same procedure is performed on the ranked modified MEM estimates. Examining the ranked spectra in Fig. 5.9, we know that averaging of the top five traces will give ragged estimation due to the bias estimate of the carrier peak. The averaging of the lower group will produce wide bandwidth spectra. Hence, we measured the averaged

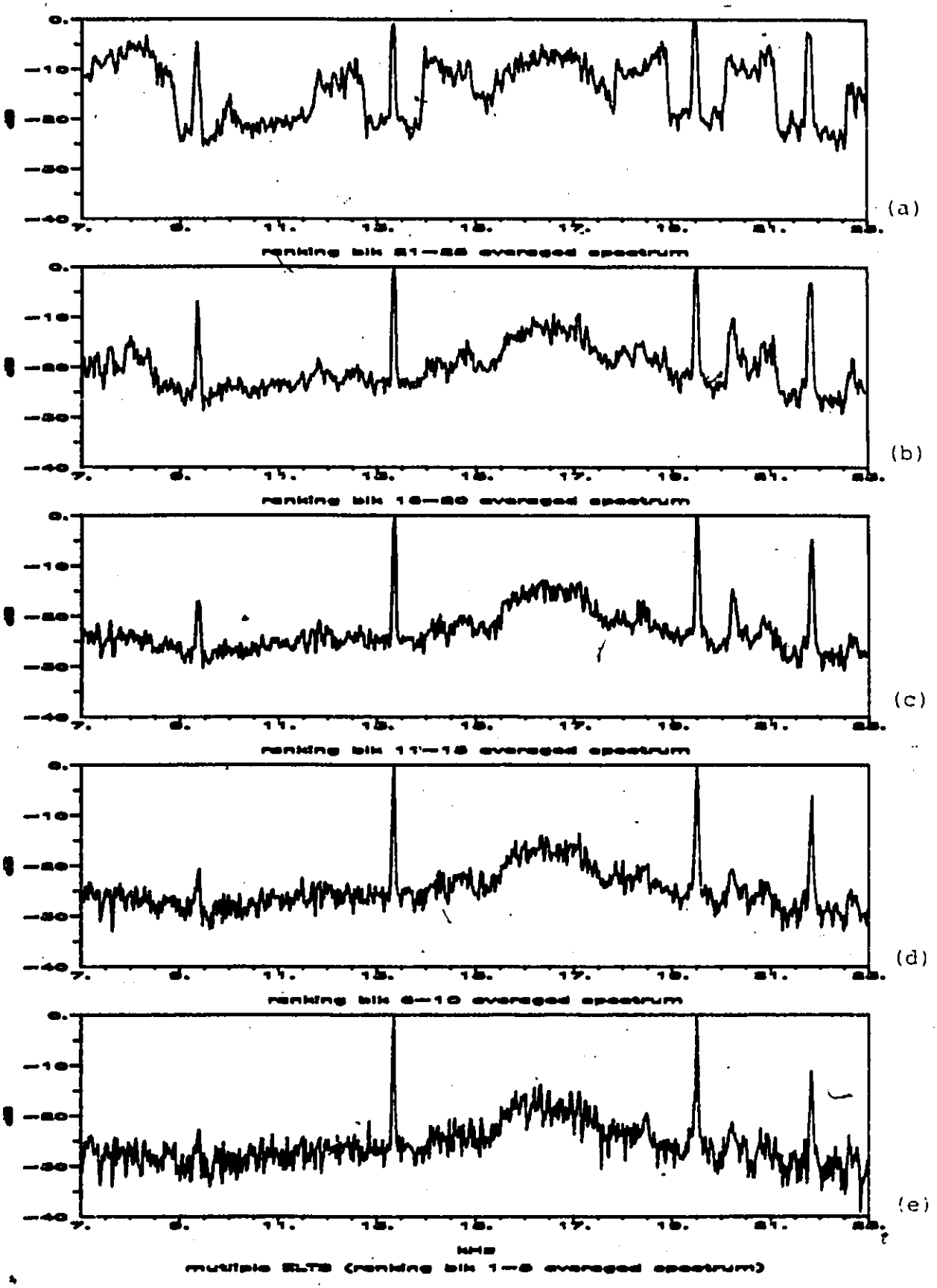

Fig. 5.10 The combined ELT signals spectra of Fig. 5.4(a) grouped five at a time and averaged.

estimate of blocks 16–20 and block 11–15. The results are shown in Fig. 5.11. Again, the spectrum calculated by averaging blocks 16–20 maintains well defined estimate and improved signal energy. Note that the spectrum obtained by averaging blocks 11–15 is similar to the median selection (Fig. 5.9(c)).

So far, we have developed methods to measure the power spectrum estimation of ELT signals. It has been shown that averaging a sub-group of the ranked spectra we receive an improved spectral performance in signal processing. For signal detection, it is necessary for the signal processor to yield a low probability of false alarm rate. This relies on the method of signal detection thresholding. A spectrum leveller can be employed to relieve thresholding problem. This issue is presented in Section 5.6

5.5 THE PERFORMANCE OF ORDERED STATISTIC BASED POST-PROCESSORS

It has been shown that spectrum estimation based on averaging a sub-group of the FFTOS and MEMOS achieves better performance than direct averaging periodogram or modified MEM. The comparison now includes noise performance.

The noise statistics for both the averaged periodogram and the averaged FFTOS were computed assuming an input signal of AWGN. Since the input to the FFT has Gaussian amplitude distribution and the FFT is a linear processor, the output amplitude distribution is also Gaussian. Taking the magnitude of the FFT in order to produce the spectrum, we obtain a Rayleigh amplitude distribution. Applying averaging to these spectra produces an amplitude distribution which can be represented approximately by Marcum's Q function [13].

For K periodograms, we order the spectral components $I_r(f_k)$ at each frequency f_k according to eq. (5.1). Then, the probability density function of the rth value of the ordered statistic is given by [34], [35]

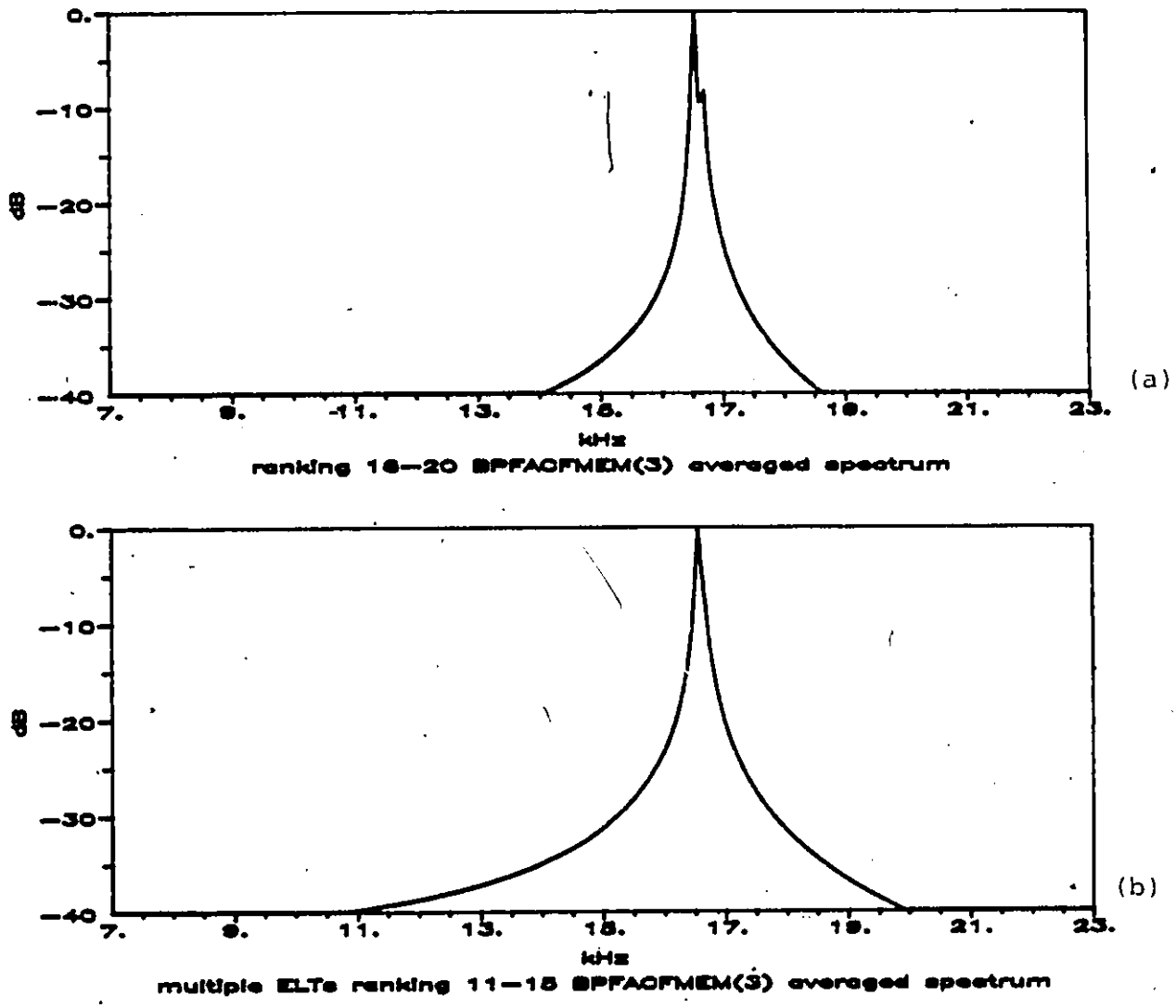

Fig. 5.11 The sub-group selection averaging of the ranked modified MEM estimates for combined ELT signals showing

(a) Averaged of block 16-20.

(b) Averaged of block 11-15.

$$p_r(x) = r\binom{K}{r}(1 - P_I(x))^{K-r} \; (P_I(x))^{r-1} \, p_I(x) \tag{5.5}$$

where $p_I(x)$ is the probability density function and $P_I(x)$ is the distribution function.

Since $p_I(x)$ for the set $I_r(f_k)$ is known to be Rayleigh, we have [11]

$$p_I(x) = \begin{cases} \dfrac{x}{a^2} \exp\left(-\dfrac{x^2}{2a^2}\right) & \text{for } x \geq 0 \\ 0 & \text{for } x < 0 \end{cases} \tag{5.6}$$

and

$$P_I(x) = \begin{cases} 1 - \exp\left(-\dfrac{x^2}{2a^2}\right) & \text{for } x \geq 0 \\ 0 & \text{for } x < 0 \end{cases} \tag{5.7}$$

where the mean is $(a^2\pi/2)^{1/2}$ and the peak is $x_p = a$.

For the minimum, $r = 1$ and

$$P_I(x) = \begin{cases} \dfrac{Kx}{a^2} \exp\left(-\dfrac{Kx^2}{2a^2}\right) & \text{for } x \geq 0 \\ 0 & \text{for } x < 0 \end{cases} \tag{5.8}$$

We see that for minimum selection, the distribution is Rayleigh with mean reduced by $K^{1/2}$ and variance reduced by K as compared to eq. (5.6). Thus, normalizing the minimum selected spectrum, we find that the distribution is exactly the same as the original spectrum.

For the maximum, we have

$$p_K(x) = \begin{cases} K(P_I(x))^{K-1} \, p_I(x) & \text{for } x \geq 0 \\ 0 & \text{for } x < 0 \end{cases} \tag{5.9}$$

For the Rayleigh distribution, we have

$$p_K(x) = (1 - \exp(-x^2/2a^2))^{K-1} \quad (Kx/a^2)\exp(-x^2/2a^2) \tag{5.10}$$

The first term on the rhs of eq. (5.10) is small for $x < 2a$ provided that $K > 10$. Thus, the distribution slides to the right and takes the appearance of a skewed Gaussian. The

peak value can be calculated approximately by first noting that the function is affected mainly by the exponentials for $x > 2a$. Thus, if we ignore the Kx/a^2 term, and differentiate eq. (5.10), we find the peak at approximately

$$x_p = a(2\ell n(K))^{1/2} \tag{5.11}$$

For the other ranked distributions, the peak of the density progresses from the Rayleigh of the minimum at $x_p = a$ to the skewed Gaussian of the maximum with peak given by eq. (5.11).

The distribution for both the averaged FFT and the averaged ranked FFT were computed for a sequence of random noise samples and the result are listed in Table 5.1. We see that the distributions for averaged periodogram and averaged block 16-20 of ranked FFT are very close both in mean and variance.

Spectral plots at different values of CNDR are presented for averaged periodogram and averaged FFTOS with spectrum leveller applied. A simulated Pointer ELT signal at 21 dBHz is used as an empirical study. From Fig. 5.12 the results show that for a fixed threshold level of -3.5 dB, the detection of signal and the number of false alarms due to noise for both methods is almost the same.

For the real multiple ELT signal case, we try two values of CNDR, namely 39 dBHz and 29 dBHz for the composite signal using computer generated noise added to the signal. Since each of the ELT signals contributes approximately equally to the CNDR, the actual levels for each ELT signals are 32 dBHz and 23 dBHz. In Fig. 5.13, both strategies of spectral estimation indicate the presence of the Pointer, Garrett and the Narco ELT17 signals at 32 dBHz. The Narco ELT19 signal cannot be detected. At 23 dBHz, both the Pointer and the Garrett ELT signals are detectable but the Narco signals are below noise, as illustrated in Fig. 5.14.

spectral amplitude distribution						
	averaged minimum selection block					25 blks 4K
amplitude	01-05	06-10	11-15	16-20	21-25	ave FFT
.00-.05	0	0	0	0	0	0
.05-.10	0	0	0	0	0	0
.10-.15	0	0	0	0	0	0
.15-.20	10	0	0	0	0	0
.20-.25	53	1	0	0	0	0
.25-.30	110	0	0	0	0	0
.30-.35	221	7	0	0	0	0
.35-.40	305	36	1	0	0	0
.40-.45	331	90	8	1	0	0
.45-.50	307	184	58	10	5	7
.50-.55	260	322	136	38	26	26
.55-.60	195	361	282	128	147	103
.60-.55	116	377	414	266	300	283
.65-.70	66	302	421	436	492	485
.70-.75	43	187	370	513	462	544
.75-.80	13	98	225	356	334	352
.80-.85	12	59	94	180	176	149
.85-.90	2	14	30	83	76	79
.90-.95	2	6	6	25	22	16
.95- 1	1	3	2	11	7	3

Table 5.1 Distributions for the averaged FFT and the averaged ranked FFT of the five sub-groups.

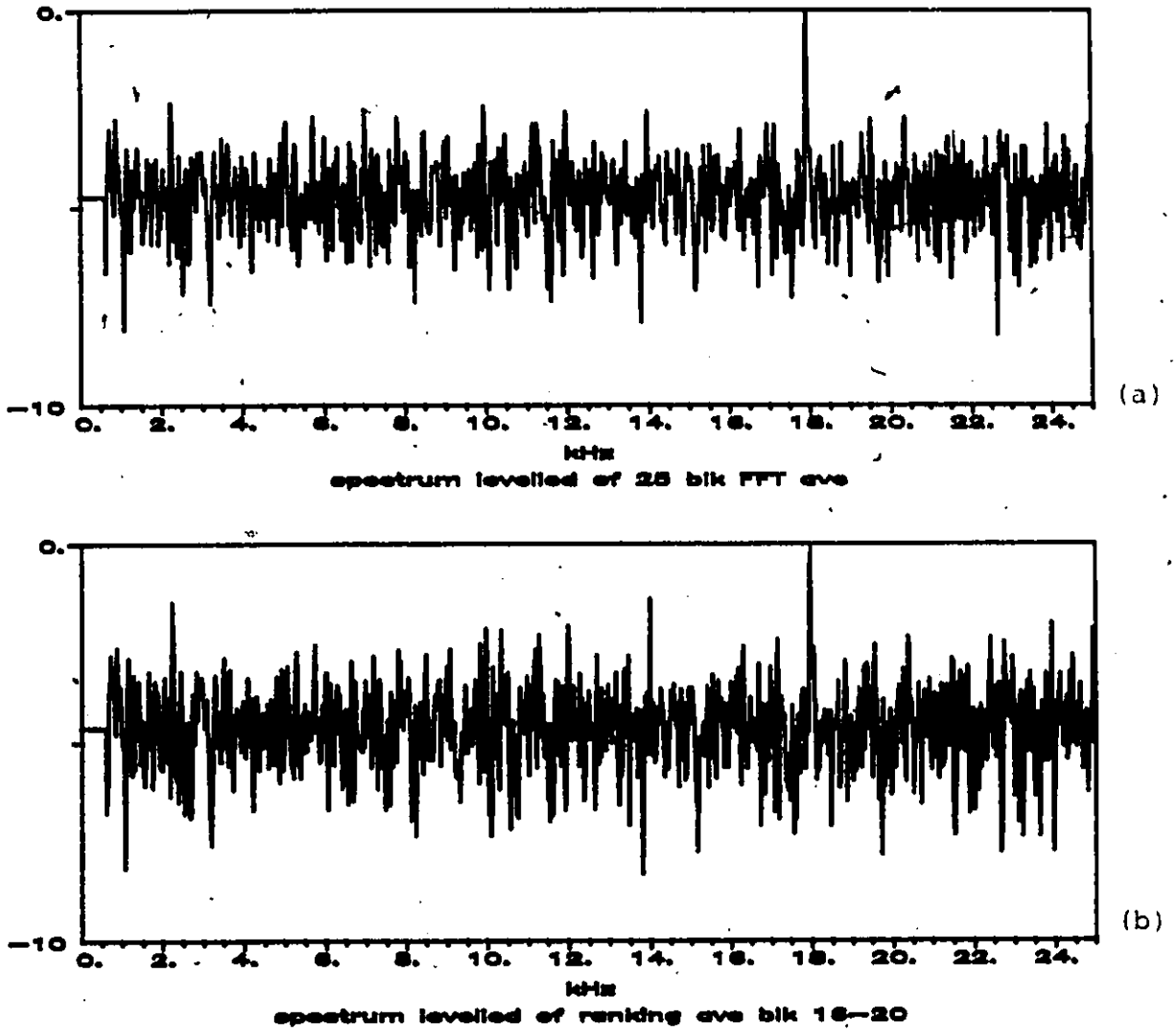

Fig. 5.12 Comparison of the averaged FFT (top) and the sub-group selection of block 16-20 averaged ranked FFT (bottom) for the simulated Pointer ELT signal with CNDR of 21dBHz. Both spectra are spectrum levelled.

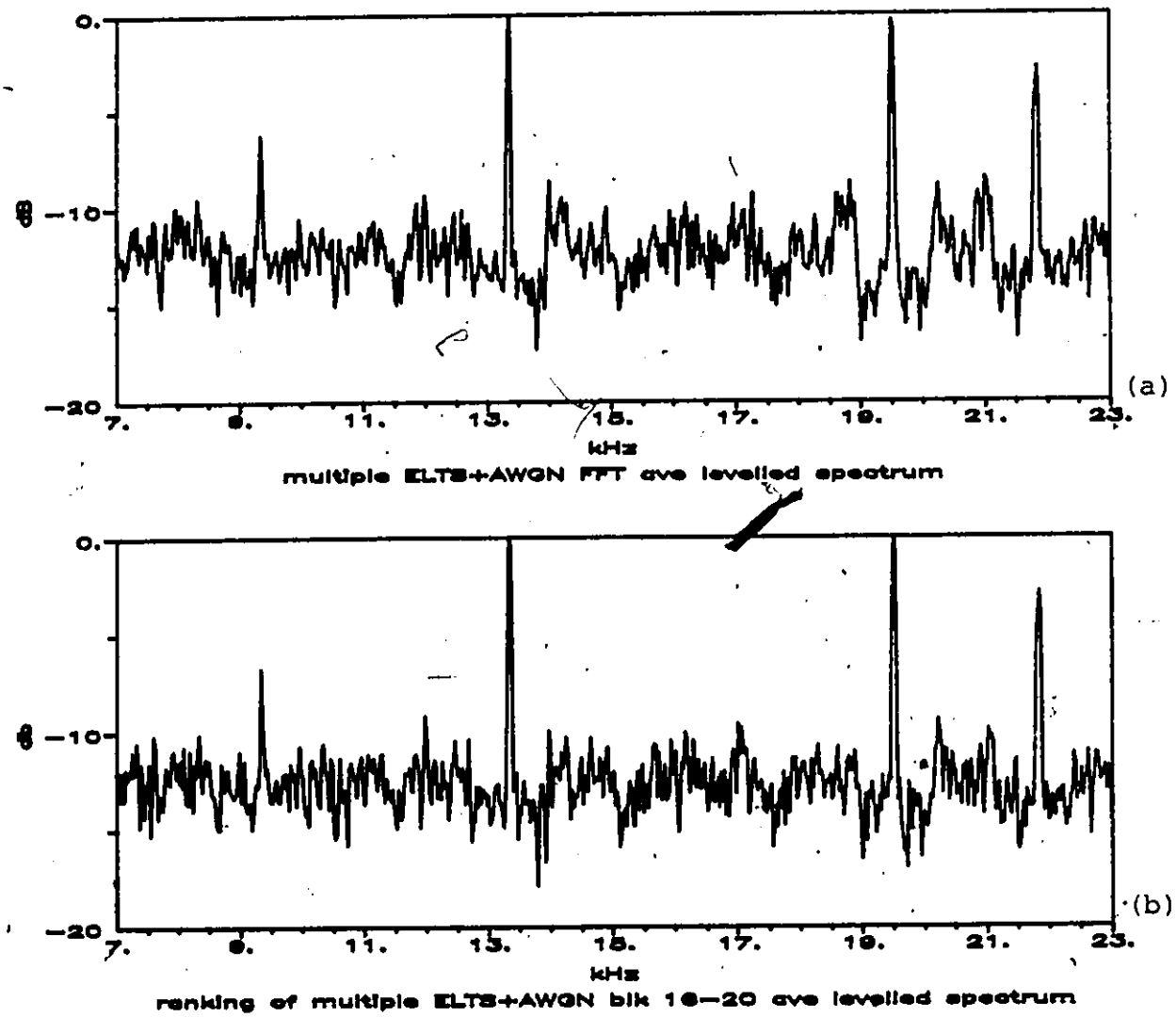

Fig. 5.13 Comparison of the averaged FFT (top) and the sub-group selection of block 16-20 averaged ranked FFT (bottom) for the combined ELT signals with CNDR of 32dBHz. Both spectra are spectrum levelled.

The modified MEM spectral estimator has been tested using CNDR values of 35 dBHz and 45 dBHz for 25 4K blocks of simulated Non-Coherent ELT signal with AWGN comprising approximately 1 s of signal. The result of one typical test with signal frequency 17531 Hz is given here. The results of the averaged spectra and ranked spectra are presented in Fig. 5.15. A prediction error filter of order 3 is used. It is found that for CNDR values less than 35 dBHz, no meaningful indication of frequency is obtained since the spectral peak occurs at the centre of the bandpass filter. This is to be expected since the averaged spectrum of Fig. 4.12(c) shows that the spectral peaks of Narco ELT19 are a full 10 dB below the good quality spectral peaks. However, as the CNDR is increased, the peak tends to sharpen and at 35 dBHz produces an estimate which is in error by only approximately 80 Hz for both averaged and averaged ranked MEM estimates. This is a considerable improvement over the averaged periodogram which gives essentially no indication of carrier frequency, even at much higher values of CNDR.

5.6 THE SPECTRUM LEVELLER TECHNIQUE

A spectrum leveller can be employed by computing a running average across a certain number of points of the averaged spectral plot in order to locate an estimate of the level. Then the averaged spectral plot is adjusted using this leveller.

The performance of this technique is best demonstrated by the detection of multiple targets embedded in an interfering background. It has been shown that for multiple ELT signals, the averaged periodogram in Fig. 4.12(c) is crowded with the combination of ELT carrier frequency peaks, sidebands interference and background noise. This clutters most often is of sufficient magnitude as compared to the carrier peak, that it exceeds confine the detection threshold. This situation is particularly significant when the spectral magnitude of a signal radiated from a weak transmitter may sometimes be dwarfed by strong interfering

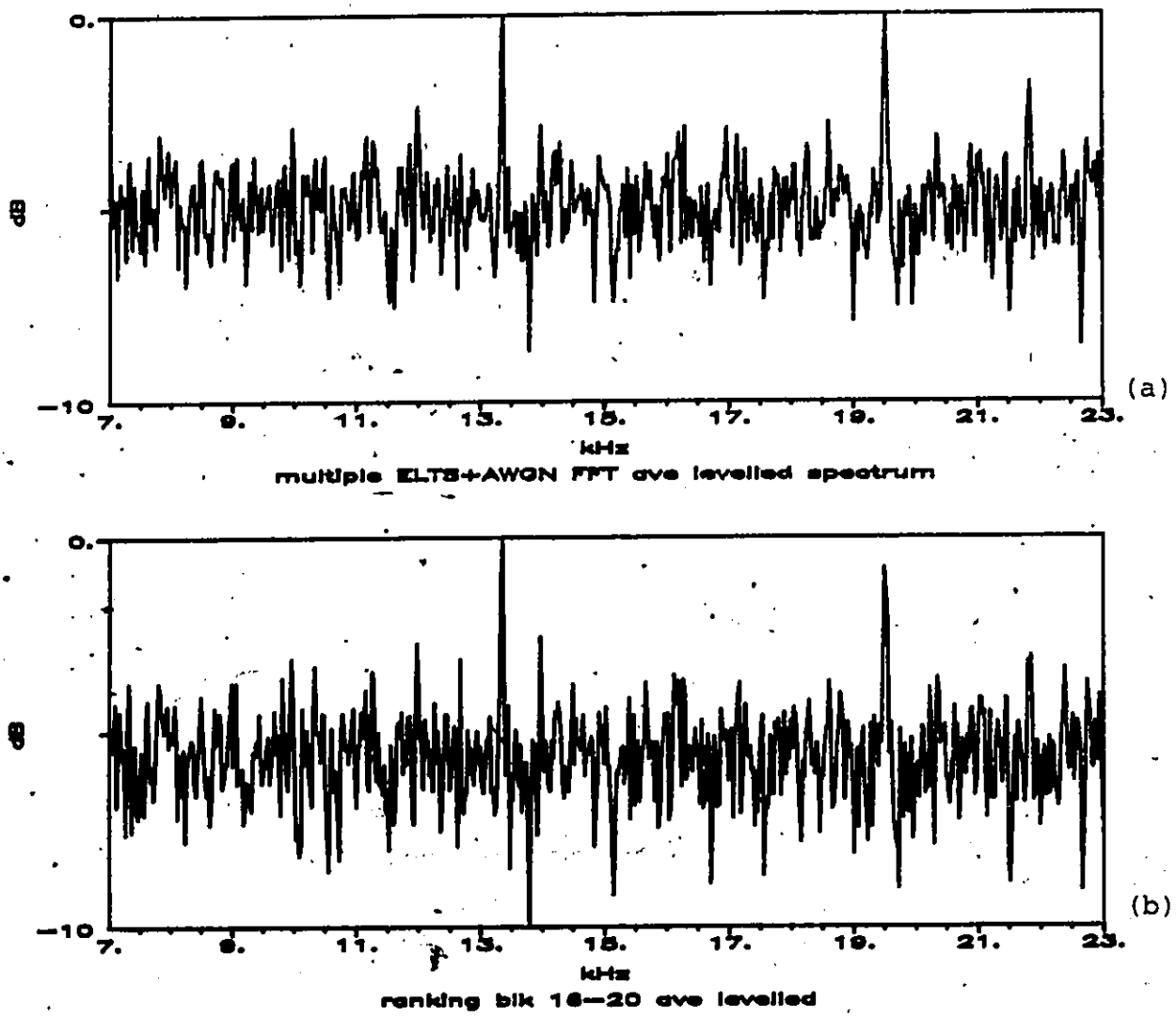

Fig. 5.14 Comparison of the averaged FFT (top) and the sub-group selection of block 16-20 averaged ranked FFT (bottom) for the combined ELT signals with CNDR of 23dBHz and spectrum levelling. Note that the Narco ELT17 signal is now embedded in noise.

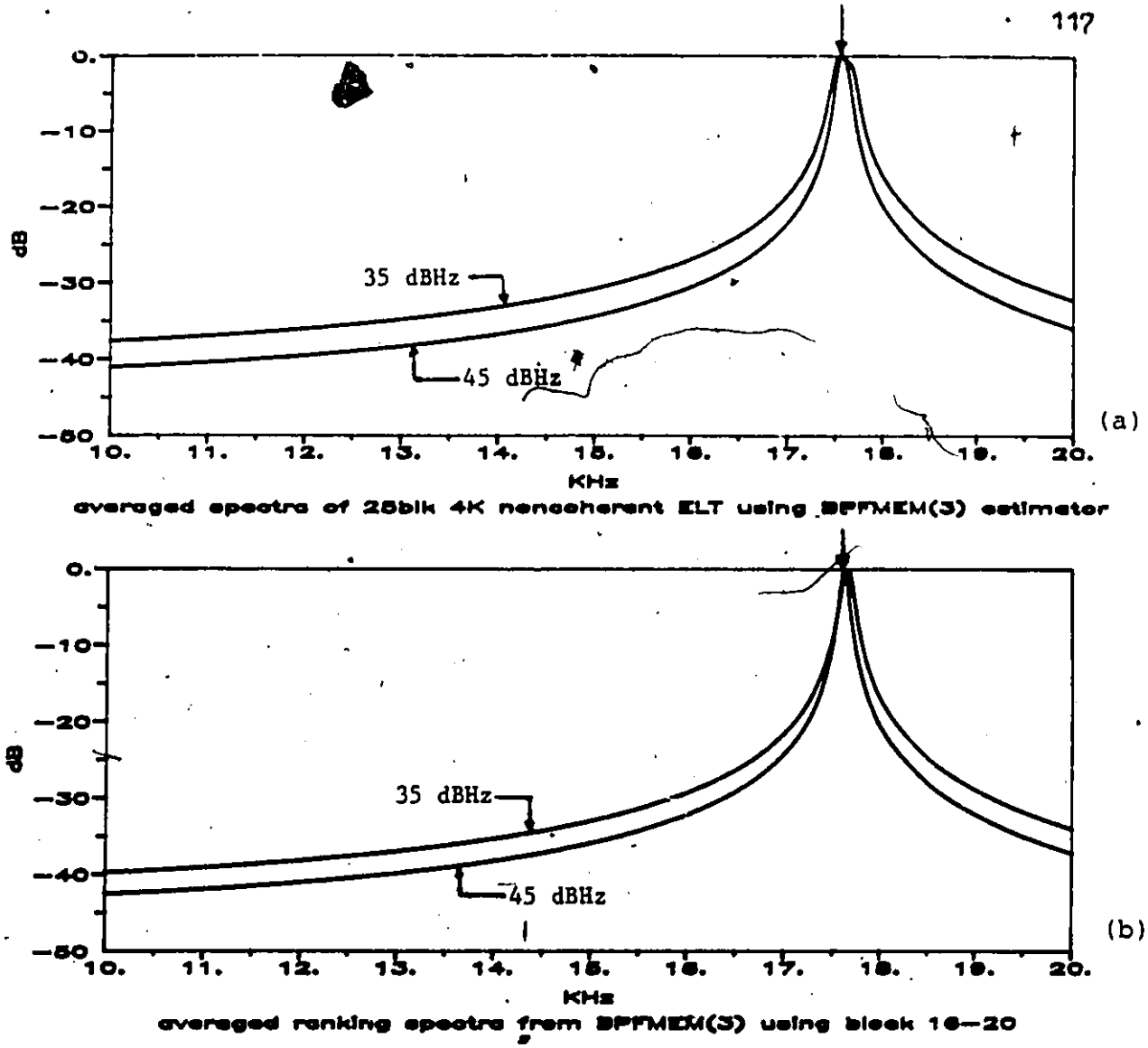

Fig. 5.15 Modified MEM estimates (order 3) of simulated Non-Coherent ELT signal with $f_c = 17731$ Hz,

(a) Averaged spectral of 25 blocks 4K data.

(b) Averaged ranked spectral of block 16-20.

source. As a result, the probability of a signal being detected is degraded. A better dynamic range can improve signal detection. This is accomplished by reducing the clutter level from the spectral plot. Thus, a more reliable Doppler-time curve will be produced for the Doppler processor whose function is to measure the range of the distressed platform [33].

This technique is applied to the spectrum of the averaged periodogram (Fig. 4.12(c)) and the averaged block 16–20 ranked periodogram (Fig. 5.10(b)) of the composite ELT signals. From both spectra, the carrier peak is represented by approximately five to ten points (the sampling rate used is 100 K samples per second and for 4K points the frequency resolution is 24.4 Hz), the average is computed over 51 points to reduce the effects of the peak on the level estimate. (Extending the window much beyond 51 samples tends to defeat the levelling process.) The levelled spectrum is defined by

$$S_{LEV}(f_k) = \frac{S_{AVE}(f_k)}{\frac{1}{2M+1} \sum_{k=-M}^{M} S_{AVE}(f_k)} \tag{5.12}$$

where a total of $2M+1$ points are averaged. The function $S_{AVE}(f_k)$ can be any of the processors defined by eq. (4.36), eq. (4.40) and eq. (5.4).

Using a 51 point average, we produce a spectrum leveller for the averaged periodogram of Fig. 4.12(c). The leveller is plotted with superimposed of the averaging spectrum in Fig. 5.16(a). The result due to eq. (5.12) is given in Fig. 5.16(b). While this result is considerably easier to threshold than the averaged plot, the effects of the sideband interference are still clearly present. Thus, it is desirable to reduce these sidebands prior to the application of spectral levelling.

The performance of spectrum leveller on the ranked periodogram is illustrated in Fig. 5.17. The top plot shows the unlevelled spectrum of the averaged of block 16–20 from the ranked periodogram of the multiple ELT signals with the levelling waveform superimposed. The bottom plot is the levelled spectrum. Comparing with the average levelled spectral plot

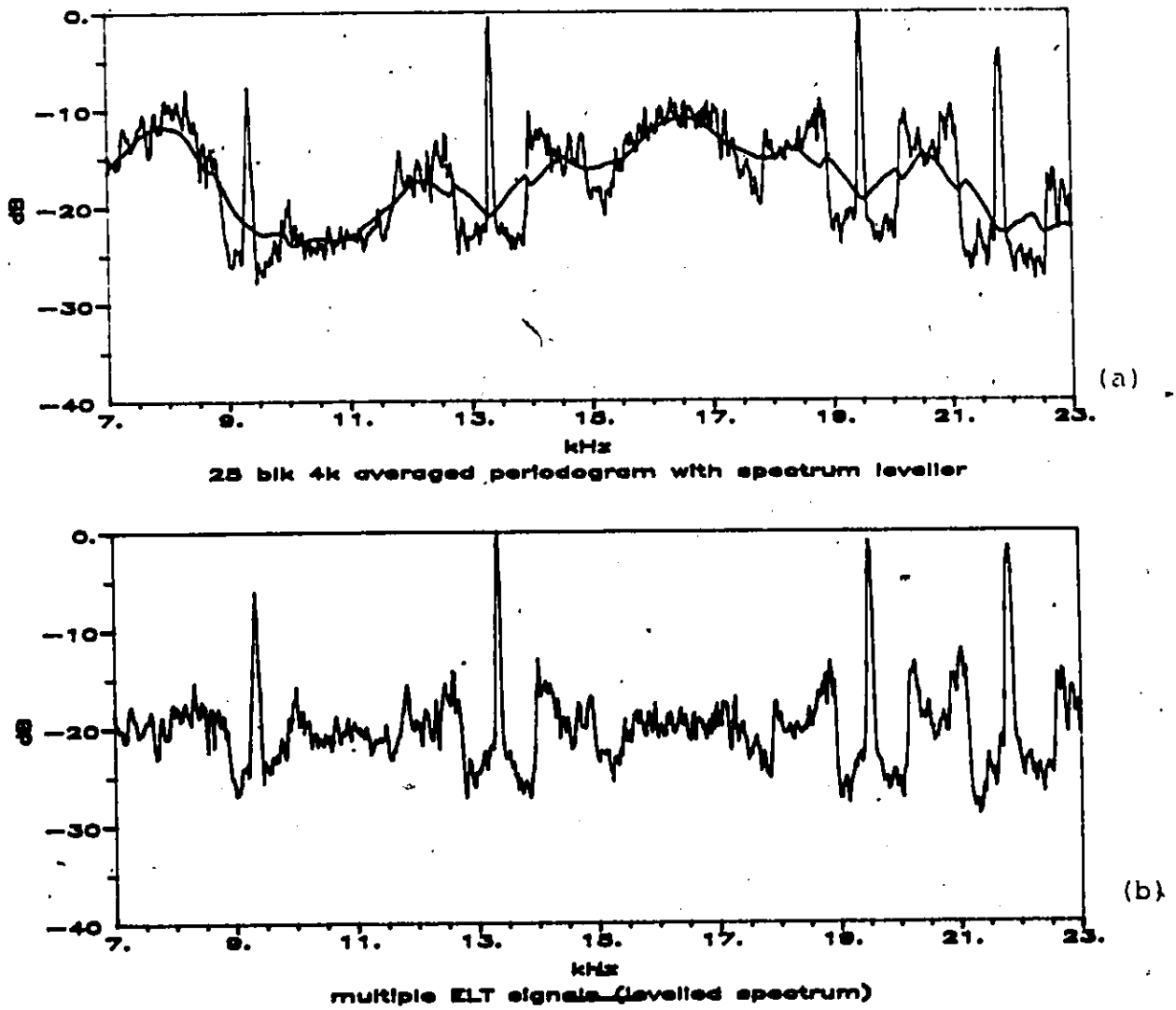

Fig. 5.16 (a) Averaged of the 25 periodograms for the combined ELT signals. The solid line indicates the level produced by the spectrum leveller.

(b) Averaged periodogram processed by the spectrum leveller.

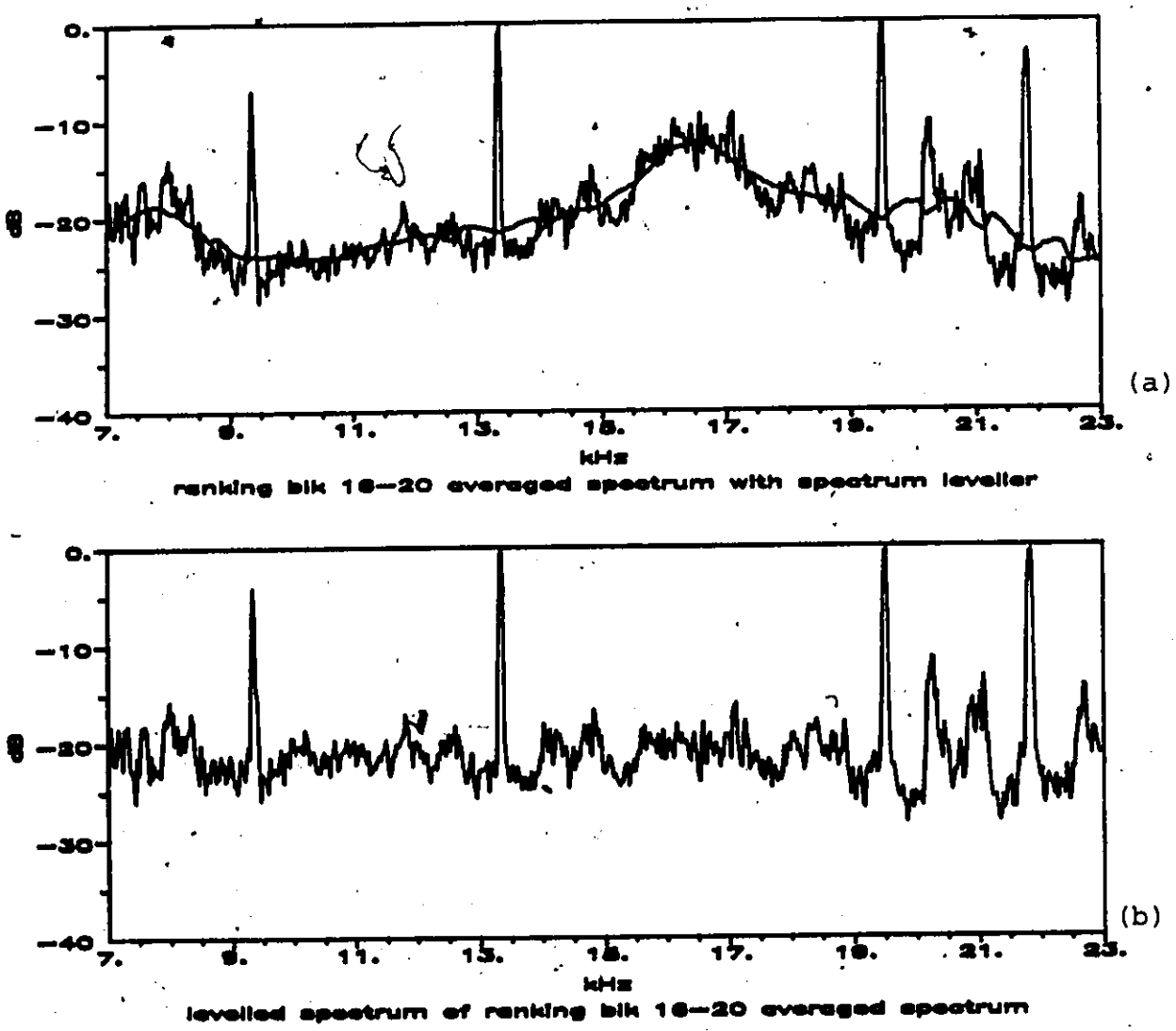

Fig. 5.17 (a) Averaged of the sub-group selection of block 16-20 of the ranked periodograms for the combined ELT signals with the level of the spectrum leveller superimposed.

(b) Averaged ranked periodogram processed by the spectrum leveller.

of Fig. 5.16(b), we see that the result is considerably better and the problems of thresholding are simplified.

The spectrum estimation based on the modified MEM is designed to combat the ill-configured signal, such as the Non-Coherent model. The spectrum of the Non-Coherent ELT signal as seen in Fig. 5.11 does not require spectrum levelling because the result obtained is already acceptable due to the sub-group averaging of MEMOS. Thus, spectrum levelling technique is seen to benefit the Fourier transformed based processor.

5.7 SUMMARY

In this Chapter, real ELT signals are processed using ordered statistics and spectrum leveller. It is found that the averaged ranked FFT equals the detection performance of the averaged FFT in Gaussian noise and, in addition, reduces intereference due to sidebands.

Spectrum levelling is found to greatly improve the performance of both the averaged FFT and the averaged ranked FFT.

CHAPTER 6

SATELLITE PASS DATA MEASUREMENT

In SARSAT signal environment it is possible to receive many (5 to 25) simultaneous emergency beacon signals combined with voice signals and interference of various types, all simultaneously occupying essentially the same frequency-time space. The uplink signals from each of these sources results in Doppler curves which are interlaced, overlapping, and often segmented due to the signal falling below the threshold for parts of the satellite pass [33].

Signals received by the SARSAT system recorded on tape at the Communications Research Centre in Ottawa are processed and found to contain a wide range of interfering sources. In the previous chapter we have investigated several signal processing strategies and found spectrum ranking, sub-group averaging and levelling, to be effective in combatting interference.

The frequency band of operation for the SARSAT system includes 121.5 and 243 MHz. A survey shows that there are many different possible sources of interference in the frequency range from 100 to 500 MHz [36]. It is therefore necessary to examine those sources of interference which enter the 121.5/243 MHz frequency bands of the SARSAT system. Since the detection of this interference is important to the processing of the SARSAT signals, several methods of measuring the satellite pass activity are proposed.

6.1 SURVEY OF THE INTERFERENCE IN THE 100-500 MHz

In the frequency band from 100 to 500 MHz, there are many different types of background noise and interference. These can be divided into two groups: natural sources such as

atmosphere noise, galactic noise, solar flare interference and the like, and man-made interference such as automobile ignition noise, power generating facility interference, scientific and industrial equipment noise, CB radio and amateur radio interference. When it is present, man-made interference is often dominant such as in the case of the urban environment.

Natural sources of interference may have either a relatively smooth spectrum such as galactic noise or may be impulsive such as atmospheric noise and solar flares. The galactic noise is relatively constant in time whereas the impulsive noise occurs relatively infrequently such as during lightning storms.

Man-made noise can take many different forms such as smooth spectrum due to a large number of automobile ignitions, impulsive noise due to power switching circuits, or harmonic interference due to unfiltered power generators or radio transmitters. Some of these sources have been examined in detail [36] to determine their possible influence on signals in the 100-500 MHz frequency band.

6.2 INTERFERENCE AT 121.5/243 MHz

Now we examine the problems of noise and interference which relate specifically to the 121.5 MHz and 243 MHz SARSAT frequency bands. We note that the 121.5 MHz band is 25 KHz in bandwidth and the 243 MHz band has a 50 KHz bandwidth. The ratio of bandwidth to centre frequency in both cases is 0.02 percent, indicating that both receivers can be classed as narrowband.

Interference may be thought of as unwanted emanations which compete with desired ELT signals in the frequency bands of interest. Normally, interference is only significant if the strength is sufficiently high to cause a noticeable degradation in the detection of the desired signal. Thus it is possible to define a threshold level which separates harmful

interference from insignificant interference. Specification of this threshold depends on the type of interference encountered.

There are two fundamentally different kinds of interference which affect receivers of the COSPAS-SARSAT type of system. These are impulsive interference and in-band interference.

6.2.1 Impulsive Interference

Impulsive interference is normally thought of as being due to (1) a small number of high power, short duration video pulses or a small number of high power, short duration pulses of carrier which shock excite the receiver, (2) a high power carrier which rapidly sweeps in and out of the receiver passband, again shock exciting the receiver, and (3) a large number or mix of low power video pulses, low power pulses of carrier and low power swept carrier sources which add together to form a broadband spectrum of interference.

The first two of these are referred to as case 1 and case 2 and described in detail. The third source of interference is considered to be broadband interference and is discussed in a later section.

A. <u>Case 1</u>

The first of these is due to short duration pulses where the pulse duration is small compared to the reciprocal of the bandwidth of the receiver. In this case, the pulse may be either video or modulated carrier. For modulated carrier pulses, the carrier frequency may be inside or outside the bandwidth of the receiver. Essentially, impulsive interference shock excites the ringing response of the receiver every time a pulse reaches the receiver input. The output of the receiver due to such an input pulse can be simplistically represented by [36]

$$r(t) = A \exp[-\alpha t] \sin(2\pi f_c t) \quad t \geq 0 \tag{6.1}$$

where A is the amplitude, α is the damping constant which is a function of the bandwidth and the phase linearity of the receiver, f_c is the centre frequency of the receiver passband (for narrowband systems), and t is the time.

Normally, this type of interference fills the bandwidth of the receiver and thus appears to be wideband interference. Since α usually results from a complicated combination of the overall bandwidth and phase characteristics of the system, its value is seldom known. However, it can be expected to lie in the range

$$B/20 < \alpha < B/5 \tag{6.2}$$

where B is the 3 dB bandwidth of the receiver.

An estimate of the jamming effectiveness of this impulsive interference can be obtained by noting that the receiver remains jammed whenever the root-mean-square value of r(t) exceeds the root-mean-square value of the desired signal and receiver noise at the output of the receiver. For an array of impulses with random amplitudes, there is an average duration T_I in seconds for which the receiver remains jammed. Since the impulses are normally generated at random times, we define the average number of impulses per second to be N_I. Then the fraction of the time that the receiver remains unjammed is simply

$$J = 1 - N_I T_I \tag{6.3}$$

We note that when $J \leq 0$, the receiver is completely jammed and no signals can be detected. Thus a threshold can be arbitrarily set, for example $J = 0.9$, which indicates that 90 percent of the time desired ELT signals can be detected.

B. <u>Case 2</u>

Impulsive interference can also be generated by sweeping a carrier from outside the passband of the receiver through the passband and back outside the passband. This type of interference causes two difficulties. First, there is the interference generated while in the

passband. The effects of this are discussed next. Second, there is the interference produced in sweeping from in-band to out-of-band or vice versa. If the sweep rate is sufficiently high, the receiver ringing response is excited and the receiver is jammed as in case 1.

6.2.2 In-Band Interference

In-band interference consists of modulated and unmodulated carriers which do not change frequency rapidly. Here the signals compete in amplitude and bandwidth with the desired signals. Examples of this include continuous wave (CW) carrier, harmonics of transmitter, and voice transmissions. In this case the threshold can be defined on a power density basis with the signal competing directly with the interference. The main factor is the number of false alarms which can be allowed (number of erroneous peaks in the power spectrum for a given threshold setting) and defined by the false alarm rate for a given probability of detection as in radar.

All such sources in the COSPAS-SARSAT system are classed as narrowband since the system bandwidth is very small compared to the carrier frequency, i.e. $B << fc$.

However within the band we may denote different bandwidths of interference. For instance, unmodulated carrier produces a near line spectrum interference. Voice produces a 5 to 10 KHz bandwidth interference, and other sources essentially fill the entire 25 KHz bandwidth. Thus for the present we will use these classifications: CW is the interference produced by an unmodulated carrier or continuous wave interference, NB is the narrowband such as that produced by voice (5 to 10 KHz), and WB is the wideband which fills most of the 25 KHz bandwidth.

6.3 CHARACTERISTIC OF REAL SATELLITE PASS DATA

During a satellite pass the field of coverage changes considerably as the antenna scans over cities with their many sources of interference, areas containing large numbers of false alarms, and other sources of electromagnetic interference. A few sample traces of waveforms received are now examined.

6.3.1 Interference From Recorded SARSAT Signals

The signal is mixed to the frequency band extending from 0 to 25 KHz prior to being processed. From SARSAT satellite S1, orbit 2614, we see a 2.5 ms duration of signal which appears to represent the case of normal Gaussian noise with the possibility of embedded ELT signals but no significant interference. This is illustrated in Fig. 6.1. Figure 6.2 gives a strong ELT signal with a small amount of noise in the background.

Contrast these with the traces from COSPAS satellite C1, orbit 6229 (Fig. 6.3) which clearly indicates an interfering phase-shift keyed (PSK) modulated sources, or Fig. 6.4 which is a strong CW interference. Figure 6.5 is an example of voice interference (an example of NB interference). In Fig. 6.3 to Fig. 6.5, it is clear that the automatic gain control (AGC) circuit in the receiver has considerably reduced the level of the background noise and any weak ELT signals by a very substantial amount. The amplitude peaks on Fig. 6.1 to Fig. 6.5 are all approximately the same amplitude; however the signal of Fig. 6.1 is mainly noise, whereas the signal of Fig. 6.3 to Fig. 6.5 is mainly interference. Thus the digitizing circuitry of the data processor must have sufficient dynamic range to combat this change.

In order to examine the existence of pulsed interference (an example of WB interference), an envelope detector was constructed. Figure 6.6 shows a short duration pulse which has entered the receiver and caused a transient in the AGC amplifier and indicates the

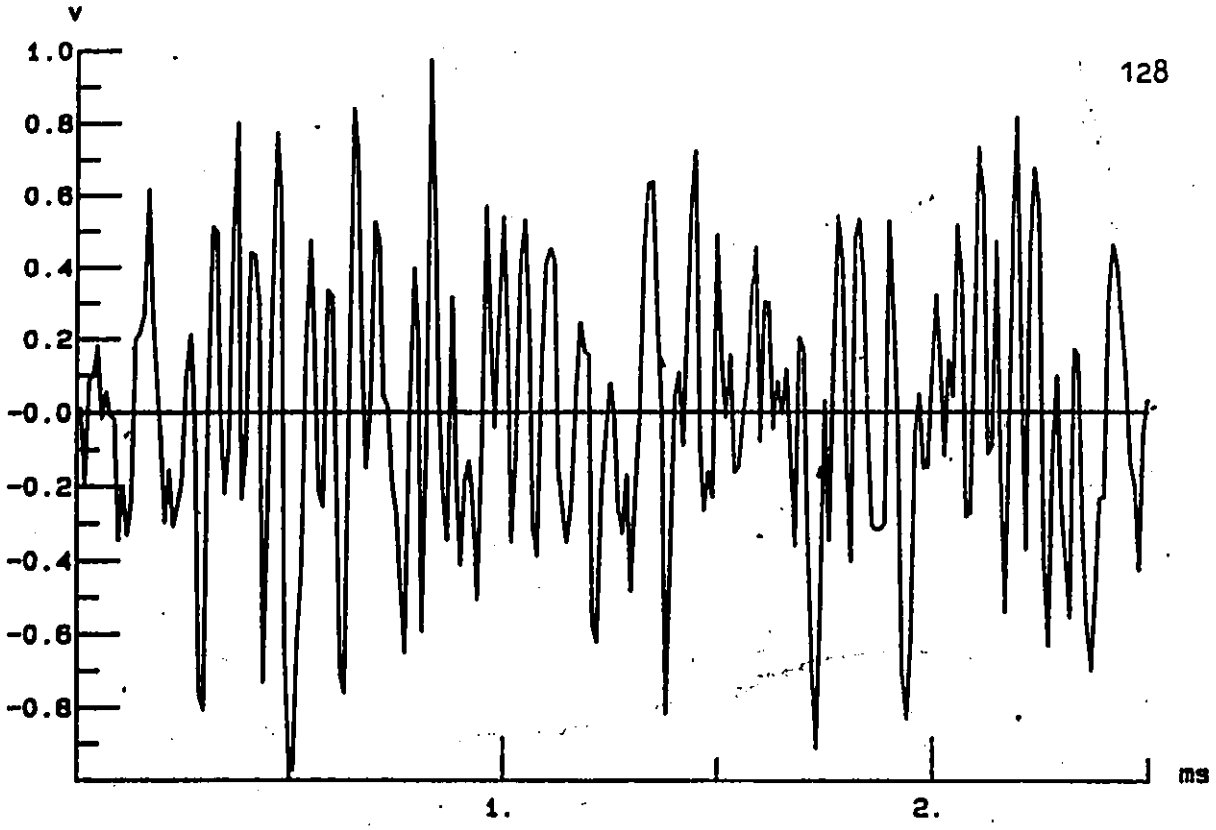

Fig. 6.1 SARSAT system receiver noise.

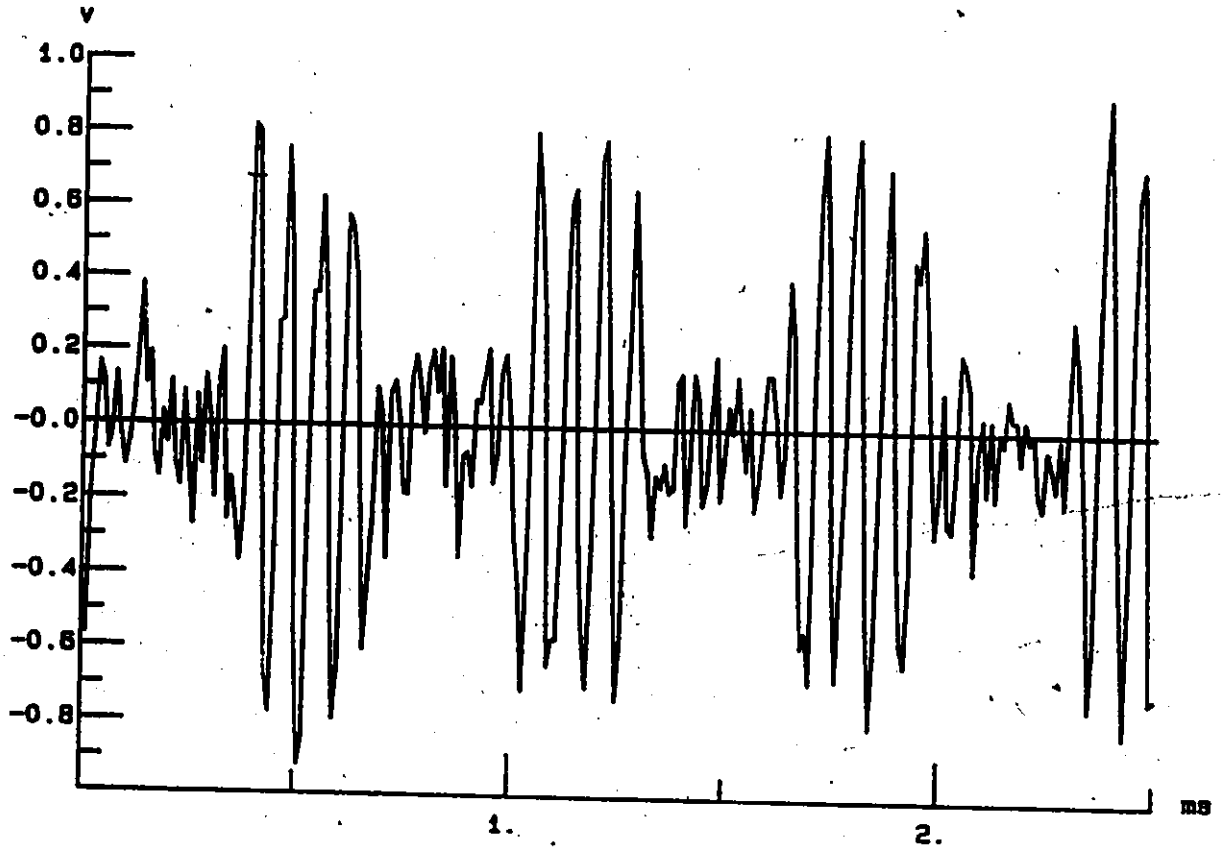

Fig. 6.2 Strong ELT signal received by the system.

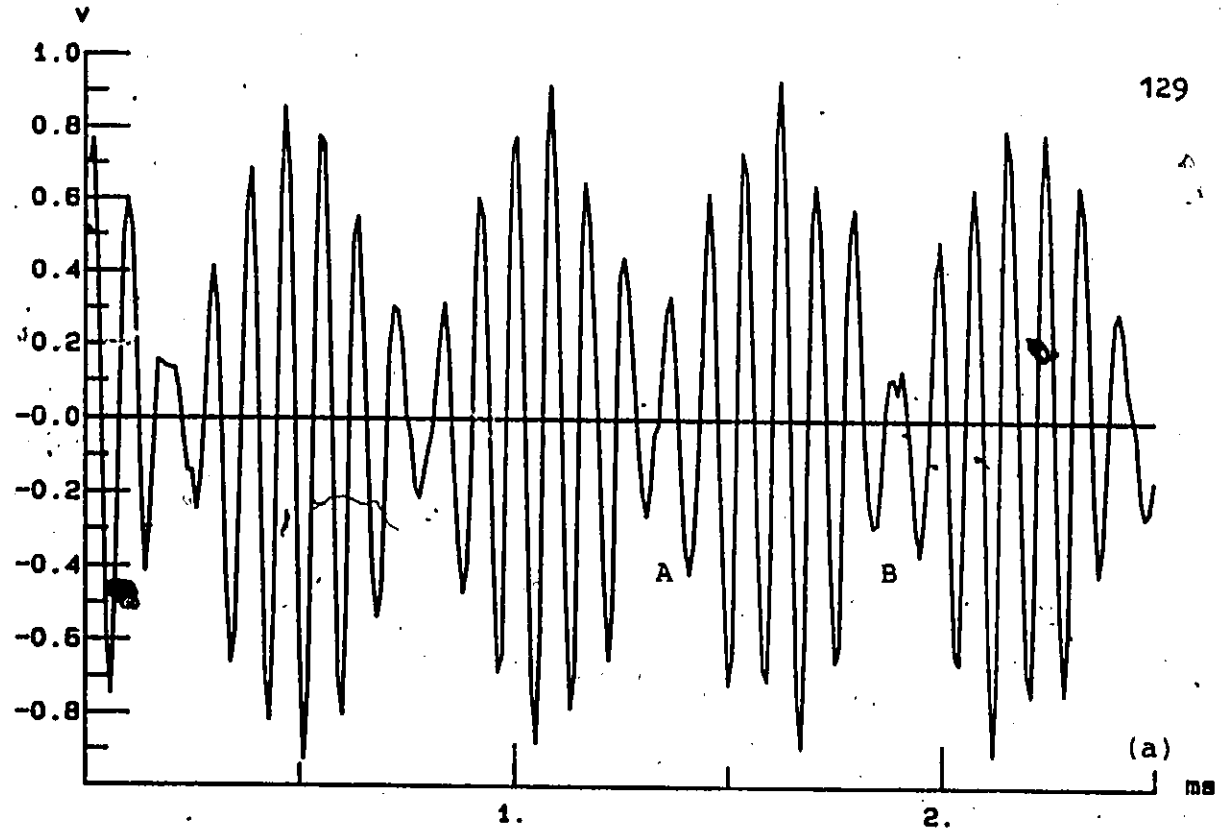

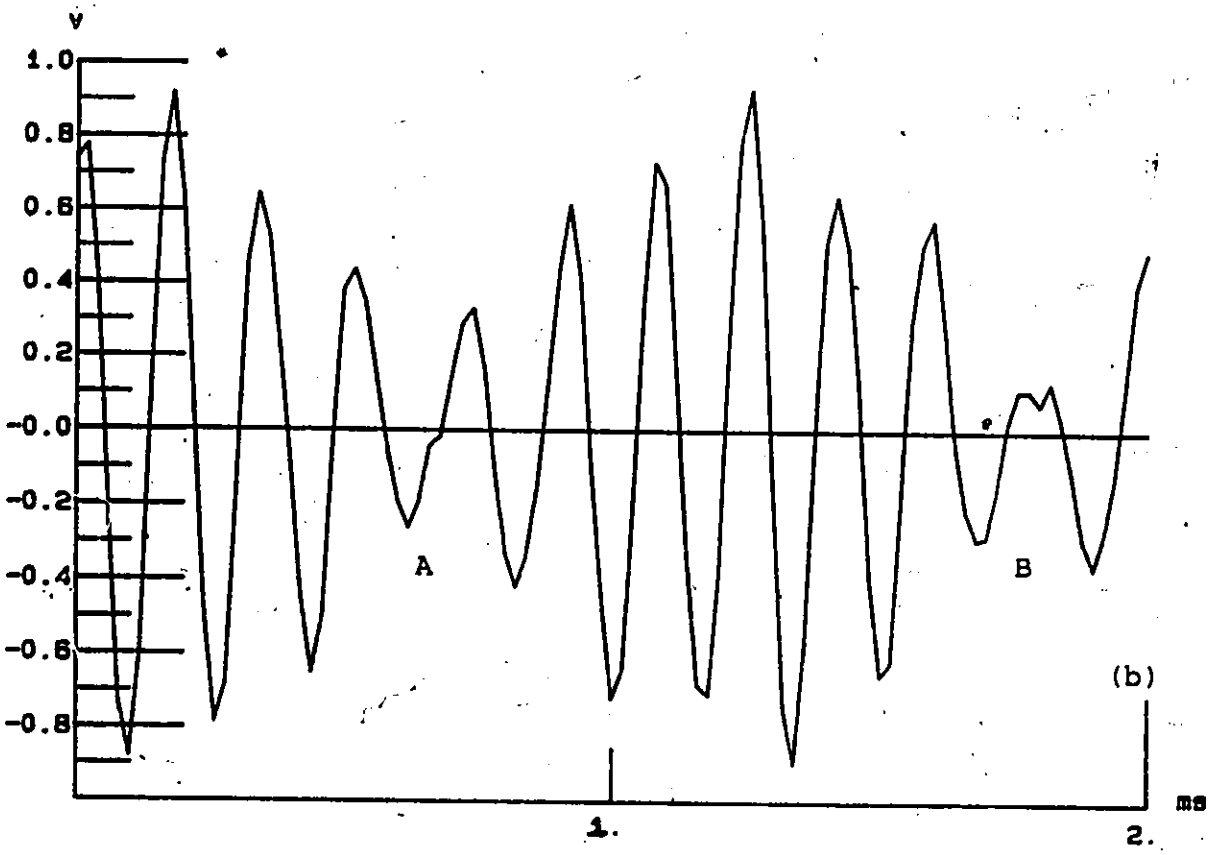

Fig. 6.3 (a) PSK modulated signal received by SARSAT.

(b) Expanded view showing the 0-1 transition at A and a 1-0 transition at B.

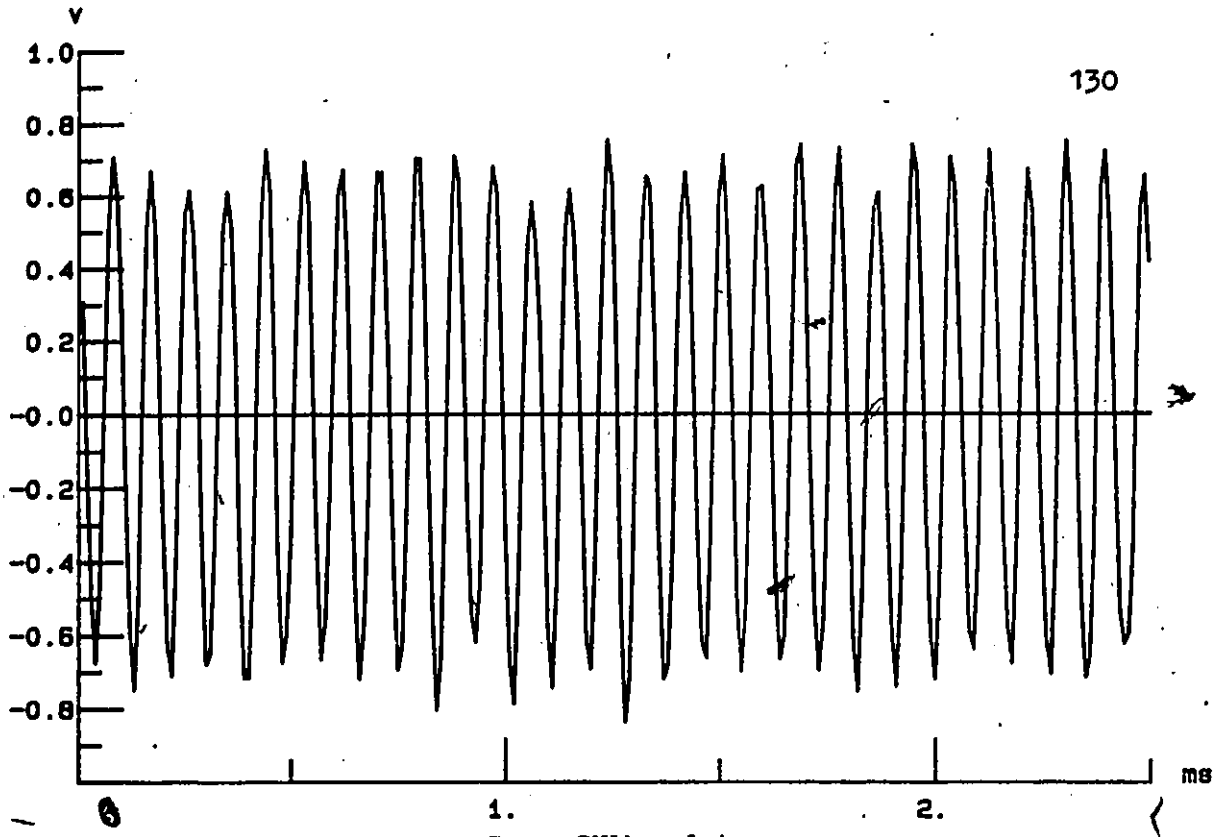

Fig. 6.4 Strong CW interfering source.

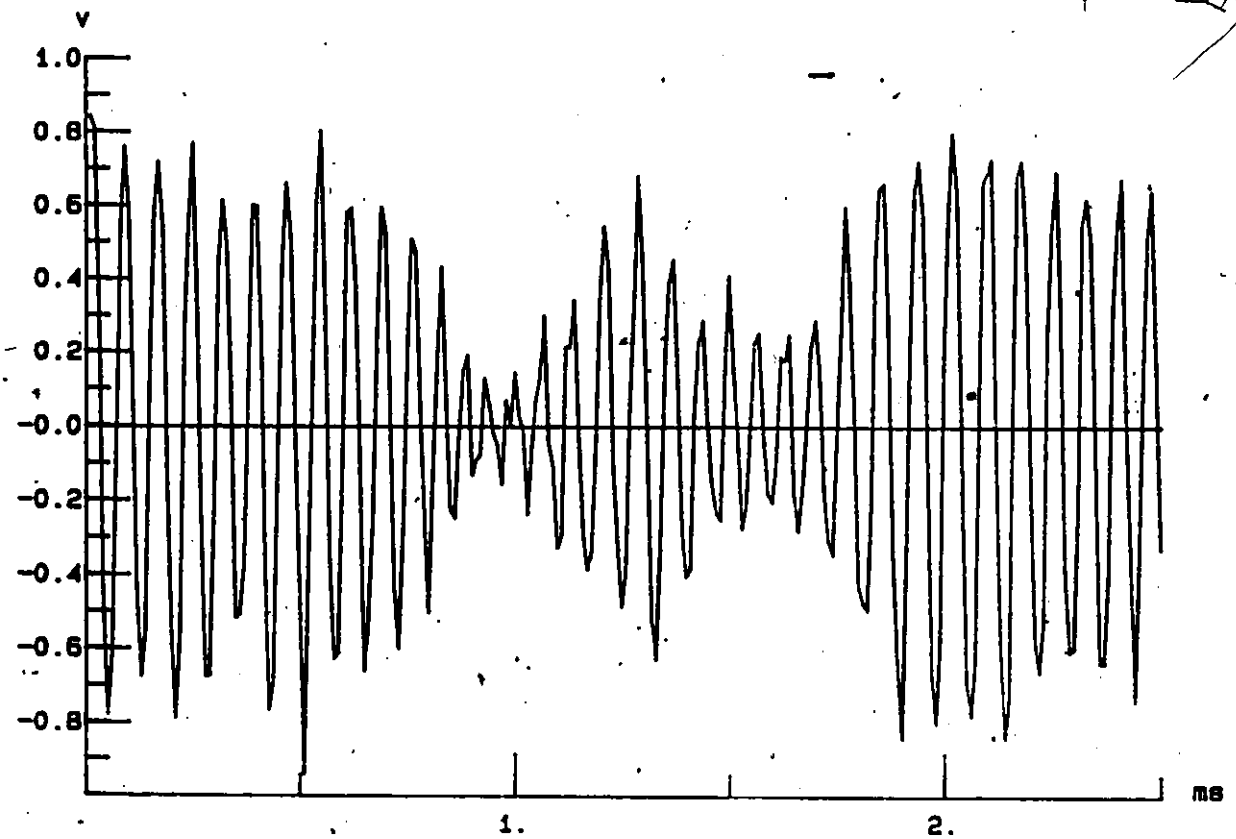

Fig. 6.5 Voice interference.

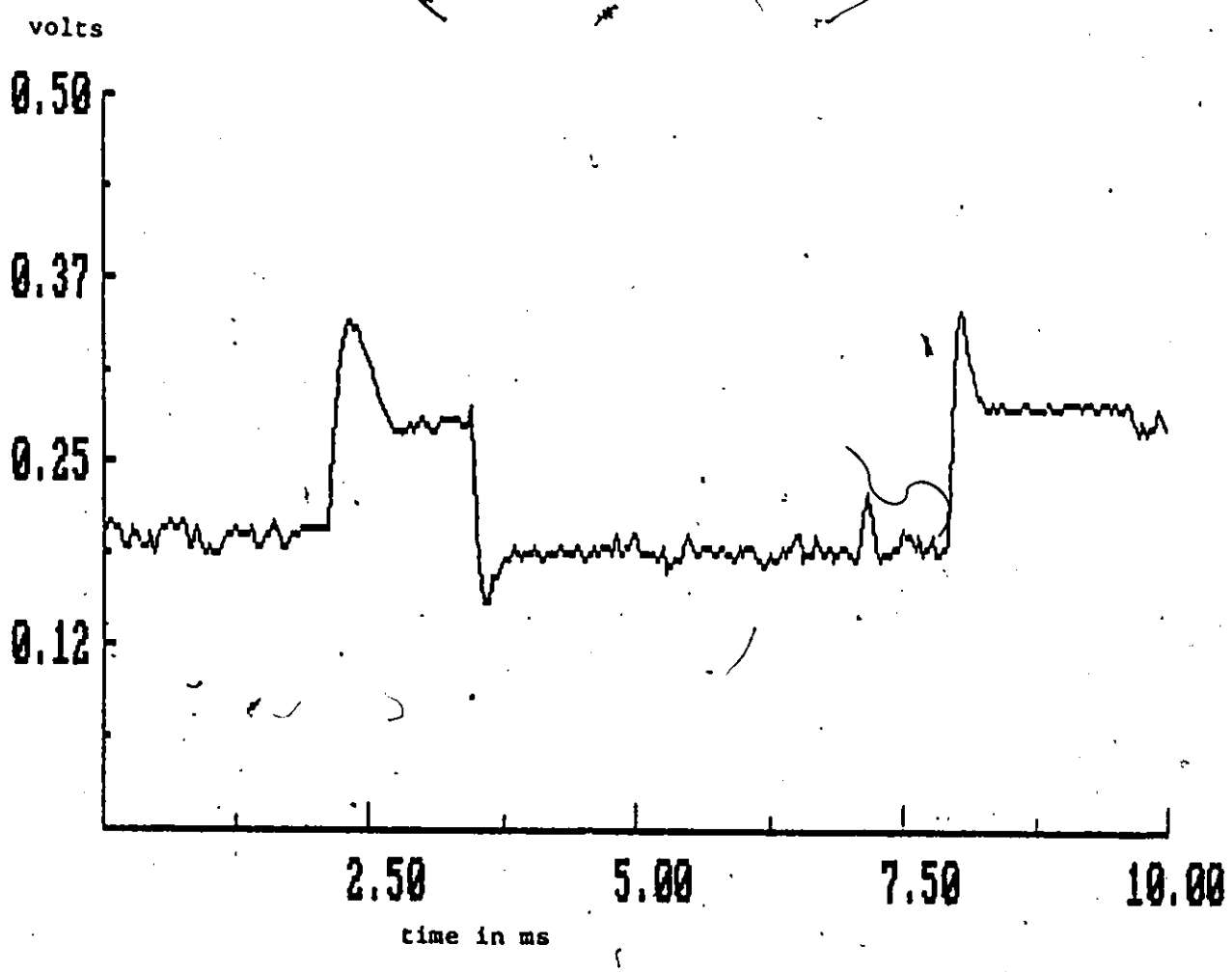

Fig. 6.6 Envelope detected SARSAT signal showing a 1.5 ms pulse followed by the leading edge of a 7 ms duration pulse.

leading edge of yet another pulse. These pulses were observed over a period of a few seconds. Many other pulse disturbances were observed in additions to these.

The CW, NB and WB interference will be discussed throughoutly in the next sections.

6.3.2 Continuous Wave Interference

Unmodulated carrier or continuous wave interference presents three problems to the SARSAT type of system. First, it produces clutter that appears on the frequency plot which increases the complexity of the signal processing strategy. Second, is the problem of dynamic range and thresholding when AGC or limiting is employed. Third, is the problem of fast Fourier transform dynamic range when a strong CW signal appears with weaker signals and background noise.

Normally the effect of increased clutter on the frequency plot is not severe since the signal occupies a very narrow band of frequencies. However the other two problems are far more serious and are examined in detail next.

A. Automatic Gain Control and Limiting

AGC and limiting produce essentially the same effect on the signal, however the implementations are slightly different. Thus, only the case of AGC will be considered.

Usually, AGC is applied to the analog amplifier stages of the receiver in the form of amplitude control of the time signal. The gain of any AGC amplifier can be written as

$$G = \frac{P_o}{P_I} \tag{6.4}$$

where

P_o = the total output power

P_I = the total input power from N sources

$$= \sum_{j=1}^{N} P_{I_j}$$

Now if we assume that the output power is constant, which is typical of most AGC systems, then the gain of the amplifier varies inversely as the input power.

Let us assume that one source, namely the i-th source of interference, is far stronger than the other sources of signal and background noise. Then the gain of the AGC amplifier is given approximately by

$$G = \frac{P_o}{P_{I_i}} \tag{6.5}$$

where P_{I_i} = input power from the i-th source.

Then, for the k-th signal, which may be an ELT, the signal out of the AGC amplifier is simply given by

$$P_{o_k} = G * P_{I_k}$$

$$= P_o * \frac{P_{I_k}}{P_{I_i}} \tag{6.6}$$

Both P_o and P_{I_k} are constant. Therefore, as the power of the i-th interfering source increases, the output power of the k-th source decreases.

In practice, what this means is that when a strong CW source is received, it captures the AGC or limiter, an effect well known in radar receiver systems. Weaker sources and background noise are greatly reduced in level and the output of the receiver is said to be 'quietened'. Naturally, this is highly undesirable since the unwanted high amplitude CW signal is easily received while the desired weaker signals disappear altogether.

A possible method of combatting this type of interference is to use a log-lin type of RF amplifier which has the characteristic gain shown in Fig. 6.7. Normally, the noise background has sufficient level to cause the amplifier to operate at point A, which is just above the logarithmic knee. When strong CW interference causes the output of the AGC amplifier to quieten, the operating point runs down the log amplifier curve which greatly reduces the change in dynamic range. Thus the background noise and weaker signals are reduced by the logarithm of the strong signal which substantially improves the detection properties of the weak signals.

B. Fast Fourier Transform Dynamic Range

A ~~second~~ problem due to thresholding can arise with the calculation of the FFT, as illustrated in Figs. 6.8, 6.9, 6.10 and 6.11 for one second interval of 13 block averaged 8K FFT spectral estimates. Here we see that the signal spectrum for COSPAS satellite C1, orbit 860 has been plotted at 9, 10, 11 and 12 minutes into the pass, respectively. At 9 min, the spectrum appears reasonably normal with a flat background and several prominent signal peaks. At 10 min, a very strong CW source is received which reduces the background level by some 30 dB. The fact that the signal is CW is demonstrated by the fact that the sidelobes of the FFT are clearly visible. At 11 min the signal exhibits modulation sidebands which are further developed by the 12 min mark where the background has again dropped below the 40 dB down level.

One solution to this problem is to filter the data using a notch filter to remove the CW source. Unfortunately the FFT would then require recalculation with the filtered data. If the spectral plot has sufficient dynamic range, then a second solution is to simply remove the CW data set from the output spectral plot. In the case documented here, at least 50 dB of dynamic range would be required and in other cases it could easily be more.

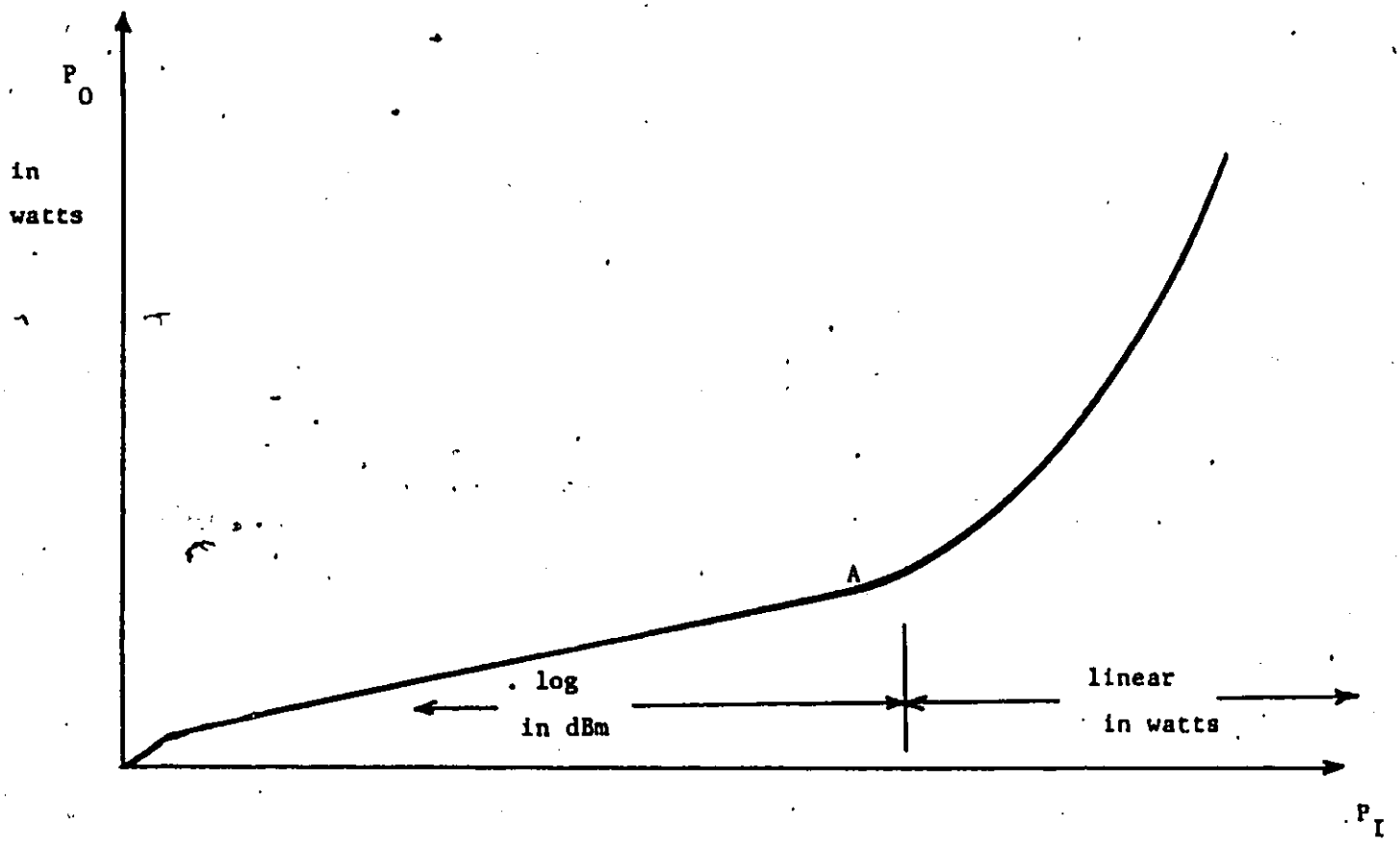

Fig. 6.7 Input-output relation for a log-lin amplifier.

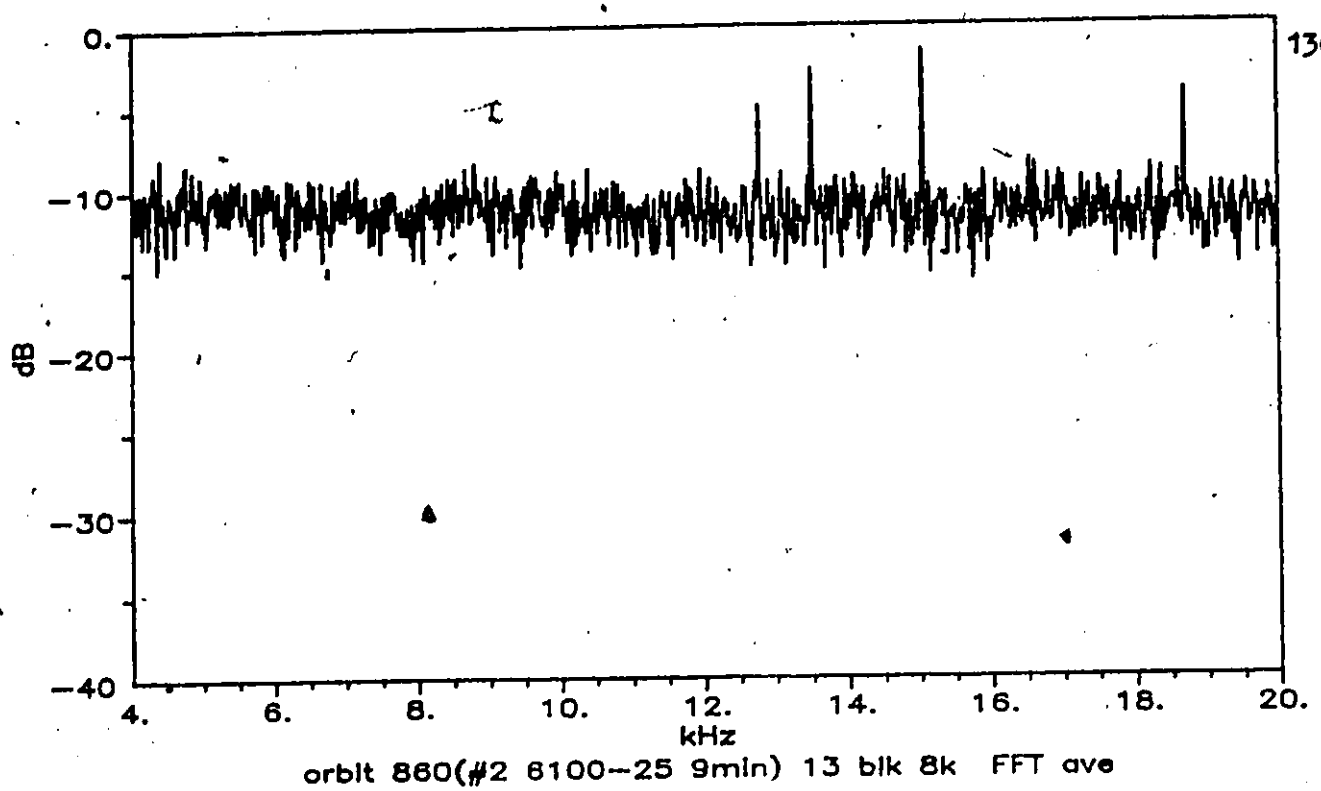

Fig. 6.8 Spectral plot for SARSAT signal with no interfering signals.

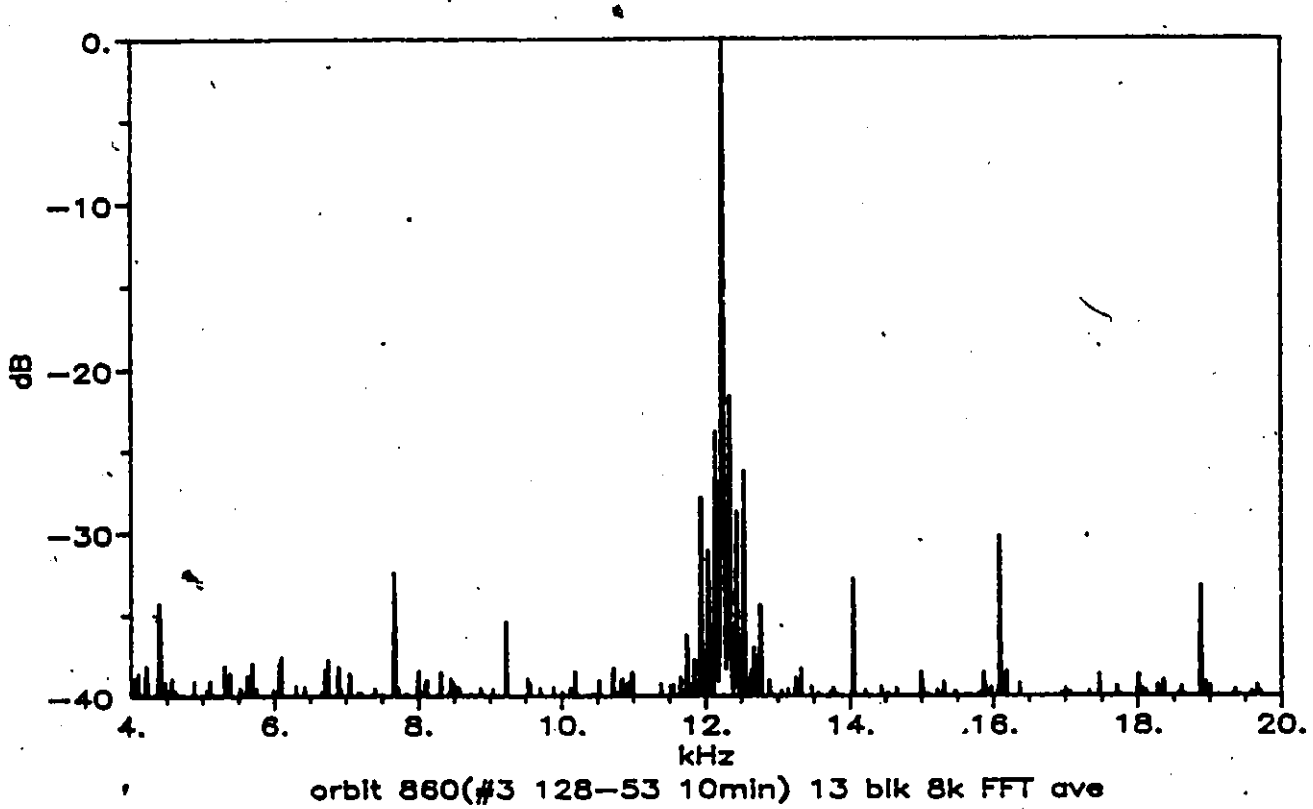

Fig. 6.9 Spectral plot for SARSAT signal with a strong CW interfering signal. Note the FFT sidelobes around the main carrier peak.

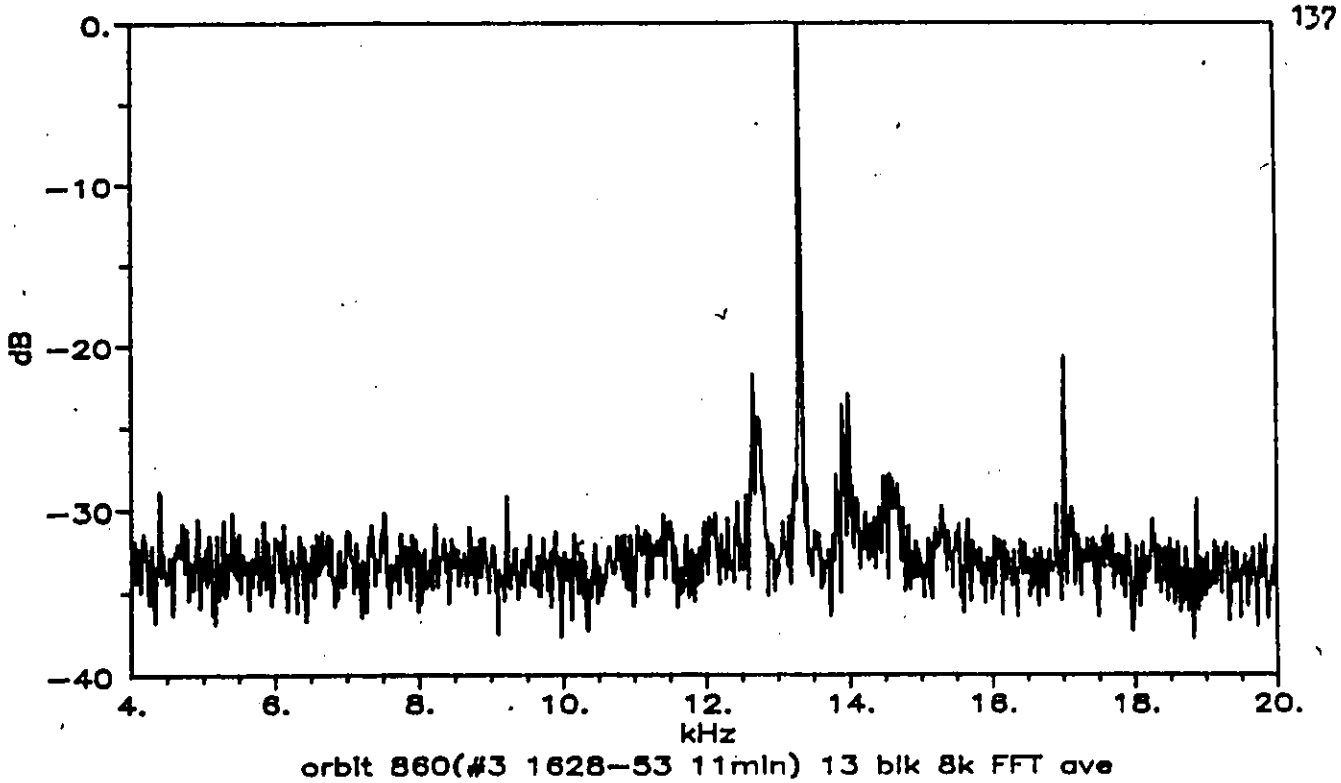

Fig. 6.10 Spectral plot for SARSAT signal with low value of modulation factor on the interfering signal.

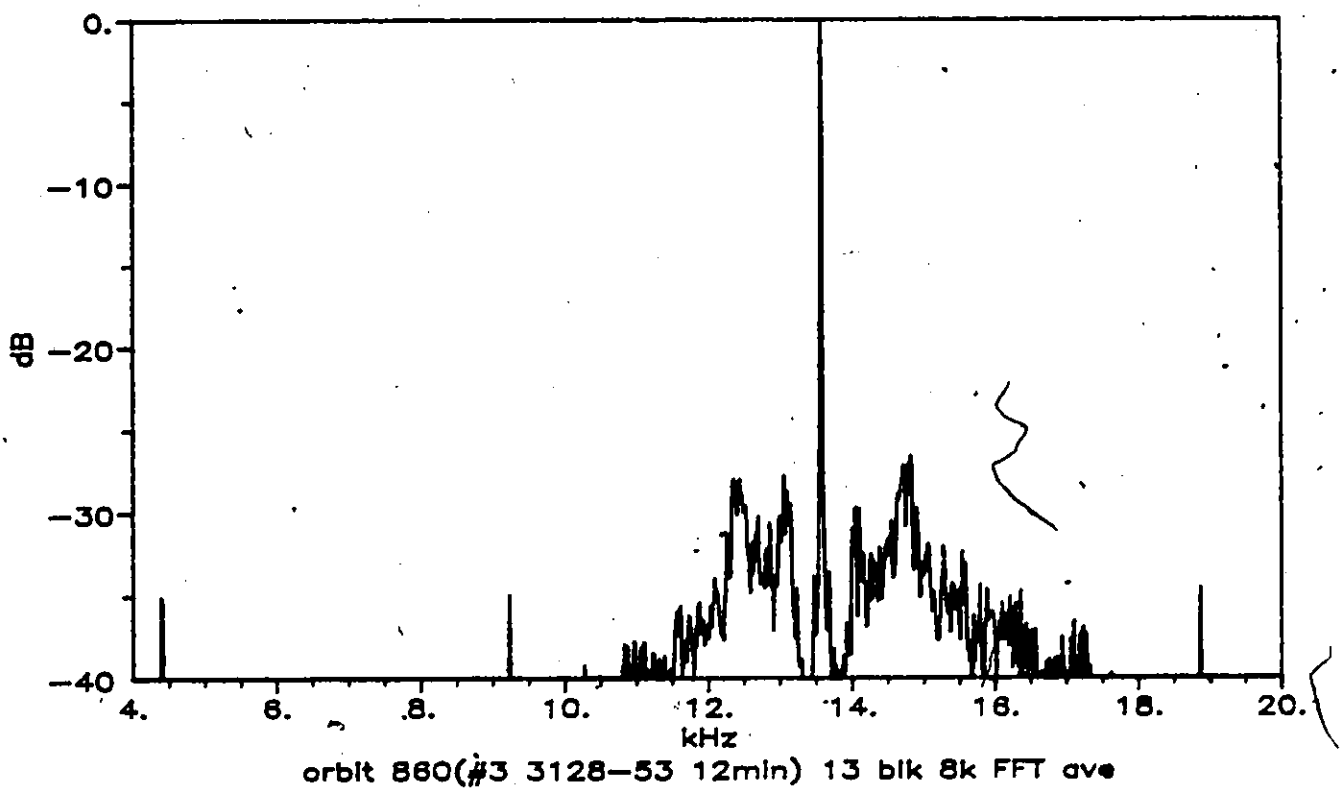

Fig. 6.11 Spectral plot for SARSAT signal with increased value of modulation factor on the interfering signal.

6.3.3 Narrowband Interference

First, we consider the use of dot plots. Figures 6.12 and 6.13 are dot plots of satellite passes prepared by the Department of National Defense of Canada. The dot plot is produced by setting a threshold for each average spectrum such as that produced in Fig. 6.8. If the N components of the average spectrum are designated by $S_{AVE}(f_k)$, for k = 1 to N, where f_k is the k-th frequency, then for some threshold level (TH) we adopt the following scheme

$$\begin{aligned} S_{AVE}(f_k) &> TH, \quad \text{plot a dot} \\ S_{AVE}(f_k) &\leq TH, \quad \text{leave a blank} \end{aligned} \tag{6.7}$$

As the pass proceeds, the dots for each spectral plot are plotted in consecutive order producing a time-frequency plot. All plots presented here range in frequency from 0 to 25 KHz and the maximum pass time is 1100 s.

Narrowband interference refers to interference having a bandwidth which is considerably less than the 25 KHz bandwidth being processed for the 121.5 MHz signal band. Typical sources of interference are shown in the dot plots of Fig. 6.12. This kind of interference can be detected by averaging across the frequency band and noting the increase in level using a threshold.

Narrowband interference can be combatted by choosing a processing strategy which has little or no effect on the ELT signal but significant effect on the interference. The suitable candidate for handling this problem is the order statistic based post-processor.

6.3.4 Wideband Interference

Wideband interference can be considered to be interference which covers most of the 25 KHz bandwidth of the ELT band, such as the dot plot examples of Fig. 6.13. In this case

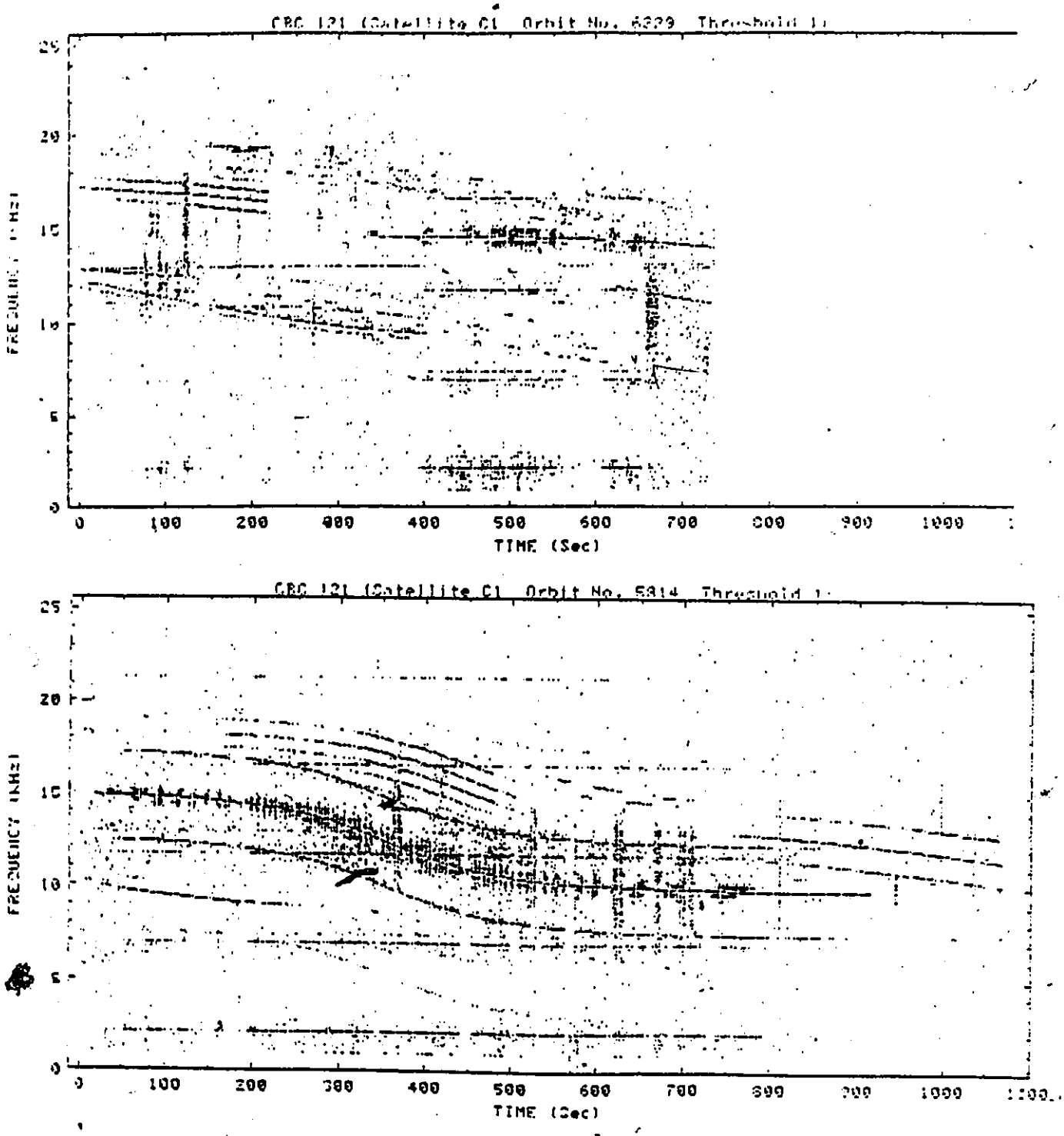

Fig. 6.12 Dot plots of two COSPAS satellite passes illustrating narrowband interference.

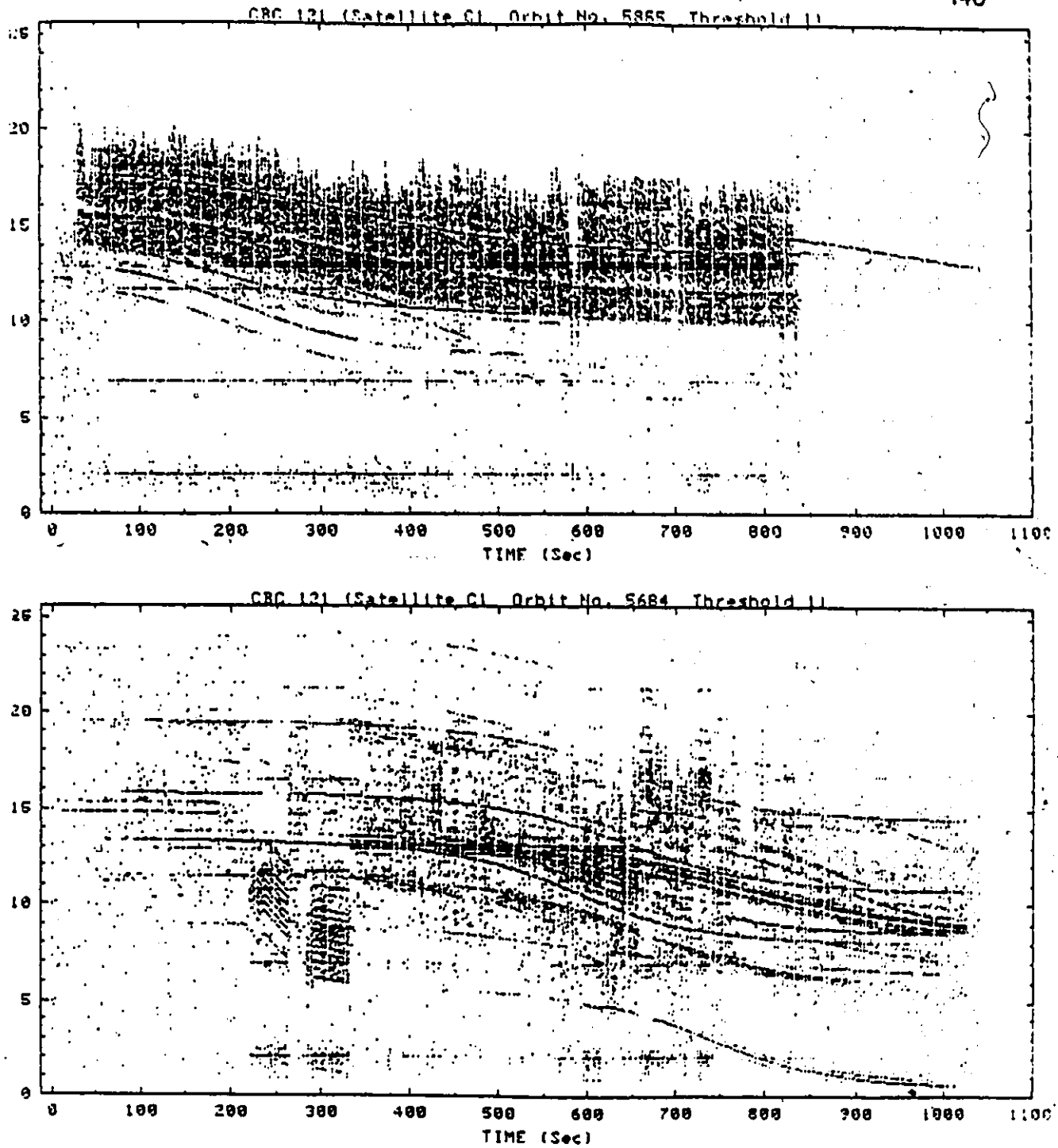

Fig. 6.13 Dot plots of two COSPAS satellite passes illustrating wideband interference.

frequency band averaging and thresholding may or may not be of use in detecting the interference since the level of most of the band may be increased by approximately the same amount. However the overall power of the output signal is increased. This can then be measured by either envelope detecting the signal itself or monitoring the AGC control level.

Wideband interference can be produced by several means, including the effects of a large number of low power impulsive sources, the shock excitation produced by a small number of high power impulses or by the wideband modulation of a carrier.

The effect of a small number of high power impulses can be reduced by employing a limiter in the RF amplifier stages of the receiver at the satellite. Essentially, it is necessary to use wide bandwidths prior to the limiter in order that the filter ringing response is not excited. Then, the limiter in effect clips off the high level impulse so that it is no longer able to shock excite the narrowband receiver. Finally, the signal is fed to a narrowband linear-phase characteristic filter (possibly a surface acoustic wave device filter) in order to establish the desired bandwidth properties. Note that very little can be done at the Earth station to solve the problem once the ringing response at the satellite has occurred.

We have, so far, identified the main sources of interference for ELT signals and we have also provided alternative solutions which may reduce their effects on signal processing. We proceed our discussion on the spectral analysis of real satellite pass data.

6.4 SPECTRAL ANALYSIS OF REAL SATELLITE PASS DATA

Signal processing of simulated and testbed ELT signals have been studied extensively in the previous chapters. These signals do not experience Doppler frequency shift effect. In this section, the analysis is focussed on spectrum estimation of real ELT signals from satellite passes. The signals are relayed from the COSPAS system satellite C1 on orbit 860 and 861 respectively.

Due to the relative motion of the spacecraft with respect to the transmitter, the ELT signals suffer Doppler frequency shift. As the satellite approaches the emergency site, Doppler shift becomes less until the minimum distance is reached. This is the shortest distance between the satellite and the ELT source. At this instance, Doppler frequency shift is zero. Beyond this point, a negative Doppler shift occurs and a plot of frequency versus time produces a S-shaped curve (see Fig. 1.2). This curve leads to the a measure of ELT position with respect to the known position of the satellite. The magnitude of the frequency shift depends on the flight path of the satellite pass. Normally, the range is approximately ±3 KHz. As expected, the satellite pass data contain information of multiple ELT signals as well as miscellaneous sources of interference. Our goal is to reduce the level of interference and hence extract spectral information from the data in order to provide reliable frequency estimates of the number of ELT signals involved during each satellite passes.

The analog tapes supplied by the Communications Research Centre in Ottawa were digitized at a sampling rate of 100 KHz. In the analysis the data being processed are the fifth minute of the pass. One second data length is assumed for each processing procedure. This is a collection of 25 records of 4096 samples. The processing methods employed are (1) periodogram which includes spectral averaging, ranking and sub-group spectral averaging (with spectrum leveller) from ranking and (2) maximum entropy method with the combinations outlined in (1).

6.4.1 Spectrum Estimations Of Signals Received From COSPAS System Satellite C1 Orbit 860

The periodograms of 25 blocks of 4K point satellite pass data, received from COSPAS system satellite C1 in orbit 860, are plotted in Fig. 6.14(a). The presentation follows the same format as described in the processing of ELT testbed signals (see Section 4.2.3).

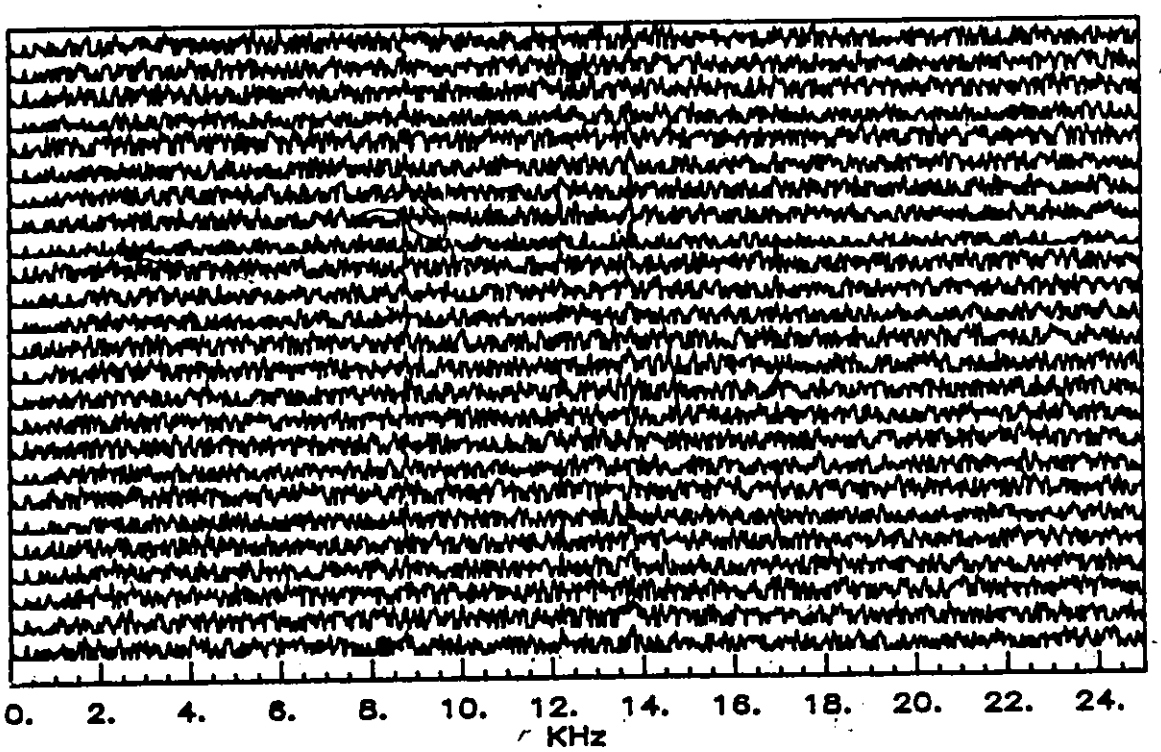

(a)

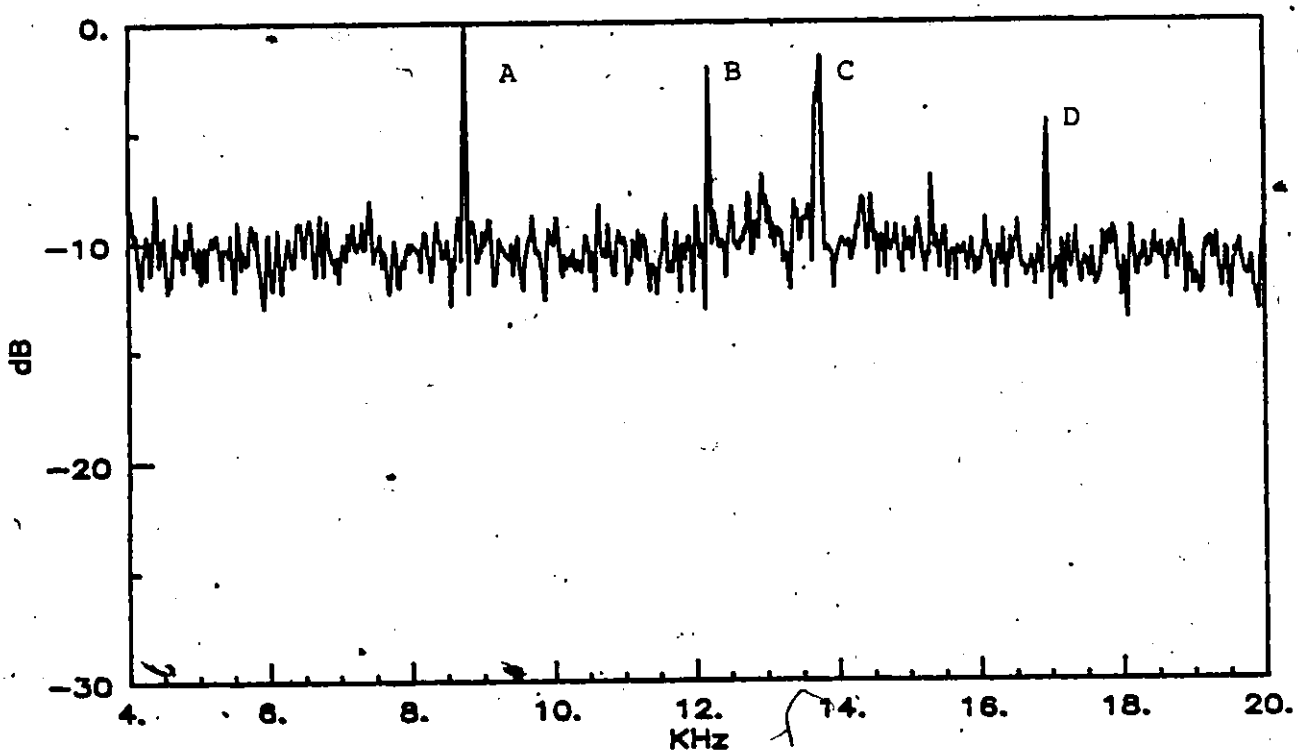

(b)

Fig. 6.14 (a) A set of 25 periodograms of the data received from COSPAS system satellite C1 orb[illegible]. Note that the backgroud noise and interference level is quite s[illegible]

(b) Averaged peri[illegible]dicates four possible carrier components for this data set.

Direct frequency measurement using the FFT is not easy as shown by the result. We note that both interference and background noise are quite significant. They dominate most of the power spectra. Large values of variance and frequency bias make frequency estimation a difficult task.

The averaging periodogram for this set of data is given in Fig. 6.14(b). The four peaks, labelled A (8.75 KHz), B (12.25 KHz), C (13.75 KHz) and D (16.8 KHz), are quite prominent in terms of signal strength. These peaks could be contributions from the frequency components of ELT signals or perhaps from sources of strong interference.

Both the MEM and averaged spectra at filter order 100 are illustrated in Fig. 6.15. We note that the performance of the averaged MEM is not as good as the averaged periodogram. The dynamic range, in this case, is reduced by more than 5 dB and peaks B and D are uncertain to be declared as spectral peaks.

It has been shown that the MEM processor is less affected by the signal length, as opposed to the FFT whose performance can be improved by processing a longer sequence of data [24]. MEM is a parametric spectral estimation technique, and the number of filter coefficients of the prediction error filter can be adjusted in order to improve the spectral performance of the processor. We applied filter order 500 to the data set. The spectral components of the signals (or interference) become more conspicuous on the spectral plots given in Fig. 6.16(a). From Fig. 6.16(b), we observed that peak C not only has about 2 dB improvement, it also exhibits a clear spectral characteristic of modulated signal, i.e. with carrier peak and two sidebands. The lower sideband is between 12.75 to 13.25 KHz and the upper sideband is from 14.25 to 15 KHz with the carrier peak at 13.75 KHz. The signal is possibly a Pointer ELT model.

The ranked spectra and block 16-20 averaging with spectrum leveller for both FFT and MEM are evaluated and the results are depicted in Figs. 6.17 and 6.18 respectively. Since

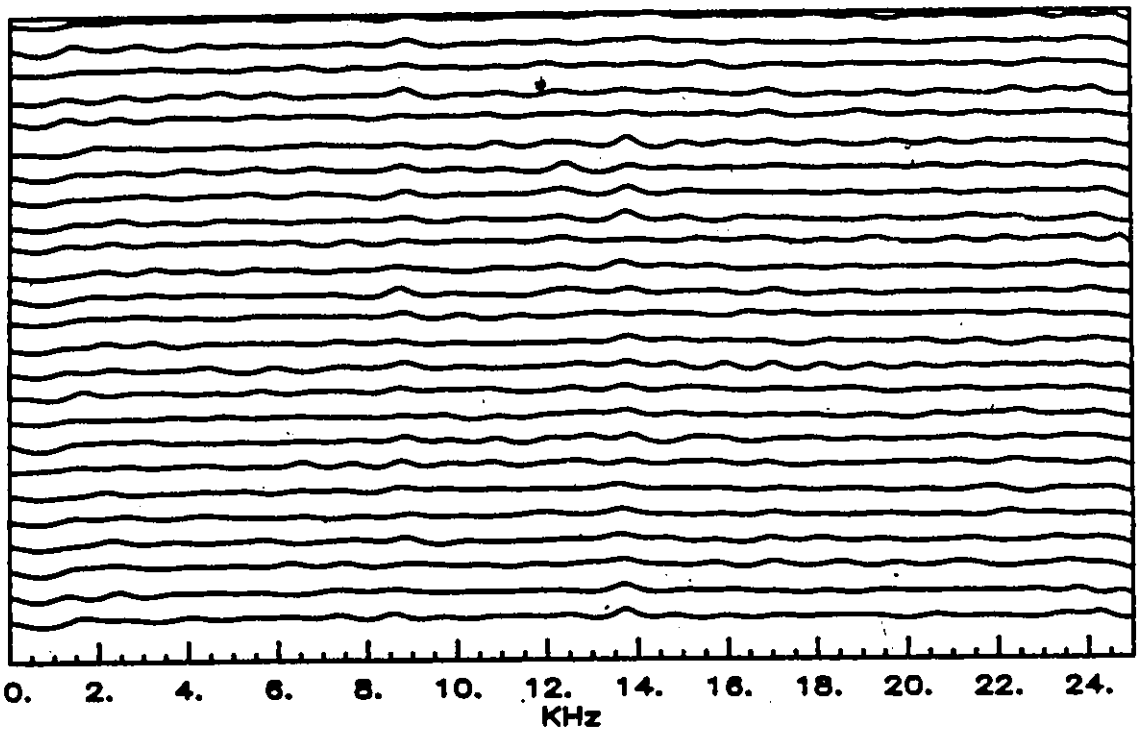

(a)

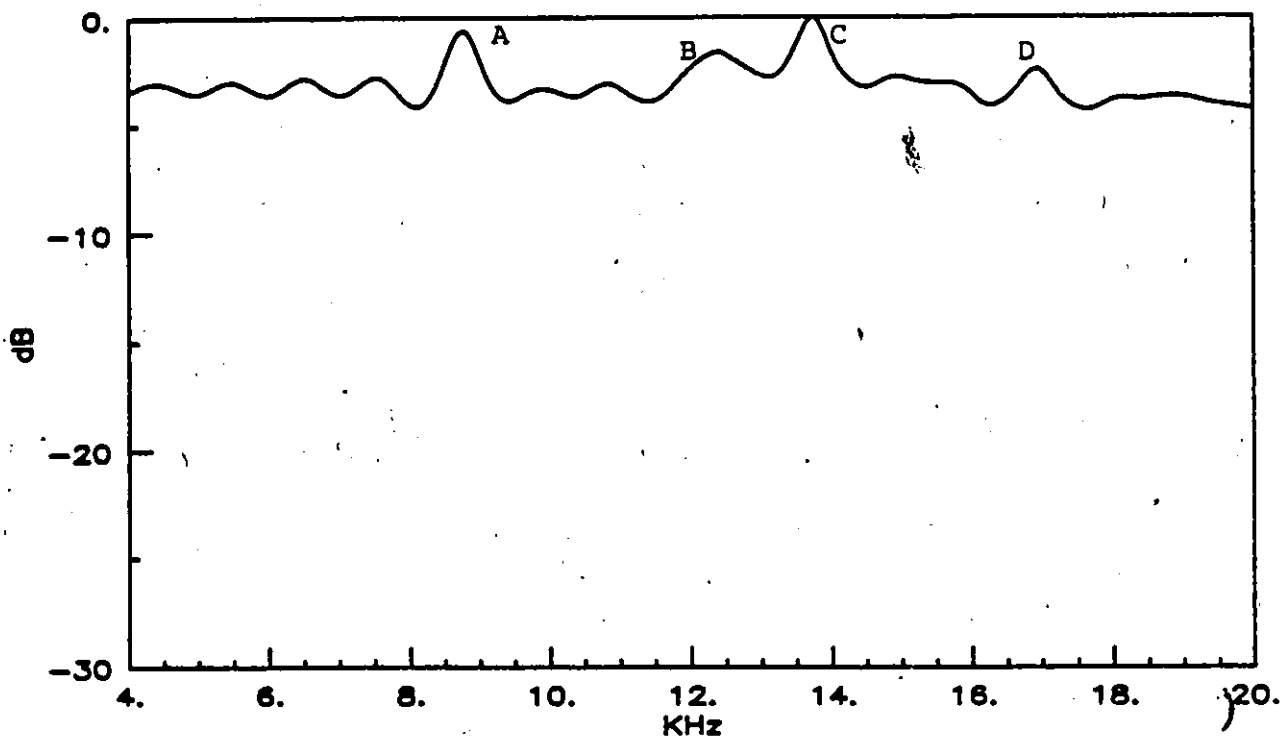

(b)

Fig. 6.15 (a) A set of 25 MEM estimates (order 100) for the orbit 860 data.

(b) Averaged MEM spectrum indicates a raw estimate of the four signal peaks.

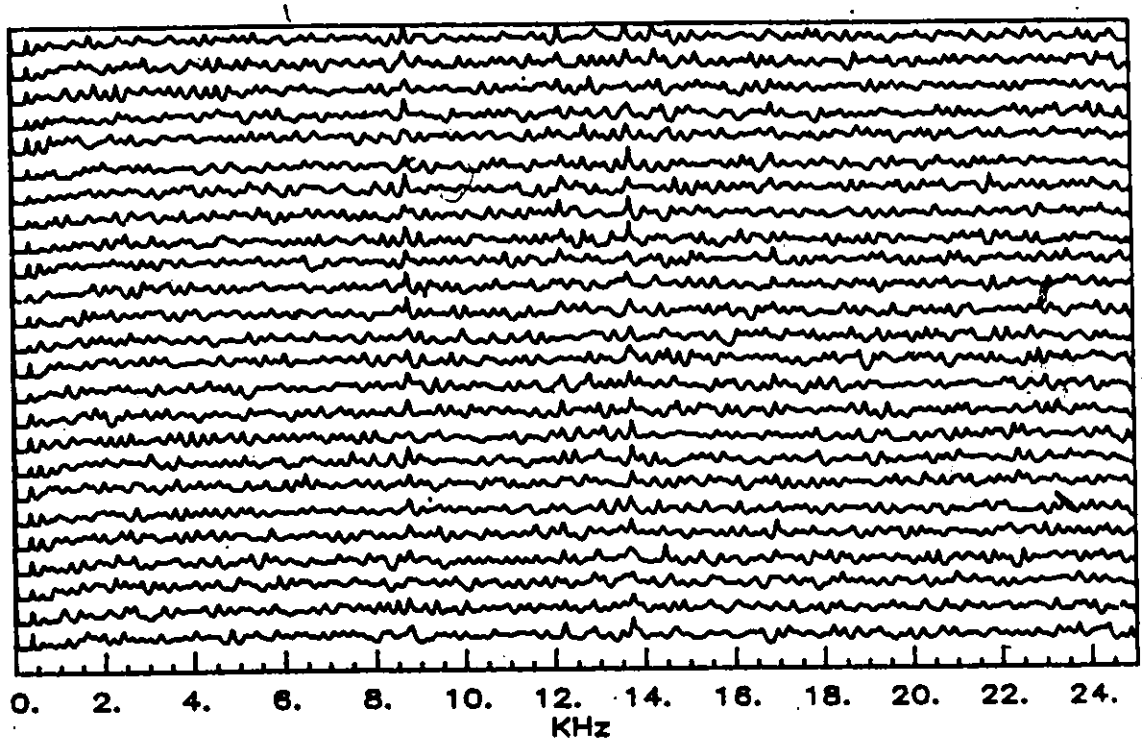

(a)

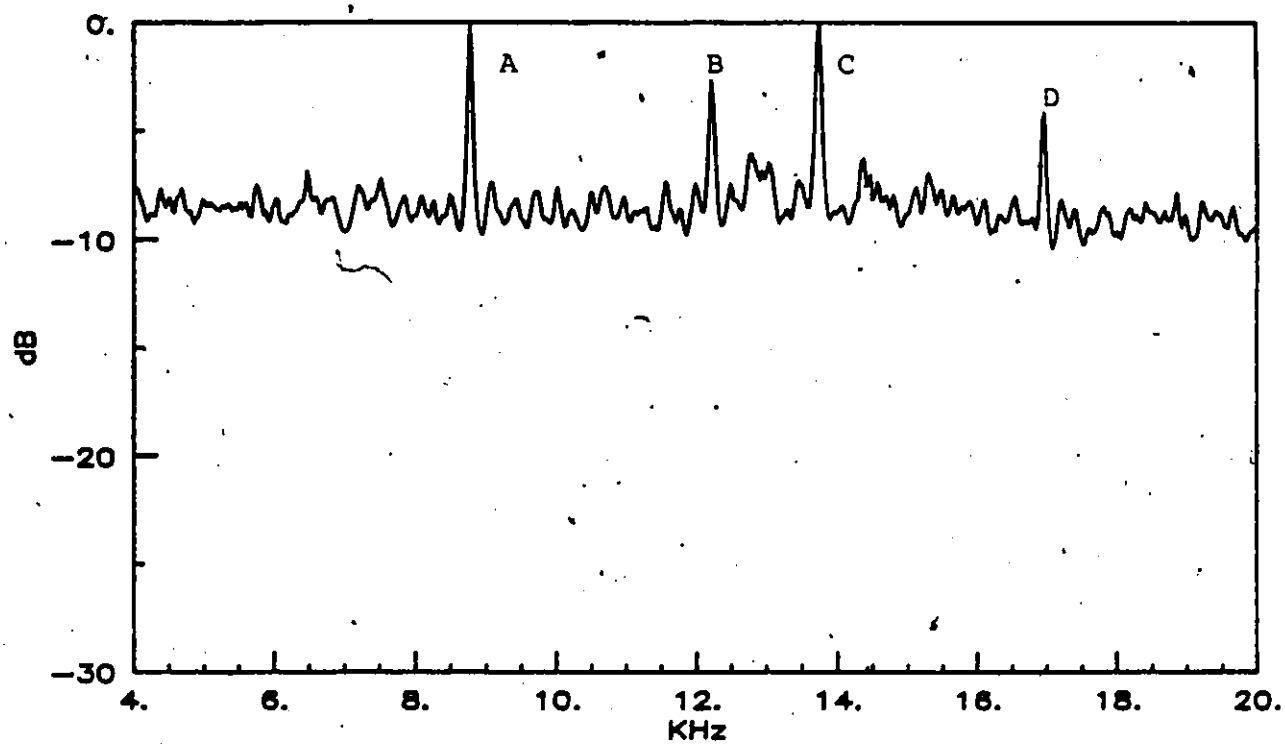

(b)

Fig. 6.16 (a) A set of 25 MEM estimates at order 500 for the orbit 860 data.

(b) Averaged MEM spectrum. Note that there is a big improvement in the signal-to-noise ratio.

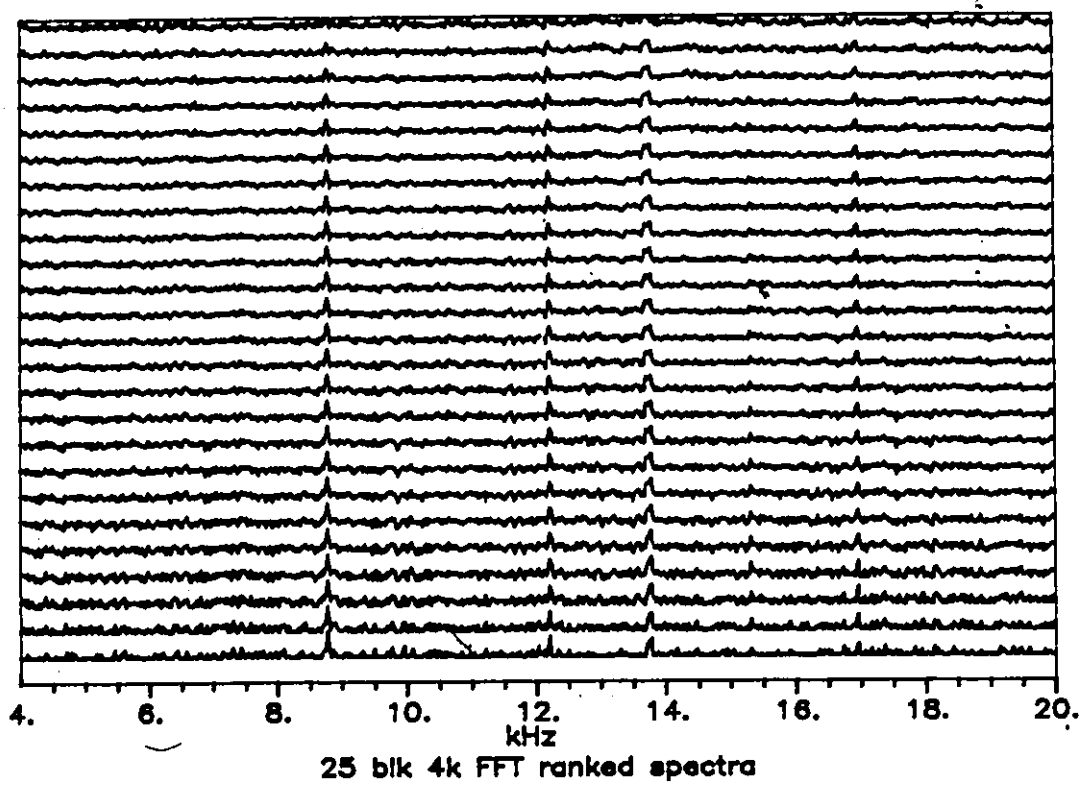

(a)

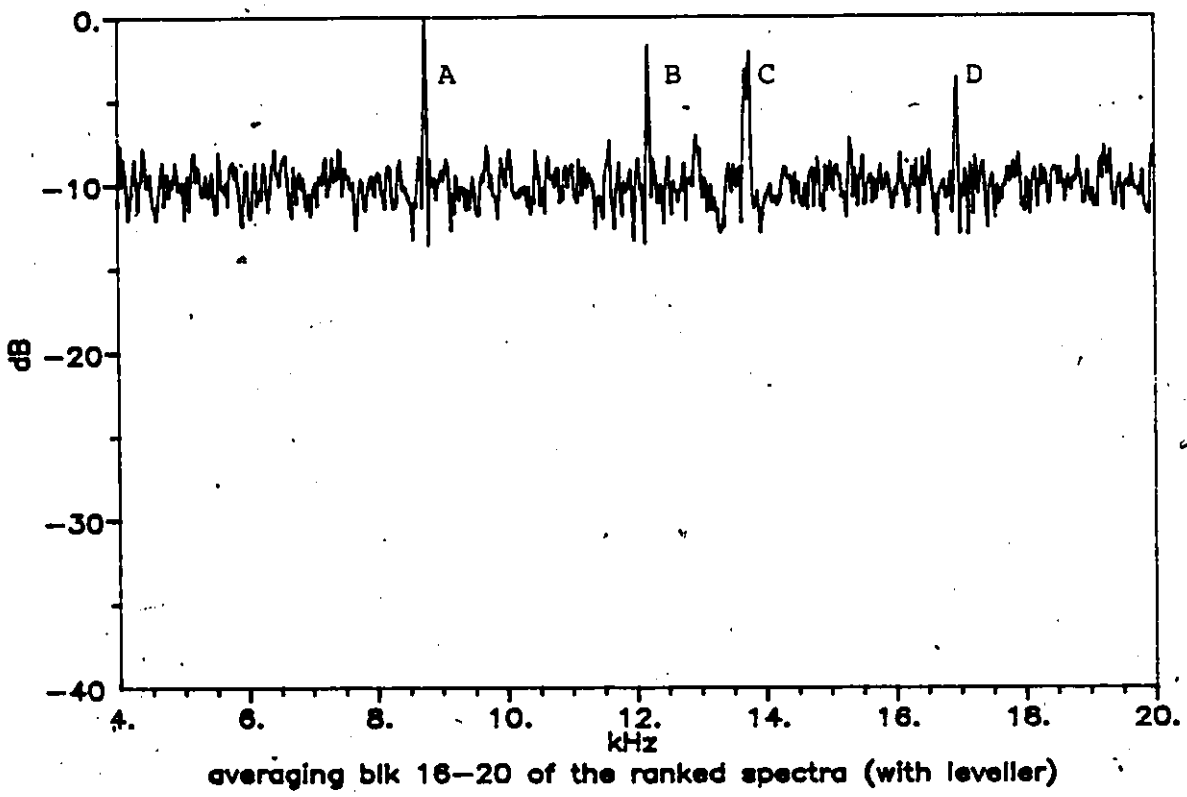

(b)

Fig. 6.17 (a) Ranked periodograms for the spectra of Fig. 6.14.

(b) Averaged ranked periodogram of the sub-group selection block 16-20 processed by the spectrum leveller.

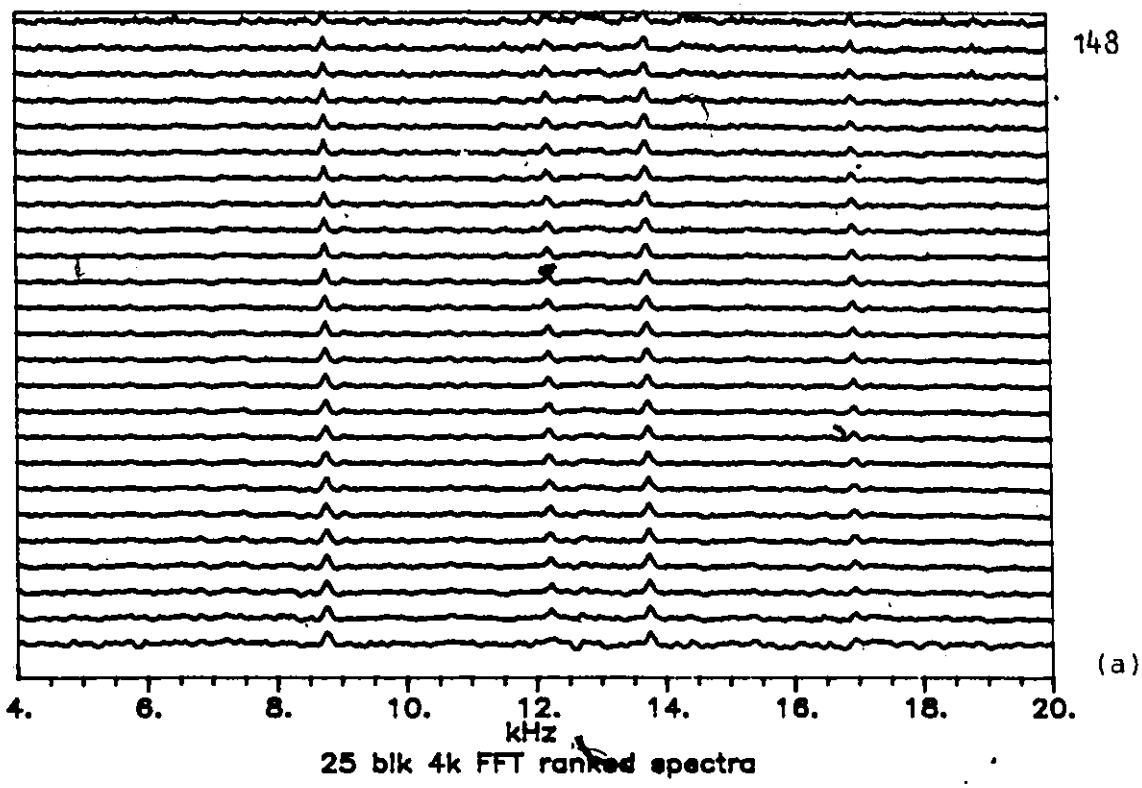

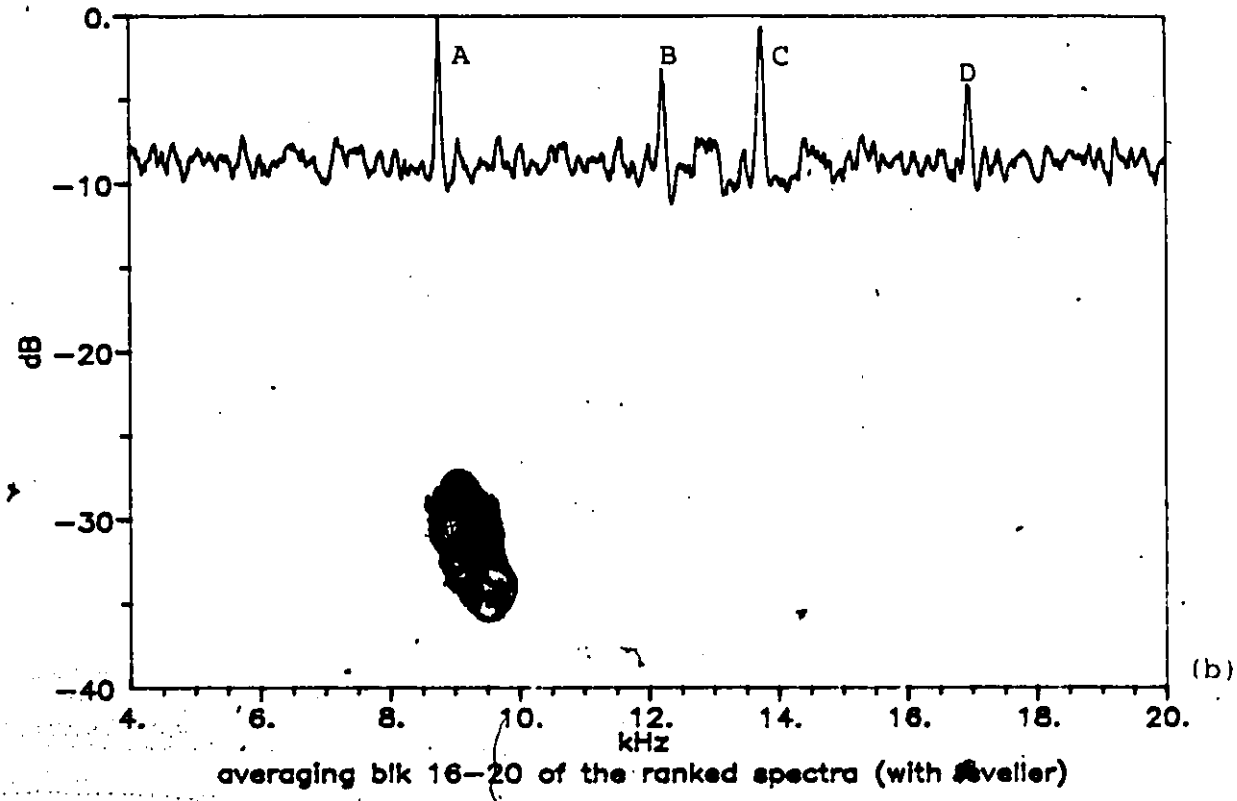

Fig. 6.18 (a) Ranked MEM estimates for the spectra of Fig. 6.16.

(b) Averaged ranked MEM spectrum of the sub-group selection block 16-20 processed by the spectrum leveller.

there is no active sidebands interference for this set of data, the order statistic method is found to provide spectral performance which is comparable to the straight averaging technique.

6.4.2 Spectrum Estimations Of Signals Received From COSPAS System Satellite C1 Orbit 861

The same procedure of signal processing is applied to the signal received from COSPAS system satellite C1 in orbit 861. The spectrum estimations measured by the periodogram and MEM (order 500) are given in Figs. 6.19(a) and 6.20(a). From both results, we detected the presence of a Narco ELT signal. The pattern of frequency drifting is clearly shown. This occurs at the 14 KHz to 17.5 KHz frequency marks. An expanded view at the vicinity is provided for both processors in Figs. 6.19(b) and 6.20(b). The spectral frequency at approximately 19 KHz is not consistent with time. Also, we received two very strong indication of carrier components at frequencies around 10.4 KHz and 12 KHz. These could be generated from sources of CW interference. Comparing the performance, the non-linear estimator provides a spectral plot with less clutter than the linear method. This enhances frequency measurement of the emergency signals at the final stage of signal processing where frequency-time plot is prepared for Doppler curve sorting.

The averaging spectra for the FFT and MEM shown in Fig. 6.21 indicate sidebands interference of the Narco ELT signal. As a result of the post-processing methods, the interference is removed and the spectra are plotted in Figs. 6.22 and 6.23. The MEM based post-processor is shown to achieve a better dynamic range for threshold detection.

Several remarks associated with the results from these two set of data are (1) a fixed threshold detection scheme is infeasible. (The background noise level for data obtained from orbit 860 is about -10 dB whereas it is -20 dB for data from orbit 861). The variation

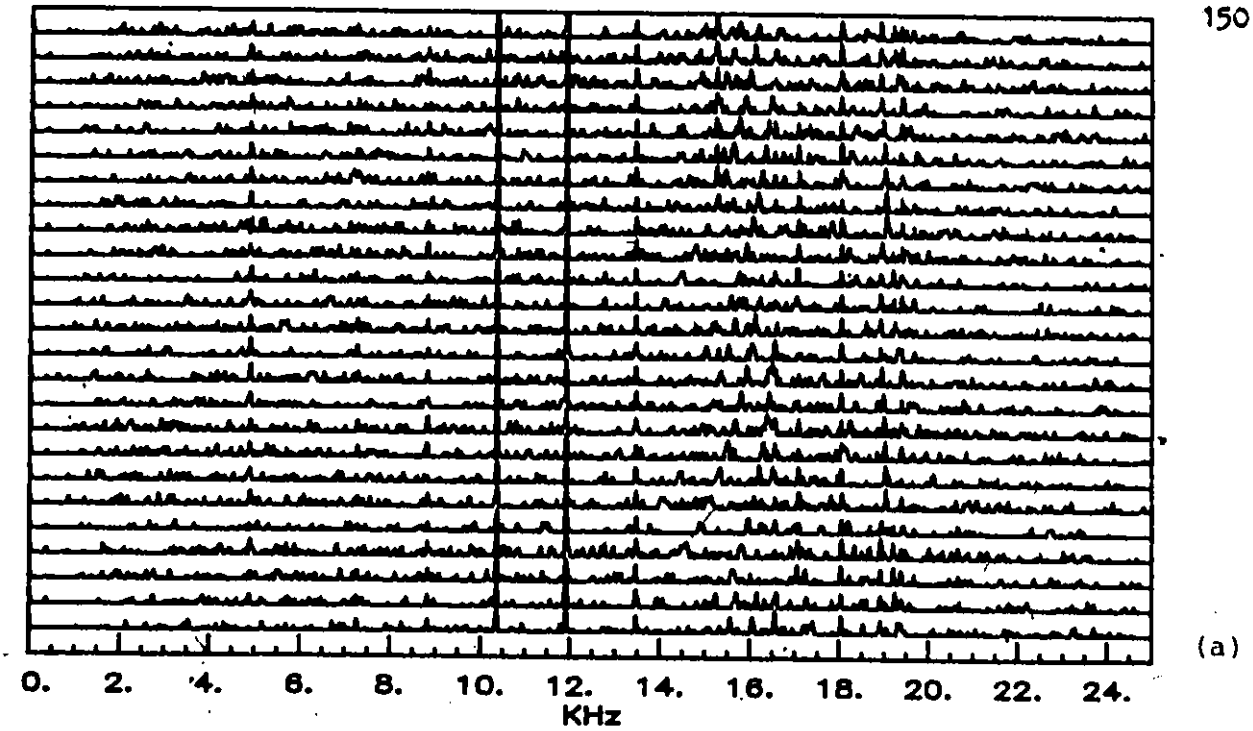

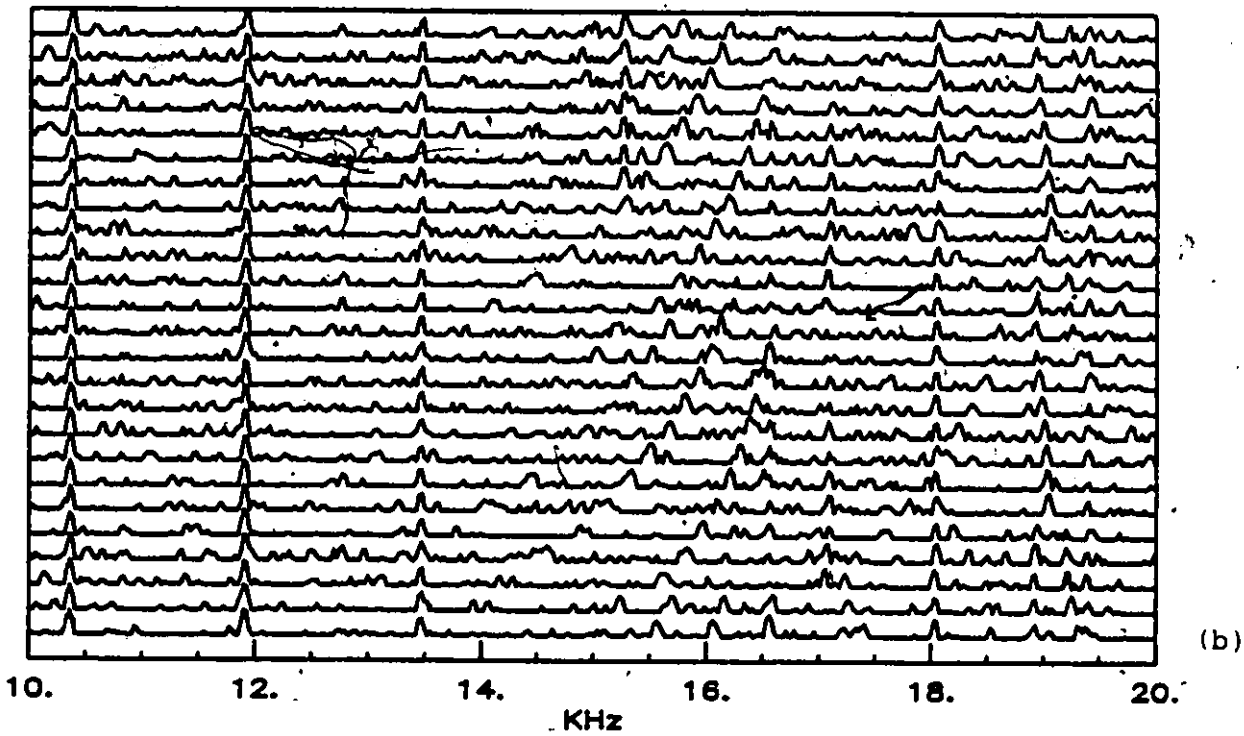

Fig. 6.19 (a) A set of 25 periodograms for the data received from COSPAS system satellite C1 orbit 861. Note that there are two strong spectral peaks at 10.4KHz and 11.95KHz which may be generated by CW interference. Also a Narco ELT signal is detected at around 17KHz.

(b) An expanded view of the periodograms.

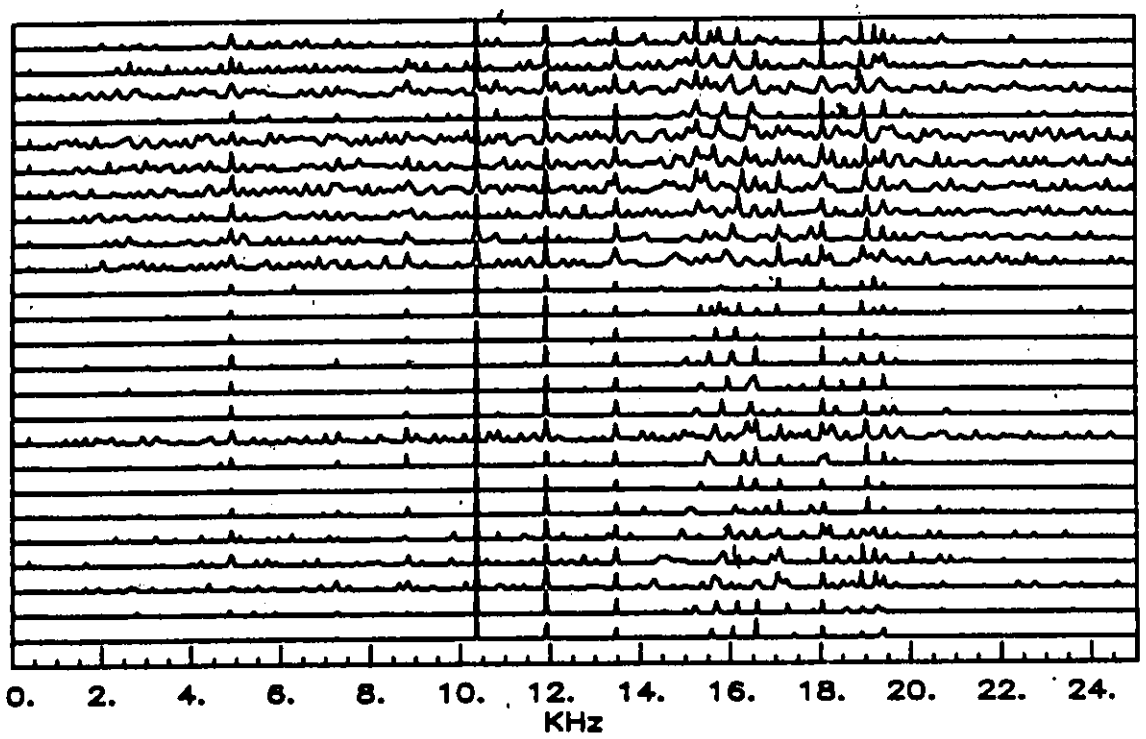

(a)

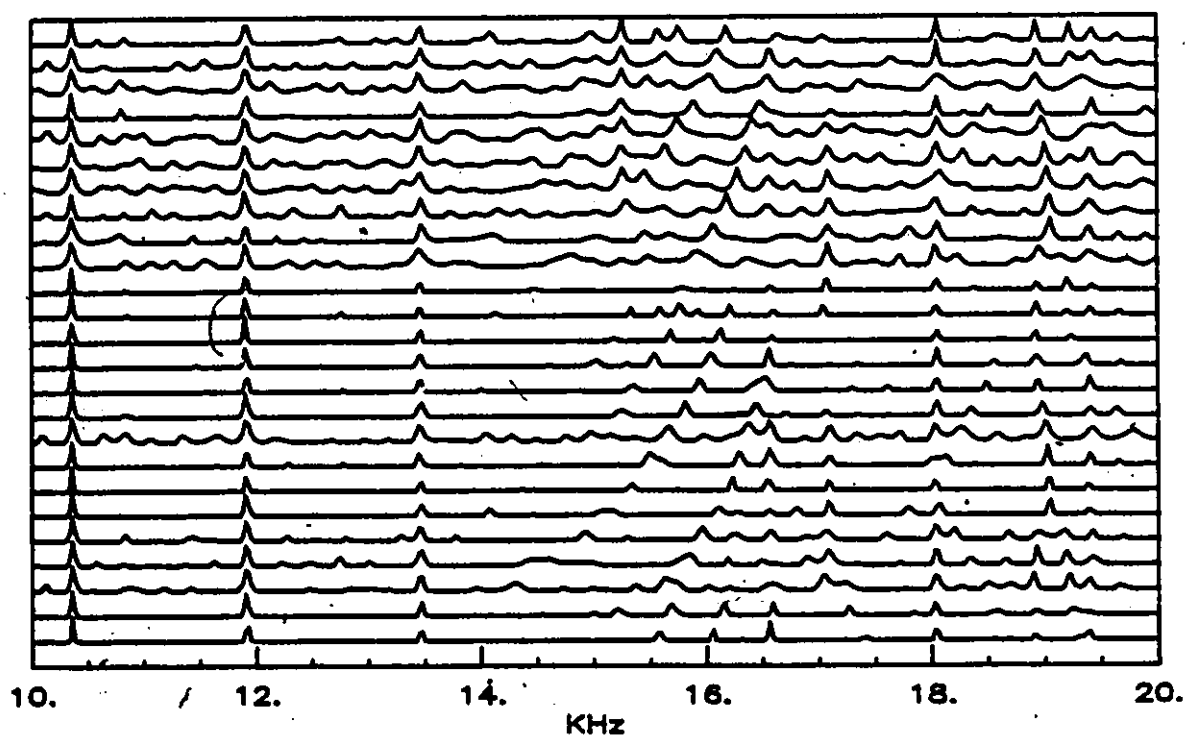

(b)

Fig. 6.20 (a) A set of 25 MEM estimates at order 500 for the data received from orbit 861. Note that the signal-to-noise ratio improvement is better than Fig. 6.19.

(b) An expanded view of the MEM estimates.

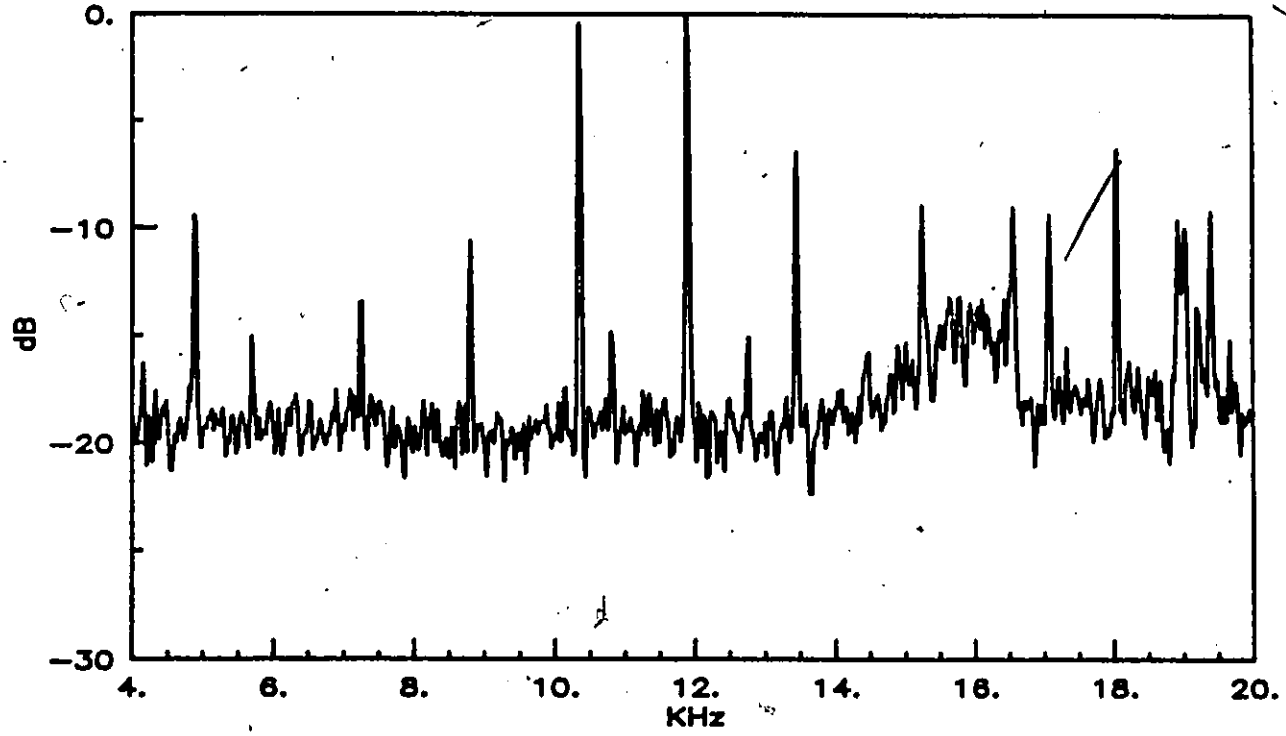

(a)

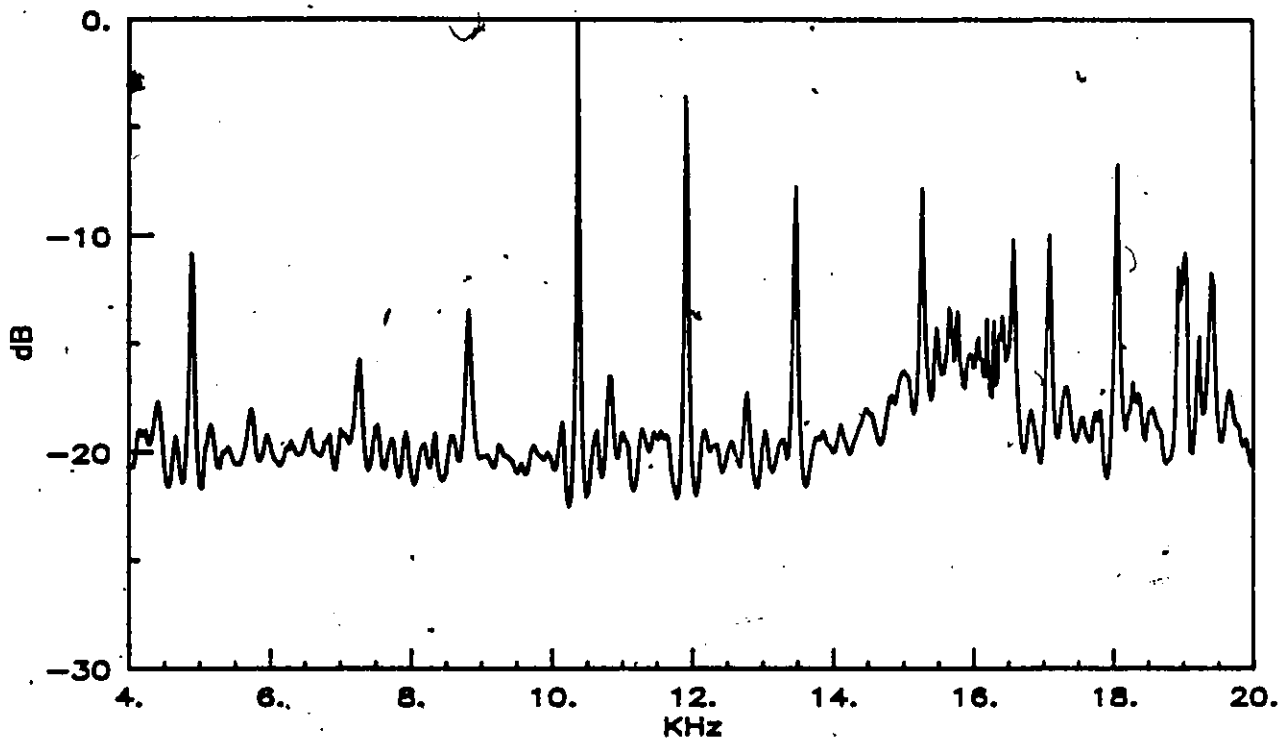

(b)

Fig. 6.21 (a) The averaged periodogram of the spectra from Fig. 6.19

(b) The averaged MEM estimates of the spectra from Fig. 6.20.

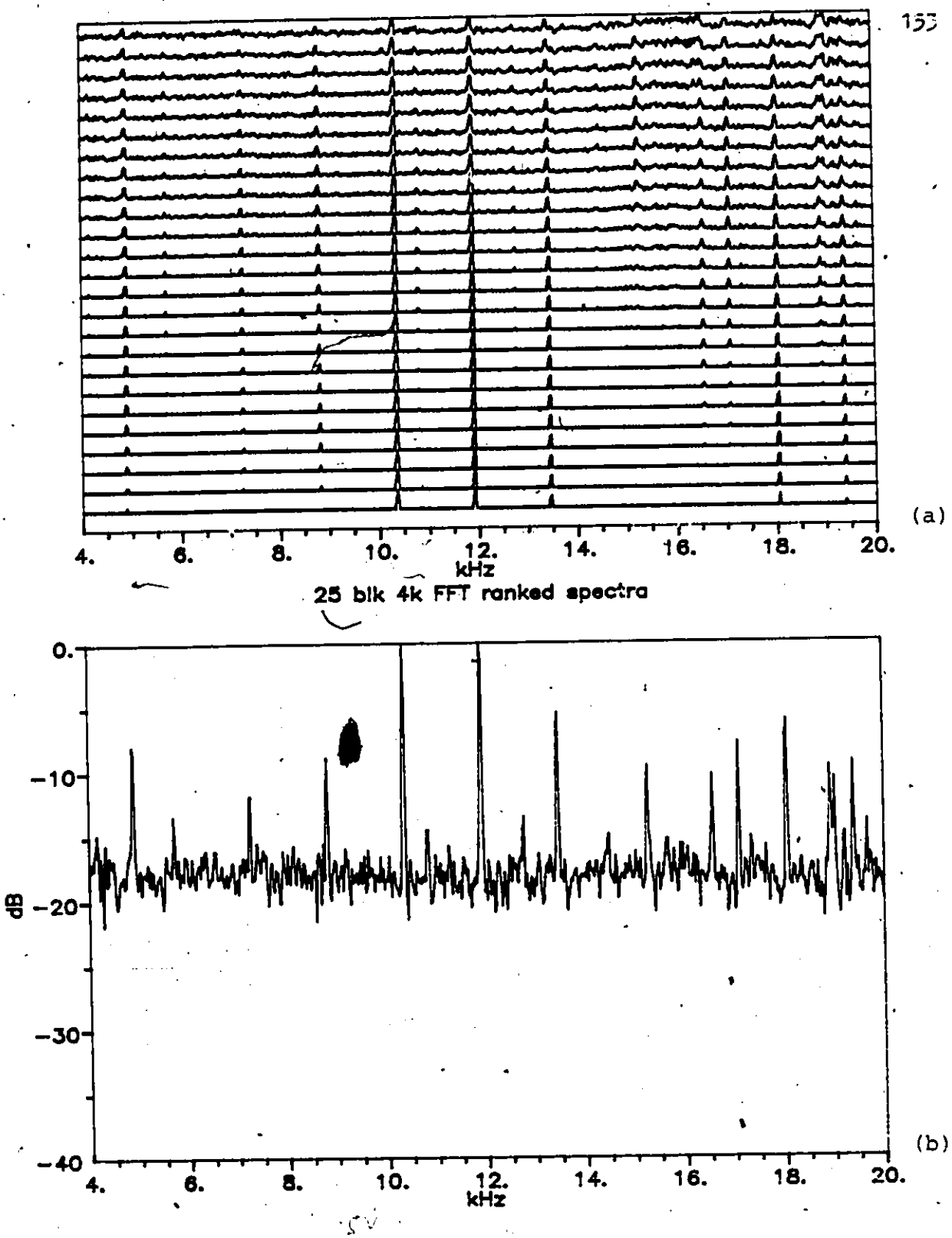

Fig. 6.22 (a) Ranked periodograms for the signal spectra of Fig. 6.19.

(b) Averaged ranked periodogram for the sub-group selection block 16-20 processed by spectrum leveller.

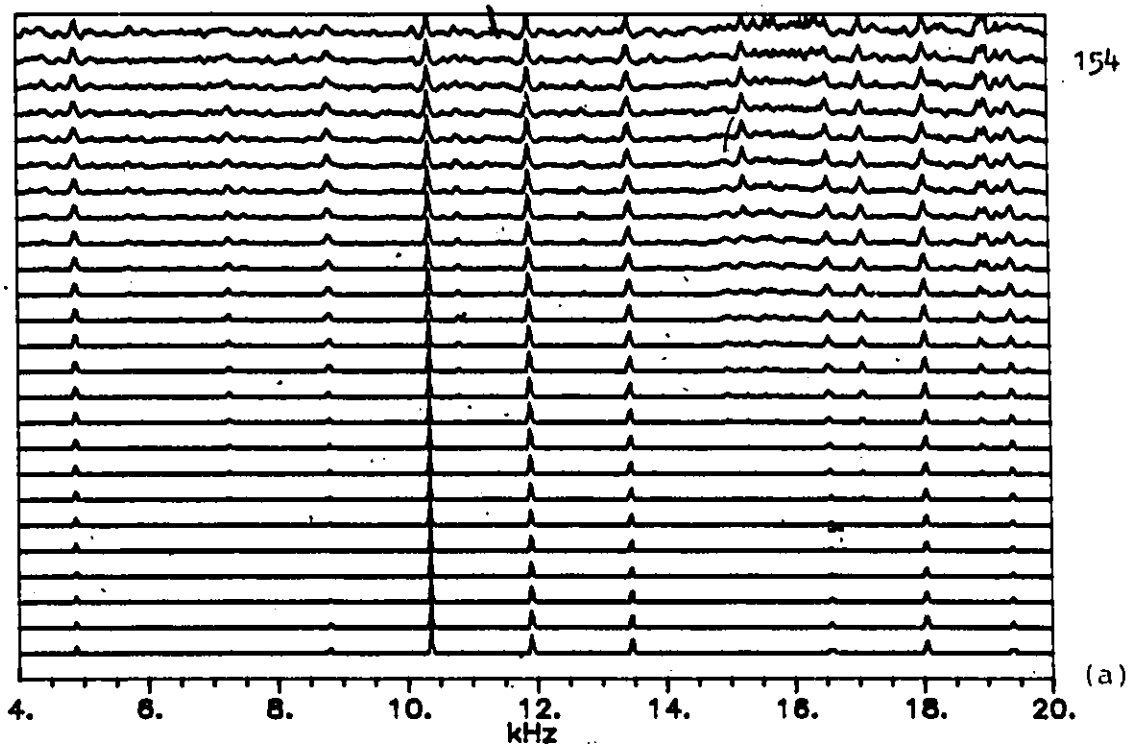

(a)

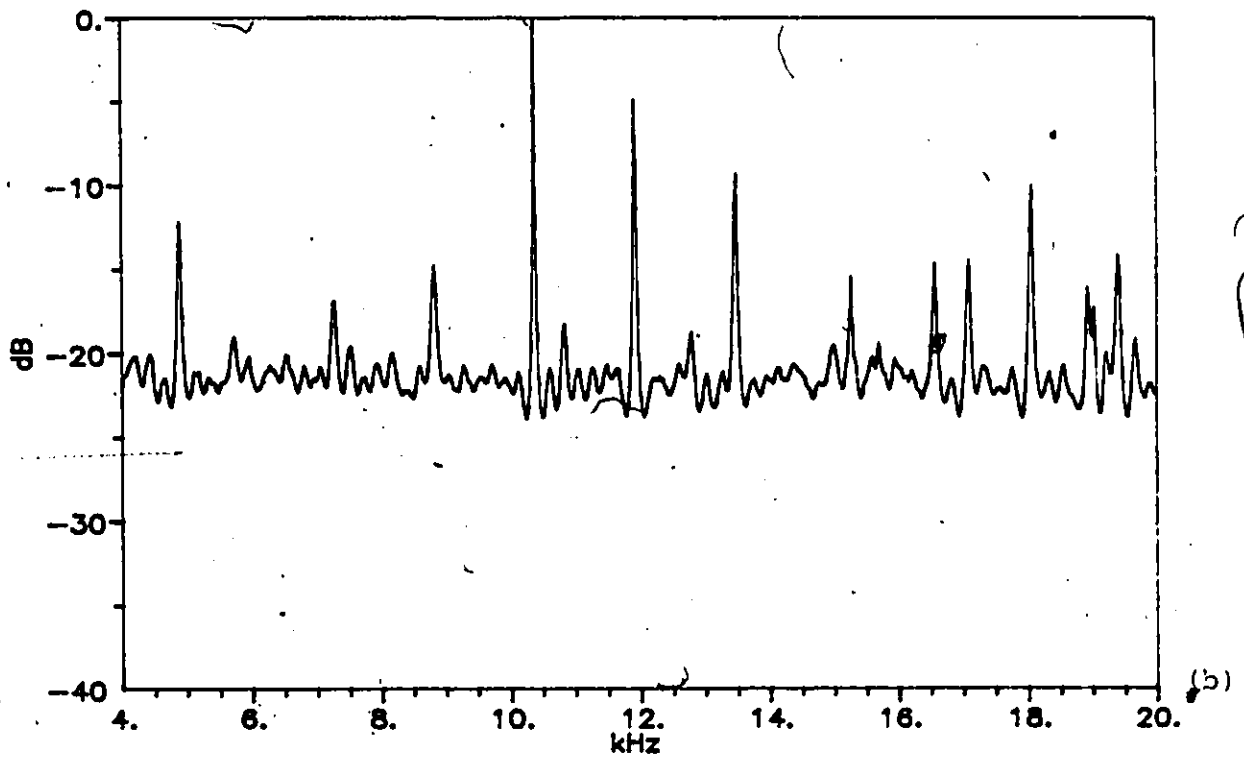

(b)

Fig. 6.23 (a) Ranked MEM estimates for the signal spectra of Fig. 6.20.

(b) Averaged ranked MEM estimate spectrum for the sub-group selection block 16-20 processed by spectrum leveller.

in background noise level also exists at different intervals from the same satellite pass. It is all depending on the amount of interference along the flight path. An adaptive thresholding technique can be employed to compensate this matter; (2) strong interference sources, such as unmodulated carrier signal, have to be identified and filtered prior to signal detection. It is because the probability of false alarm rate is always high when this interference is present and (3) valuable informations about signal and interference can be obtained by studying the satellite pass activity.

6.5 MEASURES OF SATELLITE PASS ACTIVITY

Based on the previous observations, there are two possible temporal designations which can be used to advantage in assessing the activity of the pass. First, is the short term in which interference or signals are received over a short period in time. In this case, the time designation for short term could be durations less than or equal to the output of one averaged spectral estimate, namely one second. The second designation is the long term which would include all durations over one second. For the short term, interference would include bursts of signal or interference which would alter the individual spectral estimates comprising the averaged spectra output. For the long term, the interference would include sources more continuous in time which affect many consecutive averaged spectra output.

6.5.1 Activity Of The Satellite Pass

Real satellite pass data have been reviewed by considering dot charts. It was found that a small fraction of the passes are nearly free of any significant interference, which leaves a large portion with some degree of interference. The number of dots as presented on the dot charts was arbitrarily divided into eight different levels of activity, [illegible]wn in Fig. 6.24. Approximately 100 dot charts were reviewed for each of SARSAT S1 satellite passes at

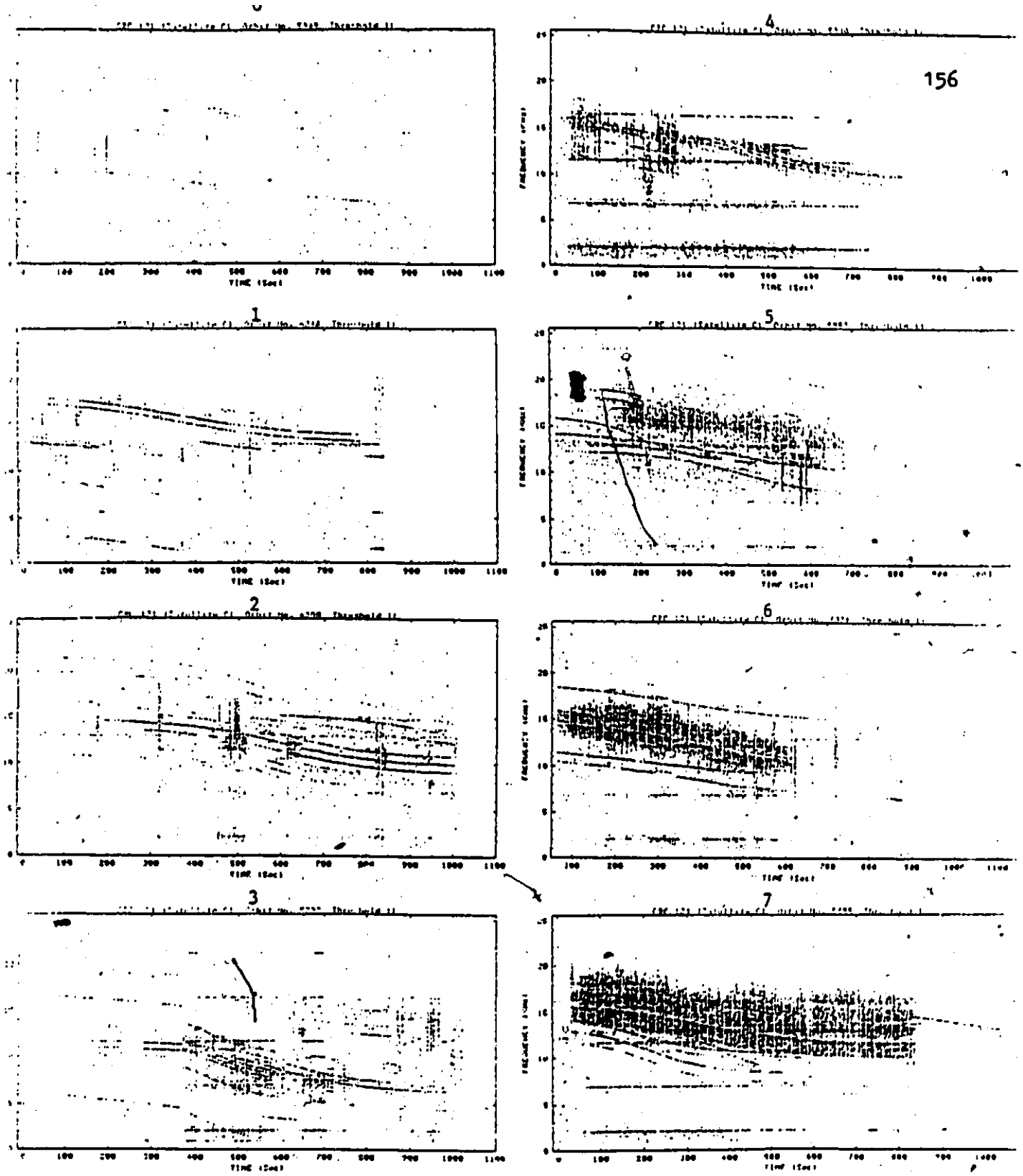

Fig. 6.24 Levels of activity for eight different backgrounds of interference.

121.5 MHz and 243 MHz, and COSPAS satellite C1 passes at 121.5 MHz, with each plot being classified in one of the activity levels. A plot of number in each activity level versus the activity level is given in Fig. 6.25. We see that the activity levels for the three curves are all approximately the same with 56 percent of the charts falling in levels 0, 1, and 2 indicating a low degree of interference. However this also shows that about half of the dot charts indicate significant interference being present.

6.5.2 Threshold Based Activity Measure

There are many independent variables which can be used to describe interference (amplitude, modulation, frequency sweep etc.) but only two which give a useful pictorial description from the dot chart, namely, length of time and bandwidth. The length of time specifies the duration that the interference is present in any one pass and may consist of many different contributions. The bandwidth of each of the contributions is a measure of the amount of frequency band which is occupied by an interfering source. Thus the interference for a given pass can be specified for N interfering sources by defining the time bandwidth (TB) product

$$TB = \sum_{n=1}^{N} T_n B_n \tag{6.8}$$

where T_n is the duration of interference from the n-th source, and B_n is the in-band bandwidth of interference from the n-th source.

If the total duration for a pass is T (600 to 900 s typical) and the bandwidth of the receiver is B (25000 Hz), then the overall goodness of the pass data can be measured by calculating

$$GP = \frac{T*B - TB}{T*B} * 100\% \tag{6.9}$$

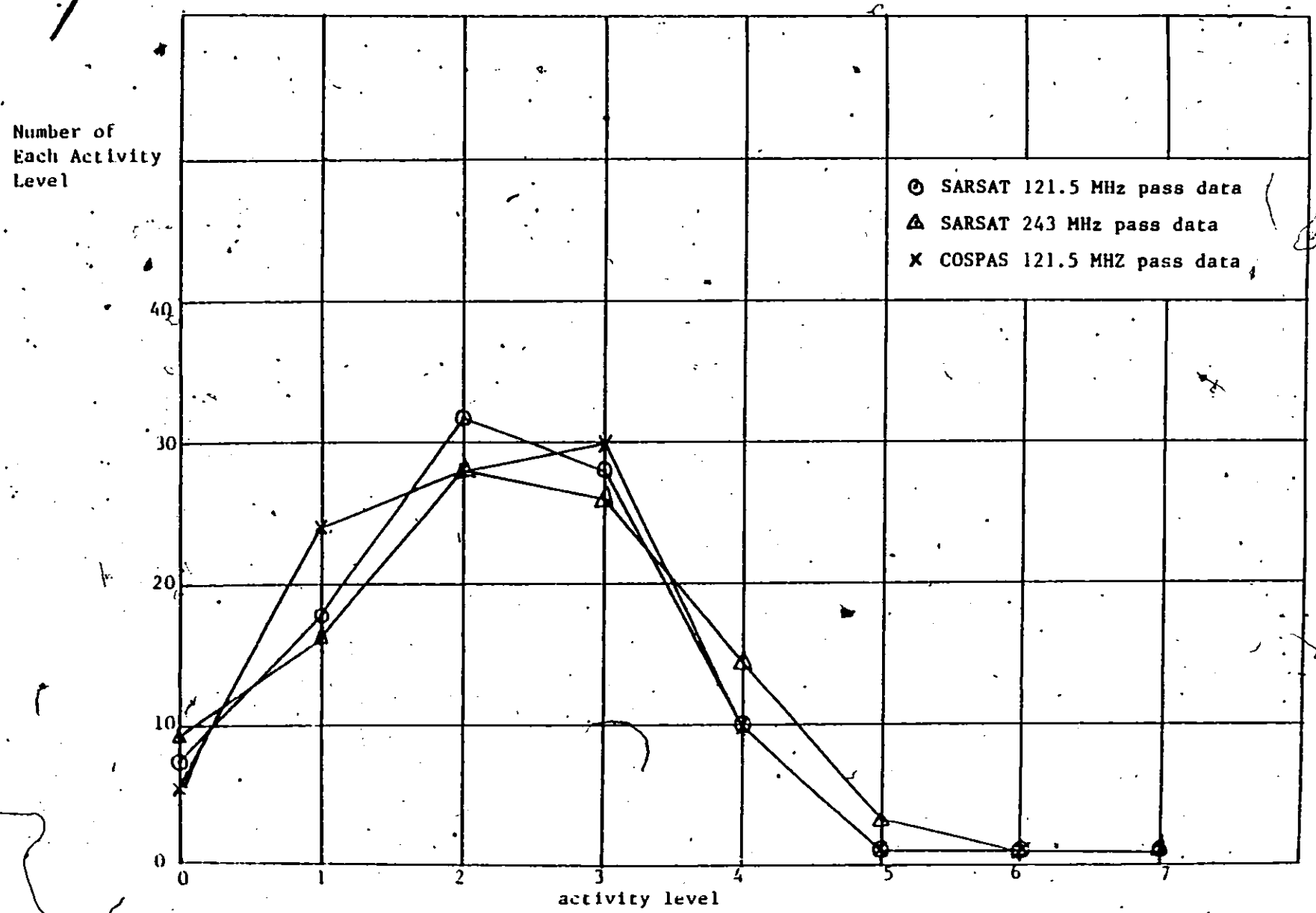

Fig. 6.25 Plot of number of each activity level versus activity level for 100 passes of COSPAS and SARSAR satellites.

For a pass with no interference, GP = 100 percent and for a pass completely jammed GP = 0 percent. In practice this can be implemented by using the threshold data used for the dot plots. The value of GP on receiver noise alone results in a baseline measure.

6.5.3 Spectrum Based Activity Measure

The averaged spectrum provides a useful means for measuring the activity of the pass since CW, NB and WB interference can all be identified easily in the frequency domain.

We have seen that interference can range in bandwidth from very narrow occupying a few tens of hertz to very wide covering thousands of hertz. In addition, the interference may be present for periods ranging from milliseconds to many tens or hundreds of seconds.

Frequency distributed interference can be described by considering the spectrum at the output of the receiver. If the input to the receiver has a flat spectrum, i.e., all components x_i for a given averaged-FFT have the same value. When ELT signals are present, there is an increase in the spectrum level in those locations where the coherent portions of the ELT signals contribute. This is mainly at the carrier peak since the sidebands are approximately 10 dB below the carrier peak (as shown in Fig. 6.26 for a typical averaged FFT estimate of a Pointer ELT). Thus the total contribution to the spectrum from ELT sources is small compared to receiver noise. Consequently, it is possible to compute a meaningful identifier for the detection of interference by calculating the mean μ and the variance σ^2 of the averaged FFT spectral estimate components, as given by

$$\mu = \frac{1}{N}\sum_{i=1}^{N} x_i$$

$$\sigma^2 = \frac{1}{N}\sum_{i=1}^{N} (x_i - \mu)^2 \qquad (6.10)$$

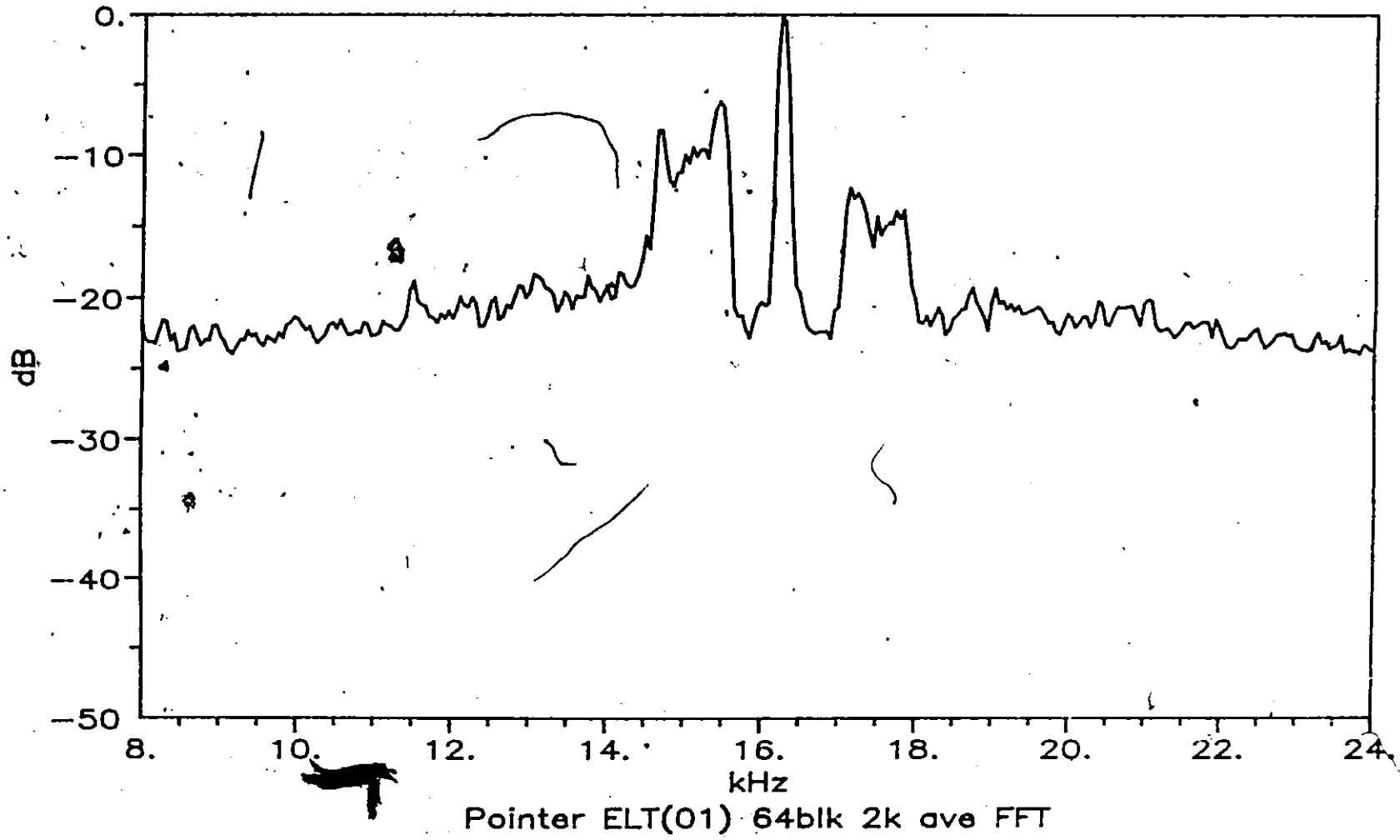

Fig. 6.26 Averaged FFT spectrum for a Pointer ELT showing the relative levels between carrier peak and sidebands.

Consider for example, the result of this computation for five different cases of output averaged spectrum with $N = 1024$.

A. Case 1: Receiver Noise Alone (Gaussian)

All values of x_i are constant since the ouput averaged spectrum is flat. Thus

$$\mu = 1$$

$$\sigma^2 = 0$$

B. Case 2: Few Coherent Sources (Fig. 6.8 for example)

A few values of x_i (say 10) have value 1 and the remaining have value 0.1 (−10 dB). Thus

$$\mu = \frac{1}{N}[10 + (N-10)*0.1] = 0.109$$

$$\sigma^2 = \frac{1}{N}[(1-0.109)^2 * 10 + (0.1-0.109)^2(N-10)] = 0.0078 \tag{6.12}$$

C. Case 3: Single Strong CW Interferer (Fig. 6.9 for example)

All values of x_i are zero except for the point at frequency of the interference. Thus

$$\mu = \frac{1}{N} = 0.00098$$

$$\sigma^2 = \frac{1}{N}(1-0.00098)^2 = 0.00098 \tag{6.13}$$

D. Case 4: Strong Narrowband Interference

Assume, for example, that 10 percent of the points have a uniformly high value with the remaining points being negligible. Then

$$\mu = \frac{1}{10} = 0.1$$

$$\sigma^2 = \frac{1}{N}[0.1N*(1-0.1)^2 + 0.9N*(0.1)^2] = 0.09 \tag{6.14}$$

E. Case 5 : Strong Wideband Interference

Assume that 75 percent of the points have uniformly high value with the remaining points being negligible. Then,

$$\mu = 0.75$$

$$\sigma^2 = \frac{1}{N}[0.75N*(1-0.75)^2 + 0.25N*(0.75)^2] = 0.1875 \tag{6.15}$$

These five cases are plotted in $\mu-\sigma^2$ space as illustrated in Fig. 6.27 and all cases are quite distinct. Thus the $\mu-\sigma^2$ measure provides a possible means for at least some determination of the activity of the pass.

The implementation is quite straightforward. As the averaged FFT estimates are being computed, calculate the μ and σ^2 values as a function of time along the pass. Thus each averaged FFT data set now comprises the spectrum values and a two number set which evaluates the set. After the pass, the μ and σ^2 values can be sorted in $\mu-\sigma^2$ space and analyzed using cluster analysis [36] to determine the characteristics of the resulting pattern.

6.5.4 Envelope Detected Activity Measure

The remaining factor which can easily be measured is the strength e of interfering signals. Since it has been shown that pulsed interference enters the system in different forms, a convenient method of detecting this pulsed interference is by means of an envelope detector.

A particularly useful implementation is to combine the envelope detection with an FFT applied to longer records from the envelope detector. All detected signals are in baseband format which gives a measure of the content of the total signal. Monitoring the zero

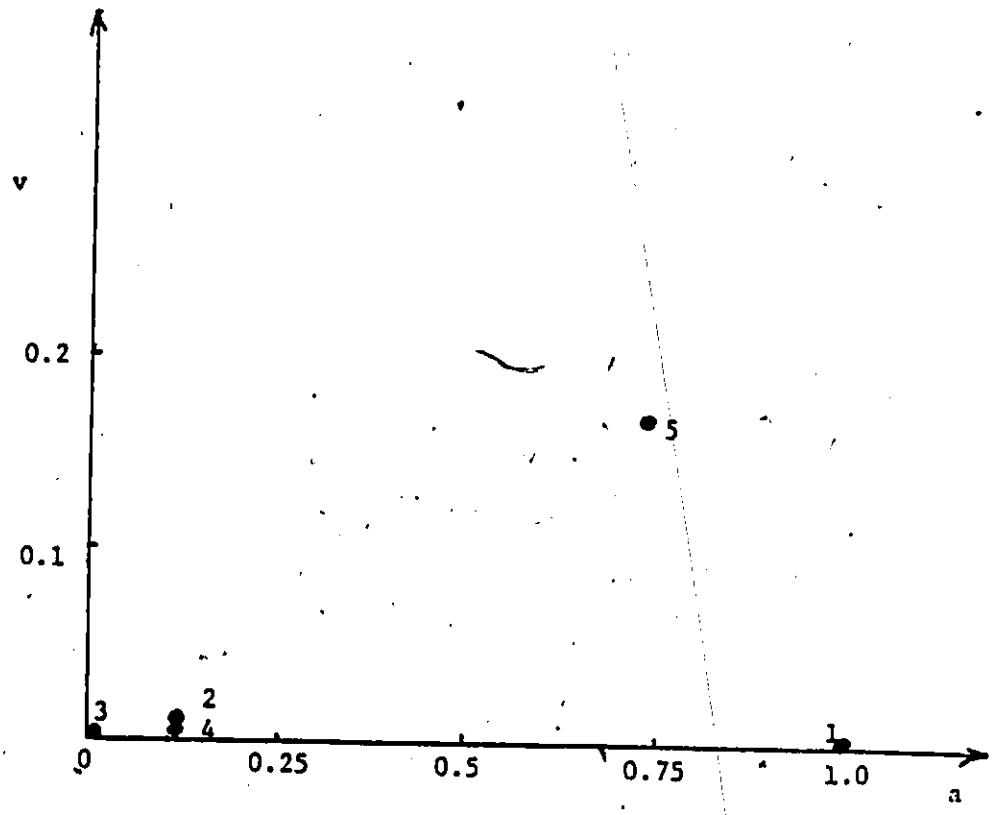

Fig. 6.27 Plot of five different cases of received signal in μ–σ^2 space.

frequency component of the spectrum gives a measure of the total received power while monitoring the bandwidth characteristics of the detected signal, *b*, provides an indication of the amount of modulated carrier in the signal.

The output of an envelope detector is monitored and data points are stored at a rate of perhaps 1024 point per second. The arithmetic sum of these points gives the strength 'e'. For the bandwidth of the interference *b*, the FFT is performed on these data. (Since the FFT is already being called 100 times per second for spectral estimation, the overhead required for this technique is only about one to two percent). Thus interference activity is now available in *e-b* space and the analysis can again proceed using cluster analysis.

6.6 SUMMARY

We have demonstrated that a wide variety of interfering signals enter the SARSAT system and compete with the ELT signals. Examples of continuous wave, narrowband and wideband interference have been presented. In addition, samples of recorded SARSAT receiver output data have been examined and shown to contain CW interference, data modulated carrier, voice modulated carrier and pulse modulated carrier.

Spectral analysis has been performed on two sets of satellite raso data. At different intervals of the pass, ELT signal is shown to experience different degrees of interference. Thus, signal detection cannot be made using simple threshold decision.

Three possible methods of measuring the pass activity have been presented which can be used as interference classifiers. Each method gives some useful information as to the activity of the pass; however further study is required in order to fully evaluate the effectiveness of the methods with real data.

CHAPTER 7

CONCLUSIONS AND RECOMMENDATIONS FOR FURTHER RESEARCH

7.1 CONCLUSIONS

Existing emergency beacons operationg at 121.5 MHz have a distinctive siren-like AM modulation characteristic. Apart from normal production variations in the characteristic of this modulation which is allowed in the specifications, there is no other information incorporated in the signal to differentiate one emergency beacon signal from another.

In the SARSAT signal environment, it is very common to receive multiple emergency signals, combined with interference of various types all simultaneously occupying essentially the same frequency-time space. Although the current signal processing software in the SARSAT system can cope with this signal situation well, the present processing algorithm is based solely on comparing the available data against theoretical Doppler data which would occur from any position in the SARSAT coverage area.

Occasions arise when the SARSAT system computes locations using segmented data available from several different signal sources, but still representing an available Doppler curve. The location thus computed does not represent the location of any real signal source, and is considered to be a generated false alarm.

In view of this, this dissertation contains contributions the areas of identifying the characteristics of ELT signals and models, as well as the signal processing strategies. Specifically, contributions include:

1. Typical ELT units use very simple circuits, having in some cases poor, short-term carrier oscillator stability due to variations in the power supply or loading of the carrier oscillator caused by the modulation being applied to the amplifier stages.

2. ELT units can be classified into three models: the Ideal Coherent, Non-Ideal Coherent and Non-Coherent model. The spectra of these ELT units have been defined accurately by mathematical models.

3. Computer generated spectra for the three ELT signal models are compared with the spectra from real ELT signals. The Non-Ideal Coherent model is found to represent a large percentage of the number of existing real ELT signals. The Non-Coherent model has very poor spectral characteristic. Any design for ELT signal using this model should be avoided.

4. The basic issues in the processing of real and simulated ELT signals are discussed. Several factors have been considered. They are: the spectral estimators; the receiver noise; the Doppler shift and the ELT carrier frequency stability.

5. For processing ELT signals, the window length of the signal affects the frequency resolution of periodogram. The choice of filter order, however, plays a major role in the maximum entropy method.

6. The minimum detectable value of carrier-to-noise density ratio has been measured using simulated Ideal Coherent ELT signal. For a one second data averaging 50 records of 1K periodograms, the calculated value of CNDR is 20 dBHz.

7. Under the changing Doppler shift condition, the minimum window length of the periodogram is deduced for an ELT signal with perfect carrier stability. At the Nyquist rate, a near optimal choice for processing one second of this data is the combination of 12 blocks of 4K periodograms.

8. The bandwidth and Doppler shift of real ELT signals can be identified by computing the averaged periodograms in two or more consecutive time intervals along the satellite pass.

9. Several spectrum estimators and post-processors are proposed to estimate the carrier frequency of ELT signals. The selections include matched filtering, periodogram, maximum entropy method, modified MEM, spectral ranking based on the order statistic, spectral averaging and spectrum leveller.

10. Replicas of ELT signal have been formulated and this can be implemented for matched filtering operation. However, this would require a very large amount of computer time.

11. The averaged periodogram is found to provide effective spectral estimations for Non-Ideal Coherent ELT signals. However, this procedure also exhibits some disadvantages: (1) it generates sidebands which is undesirable for signal detection, and (2) it is incapable of resolving signal with non-coherent characteristic.

12. The modified MEM is shown to be a special processor in evaluating Non-Coherent ELT signal. In this case, a low filter order is sufficient in estimating the carrier frequency of the signal.

13. Spectral ranking based on the order statistic offers several attractive features: (1) it reduces sidebands interference, (2) it suppresses background noise level, and (3) it enhances detection for signal with constant carrier components. Furthermore, the spectral performance can be improved by averaging a selected sub-group from the ranked spectra.

14. Spectrum leveller is shown to benefit the dynamic range for thresholding detection. It also has the ability in reducing rigorous sidebands activities.

15. The aforementioned processing strategies are tested with additive white Gaussian noise. The averaged ranked periodogram equals the detection performance of the averaged periodogram in Gaussian noise and in addition reduces interference due

to sidebands. The averaged ranked modified MEM yields acceptable performance for Non-Coherent ELT signal embedded in noise.

16. There is a significant number of interfering sources which affects the frequency bands of 121.5/243 MHz. These sources are mainly man-made and appear in the forms of impulsive interference and in-band interference. The former produces shock excitation of the receiver which effectively jams the reception of desired signals. The latter produces a competing background which may or may not mask the ELT signals.

17. Data from two satellite passes are studied. Sample traces illustrate continuous wave, narrowband and wideband interference.

18. Spectral analysis are performed on the satellite pass data. Results showed that strong interference increased the complexity of the signal processing strategy and it also reduced the detectability of weak signal sources.

19. It is possible to develop a set of parameters which can evalutate the amount of noise and interference in any satellite pass. Estimation of these parameters can be based on a simple threshold test, or more advanced processes based on spectrum or envelope detection.

7.2 RECOMMENDATIONS FOR FURTHER RESEARCH

Based on the studies carried out in this dissertation, we recommend the following:

1. A robust processing technique has to be developed for identifying ELT signals characteristics and parameters.

2. A study be made of the properties of interference in the real environment. At present, a tape containing 34 satellite passes is available. It is suggested that some

of the more interesting interfering sources be examined to determine their properties.

3. The possibility of using the characteristics of interference background and ELT signal parameters to provide data management within a satellite pass and between satellite passes should be investigated.

4. The methods of evaluation as applied to activity of the pass be tested using real data in order to determine their effectiveness and relative complexity of implementation.

REFERENCES

1. H.L. Werstiuk, "COSPAS-SARSAT: A System Overview", International Electrical Electronics Conference and Exposition, Sept. 26-28, 1983 (Toronto, Ontario), pp. 168-171.

2. M.A. Stott, "Design of the SARSAT Ground Stations", ibid., pp. 172-175.

3. R.J. Bibby and B.W. Kozminchuk, "The Location Accuracy Performance of the Canadian 121.5 MHz COSPAS-SARSAT Signal Processor", ibid., pp. 176-179.

4. J.V. King, E.J. Hayes and G.J. Jutras, "Results of COSPAS-SARSAT System Performance Testing", ibid., pp. 180-183.

5. C.R. Carter, E. Casas and T. Chung, "Emergency Locator Transmitter (ELT) Signal Models for SARSAT", Canadian Electrical Engineering Journal, vol. 11, no. 2, 1986, pp.43-49.

6. T.Chung and C.R. Carter, "Basic Concepts in the Processing of SARSAT Signals", IEEE Transactions on Aerospace and Electronic Systems, vol. AES-23, no.2, March, 1987, pp.175-198

7. F.J. Taylor, Digital Filter Design Handbook, Marcel Dekker Inc., 1983, pp.151.

8. C.E. Cook and M. Bernfeld, Radar Signals, Academic Press, New York, 1967, pp. 9.

9. M.I. Skolnik, Radar Handbook, Mcgraw Hill, New York, 1970, pp. 2-21.

10. K. Tomiyasu, "Tutorial Review of Synthetic Aperture Radar (SAR) with Applications to Imaging of Ocean Surface", Proceeding of the IEEE, Vol. 66, no. 5, May, 1978, pp. 563-583.

11. S. Haykin, Communication Systems, 2nd edition, John Wiley, 1983.

12. E. Casas and C.R. Carter, "Two Methods of Spectral Estimation for SARSAT Signals", IEEE Transactions on Aerospace and Electronic Systems, vol. AES-21, no. 4, July 1985, pp. 559-568.

13. J.M. Wozencraft and I.M. Jacobs, Principles of Communications Engineering, John Wiley, 1965, pp. 233-236.

14. A.V. Oppenheim and R.W. Schafer, Digital Signal Processing, Prentice-Hall Inc., Englewood Cliffs, N.J., 1975.

15. L.R. Rabiner and B. Gold, Theory and Application of Digital Signal Processing, Prentice-Hall Inc., Englewood Cliffs, N.J., 1975.

16. C.R. Carter, "Data Recordings of ELT Signals for Spectral Analysis", Communications Research Laboratory, CRL Internal Reoport Series, No. CRL-110, McMaster University, Hamilton, Ontario, Nov., 1982.

17. T. Chung, "Digital Bandpass Processing for SARSAT Signals Using the MEM and FFT", M. Eng. thesis, McMaster University, Hamilton, Ontario, Aug., 1982.

18. T. Chung, A. Premji and C.R. Carter, "Signal Processing Methods for SARSAT Signals", Internatinal Electrical and Electronics Conference and Exposition, Sept. 26-28, 1983 (Toronto, Ontario), pp. 194-197.

19. A. Premji, "Processing of ELT Signals for Search And Rescue Satellite Aided Tracking Using the MEM and FFT", M. Eng. Thesis, McMaster University, March, 1982.

20. IEEE Proceeding special issue on Spectral Estimation, vol. 79, no. 9, 1982.

21. S. Haykin and S.B. Kesler, "Prediction-Error Filtering and Maximum Entropy Spectral Estimation", in Non-Linear Methods of Spectral Analysis, ed. S. Haykin, Springer Verlag, Berlin, 1979, ch. 2.

22. J.P. Burg, "Maximum Entropy Spectral Analysis", Ph.D. Thesis, Stanford University, Stanford, California, May, 1975.

23. N. Anderson, "On the Calculation of Filter Coefficients for Maximum Entropy Method of Spectral Analysis", Geophysics, vol. 39, no. 1, Feb. 1974, pp. 69-72.

24. T. Chung and C.R. Carter, "Signal Processing of Real ELT Signals", Communications Research Laboratory, CRL Internal Report Series, no. CRL-133, McMaster University, Hamilton, Ontario, Oct. 1984.

25. M.A.R. Makhlouf, C.E. Goutis, H.C. Yung and C.R. Allen, "Concurrent VLSI architecture for Covariance-Lattice Computations in Maximum Entropy Spectrum Estimations", International Conference on Digital Processing of Signals in Communications, April 22-26, 1985 (Loughborough, England), IERE publication no. 62, pp. 287-292.

26. A.A. (Louis) Beex and Md. Anisur Rahman, "On Averaging Burg Spectral Estimators for Segments", IEEE Transactions on Acoustics, Speech, and Signal Processing, vol. ASSP-34, no. 6, Dec. 1986, pp. 1473-1484.

27. M.A. Lagunas-Hernandez, "Use of the Most Significant Autocorrelation Lags in Iterative ME Spectral Estimation", IEEE Transactions on Acoustics, Speech, and Signal Processing, vol. ASSP-32, no. 2, April 1984, pp. 445-448.

28. A.C. Bovik, T.S. Huang and D.C. Munson Jr., "A Generalization of Median Filtering Using Linear Combinations of Order Statistics", IEEE Transactions on Acoustics, Speech, and Signal Processing, vol. ASSP-31, no. 6, Dec. 1983, pp. 1342-1350.

29. T. Chung and C.R. Carter, "Processing of Real ELT Signals for SARSAT", Canadian Electrical Engineering Journal, vol. 12, no. 1, 1987, pp. 33-44.

30. K.M. Wong and Y.P. Lee, "Robust Spectrum Estimation Using Order Statistics", Conference on Antenna and Communication, IEEE MONTECH' 86, Sept. 29 - Oct. 1, 1986, pp. 353.

31. J.B. Bednar and T.L. Watt, "Alpha-Trimmed Means and their relationship to Median Filters", IEEE Transactions on Acoutics, Speech, and Signal Processing, vol. ASSP-32, no. 1, Feb. 1984, pp. 145-153.

32. K.M. Wong, "Sonar Data Normalization Using Order Statistical Filters", Communications Research Laboratory, CRL Internal Report Series, no. CRL-144, McMaster University, Hamilton, Ontario, Nov. 1985.

33. S.M.A. El-Naga, "Techniques For Identifying Search And Rescue Satellite Aided Tracking (SARSAT) Signals", Ph.D. Thesis, McMaster University, July, 1986.

34. H. Rohling, "Radar CFAR Thresholding in Clutter and Multiple Target Situations", IEEE Transactions on Aerospace and Electronic Systems, vol. AES-19, no. 4, July 1983, pp. 608-621.

35. H. Rohling, "New CFAR Processor Based on an Order Statistic", IEEE International Radar Conference, (Arlington, VA.), May 6-9, 1985, pp. 271-275.

36. C.R. Carter and T. Chung, "Interference in the 121.5/243 MHz SARSAT Frequency Bands", IEEE Transactions on Aerospace and Electronic Systems, vol. AES-21, no. 6, November, 1985, pp. 804-817.